AD

RSIC-721

AERODYNAMICS OF THE MODEL AIRPLANE.

PART I. AIRFOIL MEASUREMENTS

by

F. W. Schmitz

(This work was awarded the Ludwig Prandtl Prize for 1941)

Translated from the German

November 1967

DISTRIBUTION LIMITED
SEE NOTICES PAGE

REDSTONE SCIENTIFIC INFORMATION CENTER
REDSTONE ARSENAL, ALABAMA

JOINTLY SUPPORTED BY

U.S. ARMY MISSILE COMMAND

GEORGE C. MARSHALL SPACE FLIGHT CENTER

DISTRIBUTION LIMITATION

Each transmittal of this document outside the agencies of the U. S. Government must have prior approval of this Command, ATTN: AMSMI-RBT.

DISCLAIMER

The findings of this report are not to be construed as an official Department of the Army position unless so designated by other authorized documents.

DISPOSITION INSTRUCTIONS

Destroy this report when it is no longer needed. Do not return it to the originator.

22 November 1967

RSIC-721

AERODYNAMICS OF THE MODEL AIRPLANE. PART I. AIRFOIL MEASUREMENTS

by

F. W. Schmitz

(This work was awarded the Ludwig Prandtl Prize for 1941)

Translation Branch
Redstone Scientific Information Center
Research and Development Directorate
U. S. Army Missile Command
Redstone Arsenal, Alabama 35809

FOREWORD

The pronounced deviations which occur in the aerodynamic properties of airfoil profiles below a certain Reynolds number became known to me early, and I had therefore planned a systematic study of this "peacetime matter" for myself at some quieter time in the future. I am therefore happy that Mr. Schmitz has become involved so successfully, even in this time of war, with this task in the interest of working groups set up at the schools and of model-airplane flying in general. This book not only represents a very remarkable advance in model-airplane flying which will undoubtedly be an inspiration in this field to new research by scholars, but it also will give very instructive conclusions to the fluid dynamics experts through what are in part new and surprising results.

Goettingen, July 1942.

Professor L. Prandtl
Director of the Kaiser Wilhelm Institute
for Flow Research

CONTENTS

CONTENTS (Continued)

CONTENTS (Continued)

CONTENTS (Continued)

CONTENTS (Concluded)

PREFACE

The Government Minister for Science and Education made two prizes available to the Presidency of the Lilienthal-Gesellschaft fuer Luftfahrtforschung (Lilienthal Society for Aeronautical Research), at their general meeting in 1937 in Munich, to be awarded every year on the anniversary of Lilienthal's death. As explained in detail in the proclamation of 13 April 1938, these prizes are to furnish the new generations with incentive for the study of the technology and science of aviation. First is the Lilienthal Prize, which gives to qualified German secondary-school graduates the material prerequisite for the study of aeronautical sciences, and second is the Ludwig Prandtl Prize for Promotion of Aeronautical Physics in Connection with Airplane Model Building, awarded for the best accomplishments each year in the described field in the secondary schools.

According to the eligibility rules for the Ludwig Prandtl Prize, the work can be done by teachers, by pupils, or as a joint effort. These efforts of pupils or joint efforts are directed toward promotion of the selection of future engineers and scientists for aviation, since the pupils learn to apply interesting aeronautical fundamentals, so that they can be won for aeronautical study with a clearly directed vocational goal.

To supply the schools with the fundamentals constituting a connection between aviation physics, model-airplane building, and model-airplane flying, the model airplane -- as an entity in itself -- is subjected in my paper to an aerodynamic study. Since I had observed certain contradictions between practical data of model flight and the flow laws of large airplanes, I received from the National Ministry of Education in reply to my recommendations the mission of clarifying the relationships of airfoil measurements at the Reynolds numbers of model flight. The measurements were finished in June 1939, and the text was finished in June 1940. Publication was delayed by the war.

The surprising results, which can serve as the first systematic foundation for scientifically directed model-airplane building, establish the necessity for an "aerodynamics of model flight" as a special field of work to complete the total physical picture. The first group of my test results to date and their explanations are hereby submitted to the German schools and to model-airplane building for application.

Berlin, March 1942.

F. W. Schmitz

EXPLANATION OF SYMBOLS

1. Geometric Quantities

a) Profile

Symbol	Unit of Measurement	Explanation
t	m	Chord length, projection of the profile outline on the lower-surface tangent ("t" is usually the airfoil thickness and "c" the chord length in the U.S.)
d	m	Maximum profile thickness
f	m	Camber rise of the profile mean line above the theoretical chord of the profile mean line
r	m	Nose circle radius
d/t, f/t, r/t	-	Profile parameters
x, y_o, y_u	-	Profile outline coordinates
α	deg	"Geometric" angle of attack, measured between the lower-surface tangent and the direction of airflow
σ	deg	Chord angle, angle between the lower-surface tangent and the theoretical chord of the profile mean line
$\alpha_s = \alpha + \sigma$	deg	Angle of attack of the mean line chord (theoretical chord)
α_∞	deg	"True" angle of atack of the lower-surface tangent to a wing of infinite span
$\alpha_{s\infty} = \alpha_\infty + \sigma$	deg	"True" angle of attack of the mean line chord of a wing of infinite span
α_o	deg	"True" angle of attack, measured from the zero-lift direction of airflow $(c_a = 0)$
β	deg	Zero-lift angle of attack of the lower-surface tangent
$\beta_s = \beta + \sigma$	deg	Zero-lift angle of attack of the chord
α_k	deg	Critical angle of attack at breakaway of the flow

b) Wing

Symbol	Unit of Measurement	Explanation
b	m	Wingspan
F	m^2	Wing area, projection of the wing plan on the lower-surface tangent
$\Lambda = b/t = b^2/F$	-	Aspect ratio
$1/\Lambda = t/b = F/b^2$	-	Reciprocal of aspect ratio
α_m	deg	Angle of attack of the lower-surface tangent of the wing model in the wind tunnel measurement
α_5	deg	Angle of attack of the lower-surface tangent of the rectangular wing with $\Lambda = 5$ after taking into account the influence of finite airflow diameter

2. Aerodynamic Quantities

a) Air

General subscripts: o on the upper surface of the profile
u on the lower surface of the profile
∞ in the undisturbed flow

Symbol	Unit of Measurement	Explanation
γ	kg/m^3	Air density, weight of unit volume
$g = 9.81$	m/sec^2	Acceleration of gravity
$\rho = \gamma/g$	$kg \cdot sec^2/m^4$	Air density, specific mass
v or v_∞	m/sec	Velocity of undisturbed flow
$q = \rho \cdot v^2/2$	kg/m^2	Dynamic pressure
p	kg/m^2	Pressure
p/q	-	Coefficient of pressure
c = 340	m/sec	Velocity of sound
v/c	-	Mach number
η	$kg \cdot sec/m^2$	Absolute viscosity
$\nu = \eta/\rho$	m^2/sec	Kinematic viscosity
δ	mm	Thickness of the boundary layer

b) Wing

Symbol	Unit of Measurement	Explanation
$Re = v \cdot t/\nu$	-	Reynolds number
$Re_K = v_K \cdot t/\nu$	-	Critical Reynolds number
$Re_\delta = v \cdot \ell/\nu$	-	Local Reynolds number at the free edge of the boundary layer; ℓ = length of friction distance
$TF = Re_{K\,air}/Re_{K\,tunnel}$	-	Turbulence factor
$Re_{eff} = Re_{meas} \cdot TF$	-	Effective Reynolds number
A	kg	Lift $\perp v_\infty$
W	kg	Drag $\parallel v_\infty$
M	kg · m	Moment about the front projected point on the lower-surface tangent
$M_{0.25}$	kg · m	Moment about a center of rotation at 0.25 t (quarter chord) behind the leading edge and on the mean line chord
M_h	kg · m	Moment about the center of gravity
N, T	kg	Normal force and tangential force components of the resultant air force
e/t	-	Distance of the center of pressure from the leading edge
x/t	-	Distance of the center of gravity from the leading edge
$c_a = A/q \cdot F$	-	Lift coefficient ("c_L" is generally used in the U.S.)
$c_w = W/q \cdot F$	-	Drag coefficient ("c_D" is generally used in the U.S.)
$c_m = M/q \cdot F \cdot t$; $c_{m\,0.25} = M_{0.25}/q \cdot F \cdot t$; $c_{mh} = M_h/q \cdot F \cdot t$		Moment coefficients: referred to the forward center of rotation; referred to the center of rotation at t/4; referred to the center of gravity

Symbols	Unit of Measurement	Explanation
c_{wm}	-	Drag coefficient for the uncorrected measurement
c_{wk}	-	Correction value for the influence of finite stream diameter
$c_{w5} = c_{wm} - c_{wk5}$	-	Drag coefficient of a rectangular wing with $\Lambda = 5$, with finite airflow diameter taken into account
$\alpha_5 = \alpha_m - \alpha_{k5}$	deg	The angle of attack corresponding to c_{w5}
c_r	-	Coefficient for resultant aerodynamic force
c_n, c_t	-	Coefficients of normal force or tangential force; center of pressure lying on the lower-surface tangent
c_{ns}, c_{ts}	-	Coefficients for normal force and tangential force; center of pressure lying on the mean line chord
$c_f = W/q \cdot 0$	-	Coefficient of surface friction ($0 = 2$ F)

c) Profile

$c_{wi} = c_a^2 \cdot F/\pi \cdot b^2$	-	Coefficient of induced drag
$c_{w\infty} = c_{w5} - c_{wi}$	-	Profile drag coefficient
$\alpha_i = 57.3 \cdot c_a \cdot F/\pi \cdot b^2$	deg	"Induced" angle of attack
$\alpha_\infty = \alpha_5 - \alpha_i$	deg	"True" angle of attack of the lower-surface tangent, corresponding to $c_{w\infty}$
$\alpha_{s\infty} = \alpha_\infty + \sigma$	deg	True angle of attack of the chord
$dc_a/d\hat{\alpha}$	-	Slope of the lift curve
$c_a/c_{w\infty}$	-	Lift-drag ratio (for infinite span
$c_a^3/c_{w\infty}^2$	-	Ceiling factor

d) Propeller

Symbol	Unit of Measurement	Explanation
r	m	Radius
t	m	Blade thickness
v	m/sec	Air velocity in the propeller circle
v_∞	m/sec	Flight velocity
u	m/sec	Peripheral velocity
w	m/sec	Velocity of a blade element on the propeller path
$Re_{0.7}$	-	Reynolds number of the blade element at radius 0.7 r

e) Model Airplane

v	m/sec	Gliding velocity
v_y	m/sec	Sinking velocity
v_x	m/sec	Horizontal velocity
φ	deg	Gliding angle
$\epsilon = v_y/v_x = c_w/c_a$	-	Drag-lift ratio
$= W/A = H/B_3$		H = height, B = base of the glide triangle
$= \tan \varphi$		
c_w^2/c_a^3	-	Ceiling factor reciprocal
G	kg, g	Gross weight
G/F	kg/m^2; g/dm^2	Wing loading

I. INTRODUCTION

The measurements of aerodynamic force on airfoil models in the wind tunnel by means of the three-component balance are the most important basis of aeronautics. The airfoil measurements [3]*) published by the Aerodynamische Versuchsanstalt Goettingen (Goettingen Aerodynamics Research Laboratory) should be mentioned as the most widely used. They were made at a Reynolds number Re = 420,000. The Reynolds number gives the order of magnitude of the flow conditions. The Goettingen measurements correspond to the order of magnitude of the smallest manned sailplane. For model flight, where the Reynolds number range is below 200,000, these measurements have no more validity than for the airfoil flow, for example, of the Messerschmidt record-holding airplane, which at v = 210 m/sec and an average chord length of about 3 m, corresponds to Re = $44 \cdot 10^6$. For model flight, special airfoil measurements had to be made in the Reynolds number range mentioned.

The range of Reynolds numbers for model aviation covered by the following airfoil measurements extends from Re = 21,000 to 168,000. Five profiles were measured, chosen so that their results showed the greatest possible contrast, to delimit the problem of profile properties in this range of Reynolds numbers.

In the range of Reynolds numbers below 150,000, each profile passes through a critical range in which the boundary layer becomes turbulent, and the previously laminar separated flow attaches itself so that the lift coefficient c_a becomes greater, the drag coefficient c_w smaller, and thus the drag-lift ratio c_w/c_a formed from the two becomes suddenly larger, so that the model airplane first becomes able to fly.

From the comparison of test results for the five profiles there is found for the model airplane:

1. Rules for profile choice in regard to the parameters: profile thickness d/t, mean camber f/t, and leading-edge radius r/t.

2. Rules for the choice of wing plan.

3. Rules for the choice of the model airplane propeller with respect to the blade profile and blade plan.

---

*) The numbers in brackets refer to the bibliography at the end of the book.

4. Comparison of the measurements on profiles N 60 and N 60R shows to what extend the S-shaped curvature of the mean line affects the moment coefficient or aids in achieving constancy of the center of pressure at low Reynolds numbers.

5. The results turn model-airplane building again to the study of the biological example, bird flight, in the sense of Lilienthal, because bird and model airplanes fly in the same range of Reynolds numbers.

6. Measures for artificial turbulence by wall roughness, turbulence-producing edges, or wires stretched in front of the wing on the model airplane, in analogy to the classic sphere research with and without wire rings (by Prandtl and Wieselsberger) prove to have a favorable effect, in contrast to their harmful influence on the large plane.

7. An attempt is made, using the study of the individual phenomena of flow around an airfoil, to explain the flow causes in the critical region.

The measurements first became possible after the airflow could be made largely free of turbulence by modification of the wind tunnel used.

Because these measurements were to be used on one hand for physics instruction and on the other hand for model airplane building, that is, to direct the interest of youth, through the teachers, to aviation research, it appeared advantageous to formulate the basic laws of boundary layer flow and flow around an airfoil necessary for explanation of the test results.

The basic concepts of aeronautical physics required in the syllabus of physics of the secondary schools were presupposed for understanding of this. An example is the book Einfuehrung in die Physik des Fliegens (Introduction to the Physics of Flight) by Schuett, Verlag C. J. E. Volckmann, Nachf. E. Wette, Berlin-Charlottenburg). In addition, knowledge of the quantitative application of these basic ideas - corresponding, say to the Flugphsikalischen Arbeitsbuch (Workbook in Aeronautical Physics) by Kisse, Verlag G. Freytag, Berlin, and B. G. Teubner, Leipzig - is presupposed. The author published a short discussion of the basic problem in the No. 3 issue of the year 1942 of Unterrichtsblaetter fuer Mathematik und Naturwissenschaften (Instruction Sheets for Mathematics and Natural Sciences), Verlag Otto Salle, Frankfurt a.M. To allow the teacher to explain the interesting relationships to model fliers less well-educated mathematically, the January 1942 issue of the magazine Luftfahrt und Schule (Aviation and School), Verlag C. J. E. Volckmann Nachf. E. Wette, Berlin-Charlottenburg), began a series by the author under

the title "Fluid Dynamics Study of the Model Airplane," with simple examples of calculation, and flight and school experiments.

II. FUNDAMENTALS AND FORMULATION OF THE PROBLEM

1. Comparison: Sailplane, Model Sailplane, Bird

a) The Similarity Law (Re = constant)

The bird is the natural prototype of the model airplane. The contemporary model airplane builder, however, in contrast to Lilienthal, thinks little about bird flight. His prototype is the large airplane, which he seeks to copy as closely as possible in the model. This tendency in development led to contradictions between the facts of experience of model flight and the aerodynamics of the large airplane. Although there is an aerodynamic relationship between bird flight and model flight, since both occur in the ranges of similar Reynolds numbers, fulfillment of the similarity law of Reynolds is not possible between the small free-flying model airplane and the large airplane, as a comparison will show.

A model airplane, which represents the geometrically similar imitation of a large sailplane, will give a poorer drag-lift ratio in comparable flight (unaccelerated gliding flight in still air) the smaller it is. If the sailplane has, for example, a drag-lift ratio of:

$$\left(c_w/c_a\right)_F = {}^1/_{20} \ ,$$

then experience shows that with a model airplane on a 1:10 scale the gliding distance is about half, and thus the drag-lift ratio expected would be:

$$\left(c_w/c_a\right)_M = {}^1/_{10} \ .$$

(The subscript F = airplane and M = model.)

The deterioration in drag-lift ratio is caused, as is well known, by the lack of similarity of the streamlines, because the inertia forces of the air $\rho\, v^2/t$, effective along the wing chord t, decrease more than do the viscosity forces of the air, $\eta\, v/t^2$, when the model is reduced. Only if it is possible to hold constant the ratio of the two, that is, the Reynolds number:

$$\mathrm{Re} = \frac{\text{inertia force}}{\text{viscosity force}} = \frac{\rho\, v^2/t}{\eta\, v/t^2} = \frac{\rho\, vt}{\eta} = \frac{vt}{\nu}$$

(ρ = air density, v = velocity, t = wing chord, η = absolute viscosity, $\eta/\rho = \nu$ = kinematic viscosity)

will this similarity law of flow be fulfilled, allowing the model airplane to achieve the same flight performance as the large airplane. Therefore if the model airplane had a wing chord t of $^1/_{10}$ the wing chord of the large airplane, it would have to glide at 10 times the speed. Ten times the speed in unaccelerated gliding flight is not possible for free flying model airplanes, however. The reason for this is as follows. From:

$$\text{gliding speed } v = \sqrt{\frac{G}{F} \cdot \frac{2}{\rho} \cdot \frac{1}{\sqrt{c_a^2 + c_w^2}}} \quad *)$$

there follows for $v_M = 10\, v_F$ the equation:

$$\frac{v_M}{v_F} = \frac{10}{1} = \frac{\sqrt{(G/F)_M}}{\sqrt{(G/F)_F}}$$

and from this the wing loading of the model airplane:

$$(G/F)_M = 100\, (G/F)_F$$

Because a 1:10 linear reduction means an area reduction of $F_M = F_F/100$, the model airplane weight G_M required for 100 times the wing loading is calculated from

$$\frac{G_M}{F_M} = \frac{100\, G_F}{F_F} \text{ or from } \frac{G_M}{F_F/100} = \frac{100\, G_F}{F_F}$$

$$G_M = G_F$$

The fulfillment of this similarity law thus leads to the practically impossible requirement that the model airplane and the airplane must have the same weight.

---

*) The root under the fraction stroke gives the coefficient of the resultant air force c_r through use of the Pythagorean theorem for the triangle short sides c_a and c_w. For flat gliding flight, c_r can be taken as approximately c_a.

To make model flight possible, model airplane building is compelled to go in the opposite direction, using lightweight construction to make the wing loading and thus the sinking speed as low as possible, to what extent the "gust sensitivity" of model flight permits. Fluid dynamics therefore could learn little in quantitative fundamentals from measurements on free-flight small model airplanes (see [5], vol. IV, part 2, A. Betz, p. 211) because it is much more suitable to hang the model airplane in the wind tunnel, allow the air to flow by at say ten times the speed, and to measure the aerodynamic forces acting on the model airplane by means of the wire suspension attaching it to the balances. The essential experimental fundamentals for aerodynamic calculation of the airplane were found through this model testing in the wind tunnel. There was no practical economic interest in measurements at the low speeds of free-flying model airplanes, so that model airplane building - aerodynamically considered - was left to the hazard of testing. If, however, as described in this work, there are measurements both at the Reynolds number of the large airplane as well as at the Reynolds number of the model airplane, then it is possible to calculate the flight performance and flight characteristics of the model airplane and to test the correctness by flight measurements.

In the model airplanes common today, about five major classes can be differentiated, and the Reynolds number ranges of these are given in List 1. To show the aerodynamic relationship, three types of soaring birds in the same range of Reynolds numbers are added, and in addition, as a contrast, the Reynolds numbers of various airplanes.

Note on the calculation of Reynolds number:

$$\mathrm{Re} = \frac{v \cdot t}{\nu}.$$

The kinematic viscosity (also called viscosity modulus) ν has the dimension L^2/T.

For air at 13° and 760 mm Hg, $\nu = 0.143\ \mathrm{cm^2/sec} = 0.0000143\ \mathrm{m^2/sec}$. For water at 20° and 760 mm Hg, $\nu = 0.01\ \mathrm{cm^2/sec} = 0.000001\ \mathrm{m^2/sec}$.

The kinematic viscosity of air is about 14 times as great as that of water, so that in water $1/14$ of the speed is required to achieve the same Reynolds number as in air.

The numerical values for air density ρ and for ν as a function of temperature and air pressure can be taken from data in the literature ([3] I, pp. 135 and 136, or from [5] vol. IV, part 2, p. 113). The Reynolds number change caused by atmospheric fluctuations at a given reading of the dynamic indicator

is, for example, about +10 percent from B = 740 mm Hg and 20°C to 780 mm and 0°C.

For the upper range of measurement of the following airfoil measurements there resulted at a maximum velocity of v = 27 m/sec with a chord length t = 90 mm:

$$Re_{max} = \frac{2700\ cm/s \cdot 9\ cm}{0.143\ cm^2/s} = \frac{27\ m/s \cdot 0.09\ m}{0.0000143\ m^2/s} = 170,000$$

List 1

Ranges of Validity of Reynolds Numbers*)

	Mean Wing Chord t (mm)	Velocity v (m/s)	Re = v · t · 70
Zanonia plate	40	1	2800
Gliding butterfly	50	2	7000
Indoor model airplane	60	2	8400
	150	4	42,000
Swift	30	min 6.1	12,800
		max 39**)	82,000
Small model airplane	100	3	21,000
	150	6	63,000
Medium size model airplane	150	4	42,000
	200	10	140,000
Herring gull	140	10	100,000
Large model airplane	200	4	56,000
	300	10	210,000
Albatross	200	16	224,000
High-performance sailplane	900	$v_L = 10$	630,000
		$v_{max} = 60$	3,800,000

*) The Reynolds numbers are calculated from the mean wing chord. For a tapered wing, the Reynolds number at the wing tip is correspondingly smaller, and larger at the wing root. In this, v_L = landing velocity, v_R = flight velocity.

**) According to R. Schmidt (see [18], p. 84), the swift does not soar, but like the swallow, makes only short gliding flights.

List 1 (Concluded)

Ranges of Validity of Reynolds Numbers

	Mean Wing Chord t (mm)	Velocity v (m/s)	Re = v · t · 70
Training glider	1600	10	1,100,000
Small sport plane	1200	v_L = 20	1,700,000
		v_R = 40	3,400,000
Commercial Ju 52 plane	3600	v_L = 28	7,000,000
		v_R = 96	25,000,000
Messerschmitt record-holding plane (V = 755 km/h)	3000	210	44,000,000

If the comparison between model airplane and airplane is made in air of the same kinematic viscosity ν, then the similarity law will be satisfied if the characteristic E = v · t is kept constant. This simplified but incomplete form of the similarity law has not established itself and was not used here. If v is in units of m/sec and t in mm, then Re is roughly 70 times the value of E; for example:

$$Re = 27 \text{ m/s} \cdot 90 \text{ mm} \cdot 70 = 170,000$$

It should be mentioned in this connection that changes in flow dependent upon Reynolds number are called "Reynolds number influence"; rounded bodies are "Reynolds number-sensitive"; sharp-edged bodies are "Reynolds number-insensitive."

b) Wing Loading and Drag-Lift Ratio

For model airplane building there is technically no difficulty in reducing the wing loading by lightweight construction to

$$(G/F)_M = 4\text{-}0.1 \text{ kg/m}^2 = 40\text{-}1 \text{ g/dm}^2 ,$$

the lower value corresponding to the indoor model airplane covered with thin film. This is about $1/5$ to $1/200$ of the wing loading of the sailplane, which is between 20 and 10 kg/m^2. The wing loading of birds varies between the 16 kg/m^2 of the albatross and the 1.7 kg/m^2 of the swallow; that of butterflies is between 0.17 and 0.1. Here model airplane building follows the prototype of nature. The low wing loading considerably reduces the sinking velocity:

$$v_y = \sqrt{\frac{G}{F} \cdot \frac{2}{\rho} \cdot \frac{c_w^2}{c_a^3}}$$

and in spite of a low drag-lift ratio, an equal or longer flight time is achieved compared with that of the sailplane. The necessary performance required for horizontal floating in a thermal or by means of an engine is found, as is well known, at the minimum of v_y or $\left(c_a^3/c_w^2\right)_{max}$ in the polar plot. Flight at this angle of attack therefore corresponds to the longest gliding time, while the somewhat smaller angle of attack corresponding to $c_a/c_{w\,max}$ gives the longest gliding range. These two values are shown for two examples in Figure 1. For the same wing loadings $(G/F)_M = (G/F)_F$, the sinking velocities are related as the roots of the ceiling factor reciprocals c_w^2/c_a^3. Applied to the example given, there result:

$$\frac{(v_y)_M}{(v_y)_F} = \frac{\sqrt{(c_w^2/c_a^3)_M}}{\sqrt{(c_w^2/c_a^3)_F}} = \frac{\sqrt{\frac{1}{10^3}}}{\sqrt{\frac{1}{20^3}}} = \sqrt{8}\ .$$

The model airplane in this case will have a sinking velocity $\sqrt{8} = 2.8$ times as great. To bring the model airplane to the same sinking velocity, its wing loading must be reduced to $1/8$; then it achieves the same gliding duration and the same climbing ability in a thermal as the large airplane. The ratio of gliding velocities is then:

$$\frac{v_M}{v_F} = \frac{\sqrt{\frac{1}{8}\sqrt{\frac{1}{c_a^2 + c_w^2}_M}}}{\sqrt{\sqrt{\frac{1}{c_a^2 + c_w^2}_F}}} \approx \frac{1}{2}\ ,$$

and the ratio of the Reynolds numbers is:

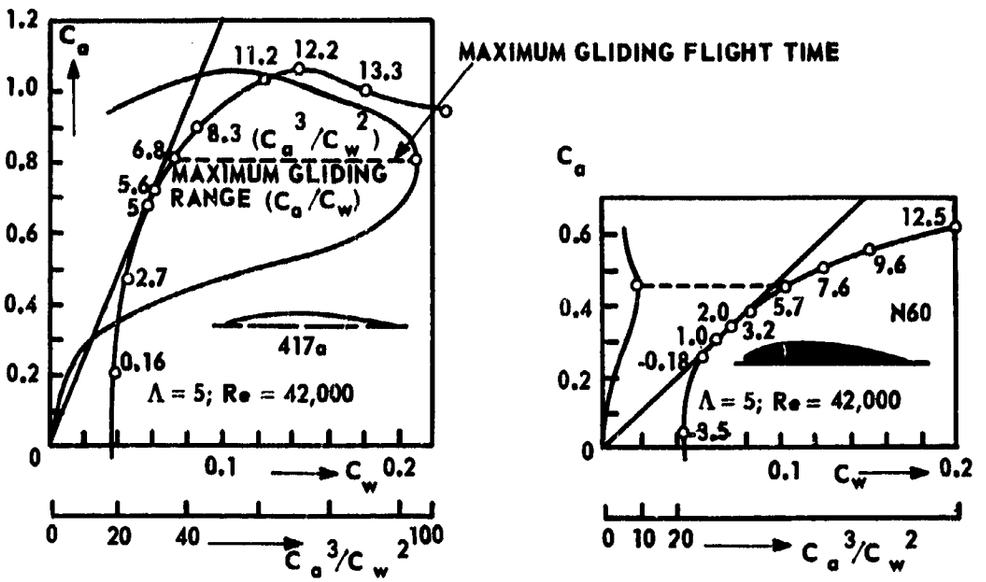

Figure 1. Comparison of two polar plots made at Re = 42,000. This Reynolds number corresponds to the order of magnitude of, for example, an indoor airplane model, which with a chord length t = 150 mm glides with a velocity of v = 4 m/sec. Comparison shows the characteristic superiority of the curved plate at low Reynolds numbers (supercritical flow conditions) compared with an airfoil profile of 12 percent thickness (subcritical separated flow). The polar line gives at the point of tangency the necessary angle of attack for the best drag-lift ratio (that is, for the greatest gliding range). On the other hand, achievement of the maximum gliding flight time, that is, the lowest sinking velocity, always requires a somewhat larger angle of attack, which corresponds to the maximum of the ceiling factor c_a^3/c_w^2.

$$\frac{(Re)_M}{(Re)_F} = \frac{(v \cdot t)_M}{(v \cdot t)_F} = \frac{1}{20} .$$

The sinking and gliding velocities are given in Figure 2 in dimensionless numbers as a function of the drag-lift coefficient for various wing loadings. The relationships can be easily seen in this diagram for transfer of tests on the airplane to the model airplane and vice versa, because the points of constant wing loading plotted in a log-log form are straight lines. The comparison is applied to practical examples in List 2. In addition, the numerical values for some soaring bird types are given there. The aerodynamical superiority of the bird

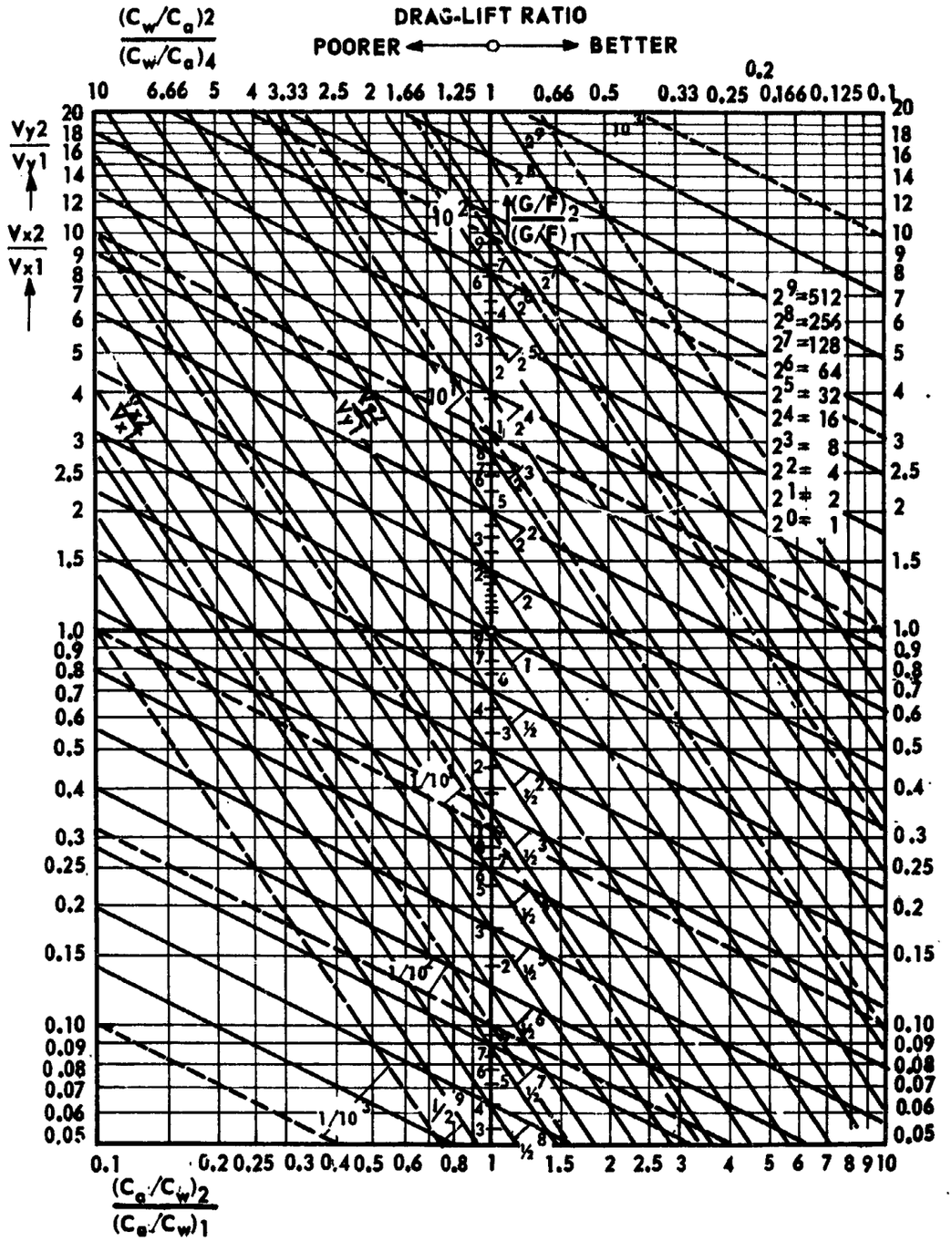
$\frac{(C_w/C_a)2}{(C_w/C_a)4}$
DRAG-LIFT RATIO
POORER
BETTER
10 6.66 5 4 3.33 2.5 2 1.66 1.25 1 0.66 0.5 0.33 0.25 0.166 0.125 0.1
0.2
$\frac{Vy2}{Vy1}$
$\frac{Vx2}{Vx1}$
$\frac{(G/F)_2}{(G/F)_1}$
2^9=512
2^8=256
2^7=128
2^6= 64
2^5= 32
2^4= 16
2^3= 8
2^2= 4
2^1= 2
2^0= 1
0.1 0.2 0.25 0.3 0.4 0.5 0.6 0.8 1 1.5 2 2.5 3 4 5 6 7 8 9 10
$\frac{(C_a/C_w)_2}{(C_a/C_w)_1}$

Figure 2

indicates that essential improvement possibilities exist for the model airplane if it is made to resemble the bird wing to achieve better drag-lift ratio. The mechanical imitation of the bird's wing will achieve only one flight condition, however, while the bird in soaring flight can change the wing profile, the wing plan, the wing twist, the dihedral and sweepback of the wing, the size of the lifting surface, the position of the center of gravity, the position of the center of pressure, and the tail feather setting, all for suitable utilization of any possible flight situation.

Figure 2. Chart for change of wing loading G/F, drag-lift ratio c_w/c_a, sinking velocity v_y or horizontal velocity v_x. The left lower corner corresponds approximately to the butterfly, the upper right to the high-speed or very large airplane. Example: If the drag-lift ratio of a model airplane $\left(c_w/c_a\right)_2$ is poor in comparison with a large airplane $\left(c_w/c_a\right)_1$, for example, if $\left(c_w/c_a\right)_2 : \left(c_w/c_a\right)_1 = 1/10 : 1/20 = 2$ (cf. horizontal scale at the upper left), then proceeding from the center of the chart outwardly toward the upper left upon intersection of the line v_{y2}/v_{y1} with the perpendicular under the 2 there is an increase in sinking velocity $v_{y2} = 2.8\ v_{y1}$, and at the intersection point underneath with the line v_{x2}/v_{x1} there is an increase in horizontal velocity $v_{x2} = 1.4\ v_{x1}$. If however, the model airplane has the same sinking velocity as the large plane (a point perpendicularly under, on the 1.0 horizontal) then the wing loading of the model airplane $(G/F)_2 = (1/2)^3 = 1/8$ of the wing loading of the large plane (as seen by going along the new v_y line from the point mentioned on the 1.0 horizontal to the lower right at the intersection with the scale of the wing loading). The horizontal velocity for this is then $v_{x2} = 0.5\ v_{x1}$, that is, half as great as in the large airplane.

The scales correspond exactly to the 12-cm slide rule, so that intermediate values can be read off on the slide-rule slide because the line grid gives directly only the changes in wing loading which correspond to the geometric series of the numbers 2 and 10 (dashed lines).

List 2

Comparison Between Sailplane, Model Sailplane and Soaring Bird

	Symbol	Unit of Measurement	Sailplane (Training Plane))	Model Sailplane (1:10 Scale)	Soaring Bird Type†)		
					Herring Gull (Female)	Kite**)	Albatross
Wingspan	b	m	13	1.3	1.3		3.8
Airfoil area	F	m^2	17	0.17	0.17	0.26	0.72
Aspect ratio	Λ	--	10	10	10		20
Mean chord length	t_m	m	1.3	0.13	0.14††)		0.2
Best drag-lift ratio $H/B = v_y/v_x = W/A = c_w/c_a$	ϵ_{best}*)	--	1 : 20	1 : 10	1 : 15	1 : 17	1 : 18
Best gliding angle	φ	deg	2° 52'	5° 43'			

*) Unaccelerated gliding flight in still air

**) Data on the kite from Idrac (see [15], p. 41), on its wing loading from R. Schmidt (see [18], p. 50), and on its weight from Dr. Heinroth

†) Data on the gull and albatross from various sources

††) The fuselage width is not assumed to be load-carrying for the mean chord length.

List 2 (Concluded)

Comparison Between Sailplane, Model Sailplane and Soaring Bird

	Symbol	Unit of Measurement	Sailplane (Training Plane)	Model Sailplane (1:10 Scale)		Soaring Bird Type		
						Herring Gull (Female)	Kite	Albatross
Weight	G	kg	270	0.17	0.34	1	0.8	7.5
Wing loading	G/F	kg/m^2	16	1	2	6	3	16
Gliding velocity at ϵ_{best}	v	m/s	16	5.6	8	10	7	16
Sinking velocity at ϵ_{best}	v_y	m/s	0.8	0.56	0.8	0.7	0.42	0.9
Reynolds number $v \cdot t_m/\nu$	Re	---	1,500,000	50,000	75,000	100,000		220,000
$Re/Re_{airplane}$	--	---	---	$1/30$	$1/20$	$1/15$		$1/6.5$
G/F: $(G/F)_{airplane}$	--	---	---	$1/16$	$1/8$	$1/2.7$	$1/5.3$	$1/1$
$c_a = \frac{G}{q \cdot F} = \frac{16\,G}{v^2 \cdot F}$ $(at\ \epsilon_{best})$	c_a	---	1.0	0.5	0.5	0.95	0.96	0.6
$c_w = c_a \cdot \epsilon_{best}$	c_w	---	0.05	0.05	0.05	0.063	0.056	0.033

2. Test Conditions and Test Installation

The measurements were made in the wind tunnel of the State Engineering School in Cologne.*)

The following difficulties are found for airfoil measurement in the wind tunnel in the Reynolds number range of model flight:

1. The aerodynamic forces are so small at low angles of attack that it is necessary to specify a measuring accuracy of tenths of a gram for the balances. For the balance used, the lower measuring limit was therefore $Re_{min} \approx 20,000$.

2. At the chosen chord length t = 90 mm, a dynamic pressure reading q = 0.75 mm water column corresponds to this Re_{min}. The "Debro" miniscope of the de Bruyn firm was used; it permitted a reading accuracy of 0.01 mm water column.

3. The key point in the work is in the study of the effect of the charge of laminar boundary layer flow on the upper side of the airfoil into a turbulent flow. Because the flow state of the free atmosphere can be considered to be practically turbulence-free, these effects in the wind tunnel appear in undistorted form only when the airstream is laminar. This condition is difficult to fulfill because the turbulence of a wind tunnel is probably always greater than that of free atmosphere. The wind tunnel used for the tests in Cologne appeared to be too turbulent in comparison with a Goettingen measurement in the first check measurement. As a rough check on turbulence, the flame probe showed a long eddying flame over the whole stream. The measurement [9] of the critical Reynolds number of the sphere $Re_k = v \cdot d/\nu$, commonly used as an indication of wind tunnel turbulence, gave for a polished wooden ball of 18 cm diameter:

$$p/q_\infty = 0 \text{ at } Re_k = 2.07 \cdot 10^5 .$$

Pressure p was measured at the rear support tube of the sphere, and q_∞ = the dynamic pressure in the undisturbed flow.

---

*) The wind tunnel was made available by Professor Grunewald, the principal, and Engr. D. Eck for the test and for the necessary modification.

After the basic changes in the wind tunnel, taking into account the guidelines developed by Prandtl on "Setting up Satisfactory Airstreams" (see [5], vol. IV, part 2, p. 65) and following the proposal of Max Kramer, Eng. D., Adlershof, $p/q_\infty = 0$ was established at $Re_k = 3.8 \cdot 10^5$, the dynamic pressure distribution in the horizontal diameter D of the stream, at distance D/2 ahead of the nozzle was:

$$\Delta q/q_m = 0.03 \ (0.10) \quad ,$$

and the static pressure in the stream center at distance D/2 was:

$$p/q_m = 0.004 \ (0.015) \quad .$$

The earlier values are placed in parentheses.

Flight tests of the DVL [Deutsche Versuchsanstalt fuer Luftfahrt (German Institute for Aeronautics Research)] made by S. Hoerner [9] with spheres gave Re_k in still air as $4.05 \cdot 10^5$. This number as the zero point of wind tunnel turbulence gave a turbulence factor [10] of the wind tunnel of:

$$TF = \frac{Re_k \text{ in still air}}{Re_k \text{ in the wind tunnel}} = \frac{4.05}{3.8} = 1.06 \ (1.99) \quad .$$

In connection with turbulence factor, an effective Reynolds number is defined in NACA Report No. 558 as

$$Re_{eff} = Re_{measured} \cdot TF \quad ,$$

in the assumption that a process observed in the turbulent wind tunnel would be seen in a turbulence-free flow at a Reynolds number depending on the turbulence factor. The NACA profiles N 60 and N 60R used in the following measurements were measured at $Re \approx 3,000,000$ in the high-pressure wind tunnel (VDT) known to be strongly turbulent. At a sphere characteristic of $Re_k = 1.55 \cdot 10^5$ (see Figure 11) the results for the NACA measurement were $TF = 2.62$ and $Re_{eff} = 3,000,000 \cdot 2.62 \approx 8,000,000$. This Reynolds number correction is not used in the following measurements, because a change of Reynolds number by 6 percent would not essentially alter the overall picture.

3. Subcritical and Supercritical Flight State for the Model Airplane

In contrast to flow around the airfoil on large airplanes, which is always supercritical, "subcritical" flow, in addition to supercritical, can appear in flow around the model airplane airfoil in the Reynolds number range under 100,000; at the subcritical condition where lift A is small, drag W is disproportionately large, so that the drag-lift ratio is very poor and is the cause of the failure of many model flight experiments. The following measurements now show why a model airplane can fly only in the supercritical flight state and how through a suitable choice of the airfoil profile the supercritical flight state can always be realized. Figure 3 gives the results of a measurement on an airfoil for an angle of attack of $\alpha = 6°$ as an example. Instead of A and W, the dimensionless coefficients, lift coefficient c_a, drag coefficient c_w, and the lift-drag ratio c_a/c_w, are plotted as a function of Reynolds number Re. The practical application of the measurement will be shown for an example. Below the critical Reynolds number Re_k the lift-drag ratio is 4 to 5, and in the supercritical region it is 10 to 11, that is, for 1-m drop the airplane model glides only 4 to 5 m subcritically but more than twice as far supercritically. In the use of this airfoil profile the model airplane with an assumed velocity of, for example, v = 6 m/sec would have to have a chord of at least 200 mm. The model airplane would then fly (in still air) at Re = 6 · 200 · 70 = 84,000 and thus in the neighborhood of the critical Reynolds number. Velocity loss from 6 to 5 m/sec would suffice to bring the model airplane into the subcritical flight stage at Re = 5 · 200 · 70 = 70,000; it would pancake or go into a spin.

These phenomena in flow around the airfoil are controlled by the flow state of the thin friction layer near the wall, called the "boundary layer" by Prandtl, who first explained its effect in 1914 [1]. Because of the viscosity of the air, the air molecules adhere to the body wall, act as a brake on the air particles moving above them, and thus generate a friction resistance. The friction loss in the boundary layer, the boundary layer thickness, the velocity distribution in it, and above all the ability to draw energy from the external flow around the foil can be basically different, depending on whether the boundary layer is laminar (from lamina = layer) or turbulent (eddying). In the subcritical flow state, the boundary layer flow is laminar on the airfoil upper side and in the supercritical flow state it is turbulent. Both flow forms have interchangeably a favorable and an unfavorable characteristic.

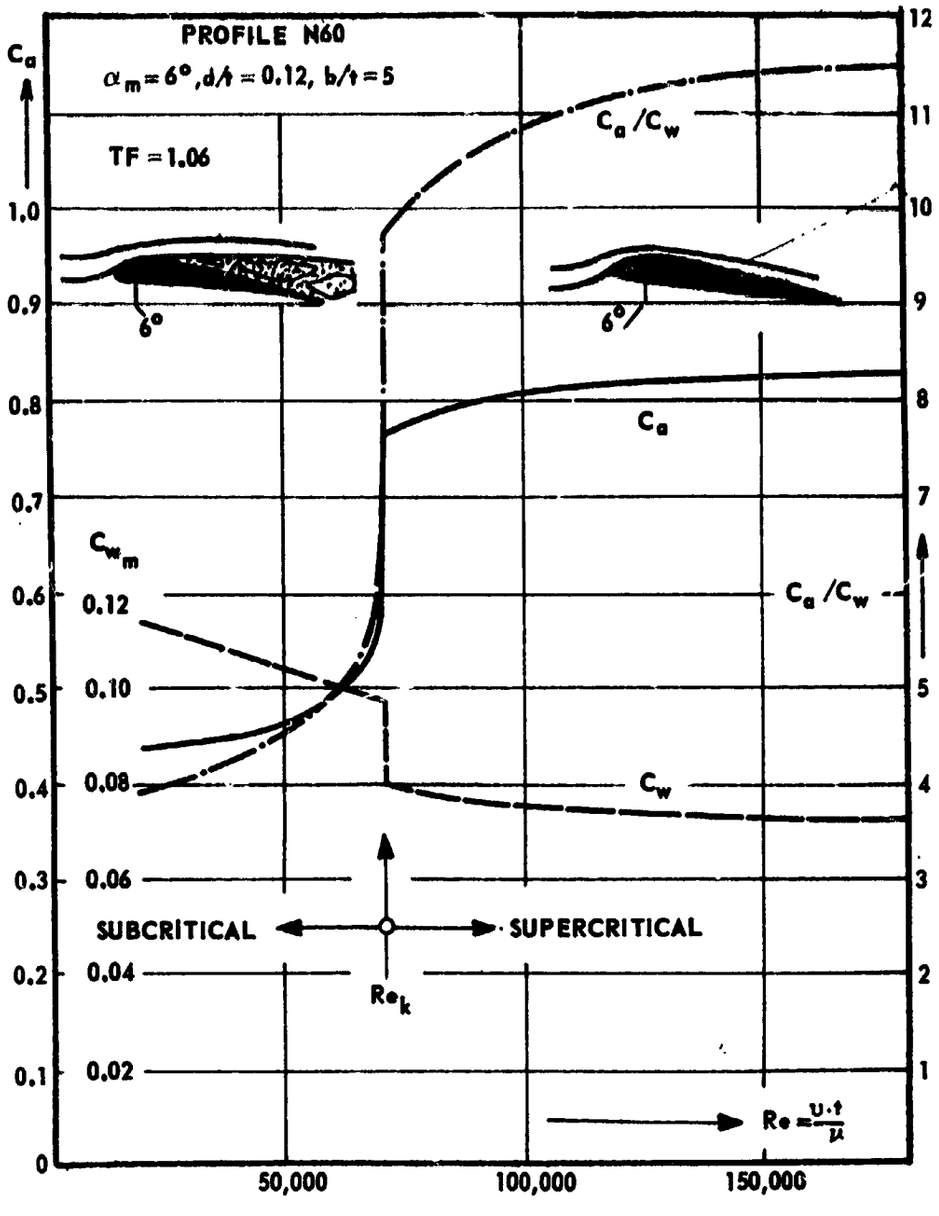
PROFILE N60
$\alpha_m = 6°, d/t = 0.12, b/t = 5$
TF = 1.06
C_a
C_a/C_w
C_a
C_{w_m}
C_w
6°
6°
SUBCRITICAL
SUPERCRITICAL
Re_k
$Re = \frac{v \cdot t}{\mu}$
1.0
0.9
0.8
0.7
0.6
0.5
0.4
0.3
0.2
0.1
0
0.12
0.10
0.08
0.06
0.04
0.02
12
11
10
9
8
7
5
4
3
2
1
50,000
100,000
150,000

Figure 3

a) The Laminar Boundary Layer

The laminar boundary layer (Figure 4), which is peculiar to the range of low Reynolds numbers, is very thin. It causes little frictional drag; wall roughness which is not excessive is smoothly covered by it, so that the nature of the surface on a small airplane model plays a different role from that on the large airplane. The laminar layer does not have the ability, however, to take energy from the outer flow, so that in spite of low friction its kinetic energy is soon used up. Consequently, it adheres poorly to curved surfaces in a divergent flow, such as at the rearward curvature of the airfoil upper side (suction side), because there, deceleration and pressure increase always prevail, through which it cannot penetrate. From the region of higher pressure, and therefore from the airfoil trailing edge, there follows shortly after beginning of flow a retrograde movement in the boundary layer which, like a wedge, moves under the decelerated boundary layer material, separates the flow from the wall, and through eddy formation creates higher drag behind the wing (Figure 5). The point of this reverse flow wedge is called the "separation point," which at "laminar separation" lies at the point of the beginning pressure increase and therefore approximately at the highest point of curvature, moving forward with increasing angle of attack. If laminar separation exists in the whole range of angles of attack (which for the given airfoil profiles can be only for Reynolds numbers less than 100,000, and therefore only on model airplane airfoils) this flow state is called "subcritical." The pertinence of the origin of laminar flow at low Reynolds numbers is understandable through the physical significance of the Reynolds number, which gives the ratio of inertia force to viscosity force; that is, at low Reynolds numbers the viscosity forces of the boundary layer conditions prevail and at higher Reynolds numbers the inertia forces.

Figure 3. Example of an aerodynamic force measurement on an airfoil model at a given angle of attack and increasing Reynolds number. The transition from subcritical (laminar and separated) to supercritical (turbulent and attached) flow state of the upper surface boundary layer occurs at the critical Reynolds number, which is $Re_k = 63,000$ here. The lift coefficient c_a increases suddenly there, the drag coefficient c_w decreases and the lift-drag ratio c_a/c_w becomes about three times as favorable (from 4 to 12).

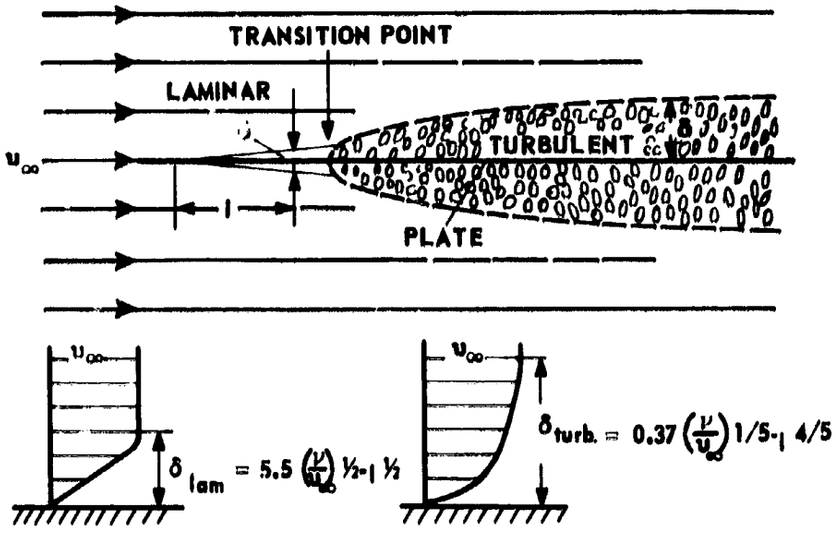

Figure 4. Variation in the boundary layer thickness δ, along a flat plate in laminar approach flow. The figure at the lower left is the velocity profile of the laminar boundary layer; at the lower right is the velocity profile of the turbulent boundary layer.

b) The Turbulent Boundary Layer

As the Reynolds number increases (that is, with increase in speed v, when the chord t and the kinematic viscosity of the air are constant) the boundary layer after initial laminar flow begins to be turbulent at a critical Reynolds number Re_k, and the lift suddenly increases, the drag decreases, and thus the drag-lift ratio becomes better by several times, and then improves slightly further as the Reynolds increases. This state of affairs, which explains the cause of the sudden changes shown in Figure 3, gives as a first basic conclusion: the model airplane will give optimum performance in its size class only if its flight state is supercritical. The following measurements answer the questions: "On what is the critical transition dependent, and how can it be artificially influenced?" It may be said beforehand that the most important result is that the attainment of supercritical state is always possible by

a) a suitable choice of airfoil profile,

b) by measures for aritificial turbulence on any arbitrary profile.

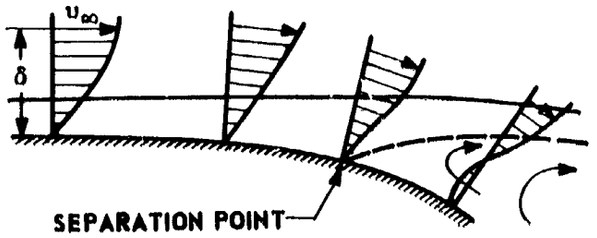

Figure 5. Velocity profiles of the boundary layer on the upper side of the airfoil before and after the separation point. The dashed line limits the reverse flow wedge.

The superiority of the supercritical flight state is the result of the peculiar ability of the turbulent boundary layer to take energy from the outer flow and transport it to the wall as a result of mixing motions of the small vortices. Through impulse exchange on a "mixing length" (see [2], p. 94) perpendicular to the principal direction of flow, the boundary layer is able largely to overcome the pressure increase at the rearward curvature of the airfoil upper side, so that the point of separation is brought closer to the trailing edge, the higher is the energy content of the outer flow or, expressed in a form easier to understand, the higher becomes the "drag effect of the outer flow" as Reynolds number increases.

The previously laminar separated boundary layer attaches itself to the upper side because of turbulence, the vortex street behind the airfoil becomes narrower, and thereby the pressure (eddy) drag (also called form drag) becomes suddenly smaller. In spite of this, in the total drag, which as is known consists of 1. the pressure drag, 2. friction drag at the body surface, turbulent friction on smooth walls can be three times as large as laminar friction, and on rough walls even more, as has been found from measurement of friction drag c_f on thin flat plates (Figure 6). The "vorticity" of the friction layer causes, in addition to increased friction loss, a sudden increase in boundary layer thickness δ at the transition point (Figure 4). Both are characteristics of an apparently increased viscosity. The thickness δ of the laminar boundary layer increases with the $1/2$ power of friction length ℓ, and the thickness of the turbulent boundary layer increases with the $4/5$ power. This considerable thickness increase because of decelerated boundary layer material finally leads, with declining drag effect of the outer flow, to "turbulent separation" at the curved upper side of the airfoil, again with a reverse flow wedge detaching the flow from the wall before the trailing edge (Figure 5). The point of separation migrates only a

slight amount at first with increasing angle of attack and then suddenly forward at a critical angle of attack; "breakaway of flow."

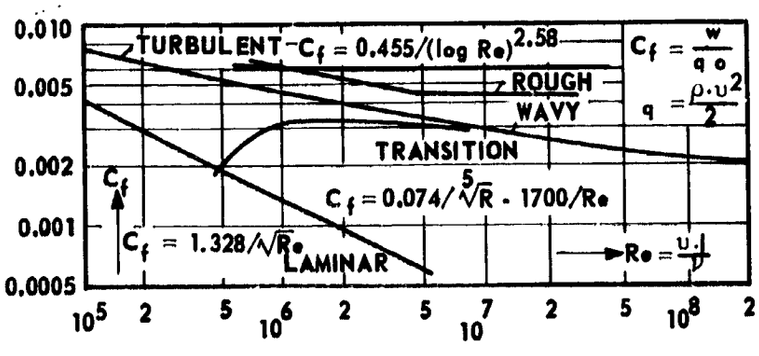

Figure 6. Drag coefficient c_f of surface friction on flat plates in the laminar and turbulent friction layer as a function of Reynolds number.

4. Dependence of the Critical Reynolds Number

A transition in flow from the subcritical to supercritical state, which the critical Reynolds number Re_k characterizes, has not been studied very much to date for the airfoil because Re_k, lying in the region of model flight, is of little importance to the large airplane. The mathematical treatment of this region is confronted by much greater difficulties because farther the considerable separation phenomena remove the flow from the easily investigated quantitatively theoretical potential flow, the poorer is the drag-lift ratio of the airfoil. In contrast to this, the subcritical and supercritical phenomena in flow in tubes along flat plates and spheres has been largely explained and calculated; for this reason, a brief study will be made of the conclusions resulting from this for the model-airplane airfoil.

a) The Critical Re Number for the Flat Plate

If a plane, infinitely thin, smooth plate "friction plate" is in a laminar flow parallel to the wall, so that no forces perpendicular to the wall but only frictional drag occurs, then a boundary layer with a laminar approach flow forms; its transition takes place after a friction length (Figure 6) a:

$Re_k = (v \cdot \ell/\nu \approx 500{,}000^*))$ (see [3], III, p. 5). This value of Re_k on the friction plate cannot be related to the model airplane, however, as can be seen immediately: the model airplane used in the following measurements has a chord length of t = 90 mm. To achieve a transition in a 90-mm friction length, the velocity v would have to be 500,000/(90 · 70) ≈ 80 m/sec. The smooth flat steel plate used in the measurement here, 2.6 mm thick and 0.5 mm nose radius at the leading edge, exhibits supercritical flow at the lower limit of the measured range, that is, even at v = 3.2 m/sec (Re = 20,000); this is therefore produced by influences other than surface friction. If the plate is thick and the leading edge rounded (Figure 7), then through local acceleration in combination with a local separation (transition vortex), this produces an earlier transition of the flow, as can be seen from the suddenly increasing boundary layer thickness in Figure 8. Wieselsberger (see [3], I, p. 123) found in his first measurement of friction drag on plates with rounded leading edge in the low-turbulence Goettingen wind tunnel only supercritical friction drag (corresponding to the upper line in Figure 6). To permit measurement of laminar friction, according to Hansen [11] the plate must be tapered to a sharp edge (Figure 8). This situation immediately reverses itself, however, if the sharpened plate is set at an angle as an airfoil so that flow takes place at a slight angle to the sharp leading edge. The stagnation point then moves away downstream from the leading edge by a small amount along the lower surface, with the consequence that the lower surface flow becomes turbulent because the sharp leading edge now has the effect of a "turbulent edge." This makes it understandable why the aerodynamic force measurements on plates and thin profiles with sharp leading edge give supercritical values even at the smallest angle of attack. The turbulence edge on the flat plate of course has

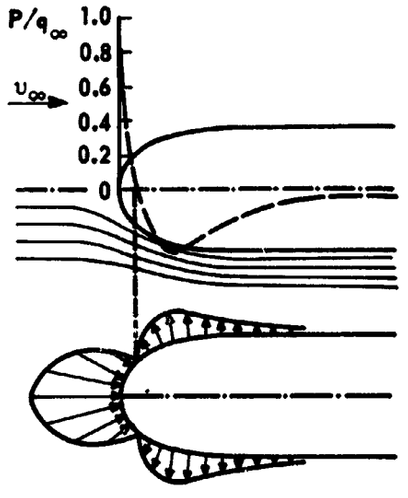

Figure 7. Pressure distribution at the rounded leading edge of a flat plate with flow parallel to the wall.

*) According to more recent research on thin plates, this number displaces toward about 1 million, depending on the shape of the leading edge in laminar approach flow, as shown by the dashed line in Figure 6.

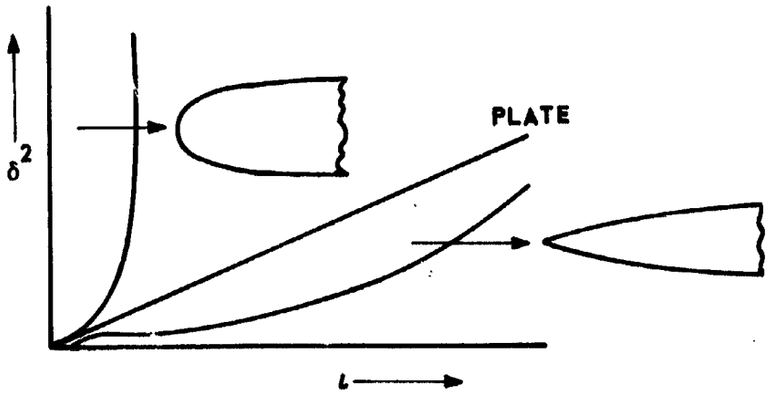

Figure 8. Development of boundary layer thickness δ along plates of various thickness and with various shapes of the leading edge (according to Hansen).

this favorable effect only to about α = 7 to 10°, because then the sharp edge becomes a "knife edge," as described elsewhere. With the plate standing perpendicular to the flow, and thus at α = 90°, at any Reynolds number and at any state of turbulence of the airflow, the same drag coefficient is measured (Figure 9). Sharp-edged bodies have no critical Reynolds number and they are "insensitive to Reynolds number" because the point of breakaway is fixed, so that here the model law of Reynolds has either no or limited validity.

b) The Critical Re Number for Rounded Bodies

In contrast to this, all rounded bodies - sphere, ellipsoid, streamlined body and round-nosed airfoil - all show a c_w jump at a Re_k and have "Reynolds number and turbulence sensitivity," as Figure 9 shows. According to Figure 9, Re_k decreases with increasing fineness. Applied to airfoils the following conclusion results: the finer the profile, the lower the Reynolds number at which the transition from subcritical to supercritical flow occurs. Because basic conclusions, both for the explanation of problems with the model airplane as well as for the utility of the wind tunnel employed for the existing measurement, result from known phenomena on the sphere, it will be valuable to summarize these phenomena briefly here. The flowing particles approaching the stagnation point S_1 of the sphere's leading side (Figure 21) come to rest, so that their kinetic energy is converted into pressure. At a hole through the sphere center and from the stagnation point this pressure can be measured by a manometer

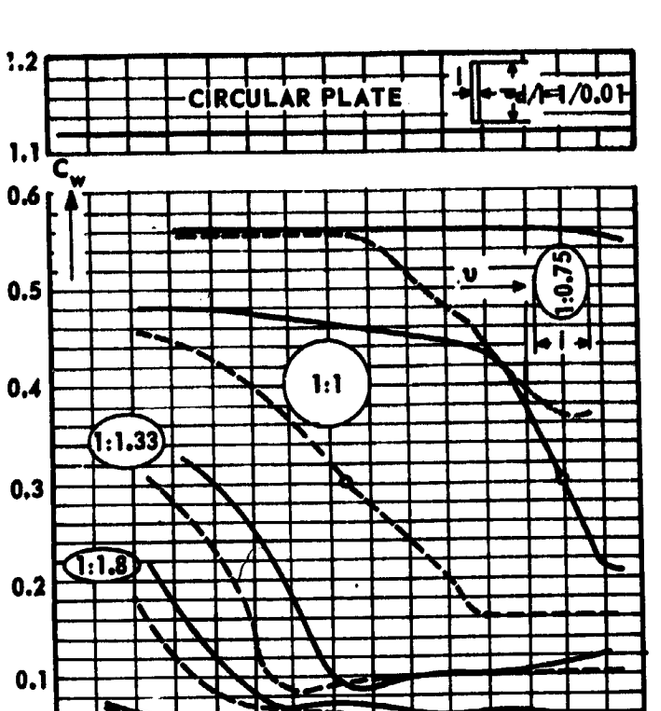

Figure 9. Reynolds-number sensitivity and turbulence sensitivity (according to Prandtl-Tietjens). The circular plate (upper part of the figure) is not sensitive to Reynolds number: c_w = constant. The rounded bodies are 1) sensitive to Reynolds number: indicated by c_w jump; 2) turbulence sensitive: with a turbulence grille (dashed lines), the c_w jump occurs at a lower Reynolds number.

For the sphere, that Reynolds number is critical at which $c_w = 0.3$; here it is at $2.58 \cdot 10^5$. The turbulence factor of the wind tunnel is:

$$TF = \frac{Re_{k\ air}}{Re_{k\ tunnel}} = \frac{4.05 \cdot 10^5}{2.58 \cdot 10^5} \approx 1.6 \ .$$

connected to the rear side of the sphere; this represents the "total pressure" P, similar to a Pitot tube measurement. After subtraction of the "static pressure" p_∞ of the undisturbed flow from it, there results the "dynamic pressure" q_∞, in accordance with the Bernoulli equation:

$$P = p + q \quad \text{or} \quad q = P - p \ .$$

In the free-flow wind tunnel, the static pressure is negligibly low. In the Cologne wind tunnel which was used, it was only 0.4 percent of the dynamic pressure ($p_\infty = 0.004\ q_\infty$) after the conversion of the installation into undisturbed flow, as has already been described in Subsection II 2, so that there can be written: $q_\infty \approx P$. In flow past bodies, on the other hand, the static pressure, as the wall pressure, plays a considerable role. In Figure 21 the space around the sphere is divided into flow tubes whose cross section is reduced most strongly at the sphere equator by constriction of the flow between the sphere and the outer flow. It is assumed that no fluid passes through the imaginary walls of the flow tubes, and therefore in a unit of time the same quantity of flow must pass through each cross section (continuity requirement): for a cross-section reduction to half, therefore, the velocity must be twice as large. Since the dynamic pressure increases with the square of velocity, however, the dynamic pressure at this place in the flow must be four times as high:

$$\text{dynamic pressure} \quad q = \frac{\rho}{2} v^2 \quad \text{and} \quad q = \frac{v^2}{16} \ ,$$

because for air at zero-meter height the air density $\rho \approx 1/8$. According to the law of Bernoulli, however, the total pressure P in the flow tube remains constant:

$$P = p + q = \text{constant.}$$

Therefore, with increasing dynamic pressure the wall pressure must correspondingly decrease, and therefore at the sphere equator there is a negative pressure. These phenomena at the leading side of the sphere always take the same course no matter whether an ideal flow of a frictionless liquid is involved, corresponding to Figure 21, or whether flow takes place around the sphere subcritically or supercritically (Figure 10). The streamline pictures of the three flow forms named are first differentiated by the phenomenon of flow on the rear side of the sphere.

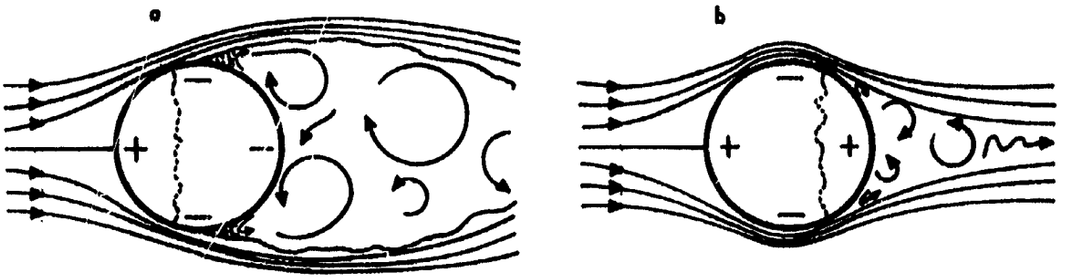

Figure 10. a) Subcritical flow around the sphere: the boundary layer flows in laminar form; separation occurs somewhat ahead of the sphere equator; negative pressure prevails at the rear side of the sphere and the large turbulent area produces high resistance: $c_w = 0.48$. b) Supercritical flow around the sphere: in the turbulence-free airstream the boundary layer on the smooth sphere is turbulent at $Re_k = 405,000$; the flow remains attached, and the turbulent region is considerably smaller. Positive pressure prevails at the rear side; $c_w = 0.08$.

At the rear side of the sphere in a frictionless fluid, that is, a fluid without viscosity, the streamline picture would be a mirror image of that at the front side of the sphere, in accordance with Figure 21. The conversion of pressure into velocity energy, effective up to the equator from the front stagnation point S_1, would be reversed without loss at the rear side, so that a second stagnation point S_2 would occur there. This lossless, practically impossible, flow (called potential flow) leads to the suprising finding that the resistance = 0 because there are no friction or vortex losses: the front-side pressure and the rear-side pressure would balance one another.*)

The streamline picture of subcritical flow around a sphere shows the greatest deviation from this ideal flow (Figure 10a) in the large turbulent region at the rear side of the sphere, in which a reverse flow wedge separates the boundary layer of the sphere front side even upstream from the equator.

*) This streamline picture of potential flow can be exactly calculated and plotted by means of the stream function. In addition, this picture can be produced by "creeping" laminar flow around a thin circular sheet between glass plates, for example, in the Pohl streamline apparatus, even though the physical causes are different.

This subcritical state is caused by the continued laminar nature of the boundary layer on the sphere front side; it transports no energy to the layer decelerated by wall friction and therefore cannot overcome the pressure increase beginning at the equator but instead separates from the sphere surface. At the rear side of the sphere, a negative pressure exists in the turbulent region (as indicated by the minus sign in Figure 10a) and can be measured by a second manometer whose tube connection terminates at the rear support tube (Figure 13), in the corner between the support tube and the sphere.

The flow picture of the supercritical state (Figure 10b) approaches the ideal picture more closely, because the rear side turbulent region is considerably smaller in comparison with that for the subcritical state. In the same manner as in model-airplane airfoils, the transition from subcritical to supercritical flow occurs when the boundary layer becomes turbulent and energy of the external flow is transported to the layer near the wall and decelerated by friction and thus in part overcomes the pressure increase at the rear side, so that the flow remains largely attached, and the resistance becomes considerably smaller, which is the decisive factor. Supercritically, the drag coefficient is only $\frac{1}{6}$:

$$\text{subcritical} \qquad c_w = 0.48 \ ,$$

$$\text{supercritical} \qquad c_w = 0.08 \ ,$$

based on the measurements of the DVL by Hoerner [9] in turbulence-free air (Figure 11).

The turbulent transition does not occur suddenly but, as with the flat plate, in a transition region in which that Reynolds number at which $c_w = 0.3$ is considered the critical Reynolds number of the sphere. Twenty years ago, considerable trouble was caused for research laboratories when each one found a different critical number for the sphere, until Professor Prandtl explained the reason: the transition must occur earlier the more turbulent is the airflow of the wind tunnel in question, and the critical Reynolds number of the sphere can thus serve as an indication of turbulence. According to Hoerner, the transition occurs for the sphere towed in still air at $Re_k \approx 405{,}000$, and in gusty air in areas surrounded by trees slightly earlier, at about 380,000. Thus in regard to its influence on the boundary layer, free atmosphere can be considered free of turbulence; the fine structure of vorticity of a boundary layer only millimeters thick is not effectively related to the large turbulence nodes of the free atmosphere. Strictly speaking, therefore, only measurements in turbulence-free air correctly correspond to free flight. This is especially true for the measurements involved here at low Reynolds numbers, because in turbulent flow the

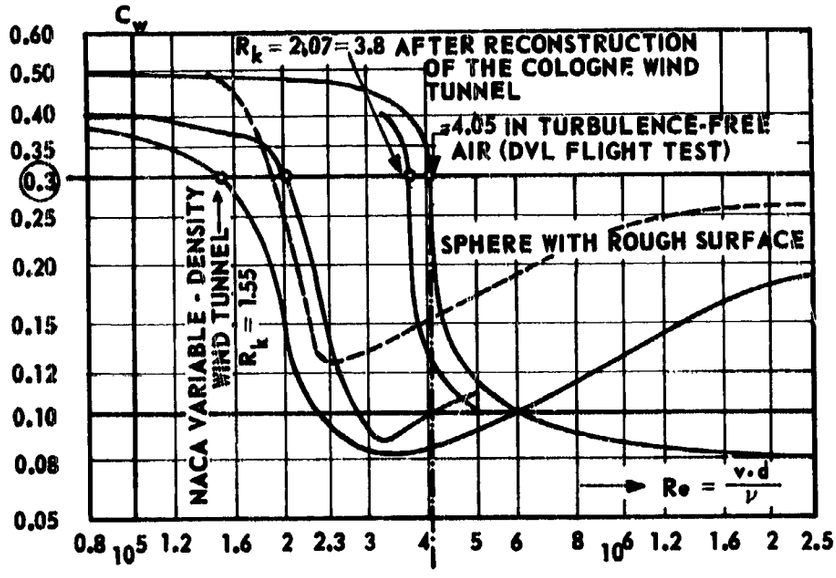

Figure 11. Measurement of the critical number for a sphere at $c_w = 0.3$ serves as an indication of turbulence of the airflow in wind tunnel. In turbulence-free air there was measured: $Re_k \approx 4.05 \cdot 10^5$. The ratio of this number to the number for a sphere measured in the wind tunnel gives the turbulence factor of this wind tunnel. For the NACA variable-density tunnel TF = 4.05:1.55 ≈ 2.6; this corresponds to the sphere measurement with a turbulence grill in Figure 9. For the Cologne wind tunnel after rebuilding, TF was 4.05:3.8 = 1.06.

subcritical state generally does not appear and the maximum value of lift is completely in error. Therefore all the previously measured polar curves in turbulent flow are worthless for model flying work, especially the American NACA airfoil measurements which were made in a strongly turbulent variable-density tunnel down to Re = 42,000.

In the wind tunnel used for the following measurements the critical transition initially occurred at Re_k = 207,000. Only after a year of effort did improvements in the utility of the wind tunnel occur, allowing the subcritical state to become measurable on the model-airplane airfoil and rewarding the laborious preliminary efforts; after rebuilding, a critical sphere characteristic of Re_k = 380,000 was measured. This favorable result was achieved by:

1. incorporation of screens between the straighteners and the nozzle, to convert the coarse turbulence into fine turbulence,

2. by a long stilling run between the last screen and the nozzle, to cause attenuation of the fine-structure turbulence,

3. incorporation of a narrow nozzle with a pronounced contraction,

4. change of diffuser and blower.

It was now easy to make virtue of necessity by using a turbulence grille (Figure 12) to make the flow completely turbulent, that comparison of measurements with and without the grille (Figures 9 and 82) would show the influence of tunnel turbulence and in addition allow test of the effectiveness of measures for

Figure 12. Turbulence grille before the nozzle of a wind tunnel, to make the airstream before the airfoil model completely turbulent.

artificial turbulence, as described in Subsection VI 4. At this point, the successful attempt of Prandtl and Wieselsberger should be referred to; in this, a wire hoop placed around the upstream side of the sphere (Figure 13) will induce the supercritical state at smaller Reynolds numbers, proving that it is merely necessary to make the boundary layer turbulent. A rough surface achieves the

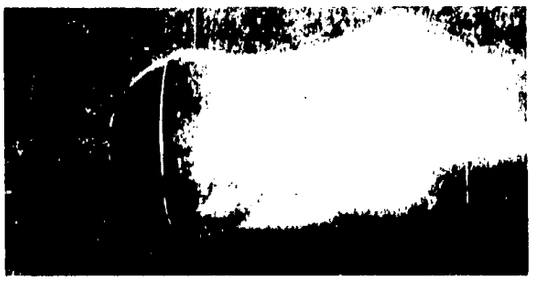

Figure 13. Fundamental experiment of Prandtl by which he proved that making the boundary layer turbulent by means of a wire hoop can compel supercritical (attached) flow around a sphere at low Reynolds number. [from Prandtl-Tietjens, Aeromechanik (Aeromechanics), vol. 2, Springer-Verlag, Berlin]

same effect (Figure 11). In addition, it may be concluded from this that 1. the sphere should be as smooth as possible, 2. the airstream before and after the sphere should not be disturbed by any kind of support wires or the like, and therefore the measurement is correct only when the sphere is held by a support tube at the back.

In conclusion, reference should be made to determination of Re_k from the measurement of the pressure transition at the rear side of the sphere. This is considerably simpler than drag measurement, for which the proper determination of the amount of resistance to be subtracted for the support is laborious. With the second manometer mentioned, the pressure p prevailing at the rear side of the sphere can be measured. In the subcritical state, it is negative but becomes positive in the supercritical state, as shown by the plus sign in Figure 10b. Pressure measurement of this type is shown by plotting the dimensionless coefficient p/q_∞ versus Re, as Figure 14 shows schematically. That value at which $p/q_\infty = 0$, that is, at which the manometer on the rear side of the sphere shows $p = 0$ upon the change from minus to plus, serves as the critical Reynolds number. The results of these measurements were briefly described in Subsection II 2.

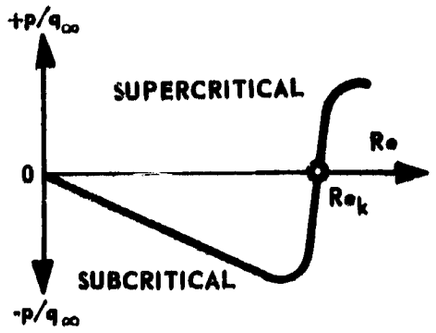

Figure 14. Pressure at the rear side of the sphere, plotted as pressure coefficient p/q_∞ versus Reynolds number. That Reynolds number at which p/q_∞ passes through the zero line going from minus to plus values serves as the critical sphere characteristic; this agrees with the critical sphere characteristic determined from drag measurement at $c_w = 0.3$.

c) Comparative Conclusions for Model-Airplane Wings

1. Round-nosed, thick wings are sensitive to Reynolds number and turbulence; thin sharp-nosed airfoils are insensitive to Reynolds number and turbulence.

2. The lower the Reynolds number, that is, the smaller the model airplane or its speed, the thinner must the profile be to achieve the supercritical flight state.

3. To achieve the supercritical flight state, it is sufficient if the upper surface flow is turbulent.

4. The critical Reynolds number of an airfoil sensitive to Reynolds number and turbulence can be reduced by artificial creation of turbulence in the upper-surface boundary layer, through

   a) pointing of the wing nose (knife edge),
   b) by a rough-surfaced wing nose,
   c) most effectively, by stretching a turbulence wire or thread parallel to the wing's leading edge, and in the wind tunnel by the use of a turbulence grille ahead of the model,
   d) in addition, the critical Reynolds number can be reduced by sonic vibrations, for example, by an intense whistle note.

d) Convergent and Divergent Flow

The conditions under which the boundary layer on the flying model airplane is laminar or turbulent are supplemented by the following study. Reproduction of the flow around the model airplane in the wind tunnel assumes that the influences stemming from turbulence of the wind stream are eliminated to as great a degree as possible, because wind-tunnel turbulence falsifies the entire picture, as Figures 9 and 11 show. An effective means for reducing tunnel

turbulence is, as is known, the constriction of the wind stream by a nozzle (see [5], vol. IV, part 2, p. 74). This can be explained approximately as follows: In addition to its motion in the direction of the principal flow, the small vortices of the turbulent flow cause disturbance motions directed transverse to the principal flow; these are damped by the constriction of flow. Conversely, widening of the flow causes increase in the disturbance motions of the vortices directed transverse to the principal motion, and thus produces an increase in turbulence. It has been observed in flow in tubes that a very small convergence considerably increases the critical Reynolds number, and a small convergence decreases it (see [4], vol. 2, p. 56). The same is true for flow around the airfoil, as will be described in the next section.

5. Flow Around the Airfoil

The airfoil positioned for lift (Figure 17) causes a downward deflection of the air mass involved, and this in reaction produces lift. As long as the flow is attached to the profile on all sides, the detailed shape of the airfoil's upper and lower surfaces is less important than the course of the profile mean line as the governing, central streamline. Since, however, in the range of low Reynolds numbers various separation phenomena depend upon the details of profile form - as a cause of the drag-lift ratio decrease - several of these phenomena will be described here.

a) Streamline Form and Bernoulli's Equation

The streamline pictures (Figures 15 and 16) made visible in flow apparatus clearly show the changes in convergent and divergent flow, and the separation phenomenon characteristic of the latter, as angle of attack increases. If the profile shown in Figure 17 is considered to be a uniform cross section of an airfoil of infinite span, then spanwise there is no flow change. At two cross sections separated by distance b in the span direction the streamline pictures are congruent (two-dimensional flow around an airfoil). If "a" designates the distance between two streamlines (Figure 17), then the flow tube delimited by it has the cross section $f_\infty = a_\infty \cdot b$ in the undisturbed flow far from the wing. If the velocity changes from v_∞ to v along this flow tube, then there results for an incompressible fluid, from the continuity requirement,

$$a \cdot b \cdot v = a_\infty \cdot b \cdot v_\infty$$

$$\frac{v}{v_\infty} = \frac{a_\infty}{a} .$$

Figure 15. Attached flow around an airfoil at a low angle of attack. On the upper surface of the wing, however, at the half-chord point, the thickening of the boundary layer can be seen, and at the bright points the deceleration in the boundary layer is the beginning of the inverse flow and subsequent separation. [from Prandtl, Abriss der Stroemungslehre (Outline of Flow Mechanics), Verlag Vieweg & Sohn, Brunswick].

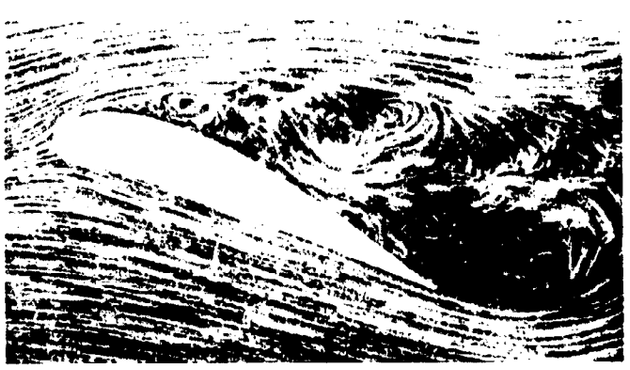

Figure 16. Breakaway of flow on the upper surface at a high angle of attack (stalled flight condition). [from Prandtl, Abriss der Stroemungslehre (Outline of Flow Mechanics), Verlag Vieweg & Sohn, Brunswick].

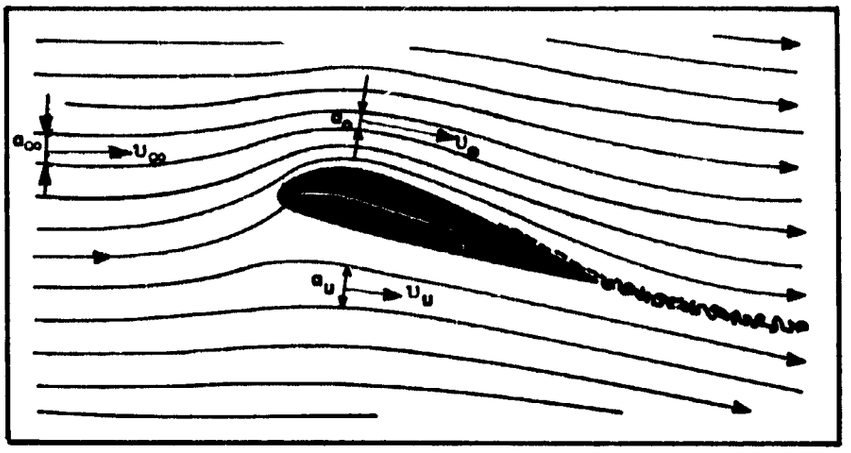

Figure 17. Streamline picture of the wing during lift.

In other words, the velocity is inversely proportional to the spacing of the streamlines. On the upper surface of the airfoil the streamlines are closer together, and on the under surface farther apart, than upstream from the airfoil: $a_o < a_\infty < a_u$: the approach flow runs convergent to the airfoil upper surface and divergent to the airfoil under surface. Convergence of streamlines denotes acceleration, and divergence deceleration, because $v_o > v_\infty > v_u$. In addition, along a flow tube the velocity v and static pressure (wall pressure) p are interrelated by Bernoulli's law:

$$p + \frac{\rho}{2} v^2 = p_\infty + \frac{\rho}{2} v_\infty^2 = P = \text{const.}$$

$$p + q = p_\infty + q_\infty$$

In other words, the sum of the static pressure p and dynamic pressure q is constant. The dynamic pressure of the external flow q_∞ is easily measurable by means of the dynamic indicator discovered by Prandtl. There then results from the dynamic pressure, $v_\infty = \sqrt{(2/\rho)\ q_\infty}$, or with $\rho \approx 1/8$ for air at 0 m height, $v_\infty = 4\sqrt{q_\infty}$.

In the study of flow pictures, the following holds:

Convergent flow: decreasing streamline spacing means acceleration and pressure drop; it acts in the sense of stabilization of laminar flow or reduction of turbulence.

Divergent flow: increasing streamline spacing means deceleration and pressure increase; it acts in the sense of transition to turbulence, or, if turbulence already exists, intensifies it.

In Figure 17 the streamline running to the stagnation point divides the flow into the flow on the upper and lower surfaces. The upper surface flow at first is convergent, especially over the nose of the airfoil, and it therefore produces an intense negative pressure which forms a principal part of the lift. From about the highest point of the upper surface camber, that is, from the pressure minimum, the flow is divergent to the trailing edge. This is the critical region of the profile, because there deceleration and excessive pressure increase can cause separation of the flow. On the lower surface, the approaching flow shows divergence and therefore pressure increase up to the stagnation point; from the stagnation point to the trailing edge there is a slight convergence and therefore decreasing pressure. At the trailing edge, there is a pressure equalization of the two flows. In reference to the effect on the boundary layer state, it must now be concluded from Subsection II 4d that along profile runs with convergent flow, that is, on the lower surface from the stagnation point to the trailing edge, and on the upper surface from the stagnation point to the pressure minimum, there is a tendency to maintain the laminar boundary flow. The divergent flow, on the other hand, tends toward formation of turbulence. The latter is favorable for the separation region on the airfoil upper surface (that is, from the pressure minimum to the trailing edge) for the model airplane, because the turbulent boundary layer can better overcome the pressure increase in this region than can the laminar, and thereby the separation does not occur until a higher angle of attack, and therefore higher $c_{a\ max}$ values are achieved.

b) Pressure Distribution Along the Chord

If the upper surface of the airfoil model is provided with small holes (0.4 mm diameter) then the effective wall pressure p can be measured at a hole if the hole is connected with a manometer by a fine tube (through the interior of the airfoil or from the other side of the airfoil). The plot of the measured wall pressures as a function of the chord then gives the curve of "pressure distribution" along the chord. In Figure 18, the pressure distribution is plotted for a thin profile and in Figure 19 for a thick profile, from Goettingen measurements (see [3], II, pp. 44 and 46). Not only is the wall pressure p plotted, but also, as customary, the dimensionless pressure coefficient p/q_∞. Because the pressures perpendicular to the chord are plotted, the resultant pressure area from the upper and lower sides corresponds to normal

force N or to the coefficient of this aerodynamic force c_n.*) The velocity distribution obtaining at the free edge of the boundary layer can be determined from the pressure distribution:

$$v = v_\infty \sqrt{1 - \left(\frac{\pm p}{v_\infty}\right)} = \sqrt{\frac{2}{\rho}\,[q_\infty - (\pm p)\,]} \approx 4\sqrt{q_\infty - (\pm p)}\ ,$$

in which negative values of p give an increase of v compared with v_∞. At the stagnation point, where $p/q_\infty = 1$, v becomes 0; at pressure equalization where $p/q_\infty = 0$, v is v_∞. Strictly speaking, the Bernoulli equation is valid only for turbulence-free flow, so that it cannot be applied to profile elements with separated flow.

At low angles of attack, the pressure distribution is fairly similar for both profiles. As the angle of attack increases, there forms on the thin sharp-nosed profile (Figure 18), as a result of a local transition vortex, a "suction peak" which at a high angle of attack lies exactly at the foremost profile point. At the suction peak, $p/q_\infty = -3.7$; the pressure minimum therefore is 3.7 times the dynamic pressure q_∞. For the thick, round-nosed profile (Figure 19), on the other hand, the pressure distribution is "more complete"; the pressure minimum extended only to x = 0.2 t of the leading edge (= smaller movement of the center of pressure), and it is $p/q_\infty = -2.4$. At the suction peak in the thin profile, $v = \sqrt{1 - (-3.7)}$, which is 2.16 times the speed of the outer flow; at p_{min} of the thick profile, $v = 1.85\ v_\infty$.

The pressure distribution surfaces give an important idea in regard to the relation of the airfoil upper surface and under surface in the production of lift. The negative pressure areas in Figures 18 and 19 are five times as great as the positive pressure areas (- plotted above, and + under the zero line), so that an airfoil can be rightly called a "suction wing."

---

*) The coefficient c_n determined on the same airfoil in a wind-tunnel measurement is somewhat larger; the difference corresponds to the friction drag, which does not appear in the pressure measurement.

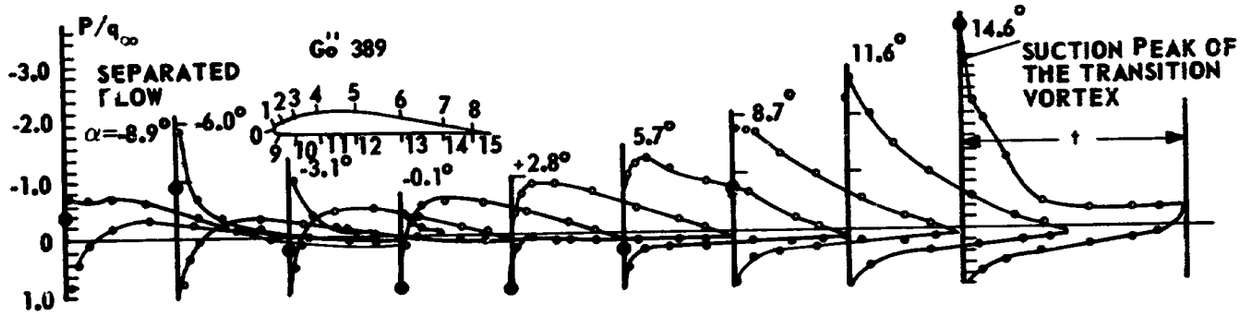

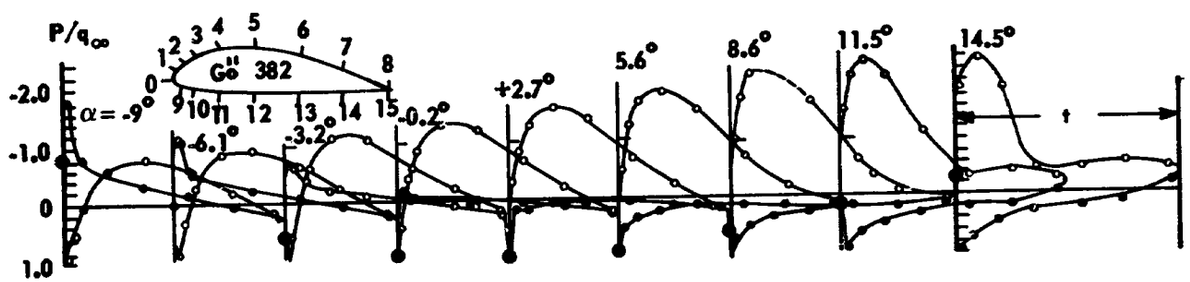

Figures 18 (above) and 19 (below). Pressure distribution on the Goettingen profiles 389 (d/t = 0.102) and 38) (d/t = 0.202) at various angles of attack. Re = 420,000.

c) The Reynolds Number of the Boundary Layer, Re_δ

The pressure distribution according to Figures 18 and 19 shows the wall pressure and thus the pressure state in the boundary layer. The local velocity v calculated from it is valid only to the edge of the boundary layer; however, while in the boundary layer itself the velocity gradient is determined by the laminar or turbulent state (Figure 4). If the local velocity v effective at the edge of the boundary layer is now used, along with the friction length ℓ as the distance from the stagnation point, to form a Reynolds number of the boundary layer $Re_\delta = v \cdot \ell/\nu$, this number differs from the Reynolds number of the plane friction plate of Figure 6 only in that now v changes with the pressure state. At the stagnation point, this Reynolds number is zero, and at the trailing edge it is approximately equal to the profile Reynolds number. Because on the lower surface the velocity v, proceeding from a zero value at the stagnation point, first reaches the value v_∞ of the external flow at the trailing edge, the increase of Re_δ to Re on the lower surface occurs more slowly and on the upper surface more rapidly, than the increase of the Reynolds number along the plane friction plate. Accordingly, the laminar approach stretch on the lower surface of airfoils is longer, even with a flat under surface, and shorter on the upper surface, than on thin plane friction plates.

To obtain a picture of this, the Reynolds numbers of the boundary layer were each determined for two angles of attack from the pressure distributions given in Figures 18 and 19, and the ratio Re_δ/Re was plotted in Figure 20 as a function of the chord t. The diagonal represents the local Reynolds number for the flat friction plate. As a consequence of circulation (acceleration on the upper surface, retardation on the lower surface) the Re number line for the suction side flow goes above the diagonal and that for the pressure side below the diagonal. It is immediately seen that this representation clearly shows the thickening of the boundary layer, or the separation point, on the upper surface as a sudden increase or bend. Although on the thick profile 382 the separation point changes only slightly with angle of attack change from 5.6 to 14.5°, with the thin profile and for the same α-range there is a pronounced migration from 0.75 t to 0.3 t. From the higher velocity v in flow around the nose of the thin profile, a higher local Reynolds number would be expected here along the upper surface than for the thick profile. Instead of this, however, Figure 20 shows higher local values of Re_δ/Re for the thicker profile.

The conclusions from pressure distribution (Re = 420,000) are:

1. The sharp leading edge gives a high suction peak but the large pressure gradient is countered by an equally great pressure increase; in

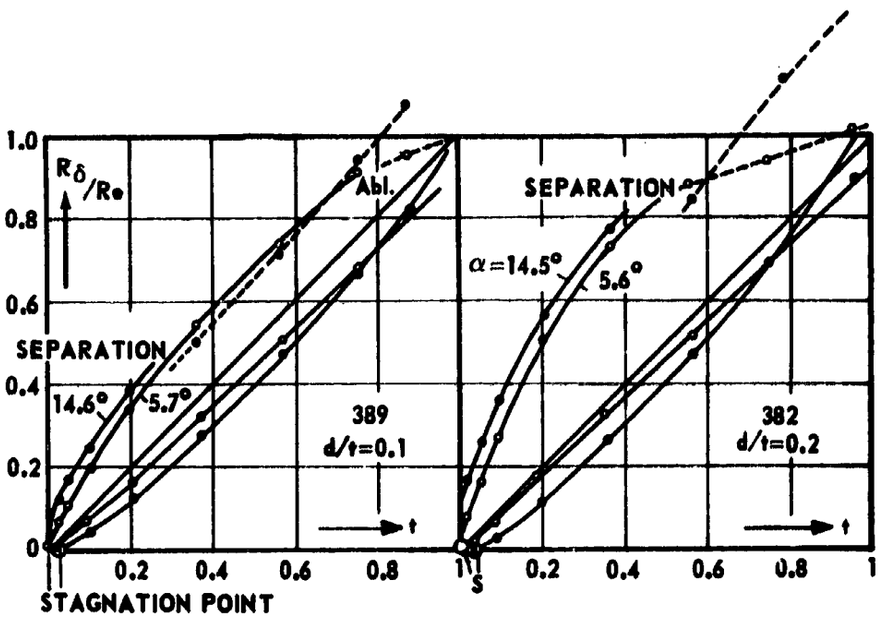

Figure 20. Evolution of local Reynolds number Re_δ on the free edge of the boundary layer for profiles 389 and 382, shown in ratio to the Reynolds number of a friction plate of length $\ell = t$. The diagonal corresponds to the Reynolds number of the friction plate. The Reynolds number of the pressure measurement used for calculation of v is 420,000.

consequence, the pressure conversion and the flow around the nose involve an energy loss which is greater as the leading edge is sharper; as a high angle of attack and high Reynolds numbers this is unfavorable, because reduced energy content of the boundary layer and higher pressure gradient effect an earlier separation of the flow. In the large airplane, accordingly, the nose should not be pointed but should be kept as round as possible to achieve a high $c_{a\ max}$ value.

2. If the surface friction were to be regarded as the sole turbulence cause for the upper-surface flow, then the transition would have to happen sooner for the thick profile than for the thin, because in spite of higher acceleration on the flow around the nose the local Reynolds number is higher than for the thin profile. The turbulent transition leading edge is based on another cause, however, which justifies the sharp nose on the model airplane in spite of the above-mentioned losses.

d) Movement of the Stagnation Point

With the increase in circulation, the stagnation point S_1 moves counter to circulation on the rotating cylinder in parallel flow; on the other hand, the rear stagnation point S_2, which in the transition from ideal to friction flow becomes the separation point A, moves with the circulation direction (Figures 21 and 22). At $u/v = 4$, S_1 and A have approached each other to such a degree that they coincide (see [4], vol. 2, p. 97); the body has been drawn completely into a negative pressure region. The streamlines move on the leading side toward the point of maximum negative pressure and on the rear side divergently with increasing pressure. As soon as the circulation becomes smaller, the convergence decreases: the stagnation point moves back. Phenomena on the airfoil are similar to this. The theory bases the origin of lift on the airfoil in the effect of the superimposition of a parallel low on a circulatory flow; their velocities are additive at the airfoil upper surface because there they are in the same direction and thus produce an acceleration and accordingly a negative pressure, and on the other hand they are subtractive on the airfoil under surface because they are counter to one another; that is, they produce retardation and positive pressure. Lift is proportional to the circulation. Analogous to the process on the cylinder, the stagnation point on the airfoil moves counter to the circulation, that is, from the forward profile point along the lower surface. At a high angle of attack and high lift, the suction effect of the upper surface is several times greater than the stagnation pressure on the lower surface, so that with the wing the flow ahead of the wing is convergently drawn up, so that the streamline striking on the stagnation point is bent sharply upward (Figures 15 and 17). If the flow detaches, then with decreasing circulation, the convergence of flow and the stagnation point backward displacement become smaller.*) Even though the movement of the stagnation point is only a few percent of the chord, nevertheless this has a considerable influence on production of turbulence, as will be shown. With increasing angle of attack, the stagnation point moves back, as far as $t/2$ at $\alpha = 90°$.

To obtain an idea of the movement of the stagnation point from the pressure distributions given in Figures 18 and 19, the pressures measured at the five holes farthest upstream are plotted on the development of the profile nose in Figures 23 and 24. The thick profile has the higher stagnation point movement. For an α-range of about 15° on the thick profile, this is about 4 percent of the chord, and on the thin profile 2.5 percent. If the wing nose is replaced approximately by circles, then the center angle traversed by the stagnation point for this α-range of 15° is about equal to 90° for the two profiles.

---

*) The phenomenon of hysteresis can be explained by this.

Figure 21

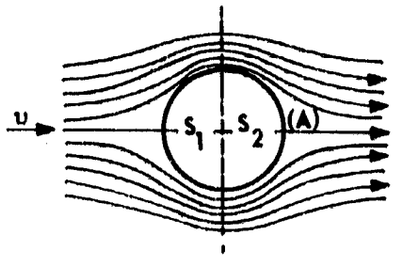

Figure 22

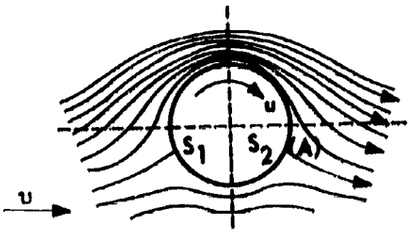

Figure 21. Theoretical flow around a cylinder (or a sphere) in an ideal frictionless fluid (potential flow).

Figure 22. Theoretical flow around the rotating cylinder in a parallel flow. The front stagnation point moves counter to the circulation and the rear one with the circulation.

e) Change in Pressure and Velocity in Flow About the Nose

In addition to center-of-pressure movement, Figures 23 and 24 show the change in pressure in the vicinity of the stagnation point. The maximum pressure gradient can be seen on the thin profile at $\alpha = 14.6°$, where the stagnation point coincides with measurement hole 9, but the pressure minimum $p = 3.7\ q_\infty$ coincides with hole 0 at the leading edge 4 mm away (Figure 23). Accordingly, from the stagnation point to the leading edge the total pressure drop is $4.7\ q_\infty$. Because the pressure measurement was made at $v_\infty = 30$ m/sec, at the leading edge (according to Subsection II 5b) the velocity $v = v_\infty \sqrt{1 - (-3.7)} = 30 \cdot 2.16 \approx 64$ m/sec prevails. This velocity develops at the edge of the boundary layer along the short stretch of $\ell = 4$ mm, so that the acceleration from $v = 0$ at the stagnation point to $v = 64$ m/sec occurs in the time of

$$t = 2\ell/v = 2 \cdot 0.004/64 = {}^1/_{8000} \text{ sec.}$$

The acceleration, assumed uniform, is accordingly

$$b = v/t = 64 \cdot 8000 = 512{,}000 \text{ m/sec}^2.$$

This means that if the acceleration were to last only one second the velocity would be 512,000 m/sec; however, since it lasts only ${}^1/_{8000}$ sec, v reaches only 64 m/sec. Close behind the stagnation point, however, the acceleration is even greater, as the slope of the osculating tangent shows. This acceleration is several times greater than that of a rifle bullet, which, for example, at the

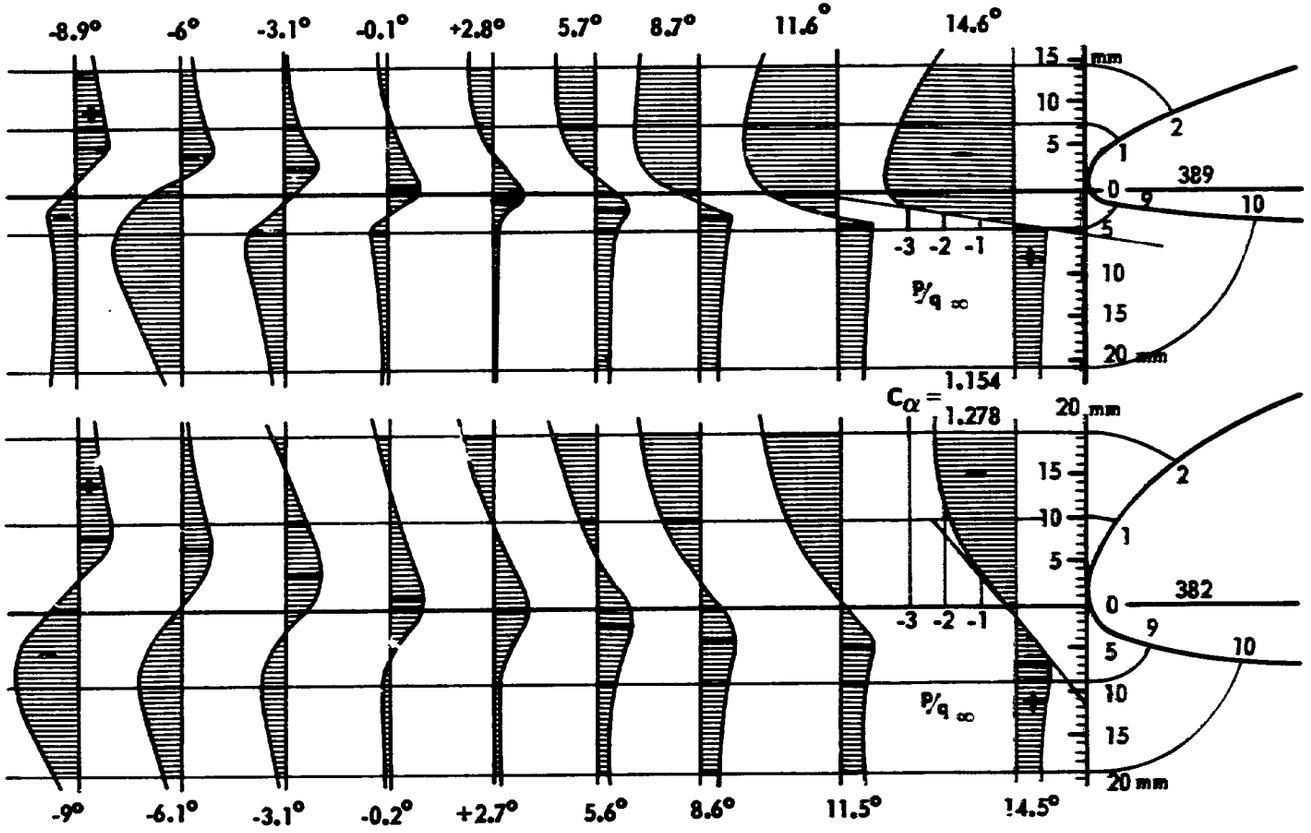

Figures 23 (above) and 24 (below). Pressure distribution in flow around the nose for profiles 389 and 382.

muzzle of an 0.8-m long rifle barrel has reached a velocity of v = 800 m sec in $^1/_{250}$ sec and thus achieved an acceleration of 200,000 m/sec^2.

On the thick profile 382 and at α = 14.5° the velocity increases from the stagnation point out up to the leading edge from 0 to 34 m/sec along a distance of 7 mm in $^1/_{2400}$ sec. Acceleration here is 82,000 m/sec^2, and thus less than $^1/_6$ that of the thin profile. The pressure minimum is farther above the back of the nose, however, and v_{max} = 55 m/sec is not reached until after 38 mm path length from the stagnation point, while on the thin profile the velocity decreases from directly above the leading edge. Accordingly, the flow on the thin profile is more likely to be turbulent sooner and separate sooner, as will be explained later.

f) The Transition Vortex

The suction peak and the velocity connected with it in the flow around the wing nose are higher as the profile is thinner. In the thin, plane plate with sharp leading edge, therefore, these phenomena must be especially prominent, so that the flow around the flat plate will be studied somewhat more closely. At α = 0° angle of attack on the thin plane plate only friction drag is produced, and at α = 90° only pressure (form) drag, while at an angle of attack as an airfoil, lift and both kinds of drag are produced. The increase in lift per degree of change in angle of attack even considerably exceeds that of the customary profiles, although of course only to about 10°, because then the flow has separated. The separating tendency is strongest at α = 90°. On the plate to which flow approaches perpendicularly (Figure 25), in the first instant of beginning flow the flow follows the rear side of the plate (potential ow). At increasing speed, the particles of the boundary layer flowing on the front side toward the edge attempt to go out transversely to the principal direction over the edge; they are diverted by the neighboring layer of fluid and forced to change direction by 180°. A point of mass ρ, which moves at velocity v and radius r on a curved path, has a centrifugal effect

$$Z = \frac{\rho \cdot v^2}{r} .$$

If the edge is knife-sharp (radius r → 0) then the centrifugal force in a frictionless fluid would have to be infinitely large and thus produce an absolute vacuum, and the flow around the edge therefore would have to occur at infinitely high velocity. Instead of this, however, the boundary layer detaches itself as a "separation surface" from the edge, forms a small vortex, which quickly becomes larger (Figures 26 and 27) and then is carried away by the flow to make space for a newly forming vortex.

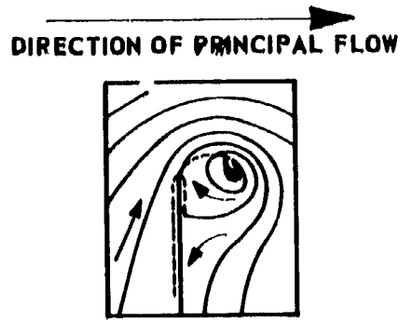

Figure 25. Starting state: potential flow.

Figure 26. Development of a curling vortex.

Figure 27. Detached separation surface: progressing vortex.

Figures 25-27. Flow around the edge of a plate perpendicular to the principal flow.

If the plate is set, as an airfoil, at an angle of attack from 0 to 3°, for example, then a substantial lift is effective, with the flow ahead of the plate acting convergently and the stagnation point moving backward, so that the boundary layer must flow from the stagnation point around a sharp leading edge with a directional change of almost 180° (Figure 28). Similar to what has been described above, there then forms over the leading edge a small eddy as a small local separation, which at first does not lead to separation of the flow, because on the rear side of the eddy the boundary layer again attaches itself turbulently (Figure 29). Because the boundary layer detaching itself in laminar form above the leading edge becomes turbulent through this eddy, it is called the "transition eddy." As the angle of attack increases, the vortex broadens and flattens itself, and the external flow forms a bridge over it, while a profile with a fluid upper side forms to a certain extent (Figures 29 and 30). With increasing angle of attack, the bridge span approaches the trailing edge more closely, and the character of the vortex changes; it is no longer local but increases. The change is from the stationary transition vortex to the curling vortex, or from the "fluid profile" to the "separation surface." Individual vortices under the bridge move backward (Figure 31), and the flow separates for an instant but again attaches after passage up to the next vortex. This phenomenon manifests itself unpleasantly as heavy vibration on a plate hanging in the wind tunnel. After a small increase in the angle of attack, the flow then remains separated, the vibration of the model decreases, and it then hangs again almost quietly in the wind tunnel.

Figure 28

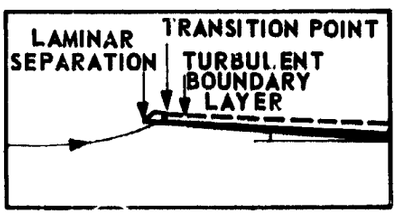

Figure 29

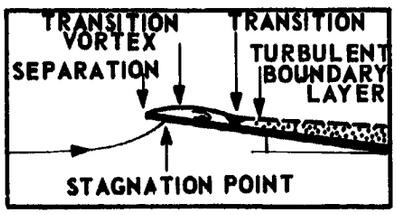

Figures 28 and 29. Flow around the leading edge of a flat plate at low angle of attack; origin of the turbulent boundary layer on the upper surface by stationary transition eddy.

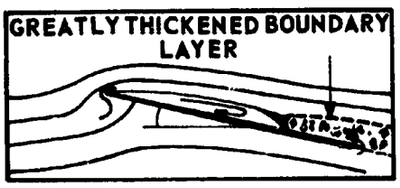

Figure 30. Extension of the transition eddy with increasing angle of attack.

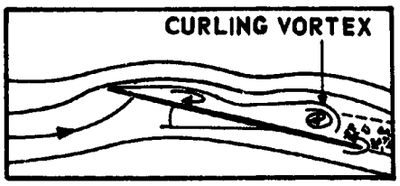

Figure 31. Transition from stationary transition eddy to periodically separating curling vortex.

The negative pressure at the leading edge acts as a "suction force" counter to the drag component; theoretically both cancel out in potential flow of the ideal fluid with circulation. The drag would then equal zero.

The phenomena were first described in principle by Prandtl (see [2], p. 145) in connection with a discussion of the behavior of the flat plate in a potential flow with circulation: "In the actual flow around a plate with a sharp leading edge, infinitely high negative pressures do not occur, of course, but there is a separation of the flow; this at small angles of attack through the action of a turbulent process again attaches itself to the upper surface so that a flow form not entirely dissimilar in general terms to the theoretical occurs, with a similarly high lift. In the absence of the suction force, a resistance is naturally obtained here which exceeds the friction drag by $A \cdot \tan \alpha$ (A = lift). The equivalent of this additional drag is to be sought in the loss in speed which occurs through the turbulent process on the upper surface." In the same place, it is said concerning the significance of the suction force: "With well-rounded profiles the suction force takes on practical meaning. If the resultant of an

airfoil inclined at a 6° angle of attack is only 2° to the perpendicular, as is frequently observed, then the effect of the suction force can be clearly seen."

If the velocity of sound ($c \approx 340$ m/sec) is achieved in the flow around the sharp leading edge at the free border of the boundary layer, then the mechanism of nose turbulence is influenced by Mach waves (see [2], p. 184). Because the flow at this point occurs in a region of lower pressure, these must be rarefaction waves. It can be assumed that this phenomenon intensifies turbulence. Its range of influence must be very small, however, because the velocity decreases rapidly again to that of the outer flow

g) The Upper-Surface Flow

This begins at the wing nose at the splitting point of the flow; the stagnation point, and therefore, because of stagnation point migration on the airfoil undersurface of an airfoil at the angle of attack, so that the distance to the trailing edge for the upper surface flow in the thick profile 382 at 14.5°, for example, is about 17 percent greater than the path along the lower surface. Four characteristic points characterize the flow state along the upper surface: stagnation point, pressure minimum, transition point, and separation point. After the pressure minimum, a pressure increase begins which, depending on the magnitude of the suction peak, can reach four times that of the stagnation pressure q_∞ (Figures 18 and 19) against which the boundary layer must flow and in the most favorable case overcome it as far as the trailing edge. Overcoming of this pressure increase is the most important phenomenon of flow around the airfoil. The closer the separation point can approach the trailing edge the greater will be the lift achieved, the less the resistance, and thus the more favorable the drag-lift ratio. The theoretical maximum would be achieved by potential flow, that is, by vortex free and frictionless flow around the airfoil in an "ideal" noncompressible fluid, as can be calculated scientifically by extensive support of mathematics. Through superposition of two potential flows - a parallel flow and a circulation flow - a lift, but no drag, can be demonstrated by calculation for an airfoil with an infinite span. This would be the most favorable limiting case of the drag-lift ratio $c_w/c_a = (1/\infty) = 0$, that is, practically a gliding flight without loss of altitude in still air. In reality, however, even with a sound flow, that is, one attached all the way to the trailing edge, because of friction and vortex losses, a drag-lift ratio of 1:30 today must be looked upon as the maximum value. From a theoretical potential standpoint, the airfoil lift increases with the angle of attack according to the equation

$$c_a = 2\pi \cdot \sin\alpha \quad ,$$

so that at $\alpha = 90°$, a $c_{a\ max} = 2\pi = 6.28$ would be achieved. Since, however, the actual flow depending on profile form and Reynolds number detaches prematurely supercritically in the range of $\alpha = 10°$ to 30° on the wing upper surface only $c_{a\ max} = 1$ to 2 is reached; with the aid of flaps 2 to 3 is reached, with suction airfoil ≈ 4, and with an airfoil out of which air is blown, > 4. A brief description will be given here of the three types of force which operate on the straight airfoil in straight flight:

1. Pressure forces act on all particles in the pressure field of the airfoil.

2. As a result of the viscosity of air, friction forces act from the wall on the particles near the wall and thereby produce a friction layer.

3. Drag forces from the outside flow act on the friction layer when it flows turbulently.

Considerable clarification is still awaited on the details of the manifold interplay of flow phenomena on the airfoil. A good idea of individual processes is obtained from flow photographs and measurements made in a closed water tunnel of the Aerodynamic Research Laboratory at Goettingen by P. Jordan (see [12], p. 191). These tests were done on the symmetric Goettingen profile 409 at Re $\approx$ 150,000, and thus still in the region of model flight. They are therefore especially worthwhile for the study at hand. Profile 409 (see [3], I, p. 94, and III, p. 29) has a thickness d = 0.127 t; the radius of the nose circle is r $\approx$ 0.017 t. The test model with an aspect ratio of $\Lambda = 2.5$ was bounded by flat walls at the airfoil ends to realize two-dimensional airfoil flow as much as possible. To make visible the phenomena in the boundary layer, colored liquid was supplied out of six holes, 0.44 mm diameter, in the middle section of the wing.*) At the negative angle of attack $\alpha = -3°$, Figure 32a shows the laminar flow along the lower surface; although at -4.5° it probably is completely attached to the airfoil, at -3° the already existent pressure increase cannot be overcome and consequently causes separation at about $\frac{3}{4}$ t. The outflow point of the colored liquid at hole 6 in Figure 32b is shown by the arrow; the reverse flow

---

*) On the side walls a secondary flow (see [3], I, p. 89 and [6], p. 103) influences the flow; this is less noticeable in the center of the wing the higher the aspect ratio. The boundary layer flow can be seen most completely in the closed water tunnel with dyestuffs emitted from the airfoil; in addition, higher speeds can be reached than in the open water tunnel where surface tension and, at high speeds, wave formation, influence boundary pehnomena.

wedge according to Figure 5 is clearly visible. From this phenomenon, it can be concluded that it would be inadvisable to camber the airfoil of an airplane model substantially on the underside as is done on modern profile sections for large airplanes.

The laminar separated boundary layer is mobile, as is any separation surface. Through the sudden increase in speed at the separation surface, it tends to form waves whose swells then cause vortices to roll up (Figure 33) and finally to break down in disordered succession of vortices: the laminar separated boundary flow becomes turbulent. At $\alpha = +1°$, the upper side has become the suction side and the stagnation point has begun its movement to the lower surface so that the turbulence effect of flow around the airfoil nose becomes effective. At 0.7 t a laminar separation can be observed (Figure 32c); the laminar separated boundary layer becomes turbulent, however, after a distance of 0.2 t, and at 0.9 t again attaches itself, because the impulse exchange occurring from the external flow just suffices to overcome the pressure increase. The separation, which is only local, can be seen through its shadow in the enlarged Figure 32d.

Jordan states further, in a note, that separated flow can again attach itself for other reasons. "If, for example, the wall forms a reentrant corner (Figure 34) then in this corner there occurs a local dead space containing vortices. At the site where the flow again attaches itself after this dead water a stagnation point occurs. The boundary layer proceeding from this stagnation point then begins in laminar form." This is an interesting example of the reduction of turbulence as a consequence of convergence of flow.

The transition location clearly indicated for $\alpha = +1°$ contracts with increasing angle of attack and moves toward the wing nose. At $\alpha = 4.5°$ in Figure 32e, laminar separation can no longer be seen. It can be concluded that this phenomenon is possible down to molecular size; probably every turbulent transition point on a wall lies behind a laminar separation point. The further observation that at $\alpha = 10.5°$ the transition point extends almost to the leading edge (Figure 32f), and here the apparently laminar separation and the turbulent transition are again clearly separated, as can be seen from the enlargement (Figure 32g), speaks further for this assumption. The colored liquid emerges at hole 1, indicated by the arrow, and thus flows, counter to the main flow, toward the leading edge. Between the wing and the outer flow above the airfoil leading edge a transition eddy acts; at its rear side the boundary layer again attaches itself turbulently. It is a phenomenon similar to that at +1°. Behind the transition vortex the boundary layer is of course much thicker, which permits a conclusion of an early breakaway. This transition point is not visible in the picture, because the nearest colored liquid hole 3 lies farther back, at the righthand arrow. The scheme is shown in Figure 35.

For Figures 32a through 32g: laminar and turbulent phenomena in the boundary layer, made visible in the water tunnel by colored liquid, which emerges from holes in the airfoil.

Re = 150,000.

Symmetric profile: Goettingen 409, d/t = 0.127; r/t 0.016. From original photos of P. Jordan, Goettingen (see [12], p. 191).

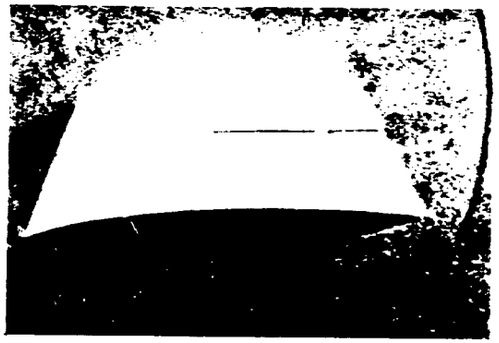

a) α = 3°. Laminar separation on the pressure side; the colored liquid filament remains laminar up to the trailing edge of the airfoil.

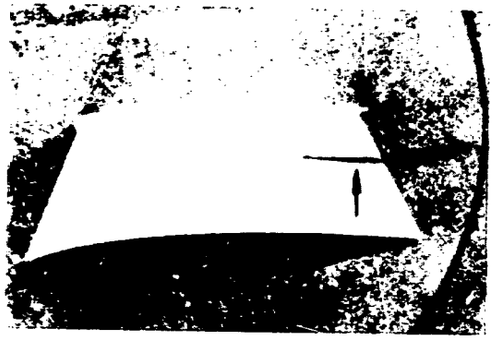

b) α = 3°. Dyestuff emission at the arrow to indicate the reverse flow in the reverse flow wedge.

c) α = +1°. At +1° (now the suction side), laminar separation at 0.7 t, and then turbulent attachment of the boundary layer at 0.9 t.

d) α = +1°. Enlarged insert from Figure c. Laminar separation at the shadow, turbulent attachment visible in the mixing zone.

e) α = 4.5°. The transition zone collapses and moves toward the airfoil nose with increasing α.

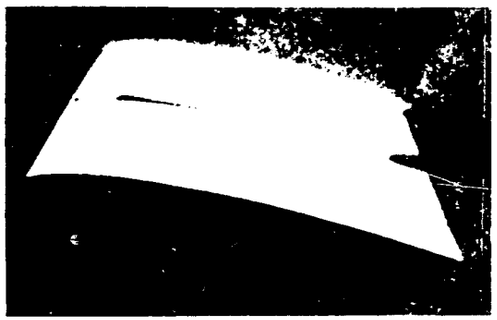

f) α = 10.5°. The transition point has reached the leading edge and expands as a transition vortex. Turbulent separation at 0.9 t.

g) Enlargement from f. Reverse flow in the transition vortex, in front the laminar separation, transition region not visible. Second dyestuff hole shows a turbulent thickened boundary layer.

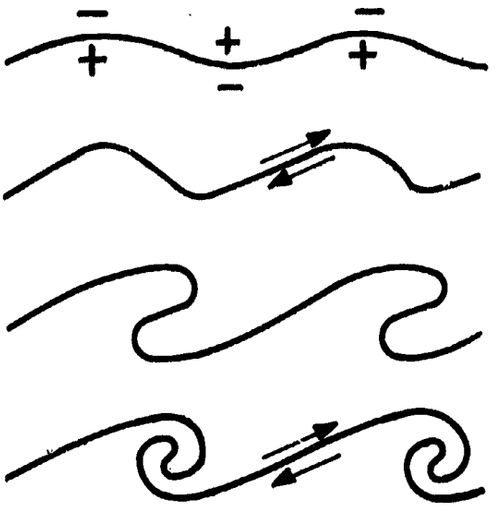

Figure 33. Origin of waves and curling vortices through sudden change in velocity at a junction surface (from Prandtl).

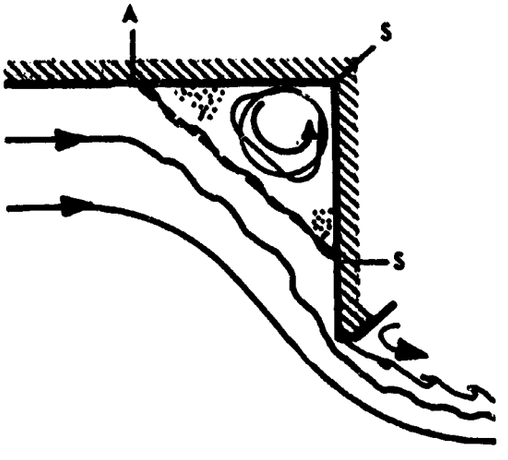

Figure 34. Constriction of flow by a wall corner (from Jordan).

Conclusions:

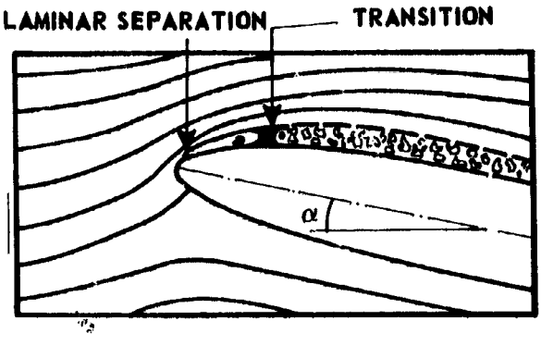

Figure 35. Scheme of the transition vortex.

1. The transition point of laminar into turbulent boundary layer flow moves along the upper surface from the trailing edge to the leading edge:

   a) with increasing Reynolds numbers in small degree through friction turbulence,

   b) essentially, however, with increasing angle of attack as the result of "nose turbulence," through the cooperative effect of stagnation point movement and acceleration at the flow around the nose, and then further by flow divergence as a consequence of the upper-side curvature and angle of attack.

2. The transition point reaches the leading edge earlier, that is, at smaller Reynolds numbers and smaller angle of attack,

   a) the smaller is the camber of the upper side, and therefore earliest for the flat plate.

   b) the sharper is the leading edge.

3. The suction peak manifesting itself on thin or slightly curved profiles with increase in angle of attack (cf. Figure 18 at 11.6° and 14.6°) shows that the transition point has reached approximately the foremost position and that its broadening into a transition vortex is occurring.

4. In general, the transition point lies behind the pressure minimum. For a high-speed airplane which flies in normal flight with a very small c_a, and therefore uses a thin, approximately symmetrical profile, it is therefore advantageous to move the maximum camber back so that the transition point lies far downstream, to achieve as long as possible a laminar run of low surface friction: "laminar profile." In contrast to this, a "turbulent profile" with a high mean camber but with a smaller rearward displacement of the maximum camber and a sharp leading edge is favorable for the airplane model, as bird wing profiles show.

5. For the thin flat plate at the minimum angle of attack, the nose turbulence effect is very great and the pressure increase is small toward the trailing edge; a small energy content of flow at Re < 20,000 suffices for the boundary layer to attach turbulently and to displace the transition vortex to the leading edge, in contrast to the round-nosed, thick, high-camber profile where at low angle of attack the nose turbulence is small and the pressure increase is great as a result of high wall curvature, so that it is not until Re ≈ 100,000 that the transition is forced; then, however, the attachment occurs suddenly along a considerable profile stretch.

6. Because the effect of nose turbulence increases faster than pressure increase for the thin plate, the approach flow in the wind tunnel can begin at any angle of attack; in addition, the flow condition is reproducible with increasing or decreasing speed and at increasing or decreasing angle of attack, since the measurement then gives the same course of aerodynamic force plots, as a proof of "lack of sensitivity to Reynolds number." The critical angles of attack α_k and $c_{a\,max}$ always are the basis for the influence of Reynolds number, since both increase further with increasing drag effect of the external flow, and therefore with increasing Reynolds number, as is valid for all profiles in the Reynolds number range studied.

h) Separation Phenomena of the Upper-Surface Flow

The separation phenomenon in the presence of a transition vortex, which has been briefly discussed for the flat plate, may be described in further analysis of the Goettingen measurements of Jordan on profile 409. At first on profile 409, intermittent separation and attachment of flow occur at $\alpha = 11.25°$. The oscillation of flow, which at first occurs slowly and then increasingly rapidly with increasing angle of attack, leads above 11.75° to a final separation. As shown by pressure recordings on a strip chart, the separations during oscillation of flow begin at the leading edge; the transition vortex broadens into a bridge, then separates from the leading edge with periodically detaching vortices, and then again attaches itself. Although separation of the boundary layer progressing from the rear forward was not seen here, it can be assumed that with a thicker profile having a sharper leading edge both separation phenomena can probably occur simultaneously.

An instructive supplement to these flow observations is supplied by the pertinent measurements of pressure distribution on profile 409, which shows in Figure 36 the transition from the attached state at $c_{a\,max}$ through the oscillation phenomenon to a fully separated state at measuring holes 1 to 6. The suction

peak is connected with the "attached state, and the negative pressure, increased with time, at hole 4 is connected with the transtion between attached and separated flow during oscillation. Both have the same pressure area; but the "center of pressure" of the resultant aerodynamic force changes between t/4 and t/3. After final break way, the same pressure obtains everywhere along the upper surface (dot-dashed pressure area). The reverse flow wedge has become a "dead water area" filled with vortices, extending to the leading edge and sucking reverse flow fluid around the trailing edge from the lower surface, so that the pressure distribution on the lower surface is essentially changed, with negative pressure prevailing from about t/3 on. As the angle of attack increases, the negative pressure again disappears on the lower surface.

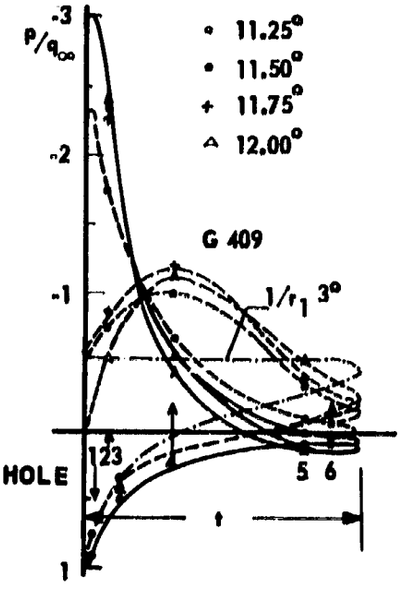

Figure 36. Pressure distribution on the symmetric profile G 409 at the transition from $c_{a\ max}$ through the oscillation phenomenon up to completely separated upper-surface flow at 14.3°.

It may be said in summary about separation phenomena:

1. In the subcritical flight state, the boundary layer remains detached in laminar form on the profile, and the separation point lies just behind the pressure minimum.

2. Separation of the supercritical flow is preceded by a thickening of the boundary layer.

3. The higher the Reynolds number the later does turbulent separation begin at the trailing edge; with increasing angle of attack and increasing profile thickness it then progresses to the leading edge.

4. At a low Reynolds number, a transition vortex is characteristic; it boradens with increasing angle of attack upon reaching the foremost position, and brief turbulent shocks give enhanced lift peaks, and then separation starts at the leading edge and proceeds along the entire chord.

If the leading edge is sharp and the camber of the upper surface small, then after separation the cause of turbulence remains, and accordingly the characteristic bridge building of the separated upper-surface flow exists: lift does not decrease but instead increases somewhat further with increasing α-value.

On the thick round-nosed profile, the separation point passes the transition point as angle of attack increases, so that a separation of flow occurs; the separation point then jumps to the point of pressure minimum corresponding to laminar separation. Lift decreases suddenly to its subcritical value and the flow then first increases suddenly at a considerably smaller α-value or at a higher Reynolds number (hysteresis loop in the polar plot).

5. The sharper the leading edge, the earlier does the transition vortex reach the leading edge, and the earlier does its broadening begin; the flow separates at a smaller critical angle of attack α_k the smaller is the achievable $c_{a\ max}$. It can be concluded from this that the incorporation of a sharp edge on an airfoil leading edge is favorable only on a model airplane, to compel the supercritical flight state, but on the large airplane, as angle of attack increases the drag-lift ratio worsens and premature separation occurs.

To keep the picture simple, up to now only the two-dimensional flow around an airfoil has been considered. In the influence of phenomena by spanwise flows, especially in separation pehnomena, the effect of the transition vortex on the twisted wing at a high angle of attack is worth mentioning in this respect. Here the flow which first separates in the center of the wing flows to the location of low pressure of the attached flow, while parts of the flow, using the transition vortex as a tunnel for transverse flow, again become boundary layer material, with the result that although the suction peak sinks there, a more complete pressure distribution (similar to that in Figure 36) occurs, permitting, for example, 2 to 4° higher angle of attack α_k before the flow separates up to the wing tip. In addition, as a result of this, the nose-down moment is greater before separation, so that the model airplane tips more favorably forward instead of stalling.

The flow picture of the transition vortex is similar to cavitation (cavity formation) on ships' propellers, where local water bubble vortices or vapor bubble vortices - on thin profiles going from the leading edge and on thick profiles from the pressure minimum - flow downstream and have a harmful action on the material of the propeller through powerful impact blows (see

[5], vol. IV, part 1, pp. 473-476, contribution by Ackeret). Just as the cavity formation decreases with increasing external pressure of the water (for example, on a diving submarine), so with increasing Reynolds number a decrease in the transition number is probable. Broadening and separation then begin as a result of the higher drag effect of the external flow at a higher angle of attack. Accordingly, the transition vortex has a greater importance in the Reynolds number range of model flight than in the Reynolds number range of the large airplane. For ships' screws it may further be concluded that measures to displace the beginning of broadening of the transition vortex to higher angles of attack are suitable for reducing cavitation, for example, by the use of profiles with rounded leading edge instead of the sickle profile with its sharp leading edge (Figure 56b); this profile's transition vortex and high suction peak are unavoidable at a low angle of attack.

i) The Flow Along the Lower Surface

Although it suffices for achieving the supercritical flight state if merely the boundary layer on the upper surface is turbulent, it is still worthwhile to see why the boundary layer of the lower surface remains laminar in general, under what circumstances it becomes turbulent, and how the transition manifests itself.

The profile underside can essentially be

1. cambered concavely, as in the bird's wing;
2. plane, as was first done by Junkers to achieve simpler manufacture;
3. moderately negatively cambered as in the case in modern high-speed airplanes;
4. made with S curvature, like the profiles of sailplanes.

The velocity is reduced on the under surface of the airfoil ($v_u < v_\infty$ in Figure 17), and the streamlines are convergent. Both phenomena are more effective in respect to maintenance of laminar state the higher is the angle of attack. Because nose turbulence is effective only on the upper surface, only friction turbulence will consequently be expected on a flat or moderately convex lower surface.

The use of profiles with convex lower surface, especially symmetrical profiles, is not to be recommended for model airplanes, however, because at angles of attack in the range of normal flight the laminar boundary layer

separates from the lower surface, as is made clear in Figure 32a for the symmetrical profile G 409 at $\alpha = 3°$ and Re = 150,000. The separation disappears as the angle of attack increases. If this attachment suddenly takes place over a lengthy profile stretch, then the change in the values of c_w and c_a must show a sudden increase in the polar plot.

For a flat lower surface, at transition from negative to positive lift, the profile is at an angle of attack where the pressure equalization $p/q_\infty = 0$ is achieved shortly after the stagnation point and, as for example in Figure 18 on profile 389 at $\alpha = 1°$, it remains up to the trailing edge, so that on this stretch Re_k of plane friction must be exactly valid. Accordingly, the length ℓ of the laminar initial stretch can be determined here. According to Figure 6, the beginning of the transition lies between Re = 500,000 and 1,000,000. For the airplane model, because of flight in the turbulent region near the ground and because of the greater relative roughness of the wing upper side, the smaller number is more likely to hold; the larger number is more probable for the large airplane. With $Re_k = 500,000$, the length of laminar initial run:

$$\ell = \frac{Re_k \cdot \nu}{v}$$

is calculated for five examples:

	v, m/sec	ℓ, mm
Model airplane	6	1200
Model airplane	12	600
Sailplane	15	480
Small sport plane	40	125
High-speed engine-powered plane	100	70

For $Re_k = 1,000,000$, the laminar initial run is twice as large in each case. In general, it is true that with increasing Reynolds number the laminar initial run becomes smaller; that is, the transition point achieved because of plane friction turbulence moves from the trailing edge toward the leading edge. In any case, the flow along the lower surface for model airplanes with profiles similar to that in Figure 17 remains laminar in the range of normal flight.

The following concept is important for understanding of flow around an airfoil: between laminar and "fully turbulent" is a transition region which according to Figure 6 extends from $Re = 5 \cdot 10^5$ to 20 times this amount or Re = 107, so that actually three flow states must be differentiated. Behind

the above-mentioned transition points, the fully turbulent flow state would not be reached until after 20 times the friction length. It can therefore be concluded that behind the transition point a flow form corresponding more or less to the transition state prevails at first.

Because in the usual aerodynamic force measurement in the wind tunnel, α is moved by steps to a positive angle of attack (raised up) from the range of negative lift, and thus a turbulent state is initially present on the wing under surface, at a setting in the neighborhood of $c_a = 0$ the nose turbulence, which up to then influenced the airfoil lower surface, now becomes effective for the upper surface. The boundary layer of the lower surface therefore becomes laminar and at times separates. This change becomes noticeable in every polar plot as a transition, jump, or point of inflection.

This phenomenon is especially apparent with bird wing profiles which are highly concave on the lower surface of the wing. Here, at a negative angle of attack, there is a transition eddy on the wing lower surface extending from the leading to the trailing edge and becoming smaller when the model is turned higher in the wind tunnel; then at tangential approach flow to the front part of the profile, and thus at relatively great positive angle of attack, it disappears, as shown in the polar plot by a c_a jump at about $c_a = 0.5$.

III. MODELS AND MEASURING METHODS

1. The Models Used

The profiles were chosen to show extreme contrasts in behavior in regard to Reynolds number and thus to show the limits of influence of the problem. The model wings are rectangular in plan.

Model dimensions:

Chord length	$t = 90$ mm
Span	$b = 450$ mm
Aspect ratio	$\Lambda = b : t = 5$

The models are not rounded at the tips but are cut off sharply. The axis of rotation is at t/4 on the mean line chord. The sting for the rear mount is located here on the lower surface to avoid disturbance on the upper surface. Trolon plastic was used as a material for the profile model. The rough-milled profile outline was cut out by spoke shave according to a glued-on template photograph, to an accuracy of 0.1 to 0.2 mm, and was worked to a good surface

List 3

Dimensions of the Wing Profile in Percentage of Chord (cf. Figure 92)

	x	0	1.25	2.50	5	7.5	10	15	20	30	40	50	60	70	80	90	95	100
G 625	y_o	5.50	9.00	10.80	13.30	14.95	16.35	18.25	19.30	20.00	19.05	17.35	15.05	12 10	8.60	4.75	2.75	0.65
	y_u	5.50	3.30	2.35	1.25	0.75	0.40	0.15	0.10	0.00	0.00	0.00	0.00	0.00	0.00	0.00	0.00	0.00
N 60	y_o	3.40	5.60	6.76	8.24	9.33	10.14	11.32	11.98	12.41	12.03	11.06	9.55	7.66	5.50	3.04	1.72	0.40
	y_u	3.40	1.91	1.46	0.96	0.62	0.40	0.15	0.04	0.04	0.22	0.48	0.71	0.78	0.64	0.37	0.19	0.00
N 60R	y	3.40	5.60	6.76	8.24	9.33	10.14	11.32	11.98	12.41	11.95	10.79	9.18	7.42	5.75	4.28	3.66	3.20
	y_u	3.40	1.91	1.46	0.96	0.62	0.40	0.15	0.04	0.04	0.14	0.21	9.34	0.54	0.89	1.61	2.13	2.80
Flat Plate	y_o / y_u	0.00	0.80	1.00	1.30	1.40	1.45	1.45	1.45	1.45	1.45	1.45	1.45	1.45	1.40	0.80	0.40	0.00
417 a	y_o	1.45	3.00	3.65	4.70	5.60	6.30	7.15	7.75	8.60	8.80	8.45	7.85	6.90	5.70	4.25	3.55	1.45
	y_u	1.45	0.05	0.45	1.55	2.50	3.30	4.20	4.85	5.70	5.90	5.55	4.95	4.00	2.80	1.30	0.60	1.45

smoothness. The flat plate and the curved plate were made of steel sheet 2.6 mm thick. Figure 37 shows the dimensions and ratios given the following lists 3 and 4, in percentages of chord length, with the exception of a few angles.

The camber f of the profile mean line is measured upward from the theoretical chord, which serves as the x-axis in profile calculations. At the forward end, this theoretical chord goes through the intersection of the profile mean line with the point r/2 of the nose circle and to a corresponding point at the rear, that is, through the apex if the trailing edge is sharp.

2. The Characteristic Measuring Method

The lower limit of the measured range of Reynolds numbers - Re $\approx$ 20,000 - corresponds, with the chosen chord of t = 90 mm, to a stagnation pressure reading of q = 0.75 mm water column. The aerodynamic force changes to be measured at this low stagnation pressure are of the order of magnitude of a tenth of a gram at low angles of attack. Every angle of attack setting produces a small change in the tare balancing in experiments with wire-hung models; this was reduced, to be sure, by journalling of the model axis in two small rollers, but it caused serious dispersion in the subcritical range of Reynolds numbers. Accordingly, the conventional polar measurement, in which speed is held constant and the angle of attack α in the wind is changed, was used only for a check. Instead of this, another measuring method was used successfully. In it, at a fixed angle of attack α the velocity v was changed by stages in two test series, first with increasing speed and then with decreasing speed. This method will be called "characteristic measurement" to differentiate it from the polar measurement. The result of the two characteristic tests series for α = 10° on profile N 60 is shown in Figure 39 as an example. The coefficients c_a, c_w, and $c_{m0.25}$ are plotted as a function of Re. The c_a line shows with increasing v, and thus increasing Reynolds number, subcritically from A' to B' an increase in lift coefficient and then at B', at Re = 147,000, a jump of c_a = 0.76 to the supercritical line at c_a = 1.06. With increasing v, the c_a line increases only slightly, but then with decreasing v at point E', where Re = 82,400, it suddenly drops down again to the subcritical line trace A'B'. The cause is that from D to E the boundary layer remains turbulent and therefore attached at the upper surface of the profile. At E', the separation point of the boundary layer reaches the transition point on the profile; the flow separates and remains separated subcritically from A' to B' because the boundary layer remains laminar. The points B' and E' correspond on the profile to the boundary layer points where the transition and separation points coincide. If the flow has attained the super or subcritical state, then the flow remains separated below B and attached above E, no matter whether increasing or decreasing v is used in measurement.

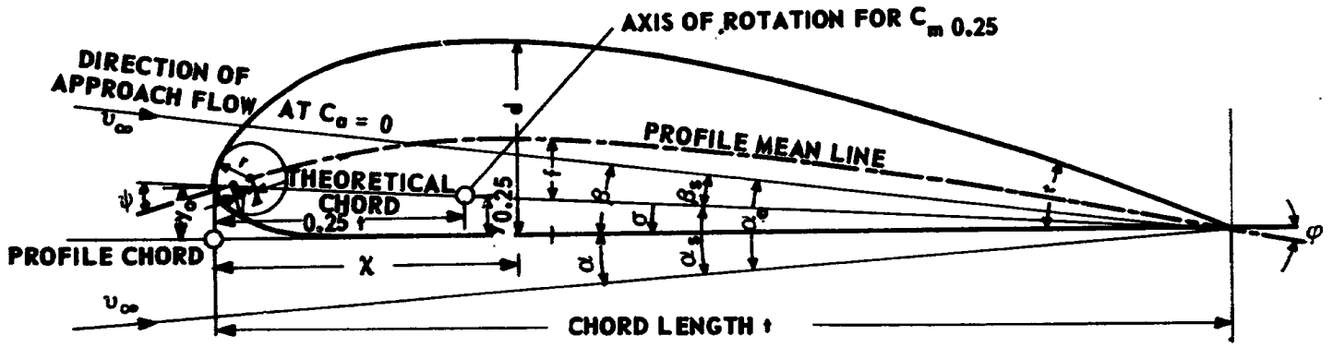

Figure 37. Sketch of the dimensional and angular relationships for an airfoil profile. (Instead of profile chord the term "lower-surface tangent" is common too.)

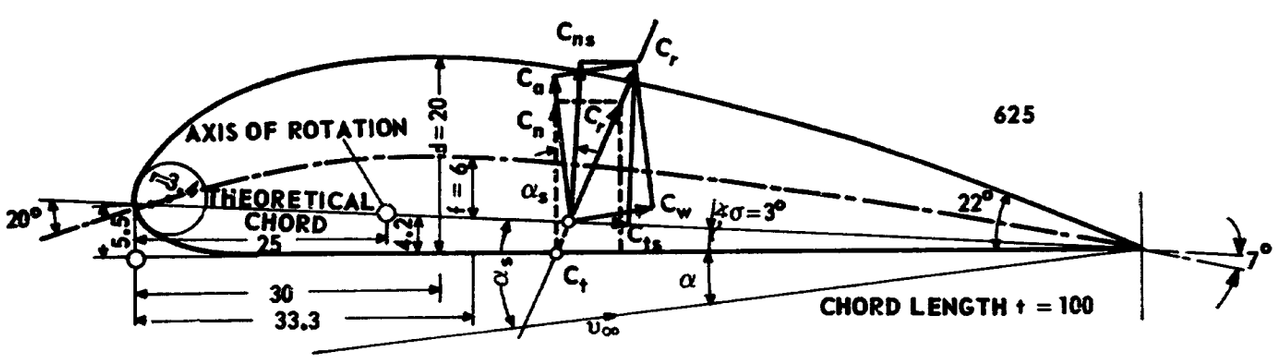

Figure 38. Measurements and angles for Goettingen profile 625. The sketch of aerodynamic force resolutions is plotted on this figure, too.

List 4

Ratios of the Wing Sections Used For Measurement

(Measurements in percentages of chord length t)

Profile No.	Maximum Thickness d at x		Camber f at x		Nose Radius r	Chord Distance y_0	Chord Distance $y_{0.25}$	Chord Angle $\sigma°$	Tangent Angle of the Mean Line $\psi°$	Tangent Angle of the Mean Line $\varphi°$	Apex Angle (Trailing Edge) $\tau°$
G 625	20	30	6	33.3	3.4	5.5	4.2	3°	20°	7°	22°
N 60	12.41	30	4	40	1.4	3.4	2.6	1.9°	15°	7°	13°
N 60R	12.41	30	3	36	1.4	3.4	3.3	0.23°	13°	0°	13°
Flat Plate	2.9	10 to 75	0	--	0.5	0	0	0°	0°	0°	12°
Curved Plate 417 a	2.9		5.8	40	1.45	1.2	1.25	0°	22°	10°	--

Wing Sections Used for Comparison

G 417	6.3	20	6.1	37	0.7	0.5	0.45	0.4°	23°	9°	88.5°
G 389	10.2	29	4.2	36	0.85	2.0	1.5	1.3°	15°	7°	13°
G 382	20.2	31	6.9	36	1.7	5.6	4.2	3.2°	25°	9°	22°
G 409	12.74	35	0	--	1.6	0	0	0°	0°	0°	17°

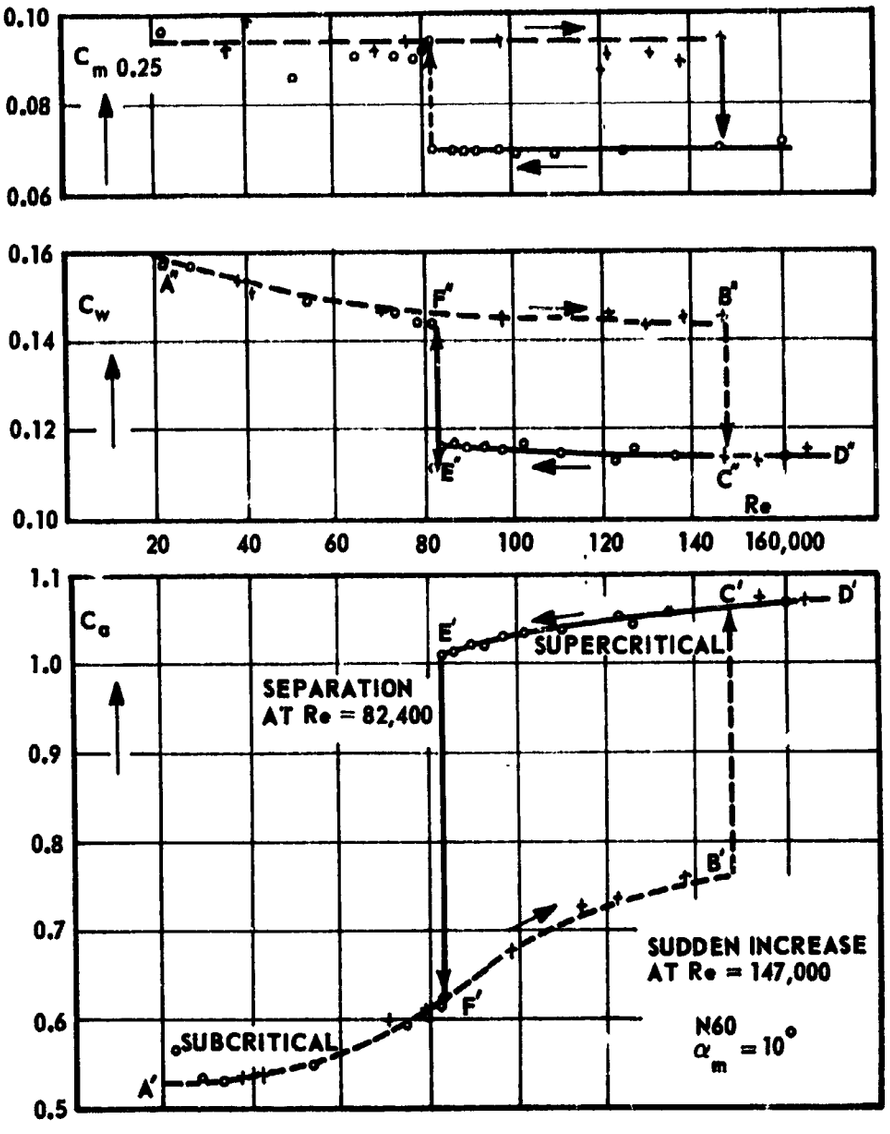

Figure 39. Measurement of the hysteresis loop in the "characteristic measuring method."

The two lines measured for drag coefficient c_w show contrary behavior in comparison with c_a; at separation (point E''), the resistance suddenly becomes greater, and therefore the moment. In this manner each profile was measured in steps of 2° in setting. With increasing angle of attack, the separation and sudden increase displaced toward higher Reynolds numbers, so that the available velocity of the test installation no longer sufficed to cause the flow to reattach. To permit supercritical measurement of the air forces at these high angles of attack, the flow had to be made to attach artificially by making the boundary layer turbulent. To cuase it to attach, a stick was placed horizontally in the flow at the height of the model axis for a few seconds.

The compilation of these characteristic test series for some 10 to 25 different angles of attack in which the α span ranged from -25° to +25 (e.g., for profile N 60 in Figures 57 through 59) gave a continuous overall picture for each profile. The polar plot can be taken from this as a cross section for any given Reynolds number of the measured region (compiled for N 60 in Table 4).

3. The Hysteresis Loop

The three-dimensional coordinate system c_a versus c_w and Re in Figure 40 makes clear the relationship between polar measurement and characteristic measurement. The rectangle CEFB represents a longitudinal section through the hysteresis loop, which appears in cross section in the polar plot. The measurement of the supercritical polar curve occurs at increasing α (raising up into the wind), beginning with attached flow at low angles of attack, until the flow separates, e.g., at 19.5° for N 60 in Figure 40 from point M to G in the polar plot for Re = 147,000. As measurement continues with α decreasing, the flow remains separated from H to E, and then first at 10° springs to point C of the polar curve. The following interrelationship exists between characteristic measurement and polar measurement:

1. Measurement with attached flow up to the point of separation: this corresponds to

   a) Characteristic measurement with decreasing v (line DCE),

   b) polar measurement at high values of α (line MCG).

2. Measurement with nonattached flow up to the point of sudden increase: this corresponds to

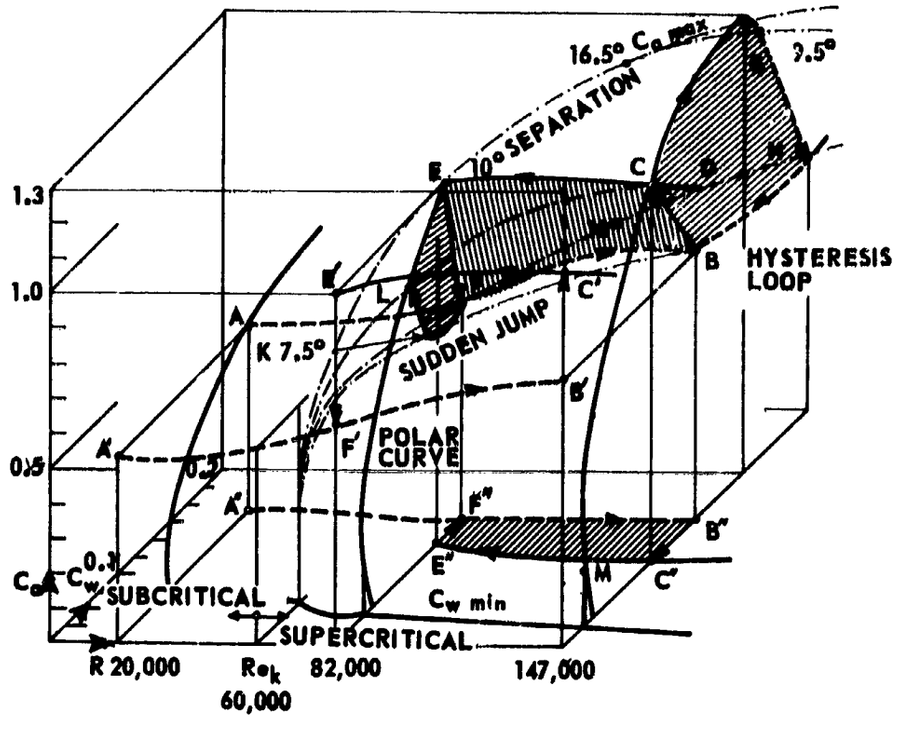

Figure 40. Three-dimensional coordinate system c_a versus c_w and Re to show the relationship between the characteristic measuring method (longitudinal section) and the polar measuring method (cross section).

c) characteristic measurement with increasing v (line AFB),

d) polar measurement with decreasing α for separated flow (line HB).

Conclusion: if a wind tunnel measurement begins in a low turbulence flow for any reason with an α-setting in the region between the limit of the sudden increase CL and the separation line EG, then - in both the characteristic and the polar measurement - the flow after attainment of the desired velocity must be "attached" by making the boundary layer turbulent, for example, by briefly placing a stick upstream.

In the negative range of angles of attack, only very thick profiles with intensively rounded nose show a hysteresis loop. The test rule must be noted as above, and thus the flow must be attached or, for the polar curve, α must be reduced.

The lines of sudden increase and separation have their origin at the critical Reynolds number Re_k (e.g., for profile N 60, Re_k is 63,000). In the subcritical region, the transition necessary for attachment of the laminar boundary layer flow remains in the turbulent region, so that no hysteresis occurs.

Most wind tunnels are afflicted with an undesirably high inherent turbulence. With increasing degree of turbulence, Re_k, as well as the sudden increase and separation belonging to a given angle of attack are displaced to a lower Reynolds number, and therefore show excessively favorable test results.

In the fully turbulent stream, e.g., with an upstream turbulence grille (Figure 12), there is no subcritical flow and no hysteresis in the range measured here; in addition, instead of the sudden separation at high α-values there is a more rounded path of the polar curve. It should be mentioned in addition that in the subcritical region and after separation corresponding to F to H the turbulence bar is effective only as long as it remains held in front. After it is removed the flow separates again both the two cases.

The flow behavior important for the study of model flight in the subcritical region is found in the characteristic measuring method to be simply the prolongation of the lower hysteresis line BF, or the area HBKF, to A. For model flight, hysteresis has practical importance for the "stalled" stage of flight, for spin conditions, and for the subsequent sudden increase after a dive (acceleration at low α) for the purpose of restoration of the normal flying position.

IV. PLOTTING OF THE TEST RESULTS

The aerodynamic forces were measured on the models at various angles of attack α_m: lift A (kg) perpendicular to the direction of airflow, drag W (kg) parallel to the direction of airflow, and moment $M_{0.25}$ (m · kg) about the axis of rotation of the model flying on the theoretical chord 0.25 t. After conversion, these are plotted as dimensionless coefficients c_a, c_{wm}, and $c_{m0.25}$ as a function of Re. In the Reynolds number pertaining to each test point, the atmospheric fluctuations of temperature and air pressure, or the changes or

air density ρ and kinematic viscosity ν, were taken into account in calculation of the Reynolds number $Re = (t \cdot v/\nu) = (t\sqrt{2\,q/\rho})/\nu$. The influence of air humidity in the test area is negligibly small.

Equations for calculation of the coefficients in the notation introduced by Prandtl are:

Lift coefficient $c_a = \frac{A}{q \cdot F}$;

Drag coefficient $c_w = \frac{W}{q \cdot F}$;

Moment coefficient $c_{m0.25} = \frac{M_{0.25}}{q \cdot F \cdot t}$;

Stagnation pressure $q = \frac{\gamma \cdot v^2}{2g}\,(kg/m^2)$.

1. G625 Wing Profile

The influence of Reynolds number is strongest in round-nosed, thick, pronouncedly cambered profiles. As a first example, therefore, the thick profile 625 of the Goettingen Aerodynamics Research Laboratory (AVA) was chosen, because this wing section was used in Goettingen as well as by the German Aviation Research Institute in Adlershof [19] for characteristic measurements, whose results the present measurements supplement. The profile has a camber of the profile mean line of $f = 0.06\,t$ at $x = t/3$ and a maximum thickness of $d = 0.20\,t$ at $x = 0.30\,t$ (Figure 38).

a) Plot of c_a Versus Reynolds Number

The rapid increase in c_a values at the critical Reynolds number, which here is $Re = 105{,}000$ (Figure 41), is especially striking. In the supercritical region, the two most important phenomena "separation" and "sudden increase" appear as perpendicular lines: separation with the arrow downward, and sudden increase with the arrow upward. The beginnings and ends of the lines are delimited by four dot-dashed line segments which have their origin at Re_k. The two upper lines correspond to the supercritical state of "attached flow," and the two lower to the state of "unattached flow."

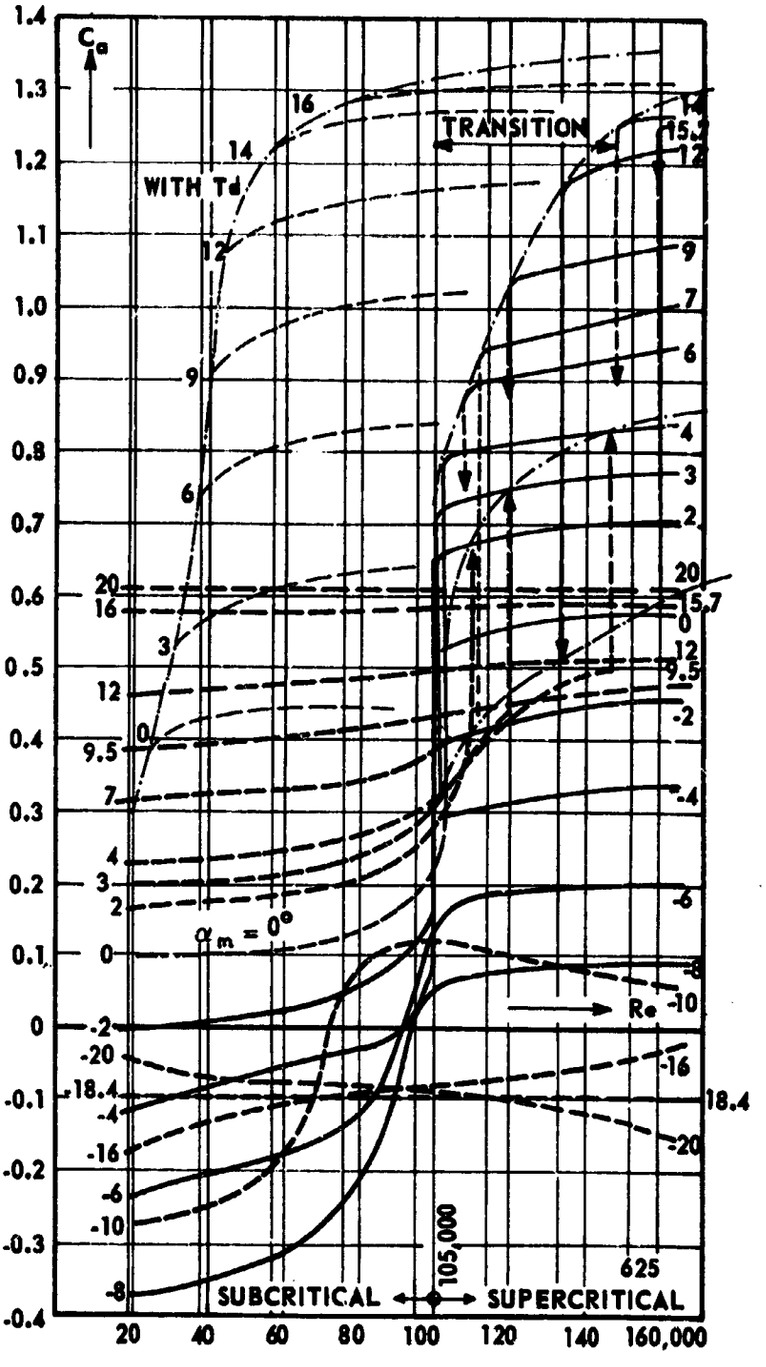

Figure 41. Test results: lift coefficient c_a as a function of Re at the transition from the subcritical to the supercritical state for profile 625. Arrows pointing downward indicate "separation"; arrows pointing upward indicate "sudden increase." A turbulence wire stretched parallel to the leading edge of the airfoil displaces the critical Reynolds number from 105,000 to about 20,000.

The behavior of several α-lines will be explained. The measurement of the 4-degree line, for example, starting at Re = 21,000, shows only the low c_a value = 0.2; at Re_k there is a stronger increase, and then at Re = 154,000 the increase is from c_a = 0.5 to c_a = 0.8. Thus it increases to four times the initial value. With attached flow, the further increase of the 4-degree line is small. Going in the direction of decreasing Reynolds number, at Re = 108,000 the flow separates, the lift coefficient drops on the 4-degree line back to "unattached flow." For angles of attack higher than 4°, the upper Reynolds number limit available in the test installation was not sufficient to cause the flow to attach. For example, to measure in the "attached" condition at 12°, a stick was held upstream for a few seconds, and making the boundary layer turbulent in this way caused the flow to attach. At Re = 141,000, the 12° line separates and drops back to the 12° line of unattached flow with c_a = 0.5. Below 155,000, as long as a turublence grid is held in place or a turbulence wire stretched across upstream (Td), a premature displacement of the critical Reynolds number to about 20,000 results.

The separation line is identical with the $c_{a\ max}$ line up to 14°. At higher angles of attack, the separation line is below the $c_{a\ max}$ line. Between the separated flow - supercritical compared with subcritical - at high angles of attack, there was no difference recognizable from the test point series, which showed pronounced dispersion here; the c_a line for 20° was plotted as a horizontal, although from comparison with other measurements at higher Reynolds numbers an increase would be expected here, too.

In the region of negative lift, the picture shows by the remarkable S-shaped curve of the $c_{a\ max}$ line an apparent reversal of the phenomena, because here the negative lift coefficient increases with decreasing Reynolds number. The value c_a = 0 results for the -8° line at Re = 100,000 and for Re = 21,000 at α = -2°. The value of $c_{a\ max}$ = -0.38 at Re = 21,000, calculated from c_a = 0, is reached with an α setting of -6°. On the other hand, to produce an equally large positive lift at Re = 21,000 about twice the α-setting, +11.5°, is necessary, that is, the less cambered lower surface is more effective at low Reynolds number because the flow here remains "attached" up to -8°, while on the strongly cambered upper profile half, the flow has largely separated. The setting -2° corresponds roughly to airflow on the direction of the mean line chord so that the profile half lying below the mean line chord at Re = 21,000 balances the lift produced by the four times more strongly cambered line of the upper side for c_a = 0. In the degree to which at an increasing Reynolds number the point of

separation moves toward the trailing edge on the strongly cambered upper surface, so that the flow produces a higher +component in accordance with the stronger camber, the smaller becomes the residual $-c_a$ value or the stronger must the negative angle of attack of the lower surface be for equalization to $c_a = 0$, e.g., -8° at Re = 100,000. The influence of Reynolds number on the change in angle of attack at $c_a = 0$ is therefore the greater the greater is the difference in the pattern of camber of the two halves of the profile, and thus it is least for symmetrical profiles and plates.

The more that separation phenomena cause the flow picture to depart from the potential flow with circulation, and the less does the flow centerline coincide with the profile mean line, the more must the study of the separation phenomena on the profile halves be drawn upon for explanation of the relationships. It may be stated here that the flat plate and the symmetrical profile at Re = 21,000 and $\alpha = 6°$ reach exactly the same value mentioned above, $c_a = 0.38$, and this then remains almost at the same level for the flat plate as Reynolds number increases (Figure 47). For the symmetrical profile it increases slowly, while in the picture at hand for profile G 625 on the path of the -8° line, $-c_a$ slowly decreases. Above -8° the flow separates on the lower surface, so that now the slowly increasing stagnation effect of the upper surface (previsouly separated in laminar form) causes the phenomena to intersect at $\alpha = -18.4°$.

b) Plot of c_{wm} as a Function of Reynolds Number

In the supercritical region, the lift increase achieved by a sudden increase or attachment of flow is connected with a sudden reduction of drag, because the vortex zone behind the separation point, displaced farther back as it is, has become smaller. The phenomena of "sudden increase" (Figure 42) and "separation" (Figure 43) are delimited by dot-dashed lines. Subcritically the -4° line, and supercritically the -6° line, form the $c_{a\ min}$ value. The 12° line for separated flow runs horizontally, while in the c_a measurement this did not occur until 20°.

In the region of negative angle of attack (Figure 44) the peculiar reversal of the phenomena is again evident, with drag first decreasing at small Reynolds numbers and large negative angles of attack. With increasing Reynolds number and decreasing minus angle of attack, the picture changes from the character of the symmetrical profile at $Re_k = 105,000$ and $c_{w\ min} = -4°$ to the region of influence of the strongly cambered upper surface.

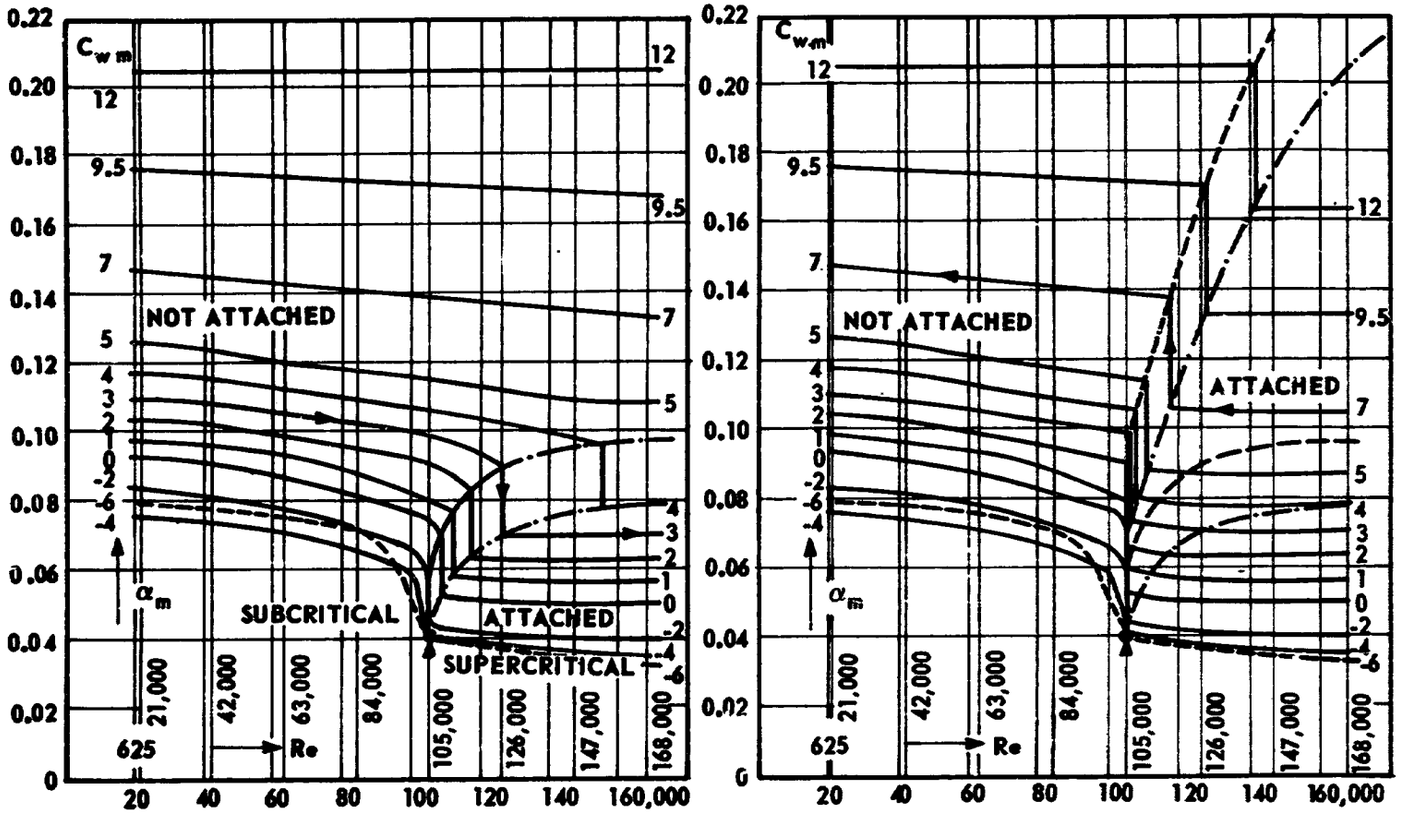

Figures 42 (left) and 43 (right). Test results for $c_{w\,m}$ as a function of Re.

Arrow →, measurement with increasing v, gives ↓ sudden change, and ← with decreasing v gives ↑ separation of flow (-6° to 12°, profile 625).

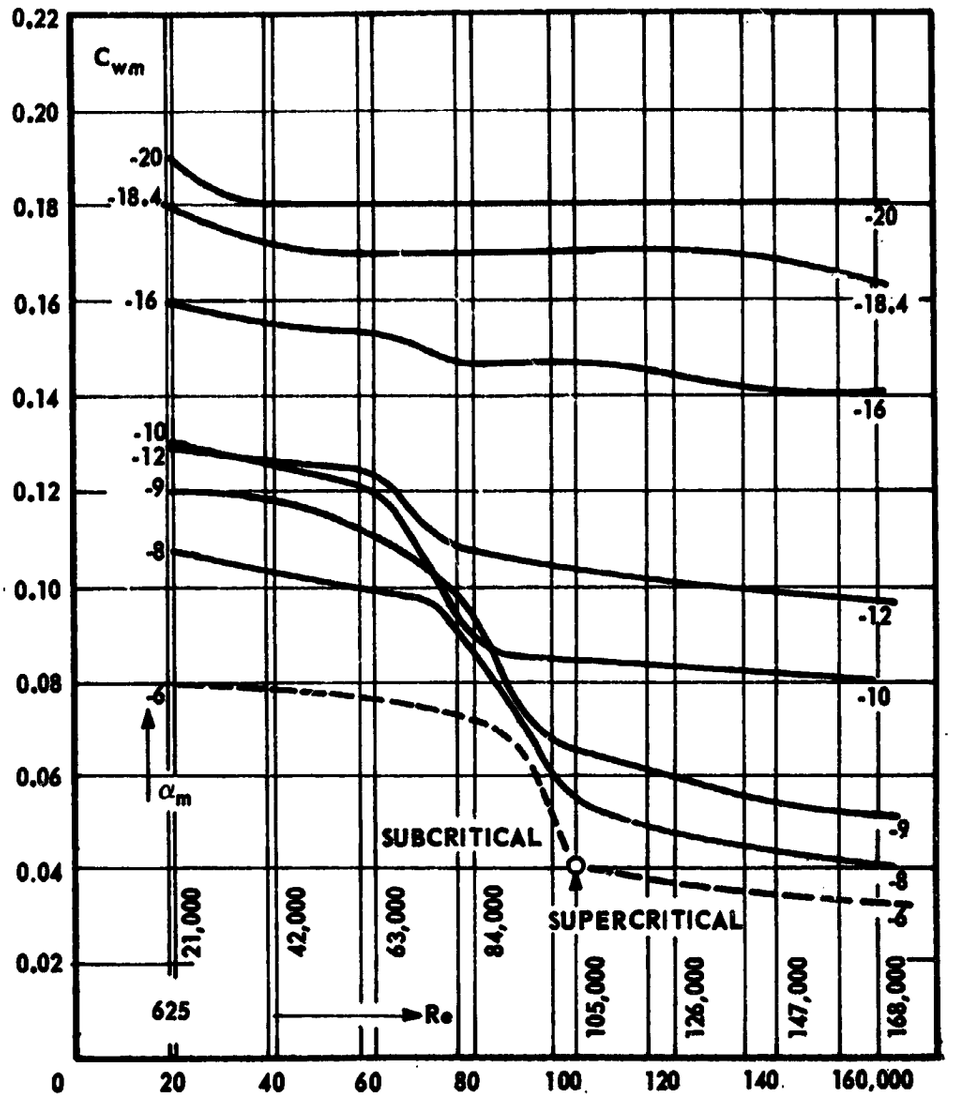

Figure 44. Test result: Drag coefficient c_{wm} as a function of Reynolds number (-6° to -20°, profile 625). Subscript m means measured value without a flow correction calculation.

c) Plot of $c_{m0.25}$ as a Function of Reynolds Number

The moment coefficient $c_{m0.25}$ is referred to an axis of rotation which (in agreement with the model axis in the measurements) lies 0.25 t behind the leading edge and on the theoretical chord of the profile mean line (Figure 38). The measured moment $M_{0.25}$ (m · kg), the moment coefficient $c_{m0.25}$, and the formerly customary value c_m, whose axis of rotation passes through the lower-surface tangent and through the foremost projection point 0 of the profile, are connected by the equation:

$$\frac{M_{0.25}}{q \cdot F \cdot t} = c_{m0.25} = c_m - 0.25\, c_n + \frac{y_{0.25}}{t}\, c_t$$

(see Figures 37, 45, and 67).

If the resultant aerodynamic force or its coefficient

$$c_r = \sqrt{c_a^2 + c_w^2}$$

is resolved (Figure 38) 1. at the intersection with the lower-surface tangent - normal and tangential to it - then the coefficients of the normal and tangential force components are:

$$c_n = c_a \cdot \cos \alpha + c_w \cdot \sin \alpha$$

$$c_t = c_w \cdot \cos \alpha - c_a \cdot \sin \alpha$$

2. at the intersection with the theoretical chord - normal and tangential to this - then instead of α, the angle $\alpha_s = (\alpha + \sigma)$ must be substituted:

$$c_{ns} = c_a \cdot \cos (\alpha + \sigma) + c_w \cdot \sin (\alpha + \sigma)$$

$$c_{ts} = c_w \cdot \cos (\alpha + \sigma) - c_a \cdot \sin (\alpha + \sigma)$$

For conversion of $c_{m0.25}$ to another moment reference axis, such as the point of rotation h, there is valid, in view of the sign data of Figure 45:

$$c_{mh} = c_{m0.25} - \frac{x}{t}\, c_{ns} - \frac{y}{t}\, c_{ts} \cdot$$

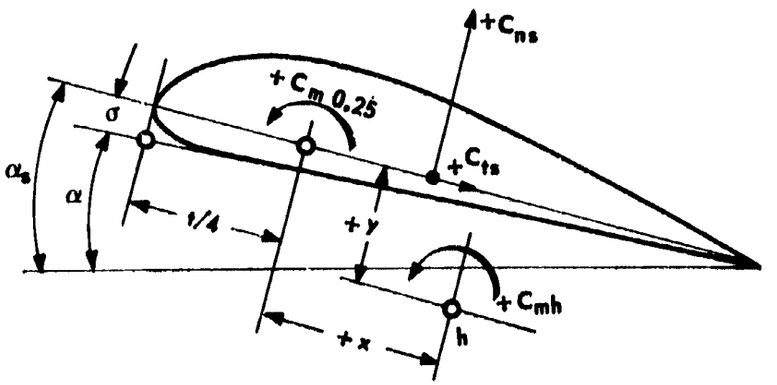

Figure 45. Conversion of $c_{m0.25}$ to another moment reference axis.

Profile G 625 has the coefficient $c_{m0.25} = 0.1$ in Figure 46, supercritically with attached flow, from -8° to about +10°. In the measured range of Reynolds numbers, this thick profile - in contrast to the other profiles (Figure 39) - shows an increase in moment coefficient at the sudden upward increase and a reduction at separation from Re = 100,000 to 130,000. The latter is for the range of angles of attack from -8° to +10°. This range of Reynolds numbers lies in the area of medium-sized model airplanes. In the flying model, the flow in this range separates in stall form even at low angles of attack. The separation, however, does not have the effect of an increase of $c_{m0.25}$ measured on other profiles, causing the downward rotation of the airfoil nose, desirably for the stabilization process; instead, the tendency to turn upward is even increased, by reduction of the moment coefficient. This viewpoint is evidence against the use of thick, strongly cambered airfoil sections for model flight. The moment coefficient of the -8° line shows the highest influence of Reynolds number: At Re = 21,000, $c_{m0.25}$ is about equal to 0 - corresponding to the behavior of the symmetrical profile - and supercritically it is 0.11. With increasingly negative angle of attack, the change in moment coefficient again becomes smaller up to the point -18.4°, for which the position of the axis of rotation at gives a minimum for $c_{m0.25}$, constant as for the profile insensitive to center of pressure, and insensitive to Reynolds number, so that the model when turning free like a weather vane always automatically takes this position and maintains itself stably in the entire range of Reynolds numbers measured here.

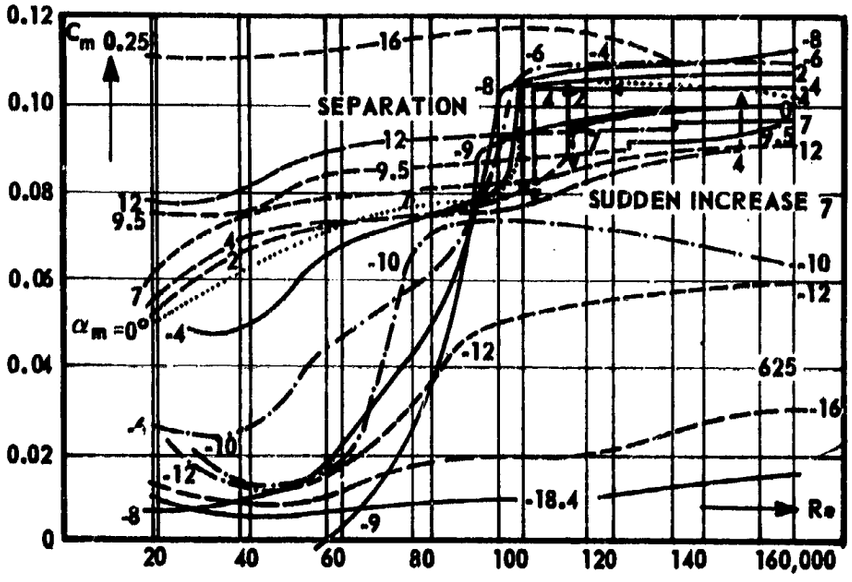

Figure 46. Test Results: moment coefficient $c_{m0.25}$ as a function of Re for profile 625.

d) Determination of Profile Drag $c_{w\infty}$

The polar plots shown in Tables 1 through 5 for the five wing profiles were obtained as cross sections from the plots of the coefficients c_a, c_{wm}, and $c_{m0.25}$ versus Reynolds number (for example, Figures 41 through 46), by taking the coefficients at intersections of ordinates Re = 21, 42, 63, 84, 105, 126, 147, and 168 · 10^3*) with the α_m lines. These values are summarized in the numerical tables (Section VIII) nd were converted to two-dimensional flow, i.e., to infinite span (b = ∞) or to the aspect ratio $\Lambda = b^2/F = \infty$ according to the airfoil theory published by Prandtl in 1918 (see [3], edition I, p. 35, Prandtl, "Outline of Airfoil Theory"). For measured c_a, the conversion furnishes the corresponding profile drag c_{w_∞} and the pertinent "true" angle of attack α_∞. After about 20 years of publication of airfoil measurements based on polar plots for $\Lambda = 5$, now the presentation for $\Lambda = \infty$ is more and more

*) A series of Reynolds numbers divisible by 70 was chosen to facilitate calculation, because for rough calculations the equation Re = 70 · v · t suffices (t in mm, v in m/sec).

becoming the basis of comparison for profile characteristics*). In addition to conversion to $\Lambda = \infty$, the influence of finite dimensions of the wind tunnel airstream and the influence of the rectangular plan of the airfoil model must be taken into account, as shown in the following sections.

1. Influence of finite dimensions of the wind tunnel flow. The pressure field of a wing has a definite range of action which is influenced the more by the finite diameter of the airstream in the wind tunnel the greater is the wing area F in relation to the flow cross section F_o and the greater the wingspan b in relation to the flow diameter D_o. The free jet nozzle of the wind tunnel used in the State Engineering School at Cologne is a regular octagon with an inner diameter of 700 mm and $F_o = 40.6\ dm^2$ jet cross section. With a dimension of the model airplane of $t = 0.9$ dm and $b = 4.5$ dm, the ratio becomes:

$$\frac{\text{airfoil area}}{\text{jet cross section}} = \frac{F}{F_o} = \frac{4.05}{40.6} = \frac{1}{10} .$$

The pressure difference producing lift is, as is known, increased in an enclosed tunnel by the tunnel wall and reduced in the free jet. The lift measured in the free jet is therefore smaller than the lift effective in open air. In Prandtl's correction, however, the lift is not used but instead the angle of attack α_m belonging to the measured lift and the drag or c_{wm}. For the free jet with circular cross section (see [5], vol. IV, part 2, p. 169, Seyferth, "Studies of Airplane Models in the Wind Tunnel") there results:

$$\text{Drag correction } \Delta c_w = \frac{-c_a^2 \cdot F}{8 \cdot F_o} \cdot \vartheta$$

$$\text{Angle of attack correction } \Delta\alpha = \frac{57.3^\circ \cdot -c_a \cdot F}{8 \cdot F_o} \cdot \vartheta$$

$$\text{Correction factor } \vartheta = 1 + \frac{3}{16}\left(\frac{b}{D_o}\right)^4 + \frac{5}{64}\left(\frac{b}{D_o}\right)^8 + \ldots$$

*) Used for the first time in 1918 by the author in the research laboratory of Professor Junkers for airfoil measurements on the study of the "Influence of Thickness Ratio on Profile Properties."

To the octagonal jet cross section $F_o = 40.6\ dm^2$ there corresponds a diameter of a circle of equal area:

$$D_o = \sqrt{\frac{4\ F_o}{\pi}} = 7.19\ dm\ .$$

With $b/D_o = 0.626$, $\delta = 1.032$, and the correction then is:

$$\Delta c_w = c_a^2 \cdot 0.01287$$

$$\Delta \alpha = c_a \cdot 0.738\ .$$

The drag coefficient corrected for the influence of finite jet cross-sectional area, and the pertinent angle of attack which corresponds to the lift coefficient c_a measured for the rectangular airfoil model ($\Lambda = 5$) are then:

$$c_{w5} = c_{wm} - c_{wk5} = c_{wm} - 0.01287\ c_a^2$$

$$\alpha_5 = \alpha_m - \alpha_{k5} = \alpha_m - 0.738\ c_a\ .$$

2. Influence of aspect ratio $\Lambda = b^2/F$. Pressure equalization at the wing tips results in lift reduction, too, so that to achieve the same lift as on a wing of infinite span, the true angle of attack α_∞ must be increased by the induced angle of attack α_i. In addition, the edge vortices arising at the wing tip produce an energy loss which is designated induced drag ($Wi = c_{wi} \cdot q \cdot F$).

For a given lift and given aspect ratio the induced drag is smallest when the lift is distributed along the span in the form of a semiellipse, as is the case for wings with an elliptical plan. According to Prandtl, then:

$$\alpha_i = \alpha - \alpha_\infty = \frac{57.3^\circ \cdot c_a}{\pi \cdot \Lambda}$$

$$c_{wi} = c_w - c_{w\infty} = \frac{c_a^2}{\pi \cdot \Lambda}\ .$$

For example, on the elliptical wing, for the transition from $\Lambda = 5$ to $\Lambda = \infty$:

$$c_{w\infty} = c_{w5} - 0.0637\ c_a^2\ ;\ \alpha_\infty = \alpha_5 - 3.65\ c_a\ .$$

On the elliptical wing, the conversion of given test values for a wing of aspect ratio Λ to any other aspect ratio follows the equations:

$$c_w - c_{wx} = \frac{c_a^2}{\pi}\left(\frac{1}{\Lambda} - \frac{1}{\Lambda_x}\right)$$

$$\alpha - \alpha_x = \frac{57.3^\circ \cdot c_a}{\pi} \cdot \left(\frac{1}{\Lambda} - \frac{1}{\Lambda_x}\right).$$

3. Influence of rectangular model plan. Lift distribution is more complete on the rectangular airfoil, and the induced resistance at $\Lambda = 5$ is about 4 percent greater than on the elliptical airfoil. According to Glauert (see [8], p. 132) the conversion equations:

$$c_w - c_{wx} = \frac{c_a^2}{\pi}\left(\frac{1+\delta}{\Lambda} - \frac{1+\delta_x}{\Lambda_x}\right)$$

$$\alpha - \alpha_x = \frac{57.3^\circ \cdot c_a}{\pi}\left(\frac{1+\tau}{\Lambda} - \frac{1+\tau_x}{\Lambda_x}\right)$$

hold for the rectangular airfoil for the transition to another aspect ratio Λ_x.

The values δ and τ can be taken from the following table:

Λ	3	4	5	6	7	8	9	10	11
δ	0.016	0.026	0.037	0.046	0.055	0.064	0.072	0.080	0.088
τ	0.097	0.122	0.145	0.163	0.183	0.201	0.216	0.228	0.240

These values agree exactly only for those cases where the slope of the lift line $dc_a/d\alpha_\infty = 2\pi$, corresponding to theory (cf. Figure 63).

Conversion of existing measurements on airfoil models of rectangular plan to infinite aspect ratio then gives as a very important result of the study of profile drag:

$$c_{w\infty} = c_{w5} - \frac{c_a^2}{\pi} \cdot \frac{1 + 0.037}{5} = c_{w5} - 0.066\, c_a^2$$

and the pertinent "true" angle of attack:

$$\alpha_\infty = \alpha_5 - \frac{57.3^\circ \cdot c_a}{\pi} \cdot \frac{1 + 0.145}{5} = \alpha_5 - 4.18\, c_a \ .$$

Compared with the elliptical wing, the profile drag is 3.7 percent higher, and the pertinent angle of attack is 14.5 percent greater.

To summarize the three conversion calculations, there result for the Cologne measurements:

$$c_{w\infty} = c_{wm} - 0.07897\, c_a^2 \qquad \alpha_\infty = \alpha_m - 4.918\, c_a \ .$$

The numerical tables given in the Appendix contain the values:

$$\alpha_m,\ c_a,\ c_{wm};\ c_{w5},\ \alpha_5;\ c_{w\infty},\ \alpha_\infty \text{ and } c_{m0.25} \ .$$

In the subcritical as well as in the supercritical separated state of flow, where the elliptical lift distribution is seriously disturbed, the conversion equations give uncertain results. Although the two states mentioned here have no practical use, the calculation was done to show a uniform comparison picture and the relationship of the subcritical with the separated supercritical flow.

Table 1*) gives a survey of wing profile G 325. Three Goettingen measurements at Re = 121, 226, and 430 · 10^3 are added as conclusion and prolongation to the eight polar plots of the authors' own measurements.

e) c_a as a Function of α_∞

The plot of c_a as a function of α_∞ shows clearly the significant lift difference between the subcritical and supercritical attached flow and also the relationship between the subcritical and supercritical detached flow, and for the latter the "transition" to the sudden increase. Because the conversion of induced drag coefficient c_{wi} and the α change connected with this are based on the constant lift coefficient $\left(c_{am} = c_{a\infty}\right)$, the perpendicular separation and sudden increase lines for $\Lambda = 5$ show a slope which is greatest at $\Lambda \to \infty$.

---

*) Tables 1 to 5 appear at the conclusion of this report.

The differences now appearing at the beginning and end of the sudden-increase lines are proportional to the c_a differences. These α differences would not appear if the equation of airfoil theory could be transformed into a uniform angle of attack.

The picture further shows especially clearly the influence of Reynolds number, 1. on the zero-lift β, which varies from -2° to -15°, and 2. on the maximum value of lift, which increases from $c_a = 0.6$ to 1.5. Up to Re = 147,000 or $\alpha_\infty = 7°$, the separation occurs at the $c_{a\ max}$ peak; then above these values, it occurs on the other side of $c_{a\ max}$, after a transition characteristic of turbulent separation and rounded off. The slope of the lift line $dc_a/d\alpha$ agrees closely with the Goettingen lines. The lines from Re = 150,000 to 430,000 coincide on the straight sections of the lift lines, which extend about to the point of sudden increase. In this region, the efficiency η of the profile (corresponding to the expression $dc_a/\widehat{\alpha} = 2\pi\eta$) is constant. Subcritically, the efficiency is very poor; only in the region of negative lift does it become more favorable with decreasing Reynolds number as a result of increasing influence of the attached flow on the profile underside. At -18°, all lines intersect in the neutral point.

f) The Polar Plot c_a as a Function of $c_{w\infty}$

Because lift and drag are both changed favorably when the boundary layer becomes turbulent, the differences between subcritical and supercritical state appear more pronounced in the polar plot. The minimum of the profile drag coefficient, which is about 0.017 at Re = 430,000 and remains constant in a 10° range of angle of attack from $c_a = 0$ to 0.9, is about double at Re = 105,000 and about five times as large at Re = 21,000. With decreasing Reynolds number, the range of constant drag becomes smaller, so that on the elongated semiellipses of similar polar plots the upper and lower curvatures, which characterize the beginning of separation of flow, become more pronounced. Because $c_{w\infty}$ is plotted to five times the scale of c_a, the polar plots of the subcritical flow state appear as segments of an ellipse with inverted axis ratio. The minimum profile drag for 21,000 occurs in the negative c_a region valid for inverted flight, where - again opposite to the supercritical trend - at small Reynolds number a more favorable (even though still nominally poor) best drag-lift ratio $c_{w\infty}/c_a$, as the tangent to this polar plot shows in the positive c_a region, occurs.

Of the Goettingen polar curves, with which the Cologne measurements agree well, only the polar plots for 121,000 show a difference in drag in the mid-c_a range. The somewhat higher $c_{a\ max}$ value and the $c_{w\infty}$ and c_a values, higher after separation, indicate a somewhat greater wind tunnel turbulence (or greater surface roughness for the model).

g) c_a as a Function of $c_{m0.25}$

For most profiles, the line of the moment coefficient referred to the t/4 axis shows a gentle S-shape for its basic figure; it starts at negative angles of attack, passes through the value $c_{m0.25} = 0$, increases rapidly, and then becomes almost constant in the entire supercritical range up to separation, which generally gives an increase in moment coefficient. Thus, profile 625 in the mean range of angle of attack has a value differing only slightly from $c_{m0.25} = 0.1$ and a somewhat decreasing value with increasing angle of attack. While separation at Re = 105,000 reduces the moment coefficient, at Re = 168,000 the generally observed increase can be seen. The two separately shown subcritical lines for 21,000 and 84,000 show, increasing from zero to 0.1, the S-shape in rough form.

2. The Flat Plate

In contrast to the case of the thick strongly curved profile, the influence of Reynolds number is least for the thin uncambered plate. The plots of Figures 47 and 48 show lines c_a and c_{wm} as a function of Reynolds number; the lines are almost horizontal over the entire measuring range without a critical sudden increase, and show low Reynolds number sensitivity. At Re = 20,000, no subcritical state could yet be seen in the test, because the flow was already turbulent over the sharp leading edge. The sharp leading edge acts as a "knife edge." For the result summarized in Table 2, the low sensitivity to Reynolds number is indicated by the closeness of the lines. While the measuring range is represented by eight polar curves for the thick profile, here two polar curves suffice, and for comparison the Goettingen measurement is added again. As the lines for c_a versus α_∞ show, the flow separates at $\alpha_\infty = 5.5$ and $6.5°$. On the flat plate, the stagnation point movement has the strongest effect, so that the leading edge at $\alpha_\infty = 5.5°$ ($\alpha_m = 8°$ in Figure 47) has the effect of a "separation edge," and thus in spite of the steep slope of the lift line at Re = 42,000, $c_{a\ max}$ is only 0.5, and at ten times the Reynolds number it is 0.7. Separation results in a pronounced increase in drag, as can be seen from

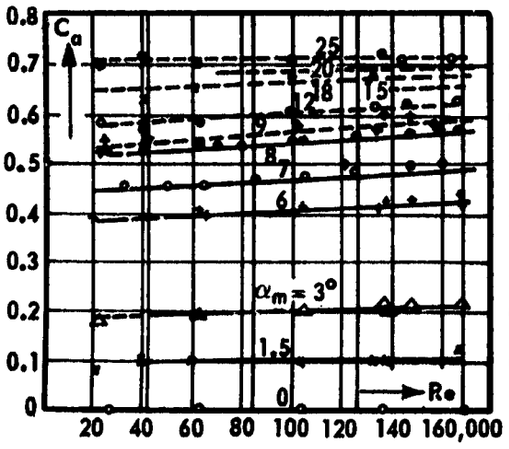

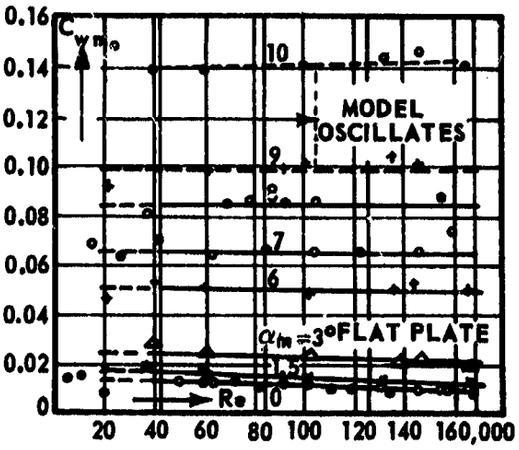

Figures 47 (left) and 48 (right). Test results: c_a and c_{wm} as a function of Re for the flat plate.

the polar curve; here lift increases further up to $\alpha \approx 25°$. In the polar curve, the Goettingen measurement shows a higher drag at low angle of attack, but at higher angle of attack there is a smaller drag increase because of the greater pulling effect at Re = 420,000. The Goettingen plate has a somewhat smaller thickness d/t and semicircular roundings at the leading and trailing edge, while the plate of the present measurements - resembling a thin symmetric profile - has an elliptical nose and a sharply pointed trailing edge from $^3/_4$ t.

The lines of the moment coefficients which show a minimum at Re = 20,000 in the plot against Re in Figure 49 up to $\alpha_m = 12°$, in Table 2 increase perpendicularly in the plot of c_a versus $c_{m0.25}$ at $c_{m0.25} = 0$ to $\alpha_\infty = 4$ to 5°. This indicates: up to $\alpha_\infty = 4°$ the flat plate is fixed in regard to center of pressure, and the point of attack of the resultant aerodynamic force is at t/4. The result is that the flat plate is longitudinally stable in flight, when the center of gravity lies at t/4. Lanchester in about 1890 experimentally demonstrated the inherent stability of the flat plate with his "flying board." The process of stabilization about the transverse axis is further promoted by the following. The rapid increase of $c_{m0.25}$ to higher plus values above 5° indicates an increase in the nose-down moment. The increase in moment begins about 1 to 2° before achievement of the separation angle of attack, as the graph shows. If the flying model, is, for example, threatened with stalling in a gust, then 2° before the separation, the restoring moment takes effect. By trimming of the center of gravity in the range of 0.25 to 0.30 t, the angle of attack at which the flat plate should fly can be varied to achieve the best drag-lift ratio or, what is more important to achieve the minimum sinking velocity for the model airplane, the best ceiling factor reciprocal.

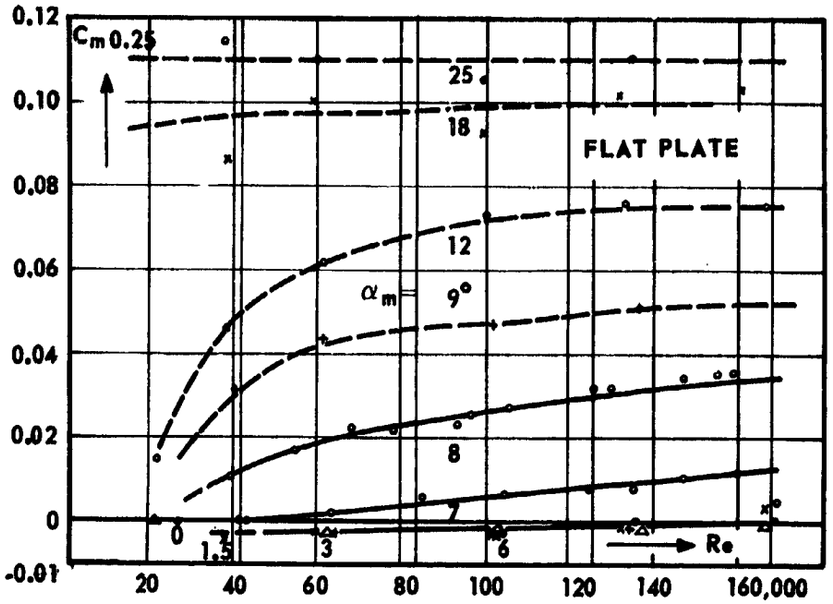

Figure 49. Test result: $c_{m0.25}$ as a function of Re for the flat plate.

For the understanding of longitudinal stability, that is, the stability about the transverse axis, the following is important. Departing from the normal flight position with decreasing α (= nose down), velocity v becomes greater, and at increasing α (= nose-up) it becomes smaller. Thus a definite speed belongs to an angle of attack desired for the neutral flight position (the resultant aerodynamic force passes through the center of gravity). How should the stabilization about the transverse axis of the airplane model be affected: Exactly as for any airplane (Figure 50):

1. The plane shoudl fly neutrally in the principal flying position at normal speed, and thus without turning moment.

2. At increasing speed or decreasing angle of attack, the airplane should be tail-heavy.

3. With decreasing speed or increasing angle of attack, it should be nose-heavy; in brief, it should always automatically return to the neutral flight position.

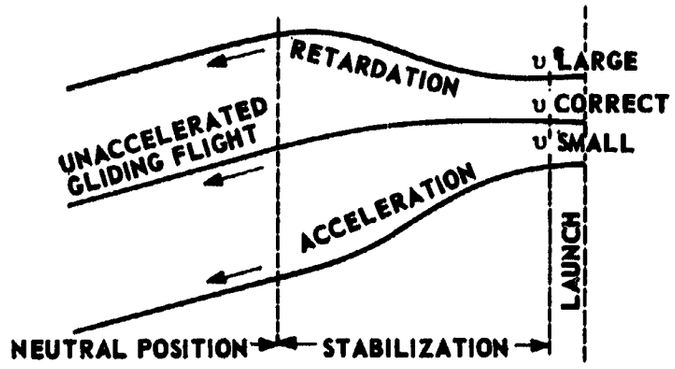

Figure 50. The properly stabilized model airplane is nose-heavy at excessively low speed, and tail-heavy at excessively high speed, so that it always automatically arrives at the proper neutral position at the right speed.

The moment about the center of gravity S (expressed by the moment coefficient c_m) of a flat plate ($\Lambda = 5$) is plotted in Figure 51 for various center of gravity rearward positions x/t as a function of α. Along the line $c_m = 0$ there is neutrality. Above it, there is nose heaviness, and below it, tail heaviness. If the center of gravity is too far forward, that is, ahead of the point of application of the aerodynamic force, say at 0.2 t, then the airplane noses over and accelerates and the angle of attack is reduced until, at zero position, that is, in the vertical diving position, the neutral position is reached. If the center of gravity is at 0.25 t, then neutrality occurs at 5°. If a disturbance causes higher angle of attack, or if the model is launched with a higher angle of attack than 5°, then it becomes nose-heavy as desired. The range useful for the model is shown hatched in the graph; at a low angle of attack or at high speed it should preferably become tail-heavy, and then have a neutral position at that angle of attack where the optimum ceiling factor reciprocal prevails, as shown by the polar plot. Finally, it should become nose-heavy. The center of gravity location between 0.25 and 0.3 t meets this requirement. Practical flight tests gave the best flying characteristics at 0.28 t. Stabilization occurs as an oscillation about the neutral position at 7°. If the center of gravity is at 0.35 t, however, then the change from pronounced tail heaviness to pronounced nose heaviness occurs over a small increase in the angle of attack. The oscillation leads to "festoon flight" (the phugoid flight curve). The restoring moment has been made excessively large, so that it makes the model dynamically unstable. At even

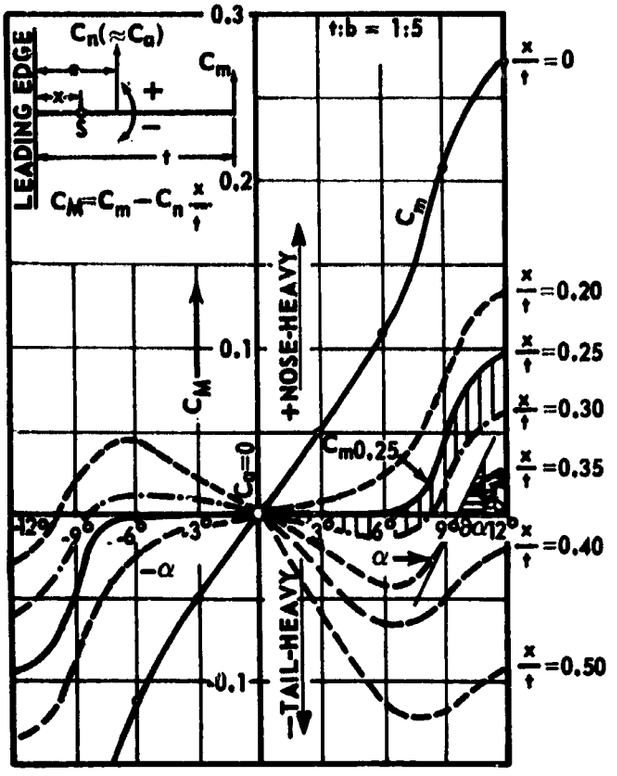

Figure 51. Explanation of the longitudinal stability of the "flying board." Moment coefficient c_m referred to the center of gravity as a function of angle of attack α.

farther rearward positions of the center of gravity - as exemplified by a falling postcard - the phugoid flight becomes zig-zag flight, and the postcard oscillates downward or spins about the transverse axis.*)

The following may be said in summary about flow over the flat plate:

The phenomena are controlled by the transition vortex occurring over the sharp leading edge and producing a high suction peak at that point. The following phenomena are explained by the rapid increase of the suction peak above the leading edge:

---

*) For a detailed treatment of these phenomena see: Schmitz, F. W., "Stability Experiments on Model Airplanes" (Luftfahrt und Schule, vol. II. No. 3).

1. The high increase in lift per degree of angle of attack, $dc_a/d\alpha$.

2. The advance of the pressure point to t/4 (on the cambered profile at low angles of attack it moves toward the leading edge to about t/2 and at large angles of attack to t/3).

3. The transition vortex is effective even at the smallest angle of attack, such as from α = 0 to 1°, as can be concluded from the lift increase and from the center of pressure advancement to t/4.

4. The bridge building extending to the trailing edge as the transition vortex broadens gives, prior to separation at a further increase in lift, a periodic sinking of the suction peaks and arching of the pressure distribution (which, dampened by the scales, is probably indicated as an average value) as an explanation of the early origin of the center of pressure movement to the trailing edge and the simultaneous large increase in drag.

When bridge-building is illustrated by a profile in liquid, it shows clearly how, by increasing the camber of the plate by filling out the transition vortex space into a sickle profile or, better, by cambering the plate especially at the leading edge, the separation following the bridge-building can be displaced.

3. Cambered Plate 417a

Otto Lilienthal showed the superiority of the cambered plate compared with the flat plate by model tests, as indicated in his book Der Vogelflug als Grundlage der Fliegekunst (Bird Flight as a Basis of Aviation) (see [14], p. 74). Nevertheless, the result of the present measurement in the range of small Reynolds numbers is surprising and interesting.

First of all, the lines in Figures 52 through 55, by their straight course without a sudden critical increase, again show the character of low Reynolds-number sensitivity of the model, expressed in Table 3 by the small difference between the lines for Re = 42,000 and the lines of ten times that Reynolds number of the Goettingen measurement. Accordingly, two polar curves at Re = 42,000 and 168,000 suffice to represent the test series here. At Re = 42,000 and α = 8°, the cambered plate at a steep angle of attack reaches a high $c_{a\,max}$ = 1.06 and thereby is superior to the flat plate by a factor of two, and superior to the thick profile 625 by a factor of 2.6 at the same angle of attack calculated from c_a = 0, because subcritical flow still prevails on the

latter. This difference is compared in Figure 1 (converted to $\Lambda = 5$). The slope of the lift line for the cambered plate surpasses the lift increase for the flat plate, up to now designated the optimum. An equally favorable picture results at Re = 42,000 from the behavior of the profile drag in the polar plot. The minimum is $c_w = 0.027$ at $c_a = 0.7$, which corresponds to an optimum "profile drag-lift ratio of $c_{w\infty}/c_a = 1/26$. The position of this optimum drag-lift ratio at as high as possible c_a gives good soaring ability; high drag at $c_a \to 0$ means a low diving speed. These two properties give an extraordinarily favorable situation for the model airplane. On the other hand, the pronounced mean-line camber $f/t = 0.06$ results in an undesirable center of pressure movement, as shown by the moment curve of c_a versus $c_{m0.25}$. For longitudinal stabilization, large rear control surfaces are required, while the flat plate flies with inherent stability (with the proper center of gravity location).

For construction reasons, however, a certain profile thickness is required for a wing section on medium-size models. The measurement given in Table 3 for Re = 420,000 gives an idea of how a thickening of the thin, cambered plate 417 a works compared with the bird-wind profile 417 at the same mean line and a thickness $d = 0.063\ t$. The polar curve shows, as do most bird-wing profiles, a sudden increase in c_w, because the resistance here decreases above $c_a = 0.5$. The slope of the lift line is less up to this turning point than for 417 a, but above it the two are equal. The influence of the thickness ratio on the moment curve can also clearly be seen: the moment coefficient $c_{m0.25}$ is smaller throughout and is nearly constant over a wide c_a range.

The superiority of the thin, cambered airfoil in the Reynolds number range under 100,000 has three causes:

1. Favorable interaction of tangential approach flow to the leading edge at large angles of attack and nose turbulence,

2. The large camber of the lower surface,

3. The relatively small curvature of the rearward upper surface.

In supplementation to the basic laws described in Section II, several essential viewpoints for profile study result from the explanation of the causes.

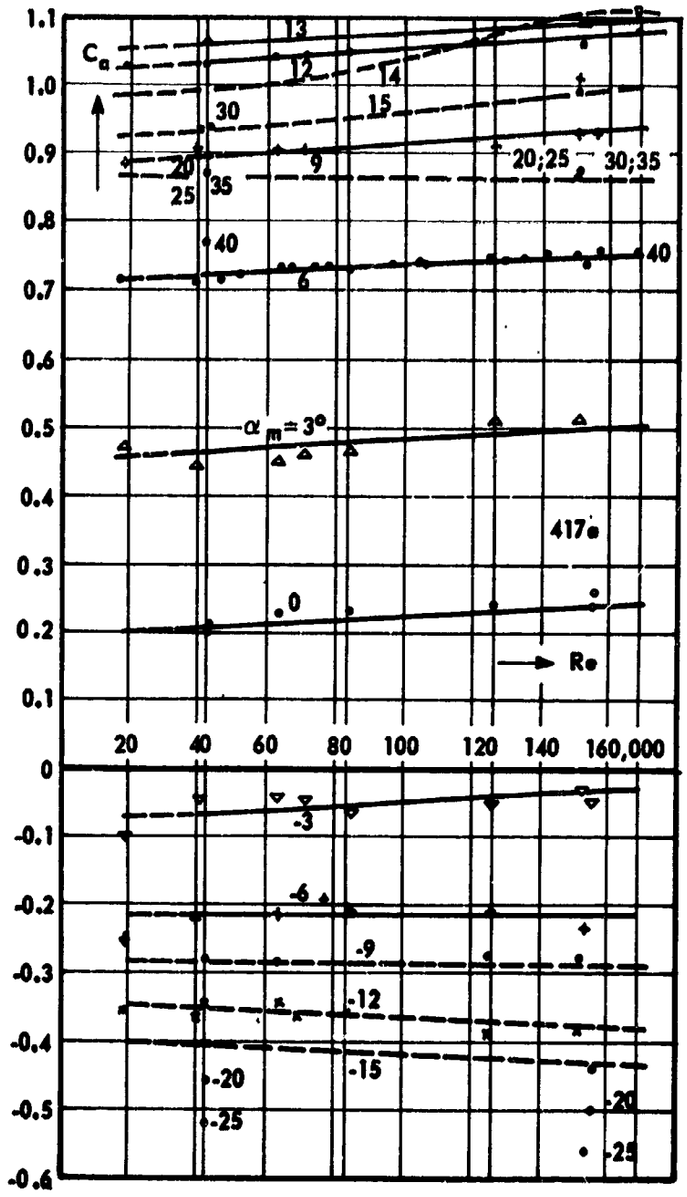

Figure 52. Test result: c_a as a function of Re for the cambered plate 417 a.

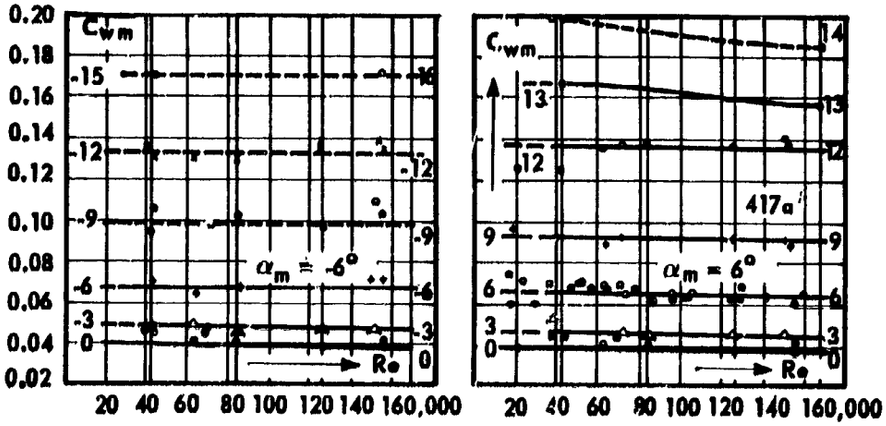

Figure 53 (left) and 54 (right). Test results: c_{wm} as a function of Re for the cambered plate 417 a.

Concerning 1. If a tangent is drawn with the theoretical chord at the leading edge intersection of the profile mean line, the front tangent angle $\psi = 22°$ is found for cambered plate 417 a (see Table 3 and List 4). This means that at 22° angle of attack the leading edge is parallel to the main flow. Tangential approach flow on the leading edge occurs even at low angle of attack, however, because of the convergence of flow before the leading edge (Figure 56a), since even at $\alpha_\infty = 0°$ a large lift is present ($c_a \approx 0.4$ at Re = 42,000; Table 3), which along with the wing also draws the flow up high ahead of the leading edge. With plate 417 a, the flow separates at $\alpha_\infty = 8°$, and the flat plate at 5.5°. If this 5.5° range of the flat plate (from tangential approach flow to separation) is used as a comparison, then the leading edge of the cambered plate would experience tangential approach flow at about $\alpha_\infty = 8 - 5.5° = 2.5°$. At this angle of attack, the lift coefficient has a relatively high value $c_a = 0.7$, and the drag coefficient $c_{W\infty}$ reaches its minimum of 0.027. This gives a profile drag-lift ratio c_w/c_a of 1:26 at Re = 42,000; converted to the aspect ratio Λ = b:t = 10 it becomes $c_w/c_a = 0.042/0.7 = 1:16.5$. Corresponding to Figure 1, at $\Lambda = 5$, it is $c_w/c_a = 1:12$. This drag-lift ratio, unusually favorable for a model wing, is little changed even at Re = 20,000, and it surpasses any other profile. This is the explanation for the astonishing flying performances of the indoor airplane models with a curved thin film skin stretched over them.

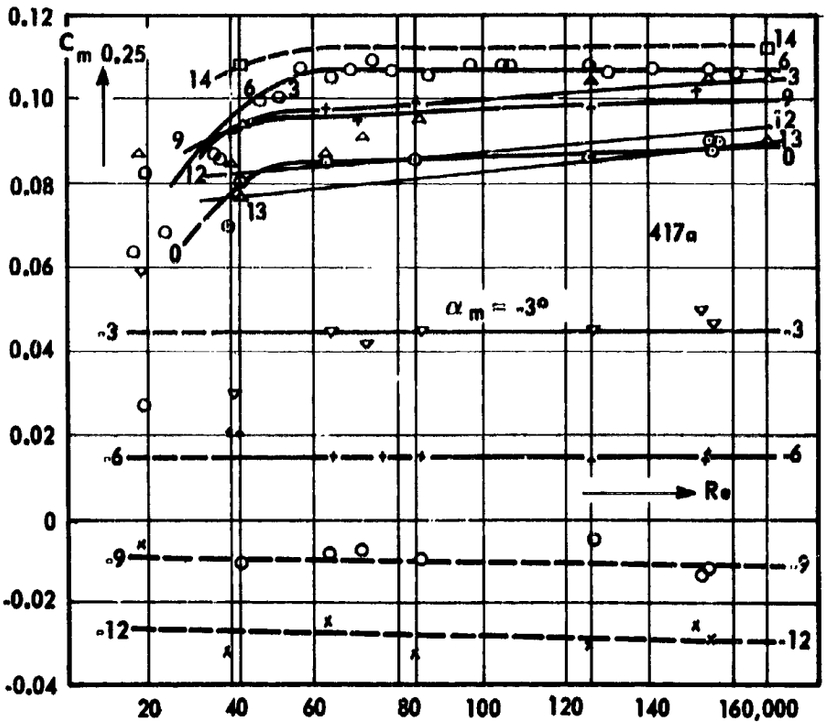

Figure 55. Test result: $c_{m0.25}$ as a function of Re for the cambered plate 417 a.

The stagnation point movement here, too, along with the nose turbulence, controls the phenomena, which can be seen more clearly on the lines of profile 417 in Table 3 than on the lines of the cambered plate 417 a. Beginning at high negative angle of attack, the flow separates on the lower surface. If the negative angle of attack is smaller, then at -8.2° (or -5°, for 417 a) the lower-surface flow attaches in part behind a transition vortex extending to the leading edge. At -8.2°, the center of pressure is at t/4, because then $c_{m0.25} = 0$ (suction peak on the lower surface, pressure peak on the upper surface). The transition vortex on the lower surface now collapses, so that the resistance becomes smaller and the pressure distribution more complete, and thus the moment becomes larger until at -2.7° the $c_{m0.25}$ line has reached approximately the constant value of 0.11, because the flow now adheres along the entire lower

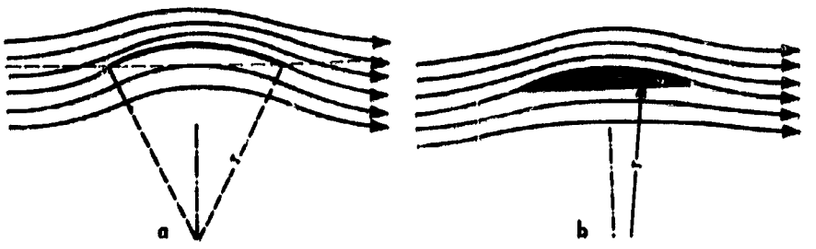

Figure 56. Circularly cambered [arc] plate (a) and sickle profile (b).

surface. Between -1.7° and -0.8°, the transition vortex remainder disappears under the leading edge, so that now the stagnation point can move around the leading edge at this point. Now the upper-surface flow can first become turbulent, and at $\alpha_\infty = 0.24$ it attaches at the trailing edge, as the turning point of the line c_a versus α_∞ at 0.24° shows. From 1° to 5°, the profile drag is nearly constant. At about 5°, the transition point has reached the leading edge. Then the broadening of the transition vortex begins which leads at 9° to separation.

The three characteristic intermediate points of profile 417 are not recognizable on the cambered plate 417 a. The difference is probably caused by the profile thickness d = 0.063 t and by the sharp leading edge of the profile, with r = 0.007 t against d = 0.029 t and r = 0.0145 t for the plate. The three measurements of the plate all in all agree well with one another.

Concerning 2 and 3. An important conclusion for profile design of the model airplane is given by study of the profile lower surface. If a circularly cambered (arc) plate with radius r (Figure 56a) has flow approach at $\alpha = 0°$, then in contrast to the flat plate a large lift is produced. The explanation of the lift as a force directed transversely to the principal direction of flow can be visualized from a mechanical pressure standpoint as a centrifugal effect. In a homogeneous parallel flow no force directed transverse to the flow is effective, because every curvature of a flow produces a force component directed radially outward. The particle of specific mass ρ moving on the curve path experiences a centrifugal effect $Z = (\rho \cdot v^2/r)$, which manifests itself on the circularly cambered plate as a positive pressure on the lower surface and as a negative pressure on the upper surface, and in both cases is greater the more pronounced is the curvature or the smaller the r/t value, and thus from a theoretical

potential standpoint at $r/t \to 1/2$. If the concavity of the lower-surface is filled, then the sickle profile used for ship's propellers (Figure 56b) occurs, where the straight lower surface obviously reduces the centrifugal effect because now the flatter profile mean line serves as mean line of curvature of the flow. Although at increasing angle of attack of the circularly cambered plate the flow on the lower surface now improves, separation begins earlier on the downstream half of the upper surface the more intensively it is cambered and the smaller the Reynolds number. The effort to camber the lower surface more and the upper surface less then leads to the thin, cambered plate as a favorable form to give high lift with low drag at small Reynolds numbers.

Forward camber, that is, the displacement of the highest camber, which is, for example, at $x = 0.5$ t on the circularly cambered plate, to $x = 0.38$ t for plate 417 a, by enlarging the leading side tangent angle and reducing the trailing side curvature gives higher $c_{a\,max}$ values and displacement of the region of the best drag-lift ratio to high c_a values, $c_a = 0.8$ to 1 here.

4. Wing Profile N 60 and N 60R

For these profiles there are comparison measurements made in America in the NACA variable-density wind tunnel at Re $\approx 3 \cdot 10^6$ (NACA Technical Notes, No. 388). Profile N 60 has at 0.4 t a mean-line camber $f = 0.04$ t and a thickness $d = 0.124$ t. Profile N 60R is derived from N 60; from 0.3 t on, the mean line is given an S curvature according to the equation

$$y = 0.3\,x(1 - x) \cdot \left(\frac{7}{8} - x\right)$$

and the raised trailing edge part of the profile, acting as a tail plane, makes the profile proof against center-of-pressure change.*) In addition to making clear the action of the S curvature, the measurements will show the influence of Reynolds number and especially to what extent resistance to center-of-pressure change still applies at low Reynolds numbers, making profile N 60R suitable for flying-wing models.

---

*) These profiles were chosen because A. Lippisch, in Profile Collection No. 4 and 5 of the periodical Flugsport (Sport Flying) (Frankfurt a. M.), using these airfoil sections as an example, has given a readily understandable calculation of the lift and moment coefficients c_{ao} and c_{mo} on the basis of the Birnbaum-Glauert equation; this is widely available because of the broad circulation of Flugsport.

a) Profile N 60

The critical Reynolds number is at Re = 63,000, from Figure 57. Up to $\alpha_m = 16.5°$, the envelope curve of the separation points is identical with the $c_{a\,max}$ line, whose steep slope ends at 16.5° or $c_a = 1.3$. This range from $Re_k = 63,000$ up to the end of the steep $c_{a\,max}$ rise at Re = 110,000 is similar to the "transition" in flow on the friction plate (Figure 6) from the laminar state at Re_k to the fully turbulent boundary layer flow. From Re = 110,000 there follows then $c_{a\,max}$ of the 17° line, while separation occurs at larger α, but smaller c_a. The origin of a test series for profile N 60 for $\alpha_m = 10°$ has already been given in Figure 39 as an example. In the plot of c_{wm} versus Re (Figure 58), the c_w lines for supercritically detached flow, which result as the horizontal prolongation of the subcritical lines, are omitted between 10° and 19°. In the graph of the moment coefficient (Figure 59) is a gathering point for $Re_k = 63,000$ at $c_{m0.25} = 0.093$, at which the two dot-dashed envelope curves of separation points have their origin. In contrast to profile G 625, separation here produces the desired increase in $c_{m0.25}$, that is, increase in nose-over moment.

Eight polar curves of the measurement from Re = 21,000 to 168,000, and for comparison the NACA measurement $Re_{eff} \approx 8$ million are plotted in Table 4. The difference between the polar curves for 21,000 and 168,000 is considerably smaller than in the polar curves of the same Reynolds numbers for the thick profile 625 in Table 1. The drag coefficients are about $\frac{1}{3}$ to $\frac{1}{2}$ smaller, but the "c_a range of approximately constant profile drag" is considerably higher. The slope of the lift line is steeper, and even in the lower part of the line for Re = 21,000 it is almost parallel to the 8 million line. The $c_{a\,max}$ values are higher than for the 625, and the influence of Reynolds number on the change of the zero-lift angle is only half as great. The lines for "unattached flow" intersect at a point at $\alpha_\infty = 16.5°$ or in the polar curves at $c_{w\infty} = 0.275$. These intersection points of the influence of Reynolds number are to be observed at large positive and large negative angles of attack in all measurements of Reynolds number influence.

The measurement gave a more uniform curve for moment coefficient than for the 625, so that the transition from the subcritical to the supercritical flow and the supercritical mean value $c_{m0.25} = 0.08$ can clearly be seen.

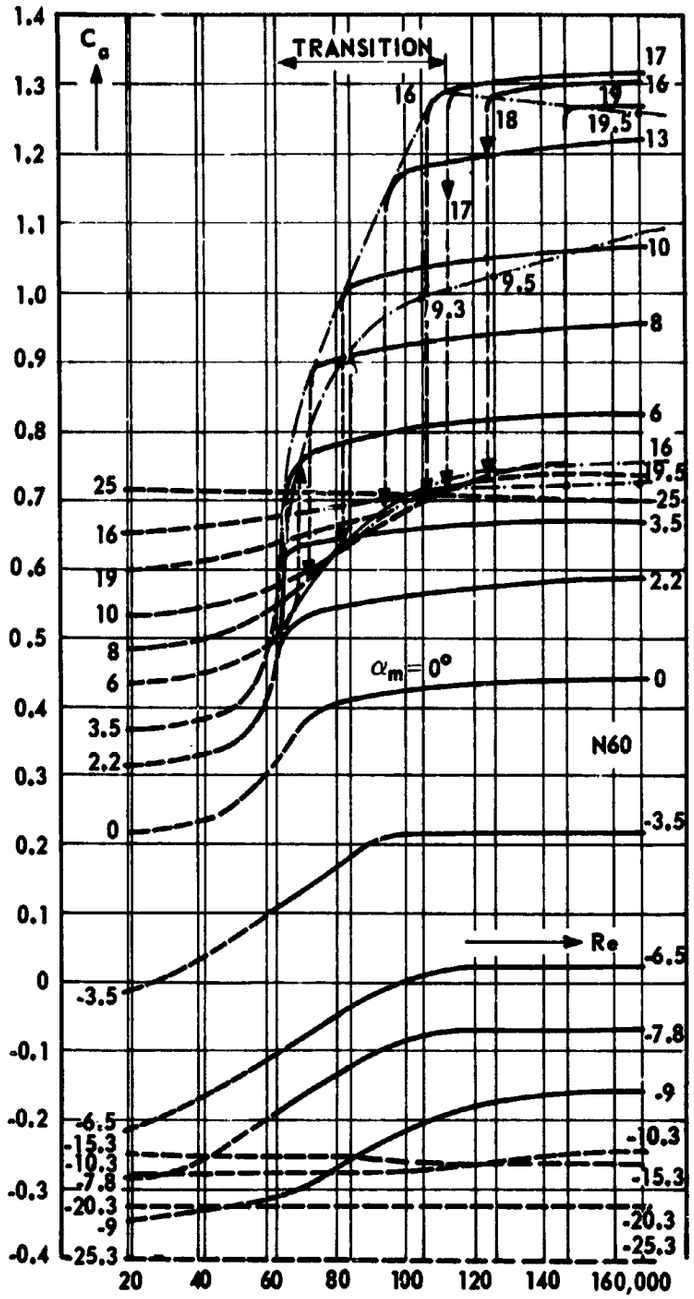

Figure 57. Test result: c_a as a function of Re for profile N 60.

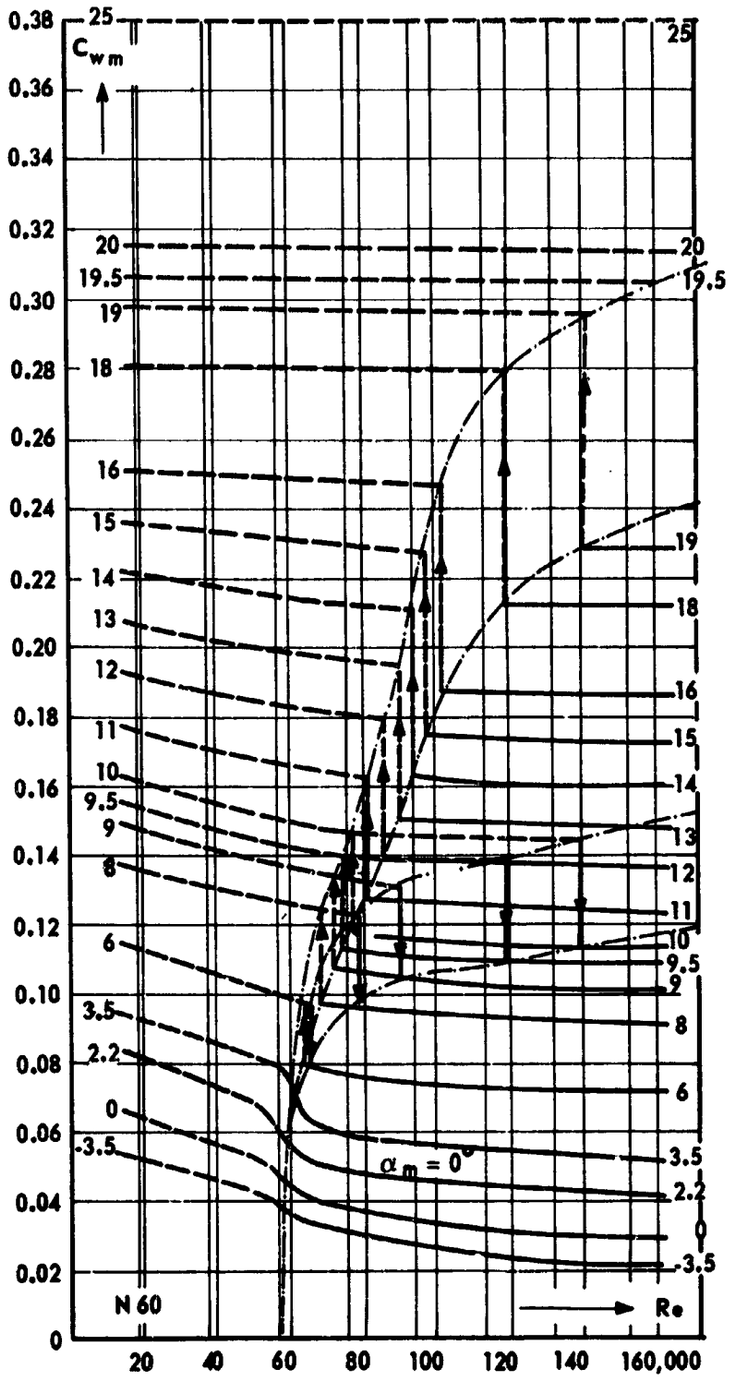

Figure 58. Test result: c_{wm} as a function of Re for profile N 60.

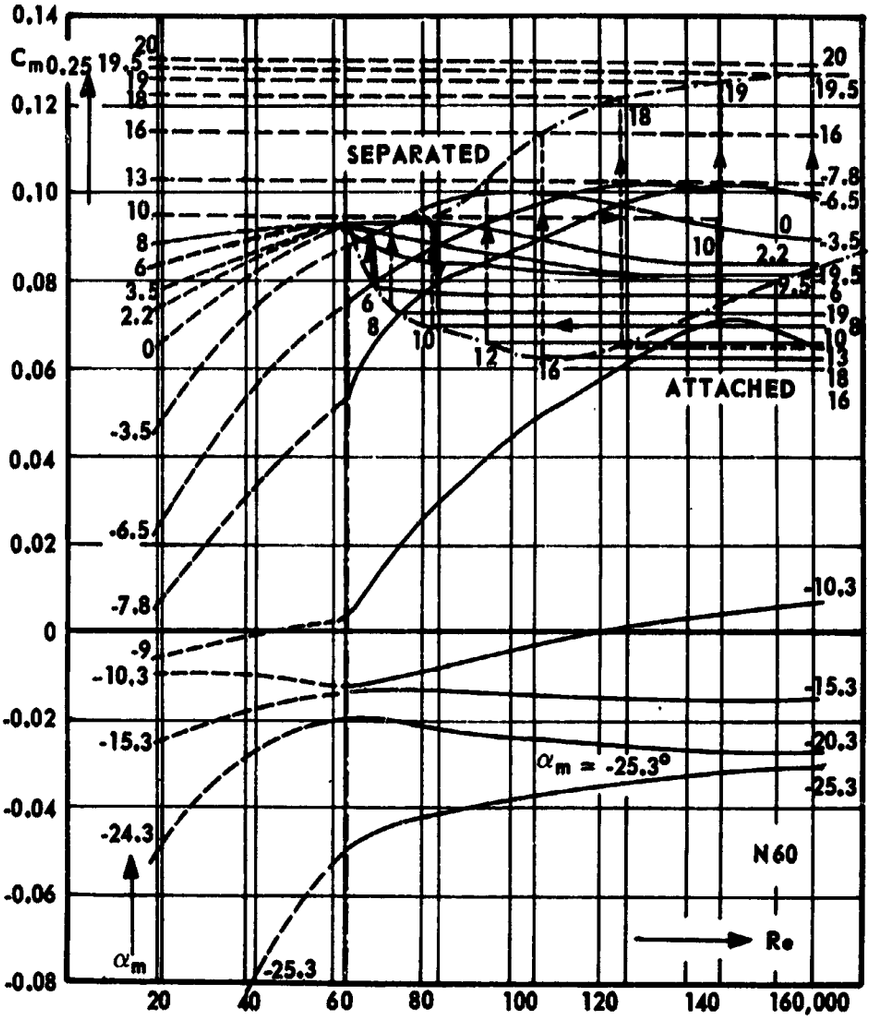

Figure 59. Test result: $c_{m0.25}$ as a function of Re for profile N 60.

b) Profile N 60R

The critical Reynolds number is Re = 73,000 (Figure 60), and thus somewhat higher than for N 60, because the upper surface from 0.3 t on is somewhat more sharply curved. From Re_k on, the slope of the $c_{a\,max}$ line is less steep, and it is still not ended at Re = 168,000. The $c_{a\,max}$ point of N 60R at 168,000 is about 15 percent lower in lift coefficient, in spite of the 50 percent higher Reynolds number, because through the S curvature the camber rise of the mean line is reduced from f = 0.04 t to 0.03 t; the stabilizing property of

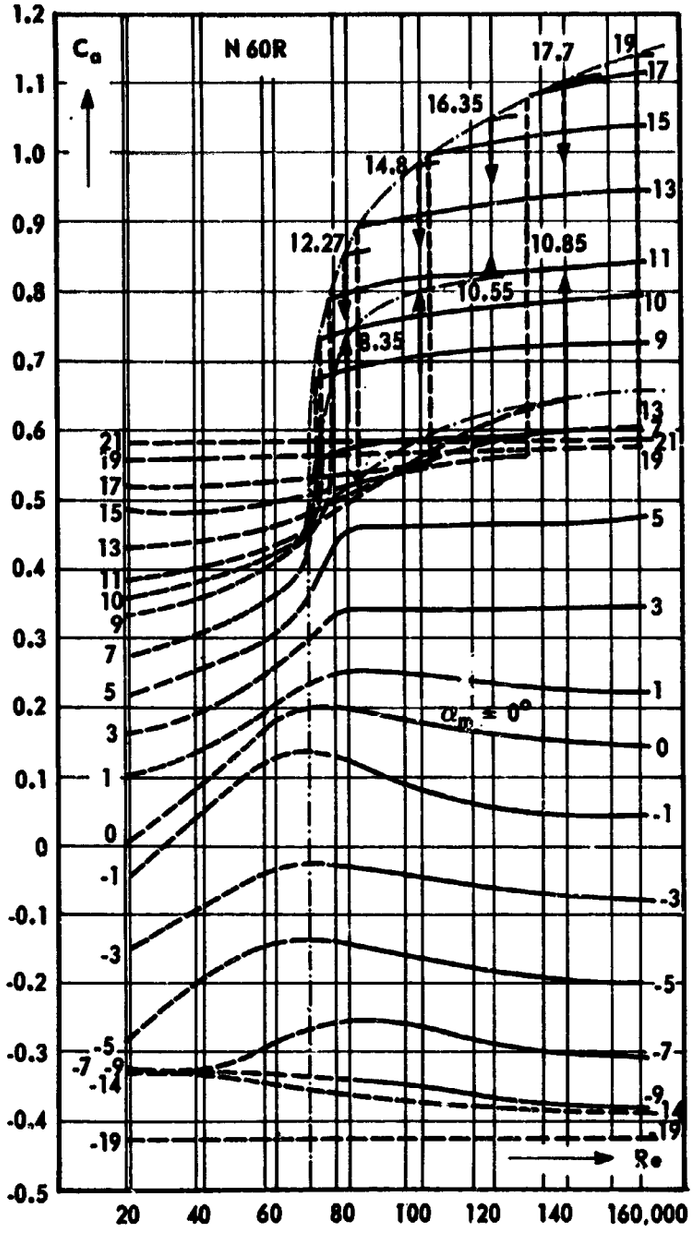

Figure 60. Test result: c_a as a function of Re for profile N 60R.

the profile is thus purchased at the cost of lift. Conversely, the c_{wm} values for a given α_m are smaller (Figure 61); in particular, however, the $c_{m0.25}$ values have become considerably smaller (Figure 62).

In the measurement of $Re_{eff} = 8,000,000$, the point $c_{a\,max} = 1.4$ for N 60R (Table 5) is about 12.5 percent lower than the 1.6 for N 60 (Table 4) while the slope of the lift line $dc_a/d\alpha_\infty$ remains the same. The plot of c_a versus α_∞ shows a remarkable path, with bending and crossing of the lines. The measurement was repeated several times to verify the correctness. Supercritically, the Reynolds number increase of 84,000 does not cause a parallel displacement of the c_a lines, as in the cambered profile, but instead, as for the flat plate, there is an angular rotation about the intersection point at $\alpha_\infty = 1°$, so that the line Re = 168,000 has the same slope up to $c_a = 0.8$ as the line of the NACA measurement. At negative angles of attack the picture changes suddenly, because now the influence of the profile lower surface predominates; seen from the mean line chord out, it appears as the profile half of a symmetrical profile with a sharp point on the trailing edge. As in profile 625, there are the effects which in profile 625 disturbed the course of the lower polar curve half because of the alternating play of separations; here, however, the polar curves in the $-c_a$ region show a smooth curve very similar to the polar curves of the flat plate (Table 2). The span of uniform profile drag extends from $c_a = 0$ to about 0.7. The $c_{w\,min}$ value is of course not at $c_a = 0.4$, as it is for profile N 60, but, for example, at Re = 84,000 it is at $c_a = 0.1$, so that the model has a large and undesirable diving speed.

The lines for the moment coefficient, which for clarity are shown separately in Table 5 for subcritical and supercritical flow, give the most significant results. The line of the NACA measurement follows the ordinate $c_{m0.25} = 0$ up to $c_a = 0.8$. The profile shows little change in center of pressure up to $\alpha_{S\infty} = 7°$ at $Re_{eff} = 8,000,000$. Above $c_a = 0.8$, an increase in $c_{m0.25}$ occurs and quickly increases in the neighborhood of the separation point. The effect of the S-shape here is the same as that for the flat plate: at $Re_{eff} = 8,000,000$ a rectangular airfoil with this profile would, like the flying board, be longitudinally stable at the correct center of gravity location of x = 0.25 to 0.3 t. As can be seen from the graph, however, with decreasing Reynolds number there is an increasing nose-heaviness moment. In addition, it is unfavorable for the process of stabilization that the moment coefficients

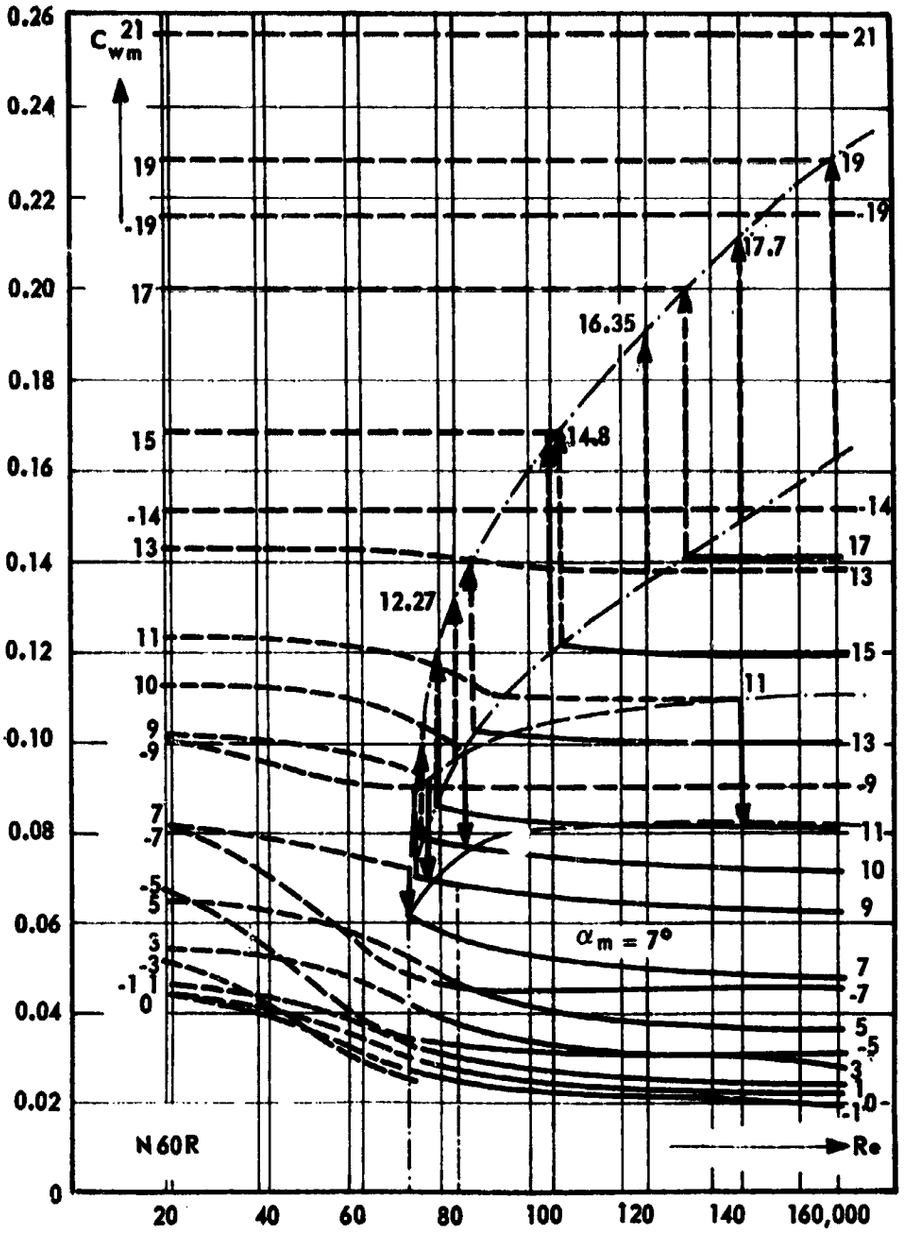

Figure 61. Test result: c_{wm} as a function of Re for profile N 60R.

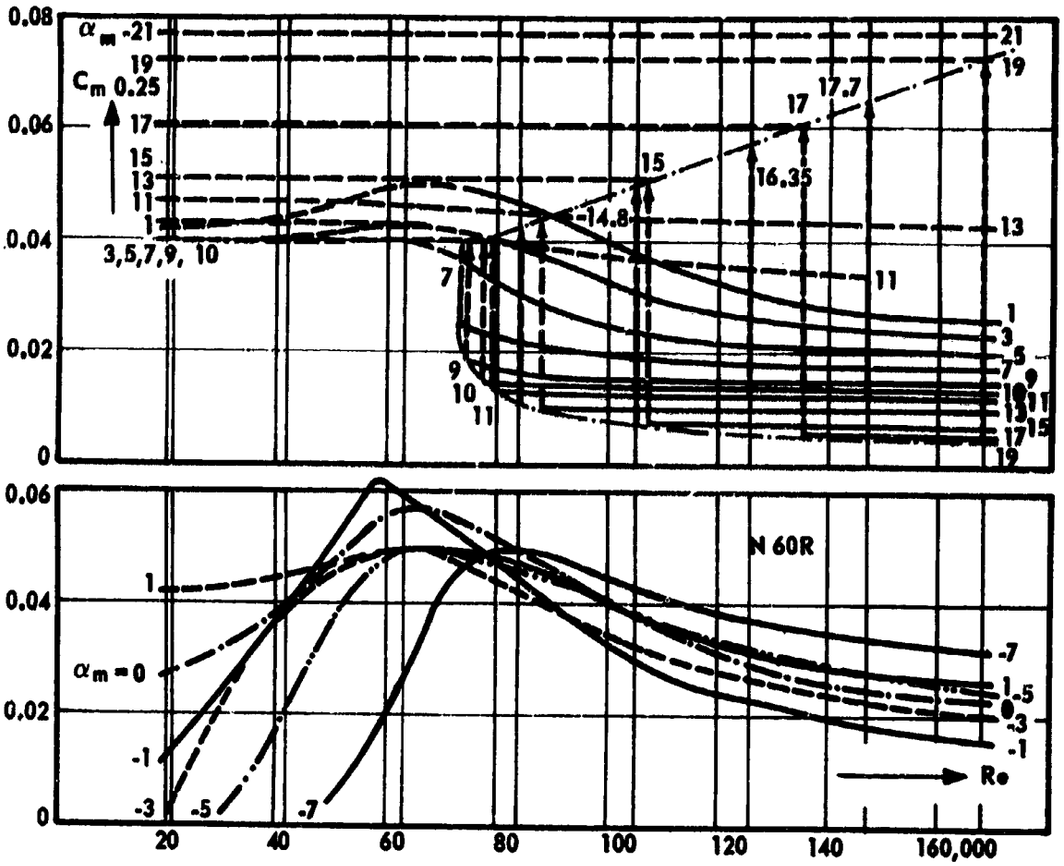

Figure 62. Test result: $c_{m0.25}$ as a function of Re for profile N 60R.

become smaller with increasing angle of attack, becoming larger only after separation. For this profile to be used on a flying-wing model, accordingly, a sharp sweepback and twist would be additionally necessary to achieve longitudinal stability.

V. COMPARISON OF THE TEST RESULTS

1. The Lift Slope $dc_a/d\alpha_\infty$

For the flat plate, the theoretical slope of the lift line is the familiar:

$$dc_a/d\hat{\alpha}_\infty = 2\pi \qquad (\alpha \text{ in degrees of arc})$$

or

$$dc_a/d\alpha^\circ_\infty = 2\pi/57.3 = 0.11 \quad . \qquad (\alpha \text{ in radians})$$

This value is used as a comparison value for lift efficiency η of a profile form through the equation:

$$dc_a/d\alpha_\infty = 2\pi\eta \quad .$$

According to Figure 63, at Re = 420,000 the line of the Goettingen measurement for the flat plate coincides exactly with the slope 2π; it corresponds to the profile efficiency $\eta = 1$. Frequently the lift slope 2π is called the theoretically achievable optimum; actually, however, the cambered plate always exceeds the value 2π, with a surprisingly steep slope of 2.77π at Re = 42,000, and in the c_a region of -0.1 to +0.6 (cf. Table 3), which corresponds to a profile efficiency $\eta = 1.38$.

The three profiles 625, N 60, and N 60R, which are very poor producers of lift subcritically, have the same lift slope of 1.67π at Re = 168,000 in the range of $c_a = 0.3$ to 0.8; at $Re_{eff} = 8,000,000$, the two profiles N 60 and N 60R achieve the maximum value of 1.8π up to $c_a = 0.9$, and thus $\eta = 0.9$. Only thin profiles similar to birds' wings, such as 417, approach the cambered plate. A disadvantage is found along with the advantage here: the steeper the lift slope, the greater is the sensitivity to gusts, because small changes in the direction of approach of air cause large fluctuations in lift. The thin highly cambered profile therefore requires a larger tail plane for balance than does a thick profile possessing the same camber. Lilienthal was the victim of insufficient gust stabilization of his cambered airfoil.

It should further be pointed out that for all profiles and plates in the supercritical range the lift slope can be only slightly improved with increasing Reynolds number, as shown by study of the plots of c_a versus α_∞ in Tables 1 to 5. On the other hand, the increase in the c_a range or α range, in which $dc_a/d\alpha$ is constant, is also greatly dependent on the Reynolds number.

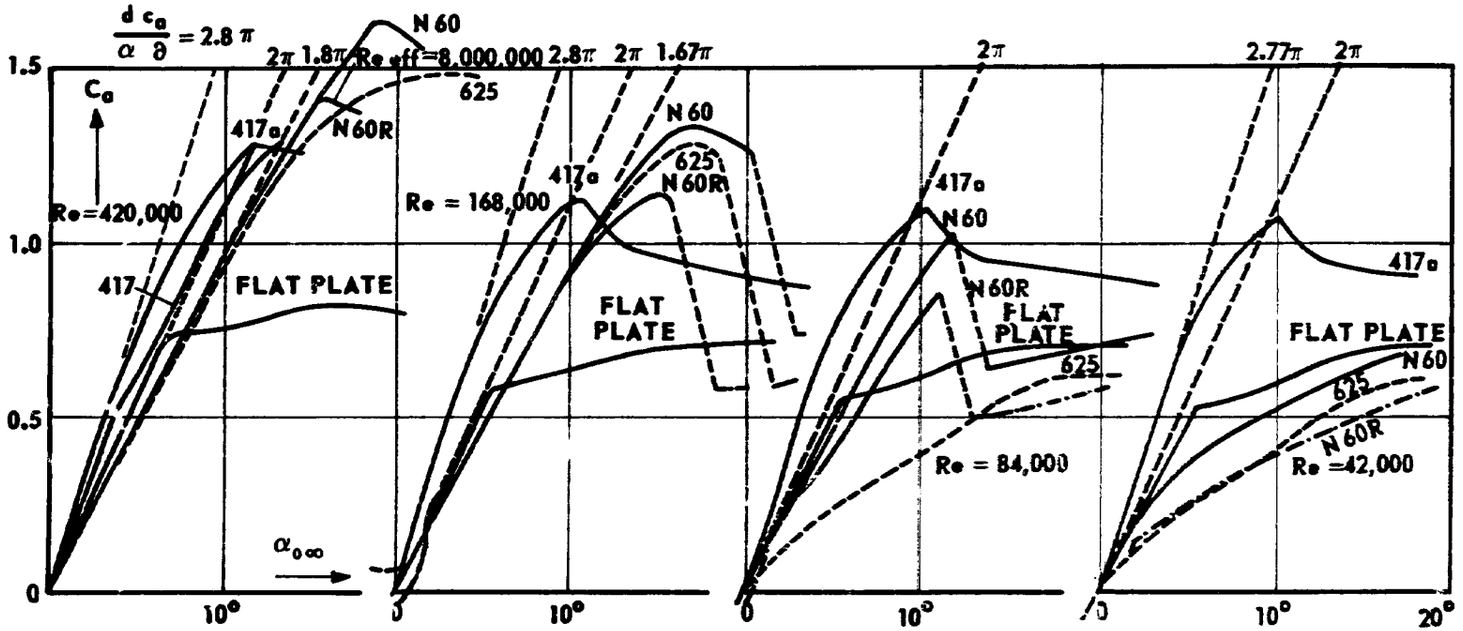

Figure 63. Comparison of lift slope for five different profiles in four different series of Reynolds numbers, in terms of the effective angle of air approach $\alpha_{o\infty}$ ($\alpha_{o\infty} = 0$ at $c_a = 0$).

2. The Zero Lift Angle β

In Tables 1 to 5 every lift line of the plot of c_a versus α_∞ intersects the line $c_a = 0$ at a different angle of attack. These zero lift angles (designated by β in Figure 37) differ from one another to a degree depending on how sensitive to Reynolds number the profile is. In Figure 64 the zero lift angles of the five profiles are plotted as a function of Reynolds number; the angles are not expressed in terms of the profile chord but of the theoretical chord and therefore are designated as β_S. The flat plate has the lowest Reynolds number influence, and the thick profile 625 has the greatest. Subcritically $\beta_S \approx 0°$ for all. At Re_k, a sudden increase occurs and the camber difference grows larger between the upper and lower surface. After an increase of β_S in the transition region, there is generally a decrease in zero-lift angle above the transition.

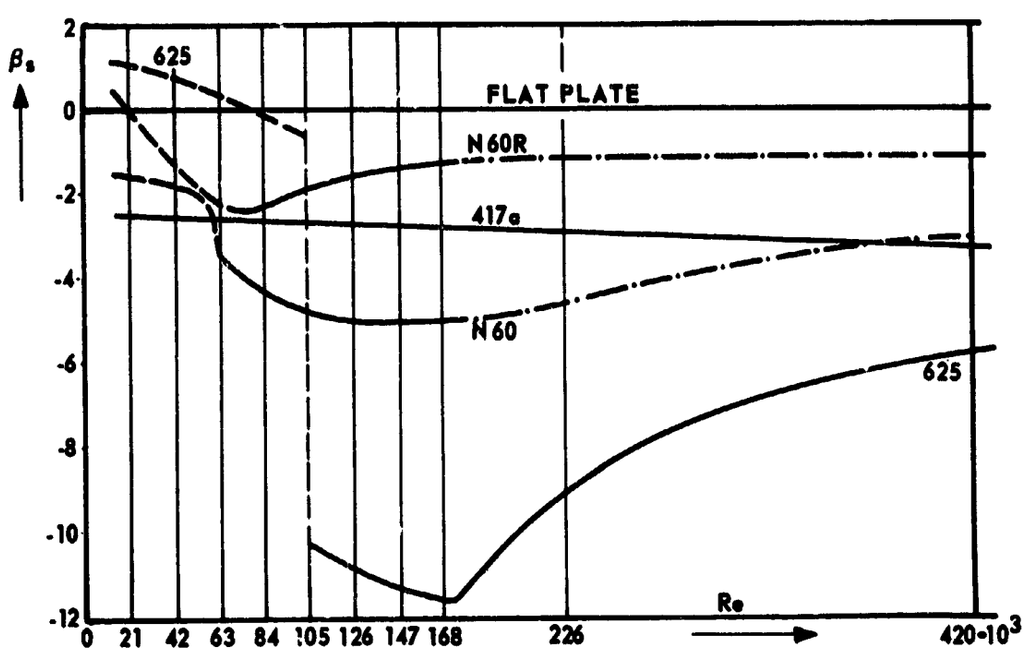

Figure 64. Change in the zero-lift angle of attack β_S of the mean-line chord as a function of Re.

The zero-lift angle plays a role in theoretical lift calculations. The true or aerodynamic angle of attack α_o in terms of the direction of approach of airflow at $c_a = 0$ (in Figure 37) was used in Figure 63 for a comparison of lift slopes.

3. $c_{a\ max}$ Slope As a Function of Re

The $c_{a\ max}$ lines of the measurements are shown in Figure 65. The steep $c_{a\ max}$ slope in the transition from the subcritical to the fully turbulent condition occurs for N 60 from Re_k = 63,000 to Re = 110,000, and for 625 from Re_k = 105,000 to Re = 157,000 as can be seen from the deviation of the dot-dashed separation line from the $c_{a\ max}$ line. According to Figure 60, there is no separation yet at the upper range of measurements for N 60R, so that the transition region extends further here. On the flat plate, no subcritical condition could be found, but its $c_{a\ max}$ value is too small in comparison with the cambered plate, which is superior to all others up to Re = 100,000. At this Reynolds number, the superiority of the profiles begins. At Re = 420,000 and 8,000,000, according to Figure 63, the cambered plate is far inferior to the profiles. The compulsion of the premature supercritical state is at the expense of the $c_{a\ max}$ value at high Reynolds numbers; this is a general rule for other measures of artificial turbulence. The gradual $c_{a\ max}$ increase found here at all Reynolds numbers measured is based on the pulling effect of the outside flow.

4. The Plot of the Minimum Profile Drag $c_{w\infty min}$ As a Function of Reynolds Number

The line of minimum drag for the flat plate in Figure 66 corresponds approximately to the laminar friction coefficient c_f on the friction plate of Figure 6, which reaches the transition at Re_k = 500,000. The $c_{w\infty\ min}$ line of the cambered plate is almost horizontal. The thick airfoil section 625 is again subject to the strongest influence of Reynolds number. The "transition" from the subcritical to the supercritical state occurs here below Re_k, in contrast to the $c_{a\ max}$ slope, where the transition lies above Re_k. With the thick airfoil section 625, the transition ranges from Re = 95,000 to Re_k = 105,000, with c_w becoming $1/3$ smaller and the angle of attack for $c_{w\infty\ min}$ changed from -4 to

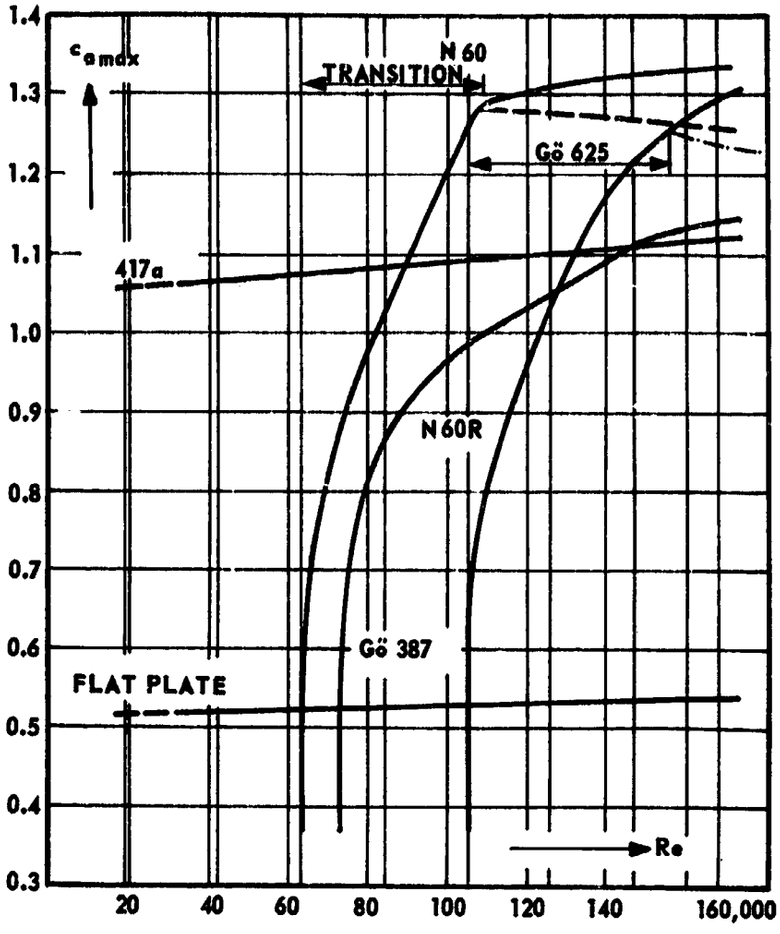

Figure 65. Comparison of the five profiles with respect to change of their supercritical maximum lift value $c_{a\,max}$ in the Reynolds number range of 20,000 to 168,000.

-6°. For the two intermediate airfoil sections, the influence of Reynolds number on their profile form is correspondingly less. The $c_{a\,max}/c_{w\,min}$ ratio determines the "velocity range" of the airplane.

5. Movement of the Center of Pressure e/t

The change of moment consists of the simultaneous change of aerodynamic force and its point of application or the change of the lever arm, as a result of movement of the center of pressure. Although the moment coefficient suffices for calculation of longitudinal stability, still the representation of the movement

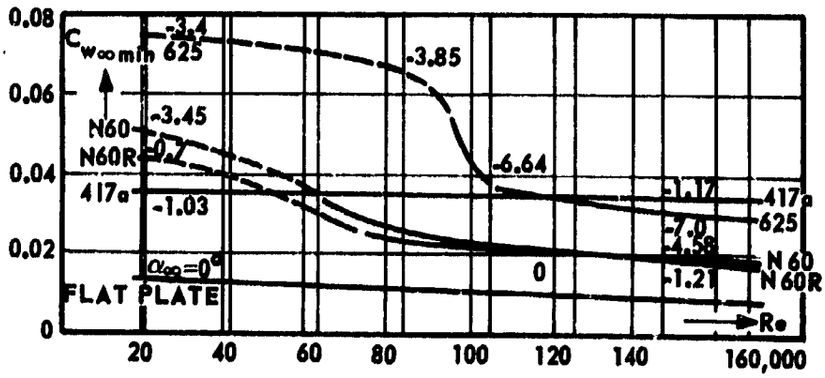

Figure 66. Comparison of the five profiles with respect to change of profile minimum drag $c_{w\infty\ min}$ in the Reynolds number range of 20,000 to 168,000.

of center of pressure or the center-of-pressure distance e/t from the leading edge, gives clearer comparative pictures. According to Figure 67 there can be set up:

$$c_{nS} \cdot (e - 0.25\ t) = c_{m0.25} \cdot t\ .$$

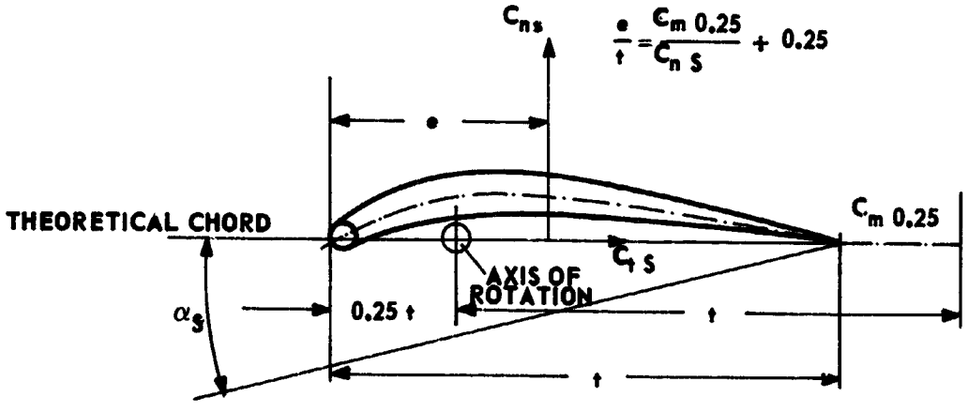

Figure 67. Sketch for determining the center-of-pressure distance e.

Accordingly, the center-of-pressure distance is:

$$\frac{e}{t} = \frac{c_{m0.25}}{c_{nS}} + 0.25 \ .$$

The center-of-pressure movements resulting for five profiles as a function of angle of attack and Reynolds number are shown in Figures 68 through 72, for airfoils of aspect ratio $\Lambda = 5$. Because the reference axis for $c_{m0.25}$ is at t/4 on the theoretical chord, here c_n and α should be referred to this chord, and thus, since $\Lambda = 5$, c_{ns5} and α_{s5} should be used in calculation.

For wing section N 60, the center of pressure at Re = 168,000 and -4° is at e/t = 1, that is, at the trailing edge; at 0° it is at 0.43 t, at 12° at 0.3 t, and then at 19° it suddenly increases to 0.41. Below -4°, the line moves toward plus infinity and at -8° returns from minus infinity and then at -12° reaches 0.25 t. With increasing Reynolds number, the lines generally show an equidistant displacement to the right, and the movement becomes greater; subcritically, the movement is smaller, but the center of pressure is farther back. The NACA measurement shows the greatest movement, with a center of pressure point moving from 0.5 to 0.31 to from 0 to 20°.

On profile N 60R, on the other hand, at Re_{eff} = 8,000,000, the center of pressure is fixed at t/4 from 0 to 10°; then at 22° it moves back favorably to 0.3 t. (Before the flow threatens to separate in a stalled condition, a stalled condition, a restoring moment is effective which moves the wing back into the normal flying position.) As Reynolds number decreases, the range of the fixed center-of-pressure position rapidly becomes smaller; at Re = 84,000, e reaches the t/4 position at only one point, 12°, and then suddenly increases to t/3 as flow separates. In comparison with N 60, the movement for low Reynolds numbers is even greater; there can no longer be center-of-pressure point fixity spoken of here.

For the thick profile 625 (Figure 70), the course of the line for Re = 168,000 is almost the same as with N 60, but the difference, as far as the line for Re = 21,000, is considerably greater, however, and the curve in the region of large negative angle of attack changes suddenly. As expected, the flat plate (Figure 71), which has a fixed center of pressure from -6° to +6°, shows the most uniform behavior. After a further increase in angle of attack of 3°, the center of pressure moves from t/4 to t/3, and after another 7°, to 0.4 t. In the measurement with the plate, it is seen that the line for Re = 42,000 even reaches a center-of-pressure position e/t = 0.23 at α = 3°.

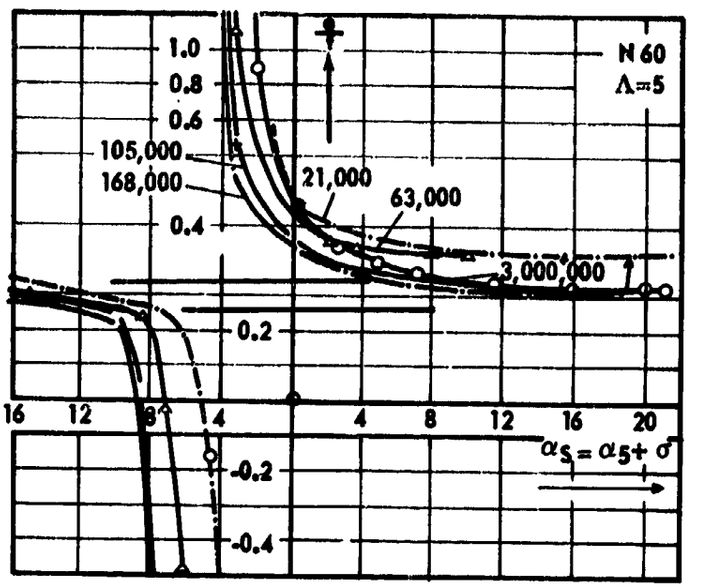

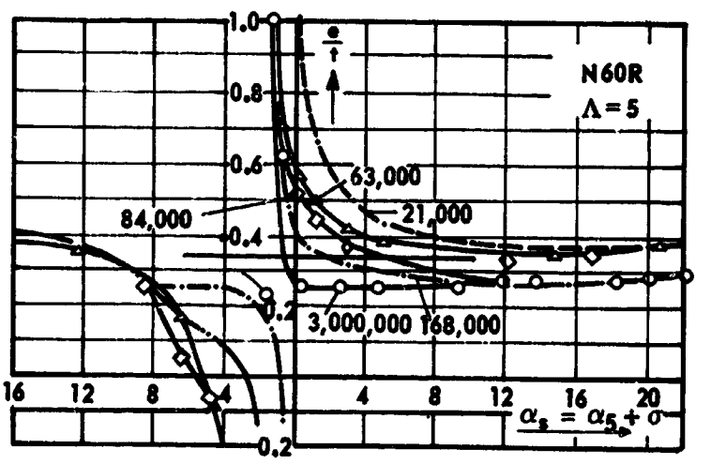

Figures 68 (above) and 69 (below). Center-of-pressure movement e/t on airfoils of Λ = 5 with profiles N 60 and N 60R, as a function of angle of attack at various Reynolds numbers. α_S is the angle of attack of the theoretical chord of the profile mean line. NACA measurement, Re = 3 million or Re_{eff} = 8 million.

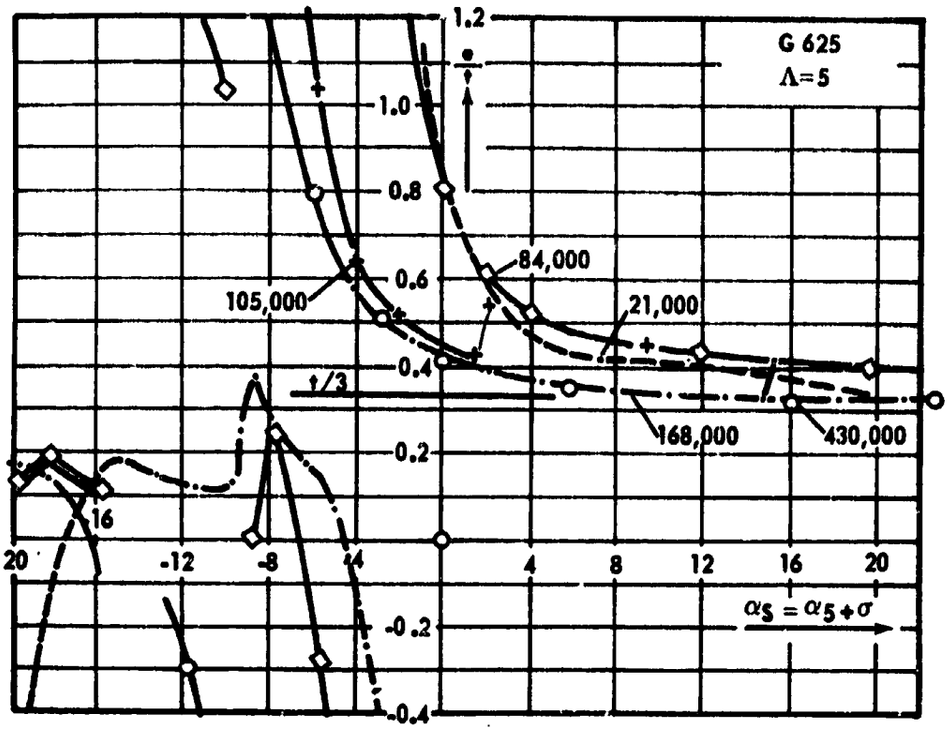

Figure 70. Center-of-pressure movement on the thick Goettingen profile 625.

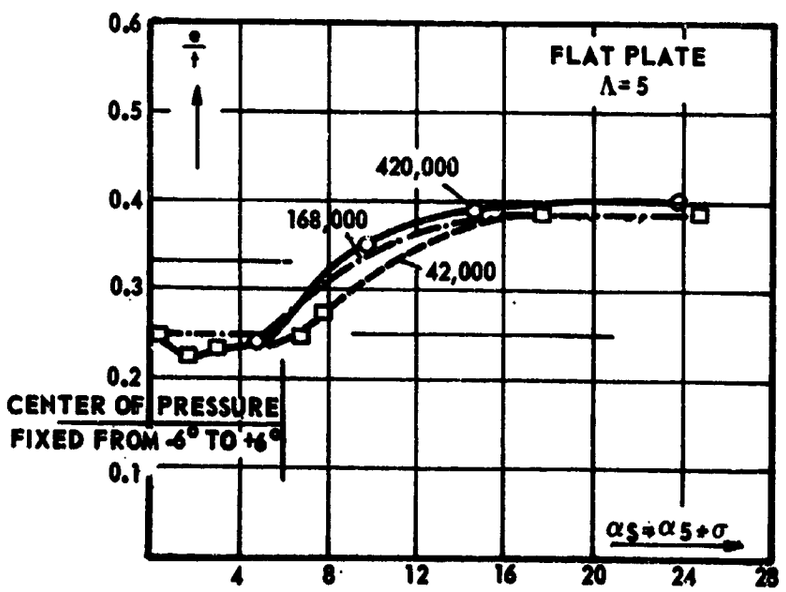

Figure 71. Center-of-pressure movement on the flat plate.

For the cambered plate 417 a (Figure 72), the lines show little deviation among themselves; nevertheless, the movement of the center of pressure is large corresponding to the high camber of f = 0.06 t: the line coincides with the line of profile 625, which has the same camber.

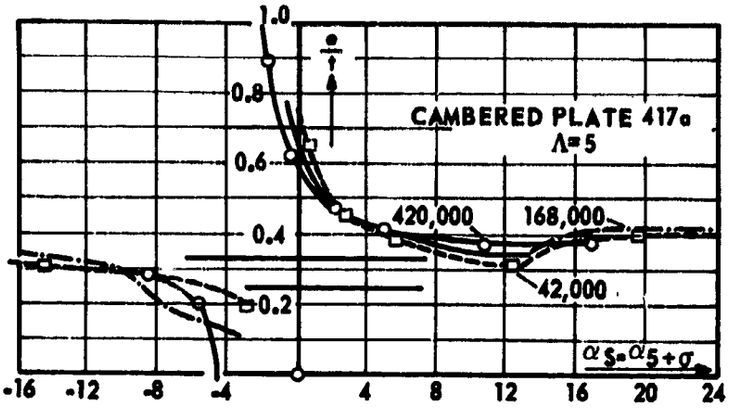

Figure 72. Center-of-pressure movement for the cambered plate 417 a.

6. Profile Drag-Lift Ratio $c_{w\infty}/c_a$ and Profile Ceiling Factor Reciprocal $c_{w\infty}^2/c_a^3$ as a Function of Re

The plot of profile drag-lift ratio $c_{w\infty}/c_a$ and profile ceiling factor reciprocal $c_{w\infty}^2/c_a^3$ as functions of Reynolds number furnishes the most important comparison. These profile evaluation coefficients are shown in Figure 73 for the five Reynolds numbers 42,000, 84,000, 168,000, and 420,000 or up to $8 \cdot 10^6$ shown in Figure 73. To avoid fractions, the reciprocals are plotted, namely, the lift-drag ratio $c_a/c_{w\infty}$ as abscissa and the ceiling factor $c_a^3/c_{w\infty}^2$ as ordinate.

The result: at Re = 42,000, the cambered plate 417 a predominates over all others (camber f = 0.06 t; thickness d = 0.029 t); at 84,000 it is still superior to profile N 60. On the other hand, at Re = 168,000, profile N 60 (f = 0.04 t; d = 0.12 t) has surpassed every other one and from then on maintains the superiority. The thick profile 625 (d = 0.20 t) is comparatively poor. In spite of this high $c_{a\,max}$ value as a result of the large camber f = 0.06 t (cf. Figure 65), it is inferior because of its high profile drag. At Re = 168,000,

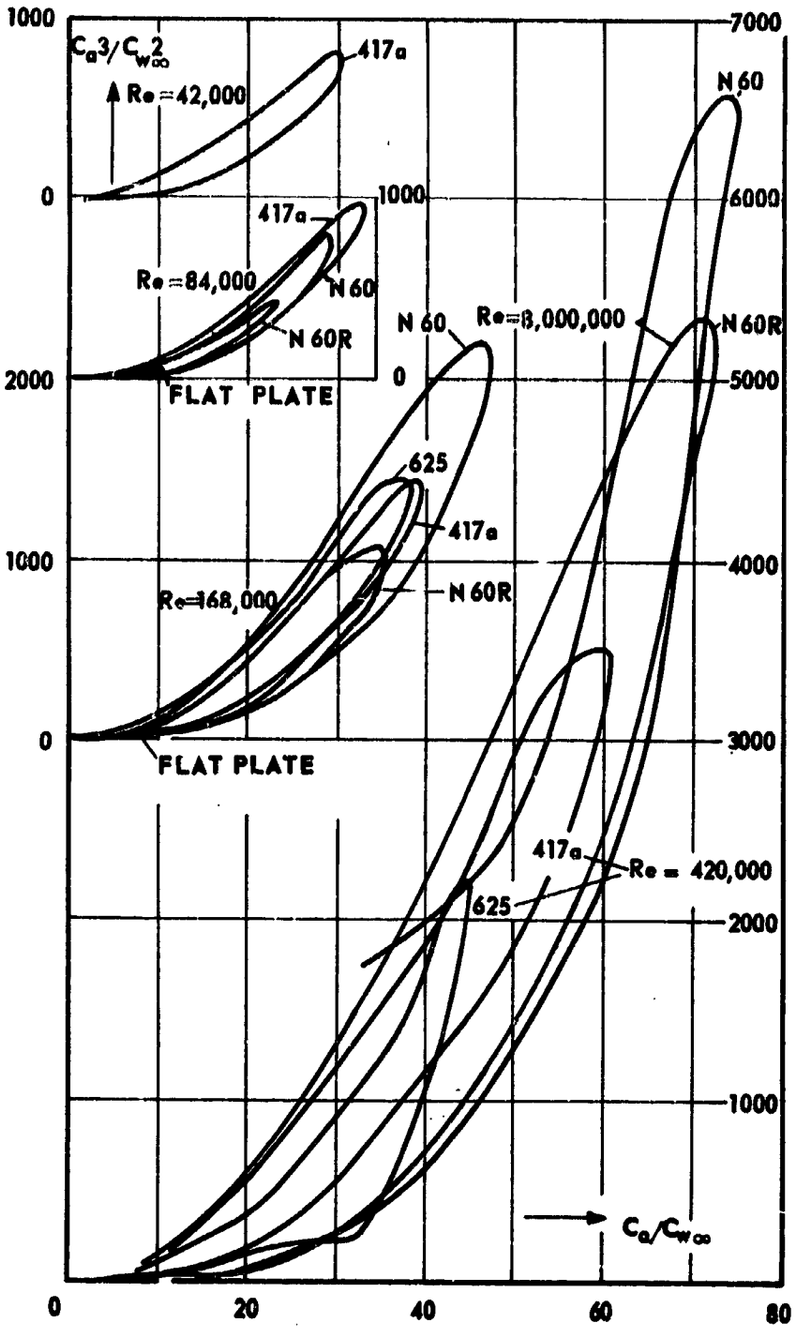

Figure 73. Comparison of the reciprocals of ceiling factors and drag-lift coefficients for the five profiles at four stages of Reynolds number.

profile 625 is equal to the cambered plate 417 a, but at higher Reynolds number, for example, 420,000, it is again inferior. Because of its relatively great thickness and its low camber, the S-shaped profile N 60R is comparatively unfavorable in the Reynolds number range of model flying, although it is favorable at higher Reynolds numbers.*)

7. Comparison of Measurements at Very Low and Very High Velocities

If flow at an air velocity v approaching the speed of sound ($c \approx 430$ m/sec) passes a profile, then the profile properties become much poorer, as is well-known, and this occurs first for thick profiles {see [5], vol. IV, part 1, p. 452; A. Busemann, Gasdynamik (Gas Dynamics)}. It therefore occurs to compare the effect of this deterioration with the present deterioration measured for profiles in the transition to the subcritical condition. Although the causes are basically different, nevertheless some similarities may be pointed out. In Figures 74 and 75, the measurement for profile G 625, converted to the same aspect ratio, is shown compared with NACA measurement for a propeller profile of the same thickness ($d/t \approx 0.2$). Just as a sudden increase to the subcritical flow occurs from Re / 105,000 to 84,000 in Figure 74, in Figure 75 a similar increase to a "hypercritical" state can be seen from $v/c = 0.5$ to 0.6.**) Its polar curve at $v/c = 0.85$ coincides with the polar curve for Re = 21,000 of subcritical flow.†). Although in Figure 74, from Re = 105,000 to about 150,000,

---

*) For the practical case with the airplane or the model airplane, where the total resistance coefficient $c_{wg} = c_{w\infty} + c_{wi} + c_{ws}$, the differences in the ceiling factor and drag-lift coefficient are considerably smaller, and thus the influence of profile differences is not so clearly evident. Here c_{ws} represents the proportion of the sum of harmful drags of fuselage, tail planes, etc., per unit of wing area F, at dynamic pressure q = 1; $c_{ws} = \Sigma\, c_w \cdot f/F$.

**) This flight speed $v = 0.6\, c = 204$ m/sec corresponds approximately to the absolute speed record of 1939 of the Messerschmidt airplane which reached 210 m/sec.

†) More recent measurements have shown that the NACA values found in the closed tunnel do not apply until velocities about 50 percent higher; this quantitatively shifts the comparative picture.

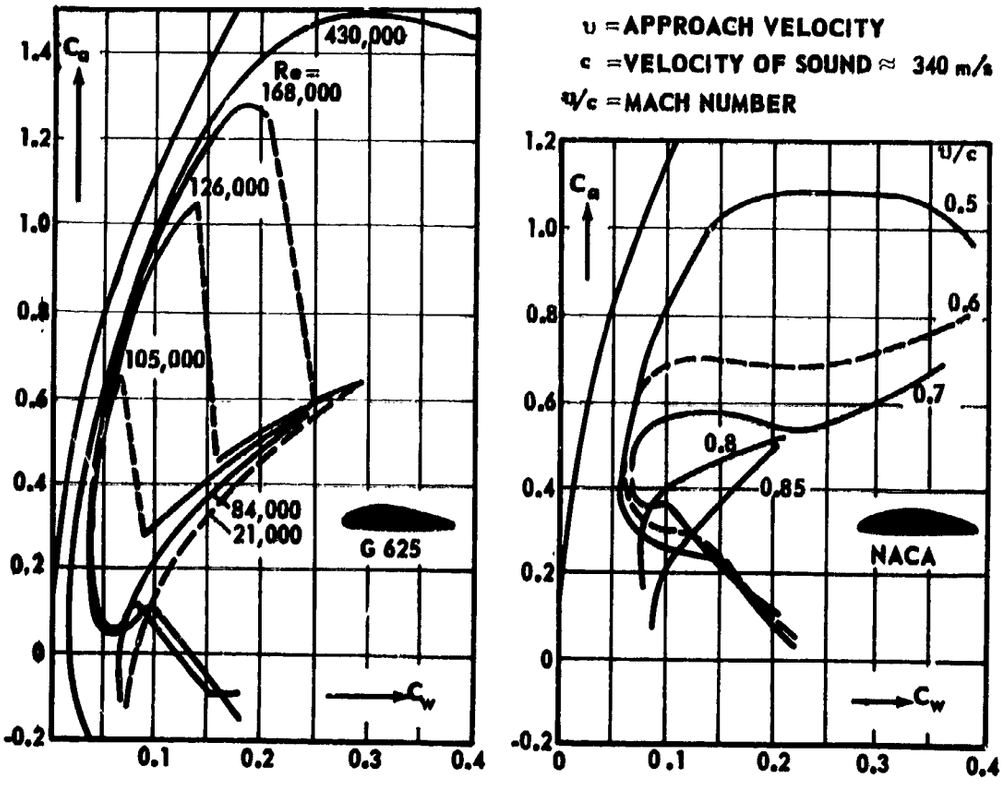

Figures 74 (left) and 75 (right). Comparison of measurements at very low and very high velocity.

separation does not occur for incompletely turbulent boundary layer flow without a transition suddenly over the entire wing, the upper polar curve branch at Re = 430,000 shows the polar curve's characteristic rounded-off behavior for a fully turbulent flow before separation, the same as the polar curves in Figure 75.

The Reynolds number influence upon approach to very high velocity as well as to the lowest velocity is less the thinner the profile. Thus the same requirement holds for both: the higher the velocity above v/c = 0.5, and the smaller the Reynolds number below Re = 100,000, the thinner must be the profile and the sharper must be the leading edge (see [2], p. 215), because thick profiles are unsuitable as a result of the very high profile drag.

VI. PRACTICAL CONCLUSIONS

1. Choice of Profile for the Model Airplane

A good range and a long duration of flight are required for the model airplane; that is, it should glide as far as possible and remain up as long as possible and thus fly with as low a sinking velocity as possible. This assumes a choice of a wing section which gives the maximum attainable values for profile drag-lift ratio and ceiling factor reciprocal for the Reynolds number at which the model airplane flies. All in all, for profile choice, only the representation shown in Figure 73 is valid. These profile evaluation numbers depend upon the profile parameters f/t, d/t, their location x/t, and in addition, on the nose radius r/t. Determination of these profile parameters is the practical goal of this study. The effort to choose profile thickness as large as permitted by aerodynamic evaluation, to achieve maximum spar depth, leads according to Figure 73 to a limiting value of profile thickness for the model airplane of d = 0.12 t, with a camber f = 0.05 t, at Re = 200,000. If, in addition, the parameters of the cambered plate 417 a are chosen as optimum for Re = 50,000, then with these guiding values in Figure 76 there results a system for profile selection or for the incorporation of existing profiles in the suitable range of Reynolds numbers. In this system, some Goettingen profiles have been plotted for choice (see [3] editions I, III, IV; profile dimensions in III, p. 27, IV, p. 63). Camber and thickness for these are generally at x = 0.3 t. More recent profile studies [13] showed as the most favorable location of maximum camber 0.15 t, for achievement of a high $c_{a\ max}$ value. For the profiles chosen here, the maximum camber actually lies farther back, but the camber of the mean line at first increases steeply, for example for profiles 375, 381, 417, and others, with a high tangent angle at the wing leading edge, so that about the same effect is achieved.

In the comparison of these profiles, it becomes clear that they are more like the sections of birds' wings than the wing sections of modern airplanes. The measurements corroborate on one hand the correctness of the model tests of Lilienthal who, starting from thin, curved bird wings, determined that these and the cambered plate are the most favorable profile forms. Since he did not know the influence of Reynolds number, however, he assumed erroneously that this result was the most favorable form for large-scale designs, too. In 1910, Junkers showed for the first time the advantages of the thick profile for the airplane of that time and thereby showed aviation the way to the cantilever monoplane Up until about 1918, however, the biplane and triplane, with thin wings, ruled the field as the most favorable from the construction standpoint, although they were aerodynamically unfavorable. On the other hand, modern model airplane building often makes the error of copying the wing section of the modern airplane as accurately as possible for the model airplane, using wing sections with

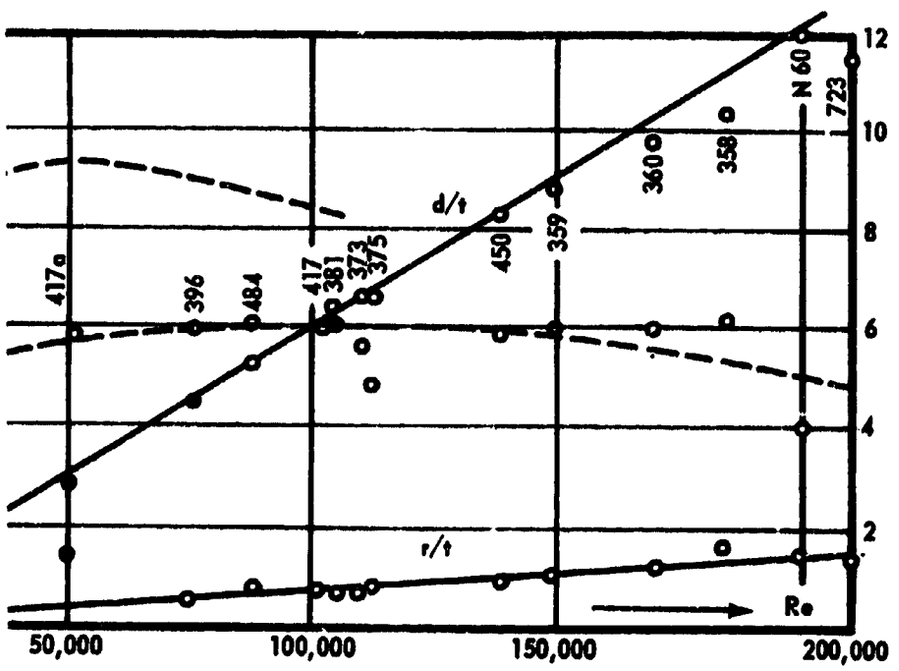

. A system for approximate determination of profile
rs d/t, f/t, and r/t.

with convex lower surface and sections with too small a mean-
example, 2 percent) or using sections from sailplane examples,
but too thick. American characteristic measurements (for
tribution by Seyferth, p. 205) have given impetus to the use of
as, too; in a plot of c_a versus Reynolds numbers, at the lower
,000 the thick heavily cambered profiles USA 35 A (d = 20
ttingen 387 (d = 15 percent) reached the highest $c_{a\,max}$ values
at the same time the lines for decreasing Reynolds number
ther increase in $c_{a\,max}$ increase to be imagined. At
owever, the plot of the minimum profile drag shows the most
s for these thick profiles. It is therefore to be recommended
max value be used to obtain a lower profile drag, because
shows that the profile drag-lift ratio and ceiling factor
are decisive for effectiveness.

in Figure 76 can serve only for a preliminary estimate
d on only two profiles, N 60 and 417 a. Accordingly, further
cambered plates and profiles in this range are necessary,
ers f/t and maximum-camber locations x/t, to make more
ble for their optimum values.

The profiles shown in Figure 76 all have 6 percent camber, and thus high moment, which must be compensated by a suitable tail plane or by sweepback. For calculation of moment compensation by a tail plane, the existing measurements of the flat plate can be used.

The "rigging angle of incidence" of the airfoil, that is, the angle at which the profile chord is attached to the longitudinal axis of the fuselage, plays an important role. The best drag-lift ratio of a wing occurs at a very definite angle of attack, which, after conversion of the $c_{w\infty}$ and α_{∞} values to a chosen aspect ratio (and after addition of the resistance of the fuselage, tail planes, etc., in terms of the wing area), is given by the polar line tangent to the polar curve in the polar plot. The optimum ceiling factor reciprocal lies at a somewhat larger angle of attack. On the Thermik model airplane, designed for optimum climb, the rigging angle of incidence should be chosen higher than for the model airplane intended for the best distance performance. The optimum value of the ceiling factor reciprocal is found in the polar plot (see Figure 1) by plot of a c_a line as a function of c_a^3/c_w^2.

An interesting possibility of profile shaping to obtain high spar depth is given by the wing section of the hawk (Figure 77b) which is known to be an excellent soarer (see [16], p. 212). The hawk profile has on the lower under surface and behind a steeply cambered thin nose, a step which is also found in the stork, crane, and flamingo. Behind the step lies the upper-arm humerus or the forearm bone and the thick extensor. The step is recessed farthest at the elbow. At the airfoil nose are the flexors, especially thin for the land soarers. Upper arm, forearm and flexor form a triangle which is covered by the leading-edge wing skin. In birds with beating wings (ornithopters), the flexor is more strongly developed and more thickly feathered. According to the observation of Hankin, birds with a section called the eagle profile in Figure 77a are superior in stroking flight; on the other hand, birds with the hawk profile (Figure 77b) are faster and can climb at a higher rate in soaring flight. Hankin found that the step is most strongly developed in the soaring birds having the best efficiency and the highest wing loading, such as the kite. He states that the kites, in spite of higher wing loading, always attack the eagles in play and are faster in turning and climb better than the eagles in horizontal paths. He further observed on birds with the hawk profile a tendency during soaring to buck (gust sensitivity) and to create noise, which could no longer be heard in steep gliding flight. Idrac (see [15], p. 41) was able to measure on the kite the lowest sinking velocity $v_y = 0.42$ m/sec, for a horizontal velocity $v_x = 7$ m/sec, corresponding to a drag-lift ratio of:

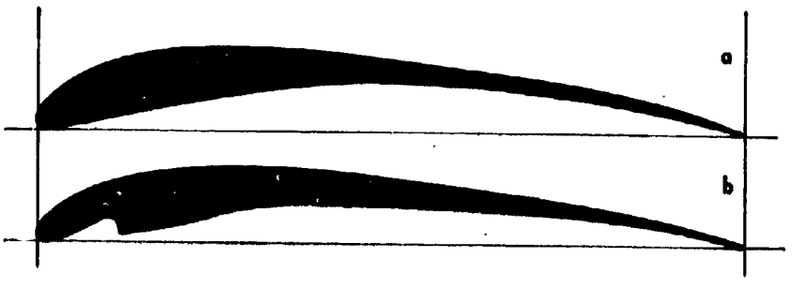

Figure 77. a) Eagle profile, b) hawk profile.

$$\frac{c_w}{c_a} = \frac{v_y}{v_x} = \frac{0.42}{7} = \frac{1}{17} .$$

These values, measured in an upwind and converted to gliding flight in still air, probably cannot be achieved by model airplanes in still air. Only flight measurement in calm - for the flying model airplane, too - gives a satisfactory basis for calculation, because only here are all wind fluctuations with respect to time and place eliminated. If the model airplane has demonstrated good performance in a calm, it will give an optimum performance in a head wind, too, and then the wing loading can be adapted to the wind strength, by additional weight, say. Instead of calm, it is better to say "nonmoving air," because below a certain height thermals can be effective locally without a noticeable horizontal wind movement on the ground.

2. The Wing Plan for the Model Airplane

Is it advisable, following the example of the large airplane, to use the elliptical or trapezoidal plan for the model airplane? The elliptical plan, as is well known, gives an elliptical lift distribution and thus the lowest induced drag for airfoils of a given aspect ratio b^2/F, according to the airfoil theory of Prandtl. The trapezoidal wing with arcs on the end represents an approach to the elliptical wing and is simpler to make from a construction standpoint. The following disadvantage counters these advantages. If the wing chord at the tips is reduced for example to t/2, for a trapezoidal airfoil, then the airfoil tips fly at half the Reynolds number. On the large airplane this influence is small, but on the model airplane it is of greater importance the smaller is the supercritical Reynolds number span in which the airplane model flies, because the airfoil tips may find themselves in the subcritical separated state even in the normal flying condition (Figure 78) .

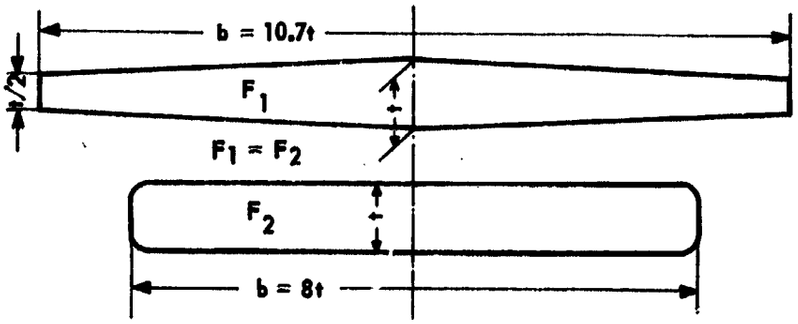

Figure 78. At the wing tip of the trapezoidal wing, the Reynolds number corresponding to the narrowing to t/2 is only half as large as at the root of the wing. In the rectangular wing, the Reynolds number is constant along the span, making this plan more favorable for the small model airplane.

The result is that the airplane with the tapered plan works correspondingly unfavorably at the wing tip because of the low Reynolds number. For the model airplane, the rectangular plan is therefore the most favorable form. Hawks and eagles have an almost rectangular wing plan when soaring.

Extremely tapered designs have been attempted in various models of high-performance sailplanes; these are to be considered unfavorable because the wing tips at low Reynolds numbers worsen the drag-lift ratio more than it is improved because of the intended reduction in induced drag. To maintain supercritical flow at these wing tips and to reduce the danger of separation in the stalled flight state, sometimes the use of wires stretched ahead of the airfoil nose at the wing tips is of advantage (cf. Subsection VI 4c).

3. The Model Airplane Propeller

Practical conclusions can be drawn from the test results for the propeller of the model airplane, too. What is true for the airfoil holds for the propeller. Of course, here centrifugal forces act on the flow, since particles of the boundary layer are directed outwardly so that the flow on the model airplane propeller is improved and thus the influence of Reynolds number is reduced here (see [17], p. 33); this influence will be ignored here. The Reynolds number of the propeller is least at the hub and increases up to the blade tip. As a consequence of the test results, the blade cross section would have to have an especially thin

and pointed profile at the hub, but for strength reasons it is generally made thicker; nor is the blade plan of the propeller of the large airplane a suitable prototype for the model airplane propeller. As shown in Figure 79, instead of the blade width decreasing outwardly, a uniform blade width - or perhaps one with a semicircular shaped blade tip - is to be recommended. The table fan with its thin, curved sheet blades and blade width increasing outwardly thus is a better example for the model airplane propeller than is the large airplane propeller. The part of the propeller lying near the hub works least efficiently. On the model airplane with a thick fuselage, it is therefore advisable to cover the hub with a hood as in the large airplane since this, as a turning fuselage point, improves approach flow. With respect to blade profile and hub covering, this also holds for the propeller of the small wind tunnel fan in instruction in aeronautic physics.

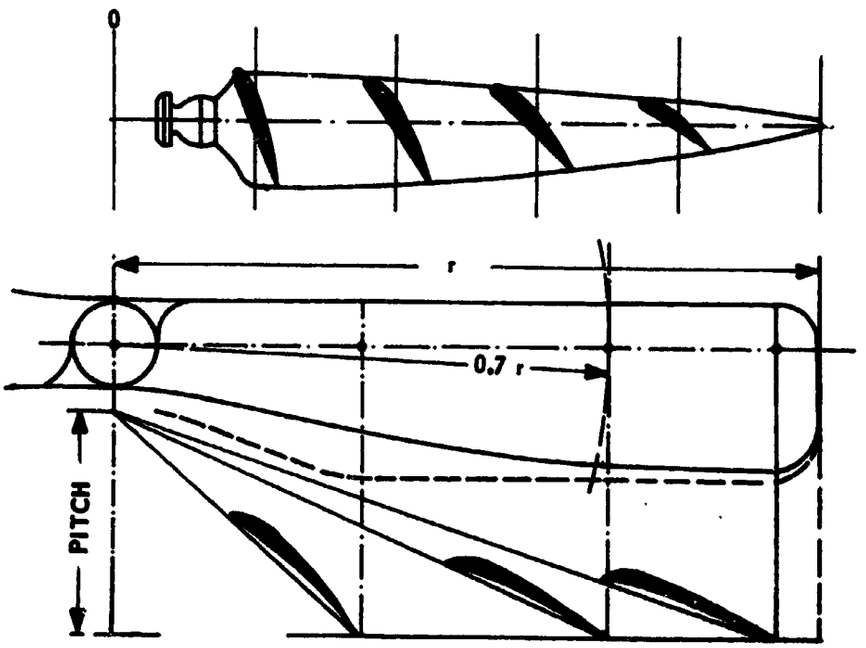

Figure 79. In contrast to the airplane propeller of the large airplane (upper picture), on the model airplane as in the table fan, constant or outwardly increasing blade depth is more favorable for achieving high Reynolds number on the most effective part of the propeller lying at about 0.7 r.

It must further be required of the model airplane propeller as an airfoil that it work supercritically. Near the hub, of course, a subcritical region

must be accepted. Because the thin cambered plate is supercritical even at Reynolds numbers of 20,000, supercritical work is possible with the proper choice of pitch and speed for this blade profile even at relatively small diameters, as will be shown in an example.

A propeller has the following dimensions: diameter d = 200 mm, chord length t = d/8 = 25 mm, speed n = 1300 rpm. The model airplane has a flight velocity of v = 5.4 m/sec. The radius at which Reynolds number 20,000 prevails is to be determined, under the assumption that 20,000 corresponds to the critical Reynolds number of the thin blade profile used.

Velocity v in the propeller circle is somewhat greater than the air velocity v_∞, because the propeller must accelerate the air to produce a thrust, as the test on the stand, where $v_\infty = 0$, makes very clear. This velocity difference is called the slip of the propeller. With a slip = $(v - v_\infty)/(v) = 0.1$ = 10 percent, v becomes 6 m/sec. If u_x designates the peripheral speed of the blade element at radius x, then the speed of this blade element on the propeller path is:

$$w_x = \sqrt{u_x^2 + v^2} .$$

The Reynolds number of this blade element would be

$$Re = \frac{w_x \cdot t}{\nu} = \frac{\sqrt{u_x^2 + v^2} \cdot t}{\nu} = 20,000 .$$

Because $u = 2 \times \pi \, n/60$ (m/sec) then:

$$x = \frac{30}{\pi} \cdot \frac{\sqrt{\left(\frac{Re \cdot \nu}{t}\right) - v^2}}{n} = 0.07 \text{ m} = 70 \text{ mm}.$$

It is customary in aeronautics to refer the initial design of a propeller to a mean radius of 0.7 r, because here is found the highest energy transfer on the propeller blade. It appears analogously useful here to give the Reynolds number of the blade element at 0.7 r as the mean Reynolds number of the entire propeller. Using

$$u_{0.7} = 2 \cdot 0.7 \, r \cdot \pi \cdot n/60 = 0.073 \cdot r \cdot n$$

then

$$Re_{0.7} = \sqrt{(0.073\ r\ n)^2 + v^2} \cdot \frac{t_{0.7}}{\nu} .$$

The 200-mm diameter propeller calculated in the example here would therefore have a Reynolds number $Re_{0.7} = 20,000$, so that the connection with profile measurement can easily be seen. F. Gutsche (see [7], p. 54) gives $Re_k = 150,000$ as the lower critical limit for the usual profiles. With the values in the example above, an Re of 150,000 would be achieved only at a radius of $x = 0.63$ m, and thus would be unattainable in the model airplane propeller. The transition from laminar to the turbulent boundary layer flow for the usual profiles of the measurements above would occur more favorably, in the range of 50,000 to 100,000. If, for example, profile N 60 were used uniformly along r, then according to Figure 57 the transition would begin at 63,000 and would be finished at 113,000. This would have the following practical results:

1. The part of this propeller operating at Re 63,000 would be subcritical, that is, would have high resistance and low thrust.

2. Flow adheres to the blade element operating at Re = 63,000, but it separates at an approach flow angle of 4°.

3. The blade element operating at Re = 113,000 works with a fully turbulent boundary layer and does not experience separation until $c_a = 1.3$, or at 16.5°. For N 60 the Reynolds number of 113,000 would be the lower limit of the supercritical condition, which would be required at least 0.7 r for a propeller.

4. The $c_{a\ max}$ increase according to Figure 57 is still small on the propeller section up to the blade tip; the separation angle of attack increases further to 19° at Re = 150,000, however.

For small model airplanes, the gain achieved by a large Reynolds number through the rectangular plan of the propeller blade (Figure 79) and the wing (Figure 78) is larger than the reduction in induced drag resulting from tapering of the plan.

4. Measures for Artificial Turbulence

With turbulence-free approach flow assumed, the boundary layer is made turbulent

a) by wall friction,
b) by knife edges,
c) by turbulence grilles and turbulence-inducing wire,
d) by sound waves.

Convergence reduces turbulence of the flow and divergence increases it.

Concerning a), on the plane, completely smooth, friction plate, the boundary layer first becomes fully turbulent at Re $\approx 10^7$, according to Figure 6; the rough wall becomes turbulent at lower Reynolds numbers, so that roughness along the wing nose can sometimes be favorable for the model airplane because the artificially increased turbulence attaches the flow sooner than on the smooth model wing.

As is well known, the rough wing surface on the large airplane has exactly the opposite effect (Figure 80). On the rough wing, the maximum lift value drops to half at high Reynolds numbers. At Re = 118,000, the influence of roughness is zero according to the chart; it has an improving effect at Re < 100,000. Figure 81 shows especially how a rough wing nose behaves at higher Reynolds numbers. Measurements on wings with rough surface are currently being made; they will show whether the gain achieved at Re < 100,000 is not countered by a worsening in the drag-lift ratio as a result of the increased supercritical resistance.

It should be mentioned at this point that birds' feathers are far removed from the smoothness of a painted surface. Their relative roughness is not much less than the waves in the sheet-metal skin of a Ju 52, with the difference that the ribbing of the bird's feather runs in every direction and transverse to the direction of flight. Dragonfly wings even have transverse folds whose depth is about 0.1 t; in addition, the leading edge is sharply notched to make the boundary layer turbulent.

Figure 11 shows how the value of Re_k for a sphere can be reduced by roughness.

In respect to b), the effect of pointing the wing leading edge has already been discussed in detail in connection with stagnation point movement and the transition vortex formation.

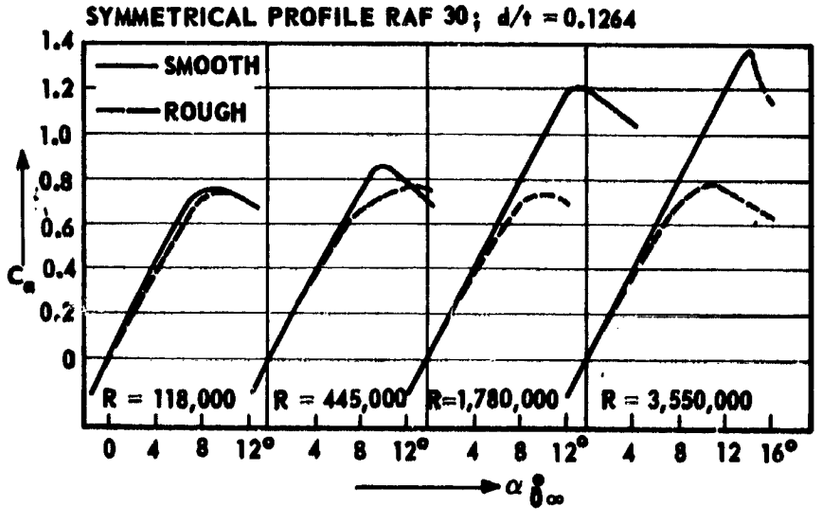

Figure 80. Influence of surface roughness on $c_{a\ max}$ at various Reynolds numbers. (From Technical Note No. 457; grain size $\approx$ 0.12 mm; relative roughness $k/t = 8 \cdot 10^{-4}$; NACA variable-density wind tunnel.) $3 \cdot 5 \cdot 10^6$ corresponds to the Reynolds number of a small sport plane, $1.78 \cdot 10^6$ to that of a sailplane. 118,000 corresponds to the Reynolds number of a model airplane of medium size; the influence of roughness on $c_{a\ max}$ here equals zero. At even lower Reynolds numbers, the rough wing has a relatively small but higher $c_{a\ max}$ value than the smooth wing.

In respect to c), all effective measures on the model airplane for artificial turbulence are analogies of the classic sphere experiment of Prandtl and Wieselsberger (Figures 10 and 13), in which the boundary layer is made turbulent by a wire loop; in turbulence-free approach flow, the critical transition is reduced thereby from Re = 405,000 to a fraction of this Reynolds number. Through the mounting of a turbulence grille ahead of the wing (Figure 12), it is very simple to make the airstream of a wind tunnel completely turbulent to allow study of the effect of turbulence by comparison of measurements with and without the grille. As an example, Figure 82 shows a Goettingen measurement (see [5], vol. IV, part 2; contribution of Seyferth, p. 189) with and without grille for profile 387 (d/t = 0.14) at Re = 84,000. Without a turbulence grille, the maximum lift value is $c_{a\ max} = 0.8$, and with a grille 1.4, nearly twice as

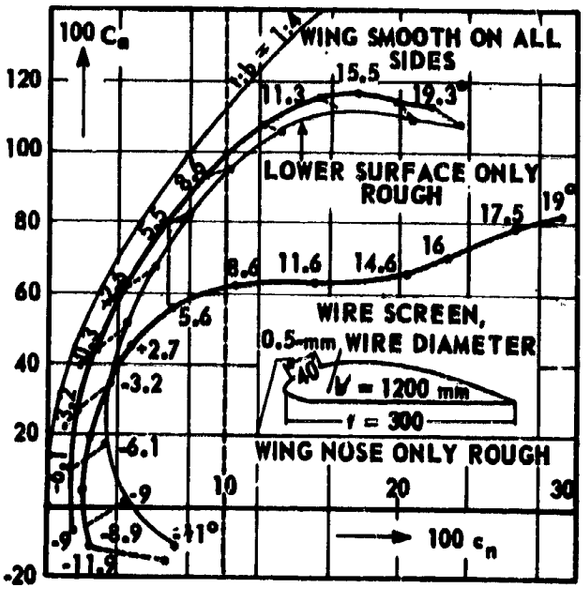

Figure 81. Influence of local roughness on the polar curves. {From Wieselsberger, Ergebnisse der AVA (Goettingen Aeronautical Research Institute Reports [3]); Re = 630,000.} For the large airplane, a rough wing nose, for example, a small amount of ice, can halve lift through premature separation as a result of large turbulent friction loss in the thickened boundary layer.

large, while the profile drag is $\frac{1}{3}$ to $\frac{1}{5}$ smaller. This attractive result makes it seem desirable to achieve a similar result by measures for artificial turbulence in the flying model airplane, too. The tests of course have not been finished, but a few essential results have clearly been shown (Figure 83). As already mentioned, it is sufficient if the boundary layer on the wing upper surface is turbulent, so that instead of the grille a single wire or twine stretched along the wing nose suffices. The result achieved is just as favorable as with a turbulence grille. According to a report by Lippisch, model airplanes with wing profile 387 showed a peculiar festoon flight path whose explanation is now simple. The model airplane flew with a Reynolds number only slightly above the critical Reynolds number Re_k = 80,000, so that in horizontal flight, for example, according to the chart here, the flow separated at -0.3°. The flying model airplane "pancaked" and became faster, so that the Reynolds number and

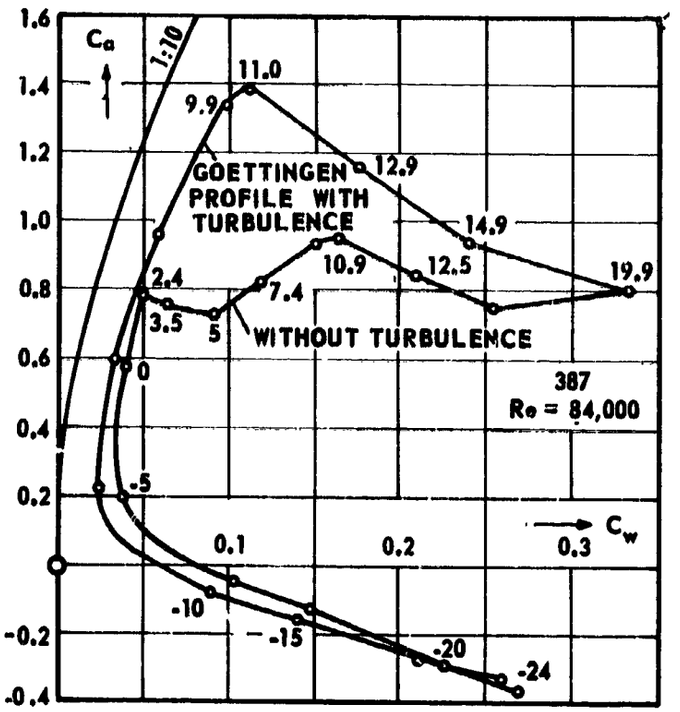

Figure 82. Polar curves of an airfoil taken with and without turbulence grille. (From R. Seyferth [5], Goettingen profile 387, d/t = 0.14, t = 60 mm, b = 600 mm, v = 20 m/sec, Re = 84,000; material, unpolished wood.)

thus the lift became greater; the model airplane again pointed upward and the process began all over again. When a new model airplane of this type was built, it was possible to reproduce the process. When a turbulence wire was stretched ahead of the wing, however, the same model airplane showed very good flight performance even in still air. For example, on a 1-km long gliding flight it had the excellent drag-lift ratio of 1:12. A single twine piece was used as a pre-stretched wire.

There is an Italian patent according to which prestretched wires or tubes delay the separation of flow in the stall condition. The patent claim does not cover the model airplane in whose Reynolds number range the wire is effective but applies only to large airplanes where it increases (?) the separation tendency.

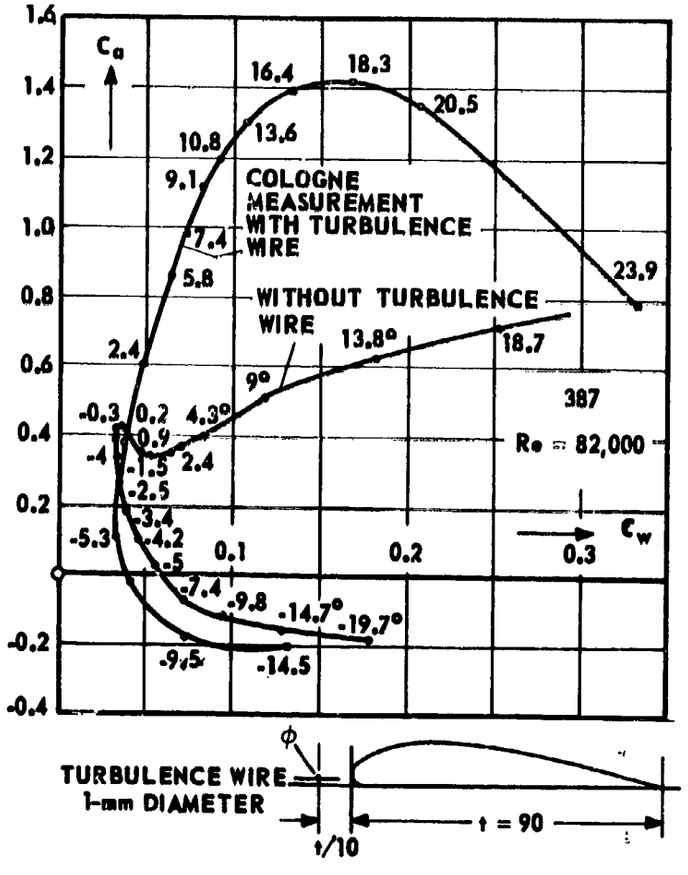

Figure 83. Polar curves taken with and without turbulence wire. Author's measurements: t = 90 mm, b = 450 mm, v = 13 m/sec, Re = 82,000; material, Trolon, shaped with profiled steel razor blades.

To permit better understanding of the effect of the turbulence wire, profile 625, which has been pronounced too thick for model flying, was tested with a prestretched wire (Figure 41). The result showed that the turbulence wire displaces the critical Reynolds number from 105,000 to Re ≈ 20,000, so that thick profiles become advantageous, too, because they give new construction possibilities.

In c ·ast to wires arranged perpendicular to the flow direction, wires
ying in the w direction reduce turbulence, as stated in a patent by M. Kramer.

The t and most interesting finding is the measurement on profile
, 60R (Tal i). This profile is derived from wing section N 60, with an
shaped c › for the mean line from 0.3 t on. The effect of this is that the
oment ab the t/4 axis equals zero, and the profile has a fixed center of
pressure u a high angle of attack, as shown by NACA measurements at
000. It is therefore suitable for the construction of tailless
off
flying-wing planes. This airplane form has its particular advantages for
model-airpl › building, too, but the results with this form have been insignifi-
and, as the easurements described here make clear. The lift values are con-
iderably s ler than on profile N 60, but it is the moment curves which show
the most im ·tant results, because unfortunately the moment becomes greater
with decreas ; Reynolds numbers. The smaller the model airplane, the more
effective an ıe measures additionally necessary to insure flight stability.

As ı as the prestretched wire makes the boundary layer turbulent
Figure 8 b owever, it makes the rear part of the wing profile effective to a
degree as a ·izontal stabilizer. The moment to be equalized does not com-
pletely dis ar, but it is only half as large. The following four advantages
are simulta usly obtained from the prestretched wire:

1. › flight state is supercritical at Re = 20,000, and thus even for
smallest model airplane.

2. ›s sweepback and wing twist suffice to stabilize the flying-wing
del airplane.

3. › relatively thick profile makes possible great construction
ength and the use of a rubber motor.

4. › prestretched wire in addition insures effective prctection in
lision against a tree or a wall edge.

As ·tice shows, with a strong up current any symmetrically con-
structed air . with any profile flies. The turbulence wire, however, furnishes
surprising simple means, easily applied to the model airplane, to make a
model sailp › able to fly even in a weak up current or in calm.

In th owered model airplane, the propeller fulfills the same purpose
s the turbu ce wire. It is thus understandable why American tests show
model airpl s, with propellers of large diameter, about $\frac{3}{4}$ of the wingspan,

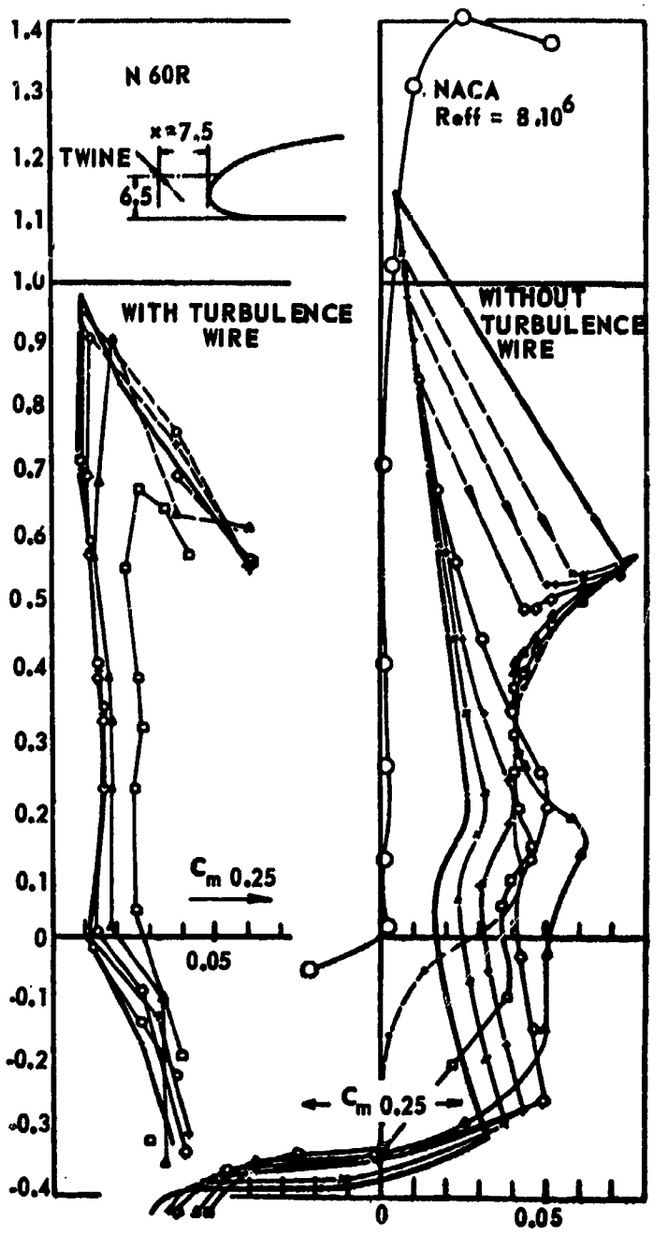

Figure 84. By the turbulence wire (or twine) stretched parallel to the airfoil leading edge, the moment in this Reynolds range is cut about in half for profile N 60R. (The $c_{a\ max}$ values are somewhat low here with the turbulence wire: the wire is mounted somewhat too high.)

to have especially favorable flight characteristics. In this sense, the use of a one-blade propeller makes possible, in addition to a large propeller circle diameter, the advantage of a high (propeller) Reynolds number because of high blade chord length. In the canard, the forward stabilizing surfaces create turbulence for the center airfoil part.

In bird flight, too, various manifestations of artificial turbulence creation can be seen. For example, the soaring flight in column of the hawk is to be explained by the turublence created by the hawk soaring ahead for the one behind. In the V-formation flight of birds of passage, in addition to the utilization of the ascending induced vortex and the airwave of the bird flying ahead in ornithopter flight, the turbulence in the wing boundary layer of the succeeding bird plays a role, too. Utilization of the two latter effects is also true for the file flight of ducks. In addition, the swarm-like flight of birds and insects can be explained as turbulence effect - in addition to the use of a local thermal.

5. Notes for Instruction in Aeronautical Physics

To show the effect of measures of artificial turbulence by means of turbulence grilles, turbulence wire, and so forth, as well as the subcritical and supercritical flow around spheres and thick, round-nosed airfoil models, the airflow of the wind tunnel fan must be made turbulence-free to some extent. A simple means for making turbulence visible is the flame probe (Figure 85). In the turbulence-free stream, the gas flame is completely smooth, like the laminar flow of a slightly opened water faucet (Figure 86), but in the turbulent flow it is disordered and undulant, especially in the peripheral zone, where outside air is entrained. The author's own experiments made a fan of conventional design (by a firm selling aids to education (casing $\approx$ 0.5 m diameter, nozzle $\approx$ 0.3 m diameter) so turbulence-free by the incorporation of a wire screen g (Figure 87) and a stilling stretch h that with a round-nosed thick airfoil model (profile 625, t = 50 mm, b = 100 mm) the placing of a turbulence grille or wire in front, gave two to three times the lift value, depending on the angle of attack, as shown by the two-component balance (Figure 88).

The following is worth noting for the fan. Inlet edge a and inlet hub b improve the approach flow to the propeller c, and the rear part of the streamlined body e improves the outflow. The spin of the airstream caused by the propeller rotation is reduced

1. by a curved guide plate d,
2. by the honeycomb f.

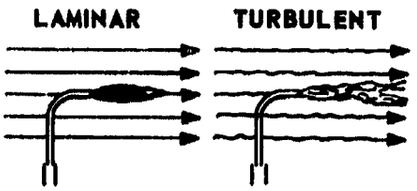

Figure 85. Flame probe for making visible the turbulence state of an airstream by a gas flame.

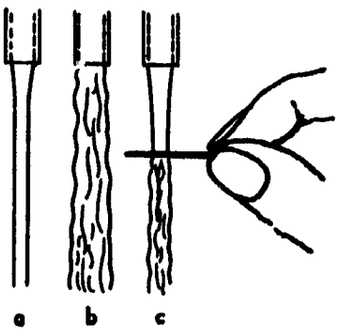

Figure 86. Water flow from a water pipe. a) laminar at low v or Re, b) turbulent at high v or Re, c) laminar flow made turbulent by a nail.

The propeller causes large globules of turbulence; these are:

1. converted into smaller globules by the honeycomb, and then
2. converted into fine-structure vorticity by the wire screen g, and
3. attenuate in the stilling stretch h, and finally
4. are eliminated as far as possible by constriction in the nozzle.

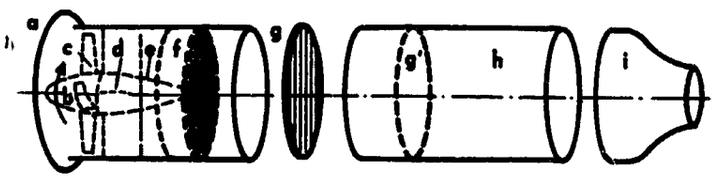

Figure 87. Wind tunnel for school experiments to produce as turbulence-free an airflow as possible.

When several screens are used, it is advantageous to place them a certain distance apart and arrange them so that the air flows through the finest screen last.

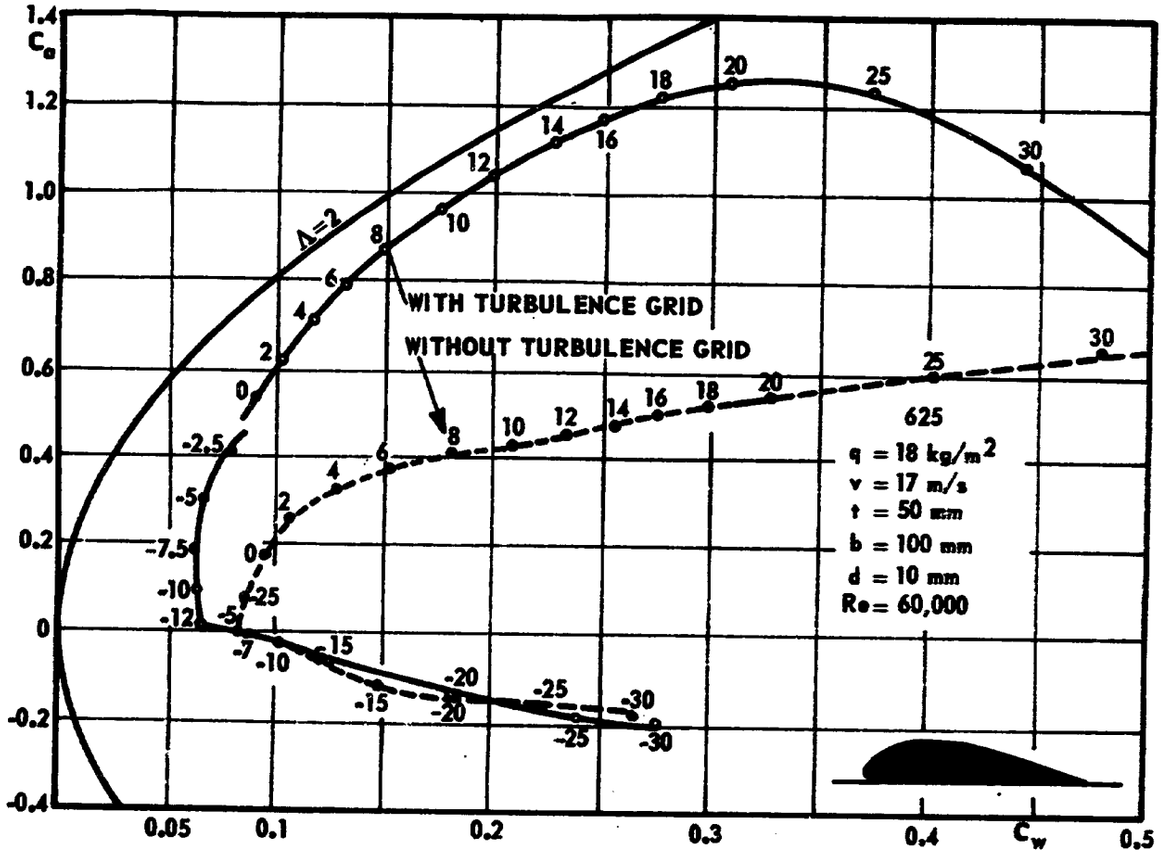

Figure 88. Example of a measurement on a thick profile (625) sensitive to Reynolds number in a fan for school experiments, 300 mm nozzle diameter, which as in Figure 87 is made free of turbulence with a screen and a stilling run.

As the experiments showed, the screen here was effective only in connection with the stilling stretch. As the screen, insect screen of as fine wire as possible was used. The stilling run was made of 1.5-mm thick plywood sheets. For the turbulence grille, a simple wooden frame with twine stretched over it at about 10-mm spacing sufficed.

6. Order of School Tests

a) Laminar and Turbulent Flow

First Experiment. Water flow in a water pipe, laminar at low Reynolds number and turbulent at higher Reynolds number (Figure 86).

Second Experiment. Turbulence of the airstream of a fan, like the one in Figure 87, made visible by a flame probe (Figure 85).

a) Laminar gas flame in a turbulence-free airstream.

b) After the placing of a turbulence grille upstream (Figure 12), the airstream and thereby the flame become turbulent.

Third Experiment. Stepwise elimination of a fan's turbulence (Figure 87) shown by means of a flame probe.

a) Fan without honeycomb and nozzle.

b) With honeycomb,

c) With honeycomb and nozzle,

d) With honeycomb, screen, and nozzle,

e) Without screen, but with honeycomb, stilling run, and nozzle,

f) With honeycomb, screen, stilling run, and nozzle.

b) The Sphere in Low-Turbulence and Turbulent Airstream

(The sphere must be fastened to a tube at the rear. No support wires or the like can be permitted to make the air turbulent on the upstream side of the sphere.)

Fourth Experiment. Measurement of the drag of the sphere with the drag balance:

a) In subcritical flow in the low-turbulence airstream,

b) At supercritical flow by the placing of a turbulence grille upstream.

This experiment shows only the "sensitivity to turbulence" of the sphere. To aid in understanding of "sensitivity to Reynolds numbers" of rounded bodies, therefore, it must be emphasized that at sufficiently high speed or high Reynolds number, as a result of the greater "entraining effect of the external flow" (= stronger impulse exchange) the boundary layer becomes turbulent or supercritical by itself, at $Re_k = 405,000$ in laminar flow and correspondingly earlier in turbulent airflow, and the critical sphere Reynolds number of a wind tunnel therefore serves as an indication of turbulence for the tunnel. The turbulence factor is $TF = 405,000/Re_k$. The following calculations are to be recommended here:

1. The Reynolds number of the fourth experiment, after the velocity is calculated from the dynamic pressure.

2. The velocity which at the given diameter of the sphere used in the fourth experiment would be necessary to attain $Re_k = 405,000$.

Fifth Experiment. Measurement of sphere drag without and with a rubber ring around the sphere equator in the low-turbulence airstream to demonstrate that only the turbulence of the boundary layer and not that of the total airstream is important (Figure 13).

Sixth Experiment. A pressure measurement to demonstrate the effect of the transition to supercritical flow on the pressure state at the downstream side of the sphere (Figure 10). The measuring tube should be led along the rear sting, with the opening within a few millimeters of the sphere.

a) Subcritical: negative pressure (- sign).

b) Supercritical: positive pressure (+ sign) with a turbulence grille located upstream.

Reference may be made here to determination of the critical sphere characteristic Re_k:

1. At change of the rear pressure from - to +, which means the value of p = 0 (Figure 14).

2. In drag measurement at the value $c_w = 0.3$ (Figure 11).

Seventh Experiment. Compulsion of the supercritical transition on a sphere with rough surface:

a) By coarse sand glued to the leading side of the sphere,

b) By a long-haired fur ring on the rear side of the sphere.

Eighth Experiment. Visualization of the subcritical, separated flow and the supercritical attached flow by threads glued ahead of the sphere equator (or by smoke; Figure 13).

Ninth Experiment. Sharp-edged bodies (flat circular plate and so forth) have the same resistance in laminar as in turbulent airflow, because the separation point is fixed. Sharp-edged bodies are insensitive to turbulence and thus are not sensitive to Reynolds number. This relationship can be demonstrated if the drag coefficient is determined for circular plates of various diameters and at various velocities, that is, at various Reynolds numbers; in all cases the coefficient will be $c_w = 1.1$ (Figure 9).

c) Airfoil Model in the Low-Turbulence and Turbulent Airstream

The discussion of Figure 9 permits an instructive transition from the sphere to the airfoil. Sensitivity to turbulence and to Reynolds number are shown there in connection with the critical Reynolds number and its dependence on the fineness ratio d/t. This figure permits the following basic conclusions to be drawn:

1. Progressing from the sphere to the slender airfoil profile, Re_k becomes smaller and enters the range of flight of the bird and the model airplane. There it has a considerable influence on ability to fly, while the flow state for a large airplane which, for example, has 10 to 500 times as large a Reynolds number accordingly is always supercritical.

2. The smaller the Reynolds number the thinner must the profile of the airplane model or the flying animal (bird, butterfly, or insect) be to permit it to fly through a turbulent boundary layer with supercritical attached flow.

Tenth Experiment. Lift and drag are measured with a two-component balance on an airfoil model with an aspect ratio $\Lambda = b : t = >2 : 1$ and a round-nosed, thick wing profile, for example, 625:

a) In a low-turbulence airstream,

b) In a turbulent airstream with a turbulence grille mounted upstream,

c) With only a turbulent boundary layer on the upper surface, with a turbulence wire mounted ahead of it.

The three measurements are done at a constant angle of attack of about 6° and at constant velocity and then at another angle of attack and velocity. For an aspect ratio smaller than 2, the two tip vortices keep the stream attached, so that the subcritical region does not occur.

Eleventh Experiment. Hardly any lift change can be seen on a thin airfoil model of the same aspect ratio no matter whether it is with or without a turbulence grille. As a result of nose turbulence of the sharp leading edge, the condition is supercritical even without a turbulence grille.

Twelfth Experiment. To verify the effect of nose turbulence, we use in this experiment an airfoil model of the same thickness as profile 625 but with a sharp leading edge.

Thirteenth Experiment. We measure two polar curves for the airfoil model with profile 625, from 0 to 30° α and then from 0 to -30° α at a constant dynamic pressure:

a) In the low-turbulence airstream,

b) With a turbulence grille.

We plot the values α, A, and W' in a table and measure the resistance of the sting; after the subtraction of the latter, W results. We know the dynamic pressure q and we calculate F and plot for each measurement c_a and c_w on millimeter graph paper, c_w at five times the c_a scale (Figure 88). In addition, the Reynolds number should be calculated after determining v.

Fourteenth Experiment. We attempt to determine the most favorable position of the turbulence wire at various angles of attack for profile 625.

Fifteenth Experiment. We construct two similar model sailplanes with profile 625, t = 150 mm, b = 1200 mm:

a) With a prestretched wire (cf. Figures 83 and 91)

b) Without prestretched wire,

and start both at the same time. Differences in construction should be eliminated by alternate application of the wire.

Sixteenth Experiment. To obtain data for calculation of the model flight, an attempt must always be made to measure the flight in still air (Figure 89): a stop watch, a measuring tape, and a protractor for gliding angle, somewhat like that shown in Figure 90, are the most essential aids. It is necessary to determine the gliding angle, the gliding velocity, the sinking velocity, the horizontal velocity, the wing loading, c_a, c_w, the ceiling factor reciprocal, the Reynolds number, and all these at various rigging angles of incidence, to find the best values. The author has given instructions, and simple calculation examples, in the magazine Luftfahrt und Schule,*) vol. VII, No. 4.

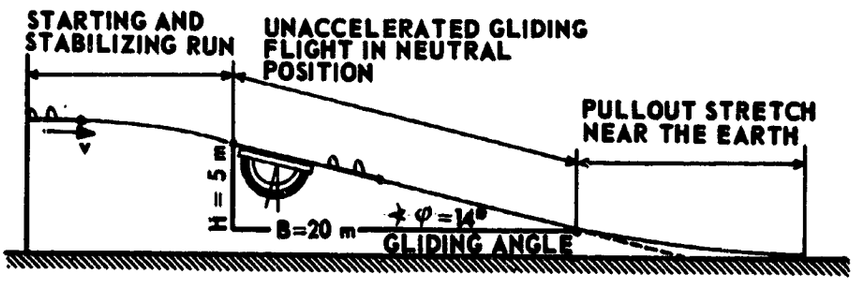

Figure 89. Flight measurement of unaccelerated gliding flight in still air by means of stop watch, protractor, and measuring tape.

*) Verlag C. J. E. Volckmann Nachf. E. Wette, Berlin-Charlottenburg 2.

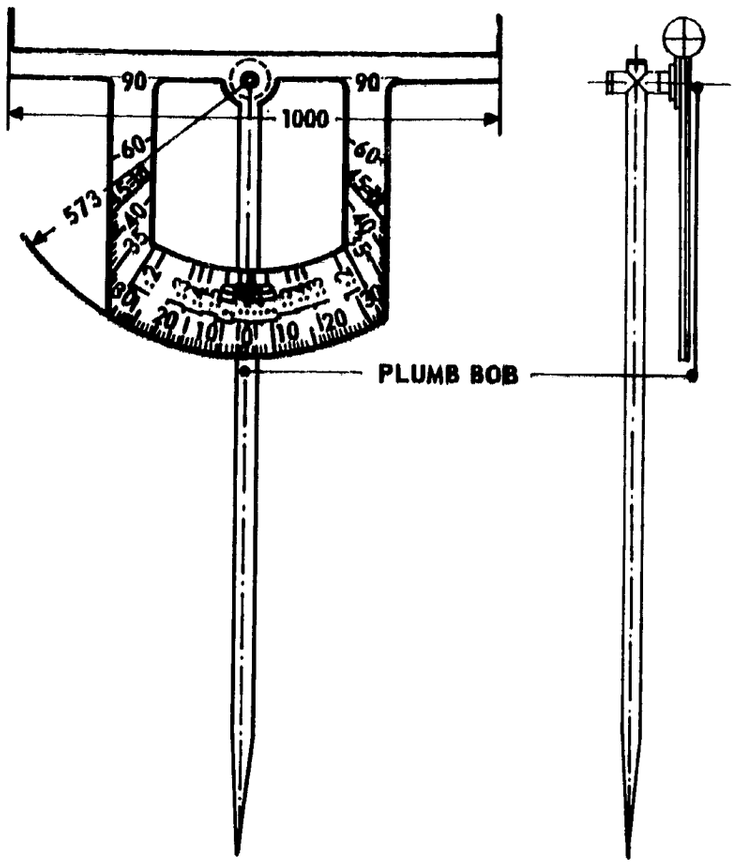

Figure 90. Protractor for determining the gliding angle. On a short flight stretch, the flight path is sighted on from a point located to the side. The protractor and the flight path are seen as in Figure 89. One pupil does the sighting and a second makes sure that the plumb bob hangs free and still and reads the angle on command of the first pupil. In contrast to this, on a longer flight stretch the protractor is set at the starting point and the model airplane is sighted on through the crosshairs by pupil No. 1 from the instant of start until it lands. Pupil No. 2 reads the angle, for example, every 5 seconds. Every 5 seconds, pupil No. 3 gives the command to read. Pupil No. 4 notes in a previously prepared table the angle. Pupil No. 5 observes the model airplane through a telescope and upon landing gives the command to stop so that total elapsed time can be read. The circumference of a circle of 57.3 cm radius is 360 cm; therefore, 1 cm on the perimeter corresponds to 1°. The protractor can easily be made as a homemade instrument.

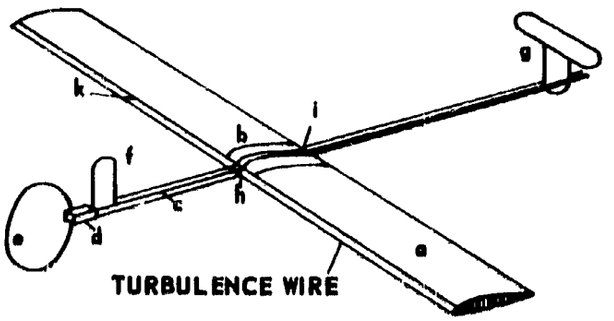

Figure 91. A simple model sailplane with prestretched wire as an inducer of turbulence.

VII. SUMMARY

The measurements study the behavior of wing sections in the low-turbulence stream (turbulence factor = 1.06) in a measuring range from Re = 20,000 to 170,000 in which the profiles pass through a critical region. This measuring region corresponds approximately to the Reynolds number range of model airplane wings.

1. Behavior of Airfoil Profiles in the Critical Range of Reynolds Numbers

a) Although for the flat friction plate the critical transition from laminar boundary flow to turbulent begins at $Re_k < 1$ million, and at $Re_k < 405,000$ for the sphere, the measurements on airfoil profiles show a beginning of transition at Re < 100,000, and for flat and cambered thin plates at the lowest angle of attack at Reynolds numbers even below 20,000; on the intermediate airfoil section N 60 (d = 12 percent, f = 4 percent, r = 1.4 percent of chord t) at $Re_k = 63,000$; for the thick airfoil section G 625 (d = 20, f = 6, r = 3.4) it is at $Re_k = 105,000$.

b) Although for the flat friction plate the "transition" to fully turbulent boundary layer flow develops over a range up to $Re \approx 10^7$, the fully turbulent condition on the two above mentioned airfoil profiles is finished after a Reynolds

number ... of 50,000 above Re_k, and at Re = 155,000 for the thick profile ... of 625. In measurements of two thin plates (1. flat, 2. curved), the transition had to considered as finished at the lower measuring limit attainable with the installation, Re = 20,000.

c) The beginning of the transition at the critical Reynolds number Re_k is characterized by a sudden increase in lift coefficient c_a and a corresponding decrease in drag coefficient c_w, because the laminar separated flow previously in the subcritical region overcomes the pressure increase at the airfoil upper surface, by reason of the boundary layer becoming turbulent or by the now effective energy transport from the outside flow, and attaches itself; at low angles of attack this occurs near the trailing edge.

The critical transition, that is, the attachment to the airfoil upper surface, begins at a lower Reynolds number the small is the camber of the upper surface and the thinner the airfoil nose, and thus at very small angles of attack for the flat plate with a sharp leading edge. The sharp nose of a thin profile acts as a turbulence edge in connection with the great acceleration effective in increasing angle of attack and circulation because of the movement of the stagnation point flow around the nose.

d) Because of the transition region, a small increase in Reynolds number movement of the rapidly increasing turbulence produces a relatively large movement of the separation position toward the leading edge and a movement of the angle of attack toward the trailing edge, so that now the attainable separation α_k and the pertinent $c_{a\,max}$ value rapidly become larger, for example, on profile N 60 from 4° to 16.5°, or c_a = 0.5 to 1.3, in the range of Re = 63,000 to 113,000. A measurement with a turbulence wire on the thick profile G 6, where Re_k and the $c_{a\,max}$ increase is displaced from Re = 105,000 to Re = 20,000, shows that the intensity of turbulence and not the entraining effect or the energy content of the external flow is decisive.

e) In the range of the transition, the $c_{a\,max}$ line in the plot of c_a versus Re coincides with the separation line. The end of the transition evidences itself through:

a break in the $c_{a\,max}$ line, which now ascends only slightly (corresponding to the entraining effect, which increases with Re);

2. from the break on, the separation line is below the $c_{a\ max}$ line.

With increasing angle of attack, the turbulent separation point moves toward the leading edge on the profile; if it passes the transition point, the flow separates, and then the separation point moves away to the pressure minimum, that is, to the highest point of the upper side camber.

f) Local laminar separation is superimposed on the incipient turbulent transition beginning at the airfoil trailing edge at low Reynolds numbers and low angle of attack. With increasing turbulence, the transition point moves toward the leading edge, where the accompanying local laminar separation collapses. The transition point reaches the leading edge more quickly, the smaller is the mean-line camber f/t and the thinner is the profile or the sharper the leading edge. When the transition point reaches the leading edge on a thin low-camber profile, it forms a transition vortex which broadens with further increasing angle of attack, since the flow separates in laminar fashion over the leading edge and then again attaches turbulently at the rear of the vortex.

Because a laminar separation precedes the transition both at the trailing edge as well as now at the leading edge, the conclusion is evident that each turbulent transition on a wall is preceded by a laminar separation - even if it is of only molecular size. The origin of the transition vortex on the leading edge is evident in pressure measurement by a suction peak. With further increase in angle of attack, the transition vortex broadens flatly to the trailing edge, as the transition point moves again to the trailing edge. The separation surface of the initially small local separation then forms a "fluid" profile upper surface with enlarged camber and a pronounced suction peak, which shortly before the final separation oscillates, in intermittent separation and impulsive attachment of the flow, between the highest value of negative pressure and the pressure of the separated flow. The separation and attachment occur from the leading edge to the trailing edge.

The development of the transition vortex is similar in character to the separation phenomena in cavitation. In addition, just as cavitation decreases with increasing total pressure in water, for example, on a diving submarine, so with increasing Reynolds number the transition vortex probably decreases, so that the transition vortex has a particular importance in the Reynolds number range considered here.

g) Flat plate. The turbulent phenomena at the flow around the nose explain the supercritical behavior at a Reynolds number as low as 20,000 for the flat and cambered plate, because of the premature widening of the transition vortex and because of the early separation of flow on the flat plate; here the

sharp leading edge acting as a turbulence edge becomes a separation edge at α_∞ = 5 to 7° angle of attack, and in spite of a steep slope in the lift line ($dc_a/d\hat{\alpha}_\infty \approx 2\pi$), a $c_{a\ max}$ of only 0.5 at 42,000 to 0.7 at 420,000 is reached.

The flat plate, after separation with further increase in angle of attack, shows no decrease in the c_a value. The $c_{a\ max}$ value increases continuously with increasing Reynolds number because of increasing entraining effect and diminishing transition vortex, and this explains why, in spite of low Re_k, the flat plate and symmetrical profiles are so unfavorable with respect to $c_{a\ max}$ at low Reynolds numbers, and why symmetrical profiles operate more favorably only at high Reynolds numbers.

h) Cambered plate. This, too, works supercritically at Re = 20,000, but it reaches double the $c_{a\ max}$ value in comparison with the flat plate; at α_∞ = 8°, a $c_{a\ max}$ = 1.06 occurs at Re = 42,000 and 1.3 at 420,000. The slope of the lift line is surprisingly steep; at Re = 42,000 the value of $dc_a/d\alpha_\infty = 2.77\pi$, and thus is even greater than for the flat plate. The superiority of the cambered plate - over profiles, too - extends to Re ≈ 100,000. There are three reasons for the superiority:

1. Favorable interaction of tangential approach flow to the leading edge at a high angle of attack with nose turbulence.

2. A maximum concave camber of the lower surface so that it participates as far as possible in the generation of lift.

3. The relatively small camber of the upper surface.

The attempt to make the lower surface as heavily cambered as possible and the upper surface as little as possible to avoid premature separation thus leads to the thin cambered plate as the most favorable profile for model airplanes and model airplane propellers to generate high lift and low drag at low Reynolds numbers.

2. Conclusions for the Model Airplane

a) Choice of Profile. A model airplane achieves optimum flight performance in its size class only when its flight state is supercritical. This flight state can always be realized in the practically required limits by a suitable profile choice following the basic principle: the lower the Reynolds number the thinner must the profile be and the sharper the leading edge.

The model airplane has a low wing loading (up to 3 kg/m^2), it flies slowly (v $\approx$ 3 to $\approx$ 13 m/sec), and accordingly has a high c_a (0.5 to 1). The cambered plate 417 a at Re = 42,000 and α_∞ = 2.5° has the high value c_a = 0.7 and the minimum of profile drag $c_{w\infty\,min}$ = 0.027. This gives a profile maximum drag-lift ratio of $c_{w\infty}/c_a$ = 1:26 which, converted to the aspect ratio Λ = 10, is 1:16.5. This drag-lift ratio, unusually favorable at Re = 42,000 for a model-airplane airfoil, surpasses any profile in this Reynolds number range and thus explains the surprising flight performances of the room airplane model covered with film. A plot of the profile ceiling factor $c_a^3/c_{w\infty}^2$ versus the profile lift-drag ratio $c_a/c_{w\infty}$ for the measured profiles shows for the profile choice, with respect to camber f and thickness d, the following guiding values:

Re	f/t	d/t	r/t
50,000	0.06 to 0.09	0.03	0.004
100,000	0.06 to 0.08	0.06	0.007
200,000	0.05 to 0.07	0.12	0.014

The most favorable location of the maximum camber appears to be at 15 and 25 percent of the chord length.

b) The Wing Plan. Wings with a tapered plan work unfavorably because of the correspondingly low Reynolds number at the wing tips: for the small model airplane, accordingly, the rectangular plan with slightly rounded tips is the most favorable form. This applies to the plan of the small model airplane propeller, too. The gain achieved in high Reynolds number by the rectangular plan is greater for small model airplanes than the reduction in induced drag achieved by tapering of the plan.

c) Constant Moment Coefficient (fixity of center of pressure) in the normal flying range is a characteristic of profiles with an S-shaped mean line only at high Reynolds number. As separation on the profile upper surface progresses because of Reynolds number reduction or stalling, the S-shape becomes ineffective. Only the flat plate and the plate with the S-curve work with a fixed center of pressure in the region of Reynolds numbers around 20,000.

d) Artificial Turbulence. By a turbulence wire or twine stretched along the airfoil nose and making turbulent the boundary layer of the airfoil upper surface the critical transition on profiles can be reduced to about Re = 20,000. This makes it possible to use favorable construction possibilities even for small model airplanes:

1. Profiles with a thickness of up to 20 percent of the chord length.

2. Profiles with an S-shaped mean line for flying-wing model airplanes.

3. Airfoils with tapered plan.

3. Comparison: Large Airplane and Model Airplane

a) The boundary layer should remain laminar as long as possible on the large airplane, to utilize the lower boundary friction as much as possible and to displace turbulent separation to as high an angle of attack as possible; on the other hand, on a model airplane, turbulence is desired as early as possible, to obtain high supercritical range of Reynolds numbers. For the large airplane a so-called laminar profile is desired, but for the model airplane a turbulence profile with a sharp leading edge is sought. The airplane wing should be especially smooth at the nose, but some roughness can sometimes be advantageous on the wing of the model airplane. In the large airplane, the elliptically tapered airfoil is advantageous, but on the model ariplane and on the propeller of the model airplane the rectangular plan is better. On the small model airplane, the sharper wing nose, acting as a turbulence edge, produces the critical transition earlier, giving an increase in the $c_{a\ max}$ value; on the large airplane, it would act as a separation edge, so that here with an otherwise equal profile the wing with the higher nose radius must achieve the highest $c_{a\ max}$ value. All measures for artificial turbulence have a favorable effect on the model airplane but an unfavorable one on the large airplane. In any case, these are crude contrasts, which require individual treatment, because the model airplane is not merely an airplane reduced in size. Thus model flying and aeronautical physics in our secondary schools are in urgent need of direction along these ways of thinking.

b) The effect of force on the profile in the transition between the supercritical and the subcritical region is similar to the effect found during the approach to the velocity of sound c, as shown by a comparison of the measurement on profile G 625 with an American measurement on a similar profile of the same thickness (d = 20 percent); the very unfavorable subcritical polar curve at Re = 21,000 for G 625 coincides with the polar curve at v/c = 0.85. The transitions are completed from the supercritical to the subcritical state of Re = 155,000 to 105,000, and then at v/c = 0.5 to 0.6 there is a new "hypercritical state." Although the fluid mechanics causes are basically different, the force effects are the same. The same practical result occurs for

the small model airplane as for the high-speed airplane: the lower the Reynolds number on one hand, and the more the flying speed approaches sonic velocity, on the other hand, the thinner must the profile be, and the smaller the camber and the more pointed the leading edge.

4. Application of Results

a) The polar curves of the measured profiles make possible for the first time the quantitative determination of flight performance and the stability of model airplanes in the Reynolds number range from 20,000 to 170,000. New fundamentals are provided for the evaluation of experiments in the free-fall tunnel and in the vertical wind tunnel for spinning tests. More far reaching conclusions than were hitherto possible can be drawn for large airplanes from these experiments, through interposition of the polar curves measured at large Reynolds numbers for the same profile. The significance of the measurements for general aeronautics is involved here, along with the expansion of the physical picture.

In addition, the test results find application in the design of small blowers, centrifugal pumps, and fans, as well as for evaluation of tests with model ship's propellers.

b) The contrasts, hitherto considered as troublesome, between the flow laws of the large airplane and the facts of experience in model flight are explained in considerable part and reasons for the causes found. This has built a new bridge between aeronautical physics and model-airplane building in the intention of the "Ludwig Prandtl Prize."

c) It is shown that model flight is closer to Lilienthal's prototype, the flight of birds, than to the large airplane, because birds and the model airplane fly in a region of similar Reynolds numbers. New and interesting connections of model flight with biology instruction, in the sense of the biophysics of flight, result from these interrelationships.

d) The desired impetus has been given to aeronautical joint efforts in the secondary schools for going beyond the usual model airplane construction and incorporating the constructive creative element of individual activity, so that the agreement between theory and practice can be proven in flight testing by measurement of flight in still air. Although the individual in the airplane factory or in the research laboratory can see only part of a large task, here the entire picture from design to flight testing is in the hands of teacher and pupil in the best form as a promising, vocationally directing incentive to the study of flying or aeronautics.

I thank Mr. B. Eck, Eng. D., Cologne; Max Kramer, Eng. D., Berlin-Adlershof; R. Seiferth, Grad. Engr., Goettingen; and Professor C. Wieselsberger (deceased), Aachen, for advice on the conversion of wind tunnels which were used and on the conduct of the measurements. Professor Prandtl and Professor Hoff are thanked particularly for reviewing the test results.

In addition, it is a pleasant task to thank the ministerial director, Professor Krümmel, Ph. D., and the ministerial adviser, H. Helbig, for the contract for this work and for promoting it in many ways.

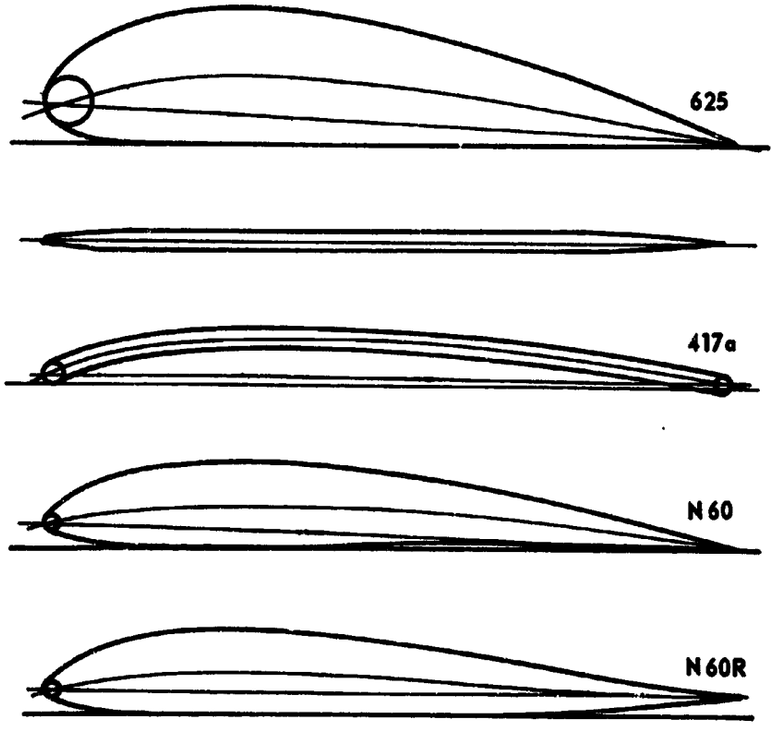

Figure 92. Summary of the five airfoil profiles measured.

VIII. NUMERICAL TABLES

A correction for the measured values $c_{w\,m}$ and α_m measured on the rectangular airfoil model (aspect ratio $\Lambda = 5$) to take into account the finite stream of the wind tunnel (cf. p. 90):

$$c_{wk5} = -0.01287\, c_a^2;\ \alpha_{k5} = -0.738\, c_a .$$

For conversion of the test values of $c_{w\,m}$ and α_m to the elliptical wing plan and to infinite span ($\Lambda = \infty$):

"Profile drag" $c_{w\infty} = c_{w\,m} - c_{wk\infty} = c_{w\,m} - 0.07897\, c_a^2$.

"True angle of attack" at the lower surface tangent $\alpha_\infty = \alpha_m - \alpha_{k\infty} = \alpha_m - 4.918\, c_a$.

625 Re = 168,000

Test Results on a Rectangular Wing Λ = b:t = 5					Conversion to the Elliptical Plan for Λ = b^2:F = ∞		$c_{m\,0.25}$
Without Stream Correction			With the Finite Stream Taken into Account				
α_m	c_a	c_{wm}	c_{w5} / $c_{wm} - c_{wk5}$	α_5 / $\alpha_m - \alpha_{k5}$	$c_{w\infty}$ / $c_{wm} - c_{wk\infty}$	α_∞ / $\alpha_m - \alpha_{k\infty}$	
-20	-0.150	0.18	0.18	-19.89	0.178	-19.28	0.015
-18.4	-0.1	0.163	0.163	-18.326	0.1622	-17.91	0.015
-16	-0.035	0.14	0.14	-15.974	0.1399	-15.83	0.03
-12	0.1	0.097	0.097	-12.074	0.0962	-12.49	0.06
-10	0.06	0.08	0.080	-10.044	0.0798	-10.29	0.062
- 9	0.05	0.051	0.051	- 9.037	0.0509	- 9.24	0.106
- 8	0.09	0.04	0.040	- 8.066	0.0393	- 8.44	0.112
- 6	0.2	0.033	0.032	- 6.146	0.0296	- 6.98	0.112
- 4	0.328	0.034	0.033	- 4.251	0.0255	- 5.59	0.106
- 2	0.452	0.04	0.037	- 2.332	0.024	- 4.21	0.105
0	0.577	0.05	0.046	- 0.424	0.024	- 2.81	0.104
2	0.710	0.063	0.056	+ 1.477	0.0231	- 1.43	0.107
4	0.835	0.078	0.069	3.383	0.0226	- 0.10	0.104
7	0.995	0.105	0.093	6.26	0.0259	+ 2.07	0.1
9.5	1.11	0.132	0.130	8.674	0.0329	3.99	0.096
12	1.213	0.163	0.161	11.005	0.046	6.02	0.096
14.2	1.270	0.188	0.168	13.062	0.0602	7.76	0.098
15.7	1.245	0.205	0.187	14.595	0.0862	9.47	0.1
Separation							
15.7	0.58	0.249	0.245	15.07	0.2225	12.64	0.1
20	0.61	0.3	0.295	19.551	0.2708	17.01	0.103

Test Results on a Rectangular Wing $\Lambda = b:t = 5$					Conversion to the Elliptical Plan for $\Lambda = b^2:F = \infty$		$c_{m\,0.25}$
Without Stream Correction			With the Finite Stream Taken into Account				
α_m	c_a	c_{wm}	c_{w5} $c_{wm} - c_{wk5}$	α_5 $\alpha_m - \alpha_{k5}$	$c_{w\infty}$ $c_{wm} - c_{wk\infty}$	α_∞ $\alpha_m - \alpha_{k\infty}$	
12	0.515	0.205	0.202	11.624	0.185	9.51	0.096
9.5	0.475	0.167	0.164	9.150	0.1497	7.18	0.091
7	0.46	0.133	0.130	6.661	0.1163	4.74	0.09
4.4	0.513	0.103	0.1	4.022	0.0826	1.89	0.089
Sudden Increase							
4.4	0.855	0.082	0.072	3.762	0.0224	0.16	0.104

625 Re = 147,000

-20	-0.12	0.18	0.18	-19.912	0.179	-19.41	0.017
-18.4	-0.1	0.168	0.168	-18.326	0.1672	-17.91	0.013
-16	-0.055	0.141	0.141	-15.959	0.1408	-15.73	0.027
-12	0.09	0.098	0.098	-12.066	0.0973	-12.44	0.058
-10	0.08	0.082	0.082	-10.059	0.0815	-10.39	0.068
- 9	0.05	0.054	0.054	- 9.037	0.0539	- 9.24	0.1
- 8	0.085	0.043	0.043	- 8.062	0.0424	- 8.42	0.11
- 6	0.192	0.035	0.035	- 6.141	0.032	- 6.92	0.109
- 4	0.320	0.036	0.035	- 4.236	0.028	- 5.57	0.106
- 2	0.440	0.040	0.037	- 2.324	0.0246	- 4.16	0.105
0	0.567	0.050	0.046	- 0.421	0.0246	- 2.79	0.103

Test Results on a Rectangular Wing $\Lambda = b:t = 5$					Conversion to the Elliptical Plan for $\Lambda = b^2:F = \infty$		$c_{m\,0.25}$
Without Stream Correction			With the Finite Stream Taken into Account				
α_m	c_a	c_{wm}	c_{w5} $c_{wm} - c_{wk5}$	α_5 $\alpha_m - \alpha_{k5}$	$c_{w\infty}$ $c_{wm} - c_{wk\infty}$	α_∞ $\alpha_m - \alpha_{k\infty}$	
2	0.70	0.063	0.057	+ 1.483	0.0242	- 1.43	0.107
4	0.822	0.078	0.069	3.394	0.0245	- 0.04	0.104
7	0.975	0.105	0.093	6.280	0.03	+ 2.20	0.099
9.5	1.087	-	-	-	-	-	0.091
10	1.112	0.138	0.122	9.181	0.041	4.54	0.092
13	1.210	0.175	0.156	12.107	0.059	7.06	0.096
Separation							
13	0.530	0.217	0.213	12.609	0.195	10.4	0.096
16	0.590	0.255	0.250	15.564	0.228	13.11	0.107
20	0.610	0.3	0.295	19.551	0.271	17.01	0.102
9.5	0.465	0.169	0.166	9.157	0.152	7.21	0.091
7	0.445	0.135	0.132	6.673	0.1195	4.81	0.09
3.7	0.50	0.095	0.092	3.331	0.0755	1.25	0.091
Sudden Increase							
3.7	0.805	0.076	0.068	3.106	0.025	- 0.26	0.105

625 Re = 126,000

Test Results on a Rectangular Wing Λ = b:t = 5					Conversion to the Elliptical Plan for $\Lambda = b^2:F = \infty$		$c_{m\,0.25}$
Without Stream Correction			With the Finite Stream Taken into Account				
α_m	c_a	c_{wm}	c_{w5} / $c_{wm} - c_{wk5}$	α_5 / $\alpha_m - \alpha_{k5}$	$c_{w\infty}$ / $c_{wm} - c_{wk\infty}$	α_∞ / $\alpha_m - \alpha_{k\infty}$	
-20	-0.105	0.18	0.18	-19.923	0.1791	-19.48	0.018
-18.4	-0.1	0.169	0.169	-18.326	0.1682	-17.91	0.010
-16	-0.07	0.144	0.144	-15.948	0.1437	-15.66	0.02
-12	+0.08	0.101	0.101	-12.059	0.1005	-12.30	0.056
-10	0.1	0.083	0.0829	-10.074	0.0822	-10.49	0.072
- 9	0.05	0.060	0.060	- 9.037	0.06	- 9.24	0.098
- 8	0.08	0.048	0.048	- 8.059	0.0475	- 8.39	0.108
- 6	0.187	0.037	0.036	- 6.137	0.034	- 6.90	0.109
- 4	0.310	0.038	0.037	- 4.228	0.0302	- 5.51	0.107
- 2	0.425	0.042	0.0396	- 2.312	0.028	- 4.09	0.105
0	0.555	0.051	0.047	- 0.410	0.027	- 2.79	0.106
2	0.685	0.064	0.058	+ 1.495	0.027	- 1.36	0.107
4	0.807	0.079	0.071	3.403	0.027	+ 0.02	0.104
7	0.955	0.105	0.0932	6.297	0.033	2.28	0.096
9	1.03	0.126	0.1224	8.241	0.042	3.91	0.096
Separation							
9	0.445	0.163	0.160	8.671	0.147	6.80	0.089
12	0.505	0.205	0.202	11.628	0.185	9.52	0.094
16	0.59	0.255	0.250	15.565	0.228	13.11	0.115
20	0.61	0.3	0.295	19.551	0.271	17.01	0.101
3	0.445	0.09	0.0874	2.671	0.074	0.79	0.09

Sudden Increase							
3	0.750	0.072	0.0647	2.446	0.028	- 0.68	0.106

625 Re = 105,000

-20	-0.09	0.18	0.18	-19.934	0.1793	-19.56	0.018
-18.4	-0.1	0.17	0.17	-18.326	0.1692	-17.91	0.009
-16	-0.085	0.147	0.147	-15.937	0.1464	-15.58	0.019
-12	0.06	0.103	0.103	-12.044	0.1028	-12.29	0.051
-10	0.12	0.084	0.084	-10.088	0.0829	-10.59	0.074
- 9	0.05	0.066	0.066	- 9.037	0.0659	- 9.24	0.093
- 8	0.05	0.055	0.055	- 8.037	0.0549	- 8.24	0.105
- 6	0.13	0.04	0.04	- 6.096	0.0387	- 6.64	0.105
- 4	0.27	0.04	0.039	- 4.918	0.034	- 5.31	0.105
- 2	0.39	0.045	0.043	- 2.288	0.033	- 3.91	0.105
0	0.51	0.055	0.052	- 0.376	0.035	- 2.51	0.105
2	0.65	0.067	0.062	+ 1.521	0.034	- 1.19	0.104
Separation							
2	0.275	0.09	0.089	1.798	0.0838	+ 0.66	0.080
4	0.32	0.106	0.105	3.764	0.0978	2.43	0.076

Test Results on a Rectangular Wing Λ = b:t = 5					Conversion to the Elliptical Plan for Λ = b^2:F = ∞		$c_{m\,0.25}$
Without Stream Correction			With the Finite Stream Taken into Account				
α_m	c_a	c_{wm}	c_{w5} $c_{wm} - c_{wk5}$	α_5 $\alpha_m - \alpha_{k5}$	$c_{w\infty}$ $c_{wm} - c_{wk\infty}$	α_∞ $\alpha_m - \alpha_{k\infty}$	
7	0.385	0.139	0.137	6.717	0.1271	5.11	0.083
9.5	0.435	0.171	0.168	9.179	0.156	7.38	0.088
12	0.495	0.205	0.202	11.535	0.186	9.58	0.093
16	0.585	0.255	0.251	15.569	0.228	13.13	0.118
20	0.61	0.3	0.295	19.551	0.271	17.01	0.099
0	0.225	0.075	0.074	- 0.163	0.071	- 1.09	0.085
- 2	0.15	0.064	0.064	- 2.110	0.062	- 2.72	0.085
Sudden Increase							
- 2	0.39	0.045	0.043	- 2.288	0.033	- 3.91	0.105

625 Re = 63,000

-20	-0.08	0.18	0.18	-19.94	0.1795	-19.61	0.016
-18.4	-0.1	0.17	0.17	-18.326	0.1692	-17.91	0.006
-16	-0.11	0.153	0.153	-15.919	0.152	-15.46	0.01
-12	-0.12	0.123	0.123	-11.912	0.1219	-11.41	0.015
-10	-0.17	0.12	0.12	- 9.877	0.1176	- 9.18	0.026
- 9	-0.27	0.11	0.119	- 8.802	0.104	- 7.68	0.000
- 8	-0.31	0.099	0.098	- 7.771	0.0913	- 6.49	0.02
- 6	-0.18	0.076	0.076	- 5.869	0.0732	- 5.13	0.046
- 4	-0.06	0.071	0.071	- 3.956	0.0708	- 3.71	0.067

Test Results on a Rectangular Wing $\Lambda = b:t = 5$					Conversion to the Elliptical Plan for $\Lambda = b^2:F = \infty$		$c_{m\,0.25}$
Without Stream Correction			With the Finite Stream Taken into Account				
α_m	c_a	c_{wm}	c_{w5} / $c_{wm} - c_{wk5}$	α_5 / $\alpha_m - \alpha_{k5}$	$c_{w\infty}$ / $c_{wm} - c_{wk\infty}$	α_∞ / $\alpha_m - \alpha_{k\infty}$	
- 2	+0.015	0.078	0.078	- 2.011	0.0779	- 2.07	0.07
0	0.105	0.087	0.087	- 0.077	0.0861	- 0.52	0.072
2	0.180	0.098	0.098	+ 1.877	0.0956	+ 1.12	0.074
4	0.245	0.1115	0.111	3.824	0.1067	2.83	0.072
7	0.33	0.143	0.142	6.758	0.1343	5.39	0.079
9.5	0.405	0.173	0.171	9.202	0.16	7.51	0.085
12	0.475	0.205	0.202	11.651	0.1873	9.67	0.09
16	0.575	0.255	0.251	15.577	0.229	13.18	0.112
20	0.61	0.3	0.295	19.551	0.271	17.01	0.092

625 Re = 84,000

-20	-0.085	0.18	0.18	-19.938	0.1794	-19.58	0.016
-18.4	-0.1	0.17	0.17	-18.326	0.1692	-17.91	0.008
-16	-0.095	0.147	0.147	-15.93	0.1463	-15.53	0.018
-12	+0.015	0.107	0.107	-12.011	0.1069	-12.07	0.038
-10	+0.080	0.089	0.089	-10.058	0.0885	-10.4	0.072
- 9	-0.125	0.093	0.093	- 8.91	0.0918	- 8.39	0.033
- 8	-0.21	0.085	0.084	- 7.847	0.0812	- 6.98	0.049
- 6	-0.12	0.071	0.071	- 5.913	0.0699	- 5.41	0.06
- 4	-0.03	0.066	0.066	- 3.978	0.0659	- 3.85	0.074
- 2	+0.055	0.071	0.071	- 2.041	0.0708	- 2.27	0.079
0	0.135	0.081	0.081	- 0.099	0.0796	- 0.66	0.076

Test Results on a Rectangular Wing $\Lambda = b:t = 5$					Conversion to the Elliptical Plan for $\Lambda = b^2:F = \infty$		$c_{m\,0.25}$
Without Stream Correction			With the Finite Stream Taken into Account				
α_m	c_a	c_{wm}	c_{w5} $c_{wm} - c_{wk5}$	α_5 $\alpha_m - \alpha_{k5}$	$c_{w\infty}$ $c_{wm} - c_{wk\infty}$	α_∞ $\alpha_m - \alpha_{k\infty}$	
2	0.21	0.095	0.094	+ 1.847	0.0912	+ 0.98	0.073
4	0.265	0.109	0.108	3.806	0.1031	2.71	0.075
7	0.344	0.141	0.139	6.751	0.1318	5.33	0.081
9.5	0.415	0.173	0.171	9.194	0.1593	7.47	0.085
12	0.485	0.203	0.202	11.642	0.1867	9.62	0.092
16	0.58	0.255	0.251	15.572	0.2287	13.16	0.115
20	0.61	0.3	0.295	19.551	0.271	17.01	0.099

625 Re = 42,000

-20	-0.075	0.18	0.18	-19.947	0.1796	-19.63	0.038
-18.4	-0.1	0.172	0.172	-18.326	0.1712	-17.91	0.005
-16	-0.135	0.155	0.155	-15.902	0.1536	-15.33	0.008
-12	-0.15	0.125	0.125	-11.891	0.1231	-11.29	0.012
-10	-0.25	0.125	0.124	- 9.817	0.1198	- 8.79	0.013
- 9	-0.31	0.118	0.117	- 8.772	0.1103	- 7.49	-0.023
- 8	-0.35	0.103	0.101	- 7.741	0.0932	- 6.29	0.009
- 6	-0.205	0.078	0.077	- 5.85	0.0745	- 5.0	0.025
- 4	-0.085	0.074	0.074	- 3.939	0.0734	- 3.58	0.049
- 2	+0.01	0.081	0.081	- 2.007	0.081	- 2.05	0.062
0	0.1	0.09	0.09	- 0.074	0.0892	- 0.49	0.063
2	0.175	0.102	0.102	+ 1.872	0.0995	1.15	0.07
4	0.235	0.116	0.115	3.828	0.1114	2.87	0.067

Test Results on a Rectangular Wing $\Lambda = b:t = 5$					Conversion to the Elliptical Plan for $\Lambda = b^2:F = \infty$		$c_{m\,0.25}$
Without Stream Correction			With the Finite Stream Taken into Account				
α_m	c_a	c_{wm}	c_{w5} $c_{wm} - c_{wk5}$	α_5 $\alpha_m - \alpha_{k5}$	$c_{w\infty}$ $c_{wm} - c_{wk\infty}$	α_∞ $\alpha_m - \alpha_{k\infty}$	
7	0.32	0.145	0.144	6.764	0.1369	5.43	0.075
9.5	0.392	0.175	0.173	9.211	0.163	7.59	0.075
12	0.47	0.205	0.202	11.653	0.188	9.70	0.08
16	0.575	0.255	0.251	15.576	0.229	13.18	0.11
20	0.61	0.3	0.295	19.551	0.271	17.01	0.06

625 R_e = 21,000

-20	-0.05	0.19	0.19	-19.963	0.1899	-19.76	0.088
-18.4	-0.100	0.179	0.179	-18.326	0.1782	-17.91	0.01
-16	-0.175	0.159	0.159	-15.872	0.1564	-15.16	0.013
-12	-0.200	0.13	0.129	-11.853	0.1267	-11.02	0.028
-10	-0.275	0.13	0.129	- 9.798	0.1239	- 8.67	0.034
- 9	-0.325	0.12	0.119	- 8.761	0.1116	- 7.39	-0.04
- 8	-0.375	0.105	0.103	- 7.724	0.0938	- 6.17	0.007
- 6	-0.24	0.079	0.078	- 5.824	0.0742	- 4.83	0.026
- 4	-0.115	0.076	0.076	- 3.918	0.0749	- 3.43	0.055
- 2	-0.005	0.083	0.083	- 1.997	0.083	- 1.98	0.06
0	+0.095	0.093	0.093	- 0.070	0.0923	- 0.47	0.05
2	0.165	0.104	0.104	+ 1.88	0.1018	+ 1.18	0.055
4	0.225	0.118	0.117	3.834	0.1133	2.91	0.05
7	0.315	0.147	0.146	6.769	0.1391	5.47	0.06
9.5	0.385	0.176	0.174	9.217	0.1642	7.61	0.078

Test Results on a Rectangular Wing $\Lambda = b:t = 5$					Conversion to the Elliptical Plan for $\Lambda = b^2:F = \infty$		$c_{m\,0.25}$
Without Stream Correction			With the Finite Stream Taken into Account				
α_m	c_a	c_{wm}	c_{w5} $c_{wm} - c_{wk5}$	α_5 $\alpha_m - \alpha_{k5}$	$c_{w\infty}$ $c_{wm} - c_{wk\infty}$	α_∞ $\alpha_m - \alpha_{k\infty}$	
12	0.465	0.205	0.202	11.658	0.188	9.72	0.075
16	0.575	0.255	0.251	15.575	0.229	13.18	0.11
20	0.61	0.27	0.265	19.551	0.241	17.01	0.06

Flat Plate Re = 168,000

0	0	0.01	0.01	0	0.01	0	0
1.51	1.05	0.013	0.0127	1.4	0.012	0.94	0
3.02	0.21	0.022	0.0208	2.8	0.0185	1.99	-0.001
6.05	0.42	0.051	0.0487	5.74	0.037	3.95	-0.001
7.13	0.49	0.065	0.0619	6.67	0.046	4.72	+0.01
8.18	0.57	0.085	0.0809	7.78	0.0592	5.38	0.035
9.2	0.59	0.10	0.0954	8.76	0.0715	6.23	0.048
12.2	0.[illegible]5	0.148	0.143	11.74	0.117	9.1	0.075
15.2	0.6[illegible]	0.192	0.1864	14.71	0.1578	11.95	0.1
18.3	0.687	0.24	0.2339	17.79	0.203	14.9	0.1
20.3	0.697	0.273	0.2668	19.79	0.235	16.9	0.1
25.3	0.715	0.356	0.3493	24.77	0.315	21.75	0.11

Flat Plate Re = 42,000

0	0	0.0135	0.0135	0	0.0135	0	0
1.5	0.096	0.017	0.016[illegible]	1.43	0.016	1.03	-0.003

Test Results on a Rectangular Wing $\Lambda = b:t = 5$					Conversion to the Elliptical Plan for $\Lambda = b^2:F = \infty$		$c_{m\,0.25}$
Without Stream Correction			With the Finite Stream Taken into Account				
α_m	c_a	c_{wm}	c_{w5} $c_{wm} - c_{wk5}$	α_5 $\alpha_m - \alpha_{k5}$	$c_{w\infty}$ $c_{wm} - c_{wk\infty}$	α_∞ $\alpha_m - \alpha_{k\infty}$	
3	0.192	0.025	0.0245	2.86	0.022	2.07	-0.003
6	0.385	0.051	0.0491	5.72	0.039	4.1	-0.003
7	0.450	0.065	0.06235	6.665	0.049	4.8	0.000
8	0.520	0.085	0.0815	7.617	0.064	5.42	0.012
9	0.535	0.099	0.0964	8.61	0.077	6.4	0.031
12	0.580	0.14	0.1358	11.58	0.114	9.3	0.050
18	0.655	0.23	0.2248	17.49	0.1925	14.7	0.096
25	0.705	0.333	0.3265	24.477	0.293	21.5	0.110

417 a Cambered Plate Re = 168,000

-15	-0.43	0.172	0.1696	-14.68	0.1577	-12.9	-0.038
-12	-0.37	0.134	0.1323	-11.728	0.1231	-10.19	-0.028
- 9	-0.295	0.099	0.0979	- 8.785	0.0919	- 7.57	-0.01
- 6	-0.215	0.068	0.0674	- 5.84	0.0641	- 4.96	+0.016
- 3	-0.03	0.048	0.0469	- 2.98	0.0479	- 2.88	0.046
0	+0.24	0.04	0.0393	- 0.17	0.0352	- 1.17	0.089
3	0.505	0.047	0.0437	+ 2.63	0.0271	+ 0.52	0.106
6.1	0.75	0.066	0.0586	5.54	0.0215	2.41	0.107
9	0.94	0.094	0.0836	8.31	0.0241	4.38	0.101
12	1.08	0.138	0.1227	11.20	0.0445	6.63	0.094
13	1.10	0.159	0.143	12.19	0.0631	7.58	0.091
14	1.11	0.187	0.171	13.187	0.0898	8.52	0.108

Test Results on a Rectangular Wing $\Lambda = b:t = 5$					Conversion to the Elliptical Plan for $\Lambda = b^2:F = \infty$		$c_{m\,0.25}$
Without Stream Correction			With the Finite Stream Taken into Account				
α_m	c_a	c_{wm}	c_{w5} $c_{wm} - c_{wk5}$	α_5 $\alpha_m - \alpha_{k5}$	$c_{w\infty}$ $c_{wm} - c_{wk\infty}$	α_∞ $\alpha_m - \alpha_{k\infty}$	
15	1.00	0.224	0.211	14.262	0.1451	10.09	0.145
18	0.94	0.295	0.284	17.308	0.2247	13.38	0.173
25	0.87	0.382	0.372	24.359	0.322	20.70	0.167
30	0.87	0.49	0.480	29.359	0.43	25.70	0.174
35	0.87	0.565	0.555	34.359	0.505	30.70	0.186
40	0.76	0.59	0.583	39.440	0.5442	36.27	0.178

417 a Cambered Plate Re = 42,000

-25	-0.523	0.315	0.3115	-24.61	0.2935	-22.4	-0.067
-20	-0.464	0.237	0.23424	-19.66	0.22	-17.7	-0.048
-15	-0.405	0.171	0.16888	-14.7	0.158	-13	-0.024
-12	-0.35	0.134	0.1324	-11.74	0.124	-10.3	-0.026
- 9	-0.29	0.99	0.9889	- 8.78	0.983	- 7.5	-0.0085
- 6	-0.215	0.068	0.0674	- 5.84	0.064	- 4.9	+0.015
- 3	-0.065	0.049	0.0489	- 2.95	0.049	- 2.7	0.045
0	+0.200	0.04	0.0394	- 0.155	0.0365	- 1.03	0.08
3	0.465	0.047	0.0452	+ 2.66	0.030	+ 0.70	0.094
6.1	0.720	0.067	0.0602	5.57	0.026	2.6	0.097
9	0.898	0.094	0.0838	8.34	0.030	4.58	0.093
12	1.03	0.138	0.1243	11.24	0.053	7.0	0.083
13	1.06	0.168	0.1433	12.21	0.078	7.75	0.077
14	0.996	0.200	0.1908	13.27	0.132	9.1	0.108

Test Results on a Rectangular Wing $\Lambda = b:t = 5$					Conversion to the Elliptical Plan for $\Lambda = b^2:F = \infty$		$c_{m\,0.25}$
Without Stream Correction			With the Finite Stream Taken into Account				
α_m	c_a	c_{wm}	c_{w5} / $c_{wm} - c_{wk5}$	α_5 / $\alpha_m - \alpha_{k5}$	$c_{w\infty}$ / $c_{wm} - c_{wk\infty}$	α_∞ / $\alpha_m - \alpha_{k\infty}$	
15	0.94	0.236	0.2246	14.31	0.166	10.38	0.13
20	0.90	0.314	0.3036	19.34	0.250	15.6	0.145
25	0.87	0.4	0.3903	24.36	0.34	20.7	0.158
30	0.94	0.532	0.5206	29.31	0.462	25.38	0.18
35	0.87	0.573	0.5633	34.36	0.513	30.7	0.154
40	0.77	0.615	0.6074	39.43	0.568	36.2	0.154

N 60 Re = 168,000

-25.3	-0.400	0.270	0.268	-25.004	0.2574	-23.34	-0.030
-20.3	-0.325	0.210	0.209	-20.059	0.2015	-18.71	-0.027
-15.3	-0.260	0.143	0.142	-15.107	0.1376	-14.02	-0.015
-10.3	-0.245	0.092	0.091	-10.118	0.0871	- 9.10	+0.007
- 9	-0.155	0.058	0.0577	- 8.884	0.056	- 8.25	0.066
- 7.8	-0.065	0.031	0.031	- 7.752	0.0307	- 7.48	0.100
- 6.5	+0.025	0.022	0.025	- 6.519	0.0220	- 6.632	0.100
- 3.5	0.220	0.0212	0.0206	- 3.663	0.0174	- 4.58	0.096
0	0.445	0.031	0.028	- 0.330	0.0153	- 2.19	0.084
2.2	0.590	0.0435	0.039	+ 1.765	0.0163	- 0.69	0.081
3.5	0.675	0.053	0.047	3.002	0.0169	+ 0.18	0.080
6	0.830	0.073	0.064	5.388	0.0183	1.91	0.0765
8	0.955	0.0925	0.0808	7.294	0.0204	3.31	0.073
10	1.070	0.114	0.0993	9.211	0.0238	4.37	0.070

Test Results on a Rectangular Wing $\Lambda = b:t = 5$					Conversion to the Elliptical Plan for $\Lambda = b^2:F = \infty$		$c_{m\,0.25}$
Without Stream Correction			With the Finite Stream Taken into Account				
α_m	c_a	c_{wm}	c_{w5} $c_{wm} - c_{wk5}$	α_5 $\alpha_m - \alpha_{k5}$	$c_{w\infty}$ $c_{wm} - c_{wk\infty}$	α_∞ $\alpha_m - \alpha_{k\infty}$	
13	1.220	0.149	0.130	12.100	0.0313	7.00	0.066
15	1.305	0.174	0.152	14.033	0.0393	8.59	0.063
16.5	1.328	0.193	0.170	15.519	0.0535	9.99	0.062
18	1.310	0.213	0.191	17.030	0.0771	11.56	0.065
19.5	1.260	0.238	0.2175	18.570	0.1122	13.30	0.083
Separation							
19.5	0.730	0.306	0.299	18.961	0.2639	15.91	0.128
25	0.700	0.380	0.374	24.482	0.3415	21.55	0
15	0.740	0.229	0.222	14.455	0.1858	11.38	0.111
10.5	0.765	0.153	0.145	9.937	0.1069	6.75	0.096
Sudden Increase							
10.5	1.095	0.1186	0.099	9.691	0.0242	5.11	0.069

N 60 R_e = 147,000

-25.3	-0.400	0.270	0.268	-25.004	0.2574	-23.34	-0.031
-20.3	-0.325	0.210	0.209	-20.059	0.2015	-18.71	-0.027
-15.3	-0.260	0.143	0.142	-15.107	0.1376	-14.02	-0.015

Test Results on a Rectangular Wing $\Lambda = b:t = 5$					Conversion to the Elliptical Plan for $\Lambda = b^2:F = \infty$		$c_{m\,0.25}$
Without Stream Correction			With the Finite Stream Taken into Account				
α_m	c_a	c_{wm}	c_{w5} $c_{wm} - c_{wk5}$	α_5 $\alpha_m - \alpha_{k5}$	$c_{w\infty}$ $c_{wm} - c_{wk\infty}$	α_∞ $\alpha_m - \alpha_{k\infty}$	
-10.3	-0.250	0.092	0.091	-10.114	0.087	- 9.07	+0.004
- 9	-0.160	0.059	0.0586	- 8.880	0.0569	- 8.21	0.071
- 7.8	-0.065	0.032	0.032	- 7.752	0.0317	- 7.48	0.102
- 6.5	+0.025	0.025	0.025	- 6.519	0.0249	- 6.623	0.101
- 3.5	0.220	0.023	0.022	- 3.663	0.0193	- 4.58	0.093
0	0.440	0.032	0.030	- 0.326	0.0169	- 2.16	0.0845
2.2	0.585	0.044	0.040	+ 1.769	0.017	- 0.68	0.0815
3.5	0.670	0.054	0.048	3.006	0.0185	+ 0.21	0.0805
6	0.825	0.074	0.065	5.391	0.02	1.92	0.0765
8	0.947	0.092	0.080	7.300	0.0207	3.33	0.073
10	1.060	0.114	0.100	9.218	0.0255	4.79	0.070
13	1.210	0.149	0.130	12.107	0.0332	7.05	0.066
15	1.295	0.147	0.125	14.043	0.0413	8.63	0.063
16.5	1.320	0.193	0.171	15.522	0.0552	10.01	0.062
19	1.260	0.229	0.2085	18.07	0.1032	12.80	0.075
Separation							
19	0.73	0.297	0.290	18.461	0.2549	15.41	0.126
15	0.74	0.229	0.222	14.455	0.1858	11.38	0.111
10	0.755	0.145	0.138	9.443	0.0999	6.29	0.0945

Test Results on a Rectangular Wing $\Lambda = b:t = 5$					Conversion to the Elliptical Plan for $\Lambda = b^2:F = \infty$		$c_{m\,0.25}$
Without Stream Correction			With the Finite Stream Taken into Account				
α_m	c_a	c_{wm}	c_{w5} $c_{wm} - c_{wk5}$	α_5 $\alpha_m - \alpha_{k5}$	$c_{w\infty}$ $c_{wm} - c_{wk\infty}$	α_∞ $\alpha_m - \alpha_{k\infty}$	
Sudden Increase							
10	1.060	0.114	0.100	9.218	0.0255	4.79	0.070

N 60 Re = 126,000

-25.3	-0.400	0.270	0.268	-25.004	0.2574	-23.34	-0.034
-20.3	-0.325	0.210	0.209	-20.059	0.2015	-18.71	-0.026
-15.3	-0.260	0.143	0.142	-15.107	0.1376	-14.02	-0.015
-10.3	-0.260	0.092	0.091	-10.107	0.0866	- 9.02	+0.001
- 9	-0.175	0.061	0.0606	- 8.870	0.0585	- 8.14	0.061
- 7.8	-0.065	0.034	0.034	- 7.752	0.0337	- 7.48	0.098
- 6.5	+0.025	0.026	0.026	- 6.519	0.0259	- 6.62	0.102
- 3.5	0.220	0.025	0.024	- 3.663	0.0207	- 4.58	0.097
0	0.435	0.033	0.031	- 0.332	0.0182	- 2.14	0.086
2.2	0.575	0.045	0.041	+ 1.776	0.0189	- 0.63	0.082
3.5	0.660	0.055	0.049	3.013	0.0207	+ 0.27	0.0815
6	0.820	0.075	0.066	5.395	0.0218	1.97	0.0765
8	0.940	0.093	0.082	7.307	0.0229	3.39	0.073
10	1.050	0.115	0.101	9.223	0.0281	4.84	0.070
13	1.200	0.150	0.1315	12.115	0.0561	7.10	0.066
15	1.285	0.175	0.1538	14.051	0.0438	8.69	0.063
16.5	1.305	0.193	0.1711	15.537	0.0583	10.09	0.062
18.1	1.275	0.216	0.1851	17.159	0.0872	11.83	0.066

Test Results on a Rectangular Wing $\Lambda = b:t = 5$							
Without Stream Correction			With the Finite Stream Taken into Account		Conversion to the Elliptical Plan for $\Lambda = b^2:F = \infty$		$c_{m\,0.25}$
α_m	c_a	c_{wm}	c_{w5} $c_{wm} - c_{wk5}$	α_5 $\alpha_m - \alpha_{k5}$	$c_{w\infty}$ $c_{wm} - c_{wk\infty}$	α_∞ $\alpha_m - \alpha_{k\infty}$	
Separation							
18.1	0.730	0.282	0.275	17.561	0.239	14.51	0.122
11	0.720	0.162	0.155	10.469	0.1210	7.47	0.097
9.5	0.745	0.138	0.131	8.951	0.0941	5.84	0.094
Sudden Increase							
9.5	1.025	0.110	0.0965	8.740	0.0271	4.47	0.071

N 60 Re = 105,000

-25.3	-0.400	0.270	0.268	-25.004	0.2574	-23.34	-0.037
-20.3	-0.325	0.210	0.209	-20.059	0.2015	-18.71	-0.024
-15.3	-0.260	0.143	0.142	-15.107	0.1376	-14.02	-0.014
-10.3	-0.270	0.093	0.092	-10.10	0.0872	- 8.97	-0.003
- 9	-0.200	0.064	0.0635	- 8.852	0.0608	- 8.02	+0.048
- 7.8	-0.075	0.038	0.038	- 7.744	0.0376	- 7.43	0.089
- 6.5	+0.013	0.0295	0.0295	- 6.509	0.0294	- 6.564	0.097
- 3.5	0.210	0.026	0.025	- 3.347	0.0223	- 4.52	0.100
0	0.430	0.034	0.032	- 0.319	0.0194	- 2.12	0.090
2.2	0.565	0.0465	0.0424	+ 1.785	0.0216	- 0.58	0.085

Test Results on a Rectangular Wing $\Lambda = b:t = 5$					Conversion to the Elliptical Plan for $\Lambda = b^2:F = \infty$		$c_{m\,0.25}$
Without Stream Correction			With the Finite Stream Taken into Account				
α_m	c_a	c_{wm}	c_{w5} $c_{wm} - c_{wk5}$	α_5 $\alpha_m - \alpha_{k5}$	$c_{w\infty}$ $c_{w1n} - c_{wk\infty}$	α_∞ $\alpha_m - \alpha_{k\infty}$	
3.5	0.650	0.056	0.051	3.021	0.0227	+ 0.31	0.082
6	0.810	0.076	0.068	5.403	0.0241	2.01	0.0765
8	0.925	0.094	0.083	7.318	0.0261	3.46	0.073
10	1.035	0.1155	0.1017	9.236	0.0313	4.91	0.070
12	1.130	0.138	0.122	11.165	0.038	6.44	0.067
14	1.225	0.163	0.144	13.095	0.0443	7.98	0.0645
15.7	1.255	0.185	0.165	14.773	0.0603	9.52	0.062
Separation							
15.7	0.715	0.241	0.234	15.172	0.2003	12.19	0.113
16	-	-	-	-	-	-	-
20	0.730	0.315	0.308	19.461	0.2729	16.41	0.130
11	0.690	0.162	0.156	10.490	0.1244	7.61	0.097
9.3	0.725	0.136	0.129	8.765	0.0942	5.74	0.094
Sudden Increase							
9.3	0.995	0.108	0.095	8.565	0.0301	4.41	0.071

N 60 Re = 84,000

Test Results on a Rectangular Wing $\Lambda = b:t = 5$					Conversion to the Elliptical Plan for $\Lambda = b^2:F = \infty$		$c_{m\,0.25}$
Without Stream Correction			With the Finite Stream Taken into Account				
α_m	c_a	c_{wm}	c_{w5} / $c_{wm} - c_{wk5}$	α_5 / $\alpha_m - \alpha_{k5}$	$c_{w\infty}$ / $c_{wm} - c_{wk\infty}$	α_∞ / $\alpha_m - \alpha_{k\infty}$	
-25.3	-0.400	0.270	0.268	-25.004	0.2574	-23.34	-0.041
-20.3	-0.325	0.210	0.209	-20.059	0.2015	-18.71	-0.022
-15.3	-0.255	0.143	0.142	-15.110	0.1378	-14.05	-0.013
-10.3	-0.275	0.095	0.094	-10.098	0.0889	- 8.95	-0.008
- 9	-0.260	0.074	0.073	- 8.807	0.0686	- 7.72	+0.030
- 7.8	-0.120	0.044	0.0438	- 7.711	0.0429	- 7.21	0.079
- 6.5	-0.035	0.036	0.036	- 6.473	0.0359	- 6.33	0.089
- 3.5	+0.185	0.030	0.0295	- 3.638	0.0273	- 4.40	0.098
0	0.410	0.039	0.037	- 0.303	0.0258	- 2.02	0.093
2.2	0.550	0.050	0.046	+ 1.793	0.0261	- 0.51	0.088
3.5	0.635	0.0585	0.0533	3.031	0.0266	+ 0.39	0.084
6	0.790	0.077	0.069	5.419	0.0277	2.11	0.077
9	0.960	0.106	0.094	8.291	0.0331	4.29	0.072
10	-	-	-	-	-	-	-
10.4	1.020	0.122	0.109	9.647	0.0401	5.38	0.0695
Separation							
10.4	0.640	0.155	0.150	9.929	0.1227	7.27	0.095
13	0.670	-	-	-	-	-	-
14.7	0.680	0.223	0.217	14.199	0.1865	11.37	0.110
16	0.695	-	-	-	-	-	-

Test Results on a Rectangular Wing $\Lambda = b:t = 5$					Conversion to the Elliptical Plan for $\Lambda = b^2:F = \infty$		$c_{m\,0.25}$
Without Stream Correction			With the Finite Stream Taken into Account				
α_m	c_a	c_{wm}	c_{w5} $c_{wm} - c_{wk5}$	α_5 $\alpha_m - \alpha_{k5}$	$c_{w\infty}$ $c_{wm} - c_{wk\infty}$	α_∞ $\alpha_m - \alpha_{k\infty}$	
20	0.730	0.315	0.308	19.461	0.2729	16.41	0.130
9	0.615	0.133	0.128	8.546	0.1032	5.98	0.094
8	0.640	0.120	0.115	7.529	0.0877	4.88	0.093
Sudden Increase							
8	0.910	0.097	0.096	7.328	0.0311	3.52	0.073

N 60 Re = 63,000

-25.3	-0.400	0.270	0.268	-25.004	0.2574	-23.34	-0.050
-20.3	-0.325	0.210	0.209	-20.059	0.2015	-18.71	-0.020
-15.3	-0.250	0.143	0.142	-15.113	0.1381	-14.07	-0.014
-10.3	-0.275	0.096	0.095	-10.098	0.0899	- 8.95	-0.012
- 9	-0.310	0.082	0.081	- 8.77	0.0743	- 7.48	+0.003
- 7.8	-0.185	0.058	0.0575	- 7.661	0.0553	- 6.90	0.053
- 6.5	-0.100	0.045	0.0449	- 6.426	0.0442	- 6.01	0.075
- 3.5	+0.110	0.037	0.0368	- 3.582	0.0361	- 4.04	0.088
0	0.325	0.049	0.048	- 0.241	0.0405	- 1.59	0.092
2.2	0.460	0.063	0.060	+ 1.859	0.0464	- 0.06	0.092
3.5	0.520	0.077	0.073	3.118	0.0559	+ 0.96	0.092
6	0.500	0.098	0.095	5.631	0.0783	3.56	0.0925
8	0.545	0.123	0.119	7.597	0.0995	5.32	0.093

Test Results on a Rectangular Wing $\Lambda = b:t = 5$					Conversion to the Elliptical Plan for $\Lambda = b^2:F = \infty$		$c_{m\,0.25}$
Without Stream Correction			With the Finite Stream Taken into Account				
α_m	c_a	c_{wm}	c_{w5} $c_{wm} - c_{wk5}$	α_5 $\alpha_m - \alpha_{k5}$	$c_{w\infty}$ $c_{wm} - c_{wk\infty}$	α_∞ $\alpha_m - \alpha_{k\infty}$	
10	0.585	0.150	0.146	9.569	0.1231	7.12	0.095
13	0.635	0.198	0.193	12.531	0.1661	9.89	0.103
16	0.680	0.248	0.242	15.499	0.2113	12.68	0.114
20	0.730	0.315	0.308	19.461	0.2729	16.41	0.130

N 60 Re = 42,000

-25.3	-0.400	0.270	0.268	-25.004	0.2574	-23.34	-0.080
-20.3	-0.325	0.210	0.209	-20.059	0.2015	-18.71	-0.027
-15.3	-0.250	0.143	0.142	-15.113	0.1381	-14.07	-0.018
-10.3	-0.275	0.096	0.095	-10.098	0.0899	- 8.95	-0.01
- 9	-0.330	0.084	0.083	- 8.755	0.0752	- 7.38	-0.001
- 7.8	-0.250	0.072	0.071	- 7.618	0.0668	- 6.59	+0.032
- 6.5	-0.160	0.057	0.0566	- 6.380	0.0549	- 5.71	0.056
- 3.5	+0.040	0.044	0.044	- 3.530	0.0439	- 3.69	0.074
0	0.245	0.057	0.056	- 0.180	0.0519	- 1.19	0.082
2.2	0.340	0.073	0.0715	+ 1.950	0.0638	0.54	0.085
3.5	0.383	0.085	0.083	3.217	0.0733	1.62	0.0865
6	0.450	0.105	0.102	5.668	0.0891	3.79	0.089
8	0.500	0.128	0.125	7.631	0.1083	5.54	0.091
10	0.550	0.154	0.150	9.593	0.1303	7.31	0.095
13	0.613	0.201	0.197	12.547	0.1715	9.99	0.103
16	0.665	0.249	0.243	15.510	0.2139	12.73	0.114
20	0.730	0.315	0.308	19.461	0.2729	16.41	0.130

N 60 Re = 21,000

Test Results on a Rectangular Wing Λ = b:t = 5					Conversion to the Elliptical Plan for Λ = b^2:F = ∞		$c_{m\ 0.25}$
Without Stream Correction			With the Finite Stream Taken into Account				
α_m	c_a	$c_{w\ m}$	$c_{w\ 5}$ $c_{w\ m}-c_{w\ k\ 5}$	α_5 $\alpha_m-\alpha_{k\ 5}$	$c_{w\infty}$ $c_{w\ m}-c_{w\ k\infty}$	α_∞ $\alpha_m-\alpha_{k\infty}$	
-25.3	-0.400	0.270	0.268	-25,004	0.2574	-23.34	-0.130
-20.3	-0.325	0.210	0.209	-20.059	0.2015	-18.71	-0.050
-15.3	-0.250	0.143	0.142	-15.113	0.1381	-14.07	-0.025
-10.3	-0.275	0.096	0.095	-10.098	0.0899	- 8.95	-0.010
- 9	-0.345	0.086	0.084	- 8.746	0.0765	- 7.31	-0.006
- 7.8	-0.290	0.076	0.075	- 7.585	0.0691	- 6.39	+0.003
- 6.5	-0.210	0.065	0.064	- 6.341	0.0614	- 5.46	0.016
- 3.5	-0.010	0.051	0.051	- 3.492	0.051	- 3.45	0.045
0	+0.215	0.063	0.062	- 0.159	0.0592	- 1.05	0.066
2.2	0.315	0.081	0.080	+ 1.967	0.0731	0.67	0.074
3.5	0.360	0.092	0.090	3.236	0.0817	1.73	0.088
6	0.436	0.112	0.110	5.679	0.097	3.88	0.084
8	0.485	0.134	0.131	7.641	0.1155	5.61	0.089
10	0.535	0.160	0.156	9.605	0.1377	7.39	0.095
13	0.600	0.205	0.200	12.560	0.1769	10.05	0.103
16	0.660	0.250	0.244	15.515	0.2157	12.76	0.114
20	0.730	0.315	0.308	19.461	0.2729	16.41	0.130
25	0.720	0.380	0.373	24.469	0.3389	21.45	-

N 60 R Re = 168,000

Test Results on a Rectangular Wing $\Lambda = b:t = 5$					Conversion to the Elliptical Plan for $\Lambda = b^2:F = \infty$		$c_{m\ 0.25}$
Without Stream Correction			With the Finite Stream Taken into Account				
α_m	c_a	$c_{w\,m}$	$c_{w\,5}$ $c_{w\,m}-c_{w\,k\,5}$	α_5 $\alpha_m-\alpha_{k\,5}$	$c_{w\,\infty}$ $c_{w\,m}-c_{w\,k\,\infty}$	α_∞ $\alpha_m-\alpha_{k\,\infty}$	
-19	-0.425	0.218	0.216	-18.688	0.2038	-16.91	-0.070
-14	-0.390	0.151	0.149	-13.712	0.1390	-12.09	-0.059
- 9	-0.386	0.09	0.088	- 8.715	0.0782	- 7.11	-0.016
- 7	-0.306	0.045	0.044	- 6.775	0.0374	- 5.48	0.032
- 5	-0.203	0.030	0.0294	- 4.851	0.0267	- 3.99	0.025
- 3	-0.079	0.022	0.0219	- 2.944	0.0216	- 2.61	0.020
- 1	0.042	0.019	0.019	- 0.971	0.0189	- 1.21	0.016
0	0.143	0.020	0.0197	- 0.103	0.0183	- 0.71	0.023
1	0.220	0.022	0.0214	+ 0.089	0.0181	- 0.09	0.026
3	0.344	0.028	0.0265	2.746	0.0184	1.29	0.023
5	0.475	0.0363	0.0334	4.649	0.0185	2.66	0.020
7	0.600	0.048	0.0434	6.558	0.0195	4.03	0.017
9	0.726	0.0623	0.0555	8.465	0.0207	5.42	0.0142
10	0.790	0.0715	0.0634	9.418	0.0223	6.10	0.0128
11	0.842	0.080	0.0719	10.379	0.0238	6.85	0.0112
12.27	-	-	-	-	-	-	-
13	0.945	0.0995	0.0880	12.302	0.0286	8.35	0.009
14.8	-	-	-	-	-	-	-
15	1.035	0.119	0.10525	14.237	0.0343	9.89	0.0065
16.35	-	-	-	-	-	-	-
17	1.110	0.1407	0.12485	16.181	0.0425	11.51	0.0050
17.7	-	-	-	-	-	-	-

Test Results on a Rectangular Wing $\Lambda = b:t = 5$					Conversion to the Elliptical Plan for $\Lambda = b^2:F = \infty$		$c_{m\ 0.25}$
Without Stream Correction			With the Finite Stream Taken into Account				
α_m	c_a	$c_{w\ m}$	$c_{w\ 5}$ / $c_{w\ m} - c_{w\ k\ 5}$	α_5 / $\alpha_m - \alpha_{k\ 5}$	$c_{w\infty}$ / $c_{w\ m} - c_{w\ k\infty}$	α_∞ / $\alpha_m - \alpha_{k\infty}$	
19	1.135	0.162	0.145	18.163	0.0601	13.41	0.0040
	0.577	0.228	0.224	18.574	0.2017	16.16	0.0725
21	0.585	0.256	0.252	20.569	0.229	18.11	0.077
Region of Sudden Increase							
13	0.605	0.1380	0.1333	12.554	0.1091	10.01	0.043
11.15	0.658	0.1098	0.1042	10.664	0.0757	7.91	0.036
	0.845	0.0810	0.0718	10.527	0.0242	6.98	0.0112
11	0.842	0.080	0.0708	10.379	0.0238	6.84	0.0112

N 60 R Re = 126,000

13	1.012	0.1195	0.1064	12.554	0.0393	10.02	0.0065
16.35	1.045	0.135	0.121	15.578	0.0487	11.22	0.0060
	0.562	0.190	0.186	15.943	0.1654	13.58	0.0574
17	0.562	0.200	0.196	16.593	0.1754	14.23	0.0605
Region of Sudden Increase							
11	0.615	0.1098	0.1050	10.547	0.0799	7.97	-
10.85	0.625	0.1085	0.1034	10.389	0.0777	7.77	-
	0.818	0.0802	0.0715	10.245	0.0272	6.83	-

N 60 R Re = 147,000

Test Results on a Rectangular Wing $\Lambda = b:t = 5$					Conversion to the Elliptical Plan for $\Lambda = b^2:F = \infty$		$c_{m\ 0.25}$
Without Stream Correction			With the Finite Stream Taken into Account				
α_m	c_a	$c_{w\ m}$	$c_{w\ 5}$ $c_{w\ m} - c_{w\ k\ 5}$	α_5 $\alpha_m - \alpha_{k\ 5}$	$c_{w\infty}$ $c_{w\ m} - c_{w\ k\infty}$	α_∞ $\alpha_m - \alpha_{k\infty}$	
17	1.093	0.1407	0.1254	16.193	0.0467	11.63	0.0052
17.7	1.100	0.148	0.132	16.888	0.0528	12.30	0.0046
	0.575	0.2105	0.2062	17.276	0.1846	14.88	0.0643
19	0.575	0.228	0.224	18.576	0.2021	16.18	0.0725
Region of Sudden Increase							
13	0.595	0.1380	0.1334	12.562	0.1102	10.08	0.043
11	0.648	0.1095	0.1041	10.522	0.0763	7.80	0.034
	0.832	0.0808	0.0719	10.387	0.0257	6.91	0.112

N 60 R Re 105,000

-19	-0.425	0.218	0.216	-18.688	0.2038	-16.91	-0.065
-14	-0.372	0.151	0.149	-13.727	0.140	-12.18	-0.051
- 9	-0.346	0.09	0.088	- 8.746	0.08	- 7.30	-0.008
- 7	-0.263	0.044	0.043	- 6.806	0.038	- 5.72	+0.043
- 5	-0.165	0.032	0.0316	- 4.879	0.030	- 4.21	0.038
- 3	-0.049	0.0235	0.0235	- 2.966	0.0233	- 2.76	0.032
- 1	+0.080	0.0228	0.0227	- 1.057	0.0224	- 1.39	0.030

Test Results on a Rectangular Wing $\Lambda = b:t = 5$					Conversion to the Elliptical Plan for $\Lambda = b^2:F = \infty$		$c_{m\ 0.25}$
Without Stream Correction			With the Finite Stream Taken into Account				
α_m	c_a	$c_{w\,m}$	$\frac{c_{w\,5}}{c_{w\,m}-c_{w\,k\,5}}$	$\frac{\alpha_5}{\alpha_m-\alpha_{k\,5}}$	$\frac{c_{w\,\infty}}{c_{w\,m}-c_{w\,k\,\infty}}$	$\frac{\alpha_\infty}{\alpha_m-\alpha_{k\,\infty}}$	
0	0.173	0.0245	0.0241	- 0.128	0.0220	- 0.84	0.038
1	0.244	0.0268	0.0260	+ 0.821	0.0217	- 0.19	0.038
3	0.345	0.033	0.0314	2.746	0.0236	+ 1.31	0.031
5	0.465	0.0407	0.0379	4.657	0.0237	2.72	0.024
7	0.590	0.0515	0.0470	6.564	0.0242	4.11	0.019
9	0.707	0.065	0.059	8.479	0.0254	5.52	0.0155
10	0.765	0.075	0.067	9.435	0.0288	6.24	0.014
11	0.820	0.082	0.073	10.395	0.0287	6.98	0.0121
13	0.914	0.100	0.089	12.323	0.0336	8.50	0.0100
14.8	0.980	0.1205	0.1082	14.078	0.0416	9.99	0.0075
	0.544	0.165	0.1612	14.398	0.1418	12.12	0.0500
15	0.544	0.1685	0.1647	14.598	0.1452	12.32	0.0510
16.35	-	-	-	-	-	-	-
17	0.550	0.200	0.196	16.593	0.1764	14.30	0.0605
17.7	-	-	-	-	-	-	-
19	0.565	0.228	0.224	18.582	0.2029	16.22	0.0725
21	0.585	0.256	0.252	20.558	0.2291	18.13	0.077
Region of Sudden Increase							
13	0.550	0.138	0.1341	12.593	0.1124	10.30	0.043
11	0.570	0.110	0.1058	10.579	0.085	8.20	0.035
10.55	0.590	0.1052	0.1007	10.114	0.0779	7.66	
	0.796	0.078	0.070	9.963	0.0279	6.64	

N 60 R Re = 84,000

Test Results on a Rectangular Wing $\Lambda = b:t = 5$					Conversion to the Elliptical Plan for $\Lambda = b^2:F = \infty$		$c_{m\ 0.25}$
Without Stream Correction			Without Finite Stream Taken into Account				
α_m	c_a	$c_{w\,m}$	$c_{w\,5}$ / $c_{w\,m}-c_{w\,k\,5}$	α_5 / $\alpha_m-\alpha_{k\,5}$	$c_{w\,\infty}$ / $c_{w\,m}-c_{w\,k\,\infty}$	α_∞ / $\alpha_m-\alpha_{k\,\infty}$	
-19	-0.425	0.218	0.216	-18.688	0.2038	-16.91	-0.063
-14	-0.360	0.151	0.149	-13.735	0.141	-12.23	-0.047
- 9	-0.340	0.09	0.088	- 8.749	0.081	- 7.34	-0.002
- 7	-0.252	0.046	0.045	- 6.817	0.041	- 5.79	+0.050
- 5	-0.142	0.033	0.0327	- 4.898	0.031	- 4.30	0.046
- 3	-0.032	0.025	0.025	- 2.978	0.0249	- 2.85	0.042
- 1	+0.122	0.0255	0.0253	- 1.087	0.0244	- 1.59	0.045
0	0.200	0.0275	0.0270	- 0.147	0.0242	- 0.99	0.050
1	0.255	0.030	0.0291	+ 0.813	0.025	- 0.24	0.048
3	0.348	0.037	0.035	2.743	0.027	+ 1.29	0.039
5	0.460	0.0455	0.0427	4.661	0.0288	2.76	0.030
7	0.573	0.056	0.052	6.576	0.050	4.20	0.022
9	0.688	0.068	0.062	8.491	0.030	5.63	0.016
10	0.746	0.076	0.069	9.448	0.032	6.32	0.0145
11	0.798	0.086	0.078	10.411	0.036	7.08	0.0125
12.27	0.855	0.100	0.091	11.639	0.042	8.06	0.0110
	0.502	0.132	0.129	11.899	0.112	9.80	0.0430
13	0.505	0.1415	0.1382	12.627	0.1215	10.51	0.0450
14.8	-	-	-	-	-	-	-
15	0.520	0.1685	0.1650	14.616	0.1475	12.44	0.0510
16.35	-	-	-	-	-	-	-
17	0.541	0.200	0.196	16.602	0.177	14.36	0.0605

Test Results on a Rectangular Wing $\Lambda = b:t = 5$					Conversion to the Elliptical Plan for $\Lambda = b^2:F = \infty$		
Without Stream Correction			Without Finite Stream Taken into Account				
α_m	c_a	$c_{w\,m}$	$c_{w\,5}$ / $c_{w\,m}-c_{w\,k\,5}$	α_5 / $\alpha_m-\alpha_{k\,5}$	$c_{w\,\infty}$ / $c_{w\,m}-c_{w\,k\,\infty}$	α_∞ / $\alpha_m-\alpha_{k\,\infty}$	$c_{m\,0.25}$
17.7	-	-	-	-	-	-	-
19	0.564	0.228	0.224	18.584	0.203	16.22	0.0725
21	0.585	0.256	0.252	20.569	0.2291	18.13	0.077
Region of Sudden Increase							
13	0.505	0.1410	0.1378	12.627	0.121	10.51	0.045
11	0.500	0.1145	0.1113	10.631	0.095	8.54	0.04
9.8	0.525	0.0965	0.0929	9.412	0.075	7.22	-
	0.735	0.0745	0.0675	9.258	0.0316	6.19	-

N 60 R Re = 63,000

-19	-0.425	0.218	0.216	-18.688	0.2038	-16.91	-0.057
-14	-0.345	0.151	0.149	-13.744	0.141	-12.31	-0.039
- 9	-0.330	0.09	0.089	- 8.758	0.081	- 7.39	0
- 7	-0.285	0.054	0.053	- 6.79	0.047	- 5.60	+0.025
- 5	-0.142	0.0385	0.0382	- 4.898	0.0369	- 4.30	0.049
- 3	-0.027	0.029	0.0289	- 2.982	0.0289	- 2.87	0.050
- 1	+0.132	0.031	0.03075	- 1.094	0.0298	- 1.61	0.060
0	0.182	0.0335	0.0330	- 0.131	0.0306	- 0.90	0.057
1	0.204	0.037	0.0364	+ 0.851	0.033	+ 0.01	0.050

Test Results on a Rectangular Wing $\Lambda = b:t = 5$					Conversion to the Elliptical Plan for $\Lambda = b^2:F = \infty$		$c_{m\ 0.25}$
Without Stream Correction			Without Finite Stream Taken into Account				
α_m	c_a	$c_{w\ m}$	$c_{w\ 5}$ / $c_{w\ m} - c_{w\ k\ 5}$	α_5 / $\alpha_m - \alpha_{k\ 5}$	$c_{w\ \infty}$ / $c_{w\ m} - c_{w\ k\ \infty}$	α_∞ / $\alpha_m - \alpha_{k\ \infty}$	
3	0.261	0.046	0.0451	2.809	0.040	1.72	0.043
5	0.309	0.057	0.0557	4.772	0.049	3.50	0.040
7	0.363	0.074	0.072	6.732	0.063	5.22	0.040
9	0.410	0.0965	0.0943	8.698	0.0833	6.99	0.040
10	0.422	0.109	0.107	9.69	0.095	7.92	0.040
11	0.432	0.121	0.119	10.686	0.1054	8.87	0.043
12.27	-	-	-	-	-	-	-
13	0.460	0.1415	0.1387	12.662	0.1247	10.74	0.0465
14.8	-	-	-	-	-	-	-
15	0.497	0.1685	0.1653	14.634	0.1492	12.56	0.0510
16.35	-	-	-	-	-	-	-
17	0.533	0.200	0.196	16.605	0.178	14.38	0.0605
17.7	-	-	-	-	-	-	-
19	0.563	0.228	0.224	18.584	0.203	16.24	0.0725
21	0.585	0.256	0.252	20.569	0.2291	18.12	0.077
Region of Sudden Increase							
13	0.460	0.1415	0.1387	12.662	0.1247	10.74	0.0465
11	0.432	0.121	0.119	10.686	0.1054	8.87	0.043

N 60 R Re = 42,000

Test Results on a Rectangular Wing $\Lambda = b:t = 5$					Conversion to the Elliptical Plan for $\Lambda = b^2:F = \infty$		$c_{m\ 0.25}$
Without Stream Correction			Without Finite Stream Taken into Account				
α_m	c_a	$c_{w\ m}$	$c_{w\ 5}$ / $c_{w\ m} - c_{w\ k\ 5}$	α_5 / $\alpha_m - \alpha_{k\ 5}$	$c_{w\ \infty}$ / $c_{w\ m} - c_{w\ k\ \infty}$	α_∞ / $\alpha_m - \alpha_{k\ \infty}$	
-19	-0.425	0.218	0.216	-18.688	0.2038	-16.91	-0.053
-14	-0.330	0.151	0.150	-13.757	0.1421	-12.38	-0.026
- 9	-0.325	0.095	0.094	- 8.761	0.0865	- 7.40	0
- 7	-0.325	0.07	0.069	- 6.761	0.0615	- 5.40	0
- 5	-0.195	0.0516	0.0511	- 4.857	0.0485	- 4.03	0.021
- 3	-0.070	0.042	0.0419	- 2.951	0.0414	- 2.66	0.038
- 1	+0.053	0.0387	0.0387	- 1.038	0.0385	- 1.27	0.039
0	0.087	0.0400	0.0399	- 0.062	0.0393	- 0.44	0.04
1	0.140	0.043	0.0427	+ 0.899	0.0414	+ 0.30	0.045
3	0.200	0.051	0.0505	2.852	0.0478	2.00	0.041
5	0.254	0.062	0.0611	4.812	0.0568	3.73	0.040
7	0.311	0.078	0.0767	6.771	0.0702	5.45	0.040
9	0.360	0.100	0.098	8.734	0.0896	7.22	0.040
10	0.384	0.1115	0.1096	9.716	0.0996	8.09	0.040
11	0.402	0.122	0.120	10.703	0.1092	9.01	0.043
12.27	-	-	-	-	-	-	-
13	0.441	0.1425	0.1400	12.675	0.1274	10.83	0.047
14.8	-	-	-	-	-	-	-
15	0.482	0.1685	0.1655	14.643	0.1503	12.62	0.051
16.35	-	-	-	-	-	-	-
17	0.523	0.200	0.1965	16.614	0.1782	14.41	0.0605

Test Results on a Rectangular Wing $\Lambda = b:t = 5$					Conversion to the Elliptical Plan for $\Lambda = b^2:F = \infty$		$c_{m\ 0.25}$
Without Stream Correction			Without Finite Stream Taken into Account				
α_m	c_a	$c_{w\,m}$	$c_{w\,5}$ / $c_{w\,m}-c_{w\,k\,5}$	α_5 / $\alpha_m-\alpha_{k\,5}$	$c_{w\,\infty}$ / $c_{w\,m}-c_{w\,k\,\infty}$	α_∞ / $\alpha_m-\alpha_{k\,\infty}$	
17.7	-	-	-	-	-	-	-
19	0.562	0.228	0.224	18.587	0.203	16.22	0.0725
21	0.585	0.256	0.252	20.569	0.229	18.11	0.077
Region of Sudden Increase							
13	0.441	0.1425	0.1400	12.675	0.1274	10.83	0.047
11.15	-	-	-	-	-	-	-
11	0.402	0.1220	0.1199	10.703	0.1092	9.01	0.043

N 60 R Re = 21,000

-19	-0.425	0.218	0.210	-18.688	0.2038	-16.91	-
-14	-0.330	0.151	0.150	-13.757	0.1421	-12.38	-
- 9	-0.325	0.100	0.099	- 8.761	0.0915	- 7.40	0
- 7	-0.325	0.0802	0.0788	- 6.761	0.0717	- 5.40	0
- 5	-0.285	0.0632	0.0621	- 4.791	0.0565	- 3.60	0
- 3	-0.150	0.0501	0.048	- 2.891	0.0482	- 2.26	0.002
- 1	-0.050	0.0437	0.0437	- 0.966	0.0435	- 0.75	0.013
0	+0.002	0.0438	0.0438	0	0.0438	- 0.01	0.027
1	0.102	0.045	0.0449	+ 0.928	0.044	+ 0.50	0.042
3	0.160	0.0535	0.0531	2.882	0.0514	2.21	0.040

Test Results on a Rectangular Wing $\Lambda = b:t = 5$					Conversion to the Elliptical Plan for $\Lambda = b^2:F = \infty$		$c_{m\ 0.25}$
Without Stream Correction			Without Finite Stream Taken into Account				
α_m	c_a	$c_{w\,m}$	$c_{w\,5}$ $c_{w\,m}-c_{w\,k\,5}$	α_5 $\alpha_m-\alpha_{k\,5}$	$c_{w\,\infty}$ $c_{w\,m}-c_{w\,k\,\infty}$	α_∞ $\alpha_m-\alpha_{k\,\infty}$	
5	0.220	0.0645	0.0639	4.838	0.0604	3.97	0.040
7	0.277	0.081	0.080	6.796	0.075	5.65	0.040
9	0.336	0.101	0.100	8.752	0.092	7.36	0.040
10	0.361	0.112	0.110	9.734	0.102	8.23	0.040
11	0.386	0.1227	0.1208	10.716	0.1108	9.15	0.043
12.27	-	-	-	-	-	-	-
13	0.431	0.1425	0.1401	12.682	0.1278	10.89	0.047
14.8	-	-	-	-	-	-	-
15	0.477	0.1685	0.1656	14.648	0.1506	12.68	0.051
16.35	-	-	-	-	-	-	-
17	0.522	0.200	0.196	16.614	0.178	14.44	0.0605
17.7	-	-	-	-	-	-	-
19	0.561	0.228	0.2239	18.587	0.2034	16.25	0.0725
21	0.585	0.256	0.252	20.569	0.2291	18.13	0.0770
Region of Sudden Increase							
13	0.431	0.1428	0.1404	12.682	0.1281	10.89	0.0470
11	0.386	0.1227	0.1208	10.716	0.1108	9.15	0.0430

BIBLIOGRAPHY

[1] Prandtl, L., and Betz, A., Vier Abhandlungen zur Hydrodynamik und Aerodynamik (Four Discussions of Hydrodynamics and Aerodynamics), Springer-Verlag, Berlin.

[2] Prandtl, L., Abriss der Stroemungslehre (Outline of Fluid Mechanics) 2nd edition, Friedr. Vieweg & Sohn, Brunswick, 1935.

[3] Prandtl, L., Ergebnisse der Aerodynamischen Versuchsanstalt zu Goettingen [(Findings of the Aerodynamic Research Laboratory at Goettingen)], edition I, 1920; II, 1923; III, 1926; IV, 1932; R. Oldenbourg, Munich.

[4] Prandtl-Tietjens, Hydro- und Aeromechanik (Hydro- and Aeromechanics), Vols. 1 and 2, Springer-Verlag, Berlin.

[5] Handbuch der Experimentalphysik (Handbook of Experimental Physics), published by Wien and Harms, Vol. IV, Parts 1 through 3, Akademische Verlagsgesellschaft m. b. h., Leipzig.

[6] Fuchs-Hopf-Seewald, Aerodynamik (Aerodynamics), Vol. 1: Mechanics of the Airplane; Vol. 2: Theory of Air Forces; Springer-Verlag, Berlin.

[7] Weinig, F., Aerodynamik der Luftschraube (Aerodynamics of the Airplane Propeller), Springer-Verlag, Berlin.

[8] Glauert, H., Grundlagen der Tragfluegel- und Luftschraubentheorie (Fundamentals of Airfoil and Propeller Theory), Springer-Verlag, Berlin.

[9] Hoerner, S., "Tests with Spheres for Coefficients, Turbulence, and Surface Condition," Luftfahrtforschung (Aviation Research), Vol. 12, 1935, p. 42.

[10] Doetsch, H., and Kramer, H., "Systematic Profile Studies in the Large Wind Tunnel of the DVL," Luftfahrtforschung, Vol. 14, 1937, p. 480.

[11] Hansen, M., "Velocity Distribution in the Boundary Layer," Z. fuer angew. Math. Mech. (Journal for Applied Mathematics and Mechanics), Vol. 8, 1928, p. 31.

BIBLIOGRAPHY (Concluded)

[12] Jordan, P., "Lift Calculation and Flow Phenomena When Maximum Lift Is Exceeded," Dissertation at Goettingen, 1939, in Luftfahrtforschung, Vol. 16, 1939, p. 184.

[13] Riegels, F., "New Studies on Profile Properties," Luftwissen (Aeronautics), Vol. 6, 1939, p. 301.

[14] Lilienthal, O., Der Vogelflug als Grundlage der Fliegekunst (Bird Flight as a Basis of Flying), 2nd edition, R. Oldenbourg, Munich, 1910.

[15] Idrac, P., Experimentelle Untersuchungen ueber den Segelflug der Voegel (Experimental Studies of Soaring Flight of Birds), translation by F. Hoehndorf, R. Oldenbourg, Munich, 1932.

[16] Dreisch, T., Der Segelflug der Voegel (Soaring Flight of Birds), Reports and Discussions of the WGL [Wissenschaftliche Gesellschaft fuer Luftfahrt (German Scientific Society for Aeronautics)] No. 9, 1922, R. Oldenbourg, Munich.

[17] Gutsche, S., "Experiments on Wing Sections with Separated Flow," Jahrbuch der Schiffbautechnischen Gesellschaft (Yearbook of the Shipbuilding Society), 1940.

[18] Schmidt, R., Flug und Flieger im Pflanzen- und Tierreich (Flight and Fliers in the Plant and Animal Kingdom), Klasing & Co., Berlin, 1939.

[19] Hoerner, S., "Influence of Reynolds Number on the Maximum Lift of Airfoils," Research Report 65/26 of the Zentrale fuer wissenschaftliches Berichtswesen (Headquarters for Scientific Instruction), Berlin, Adlershof.

TABLE 1: Polar Chart of Wing Section G 625

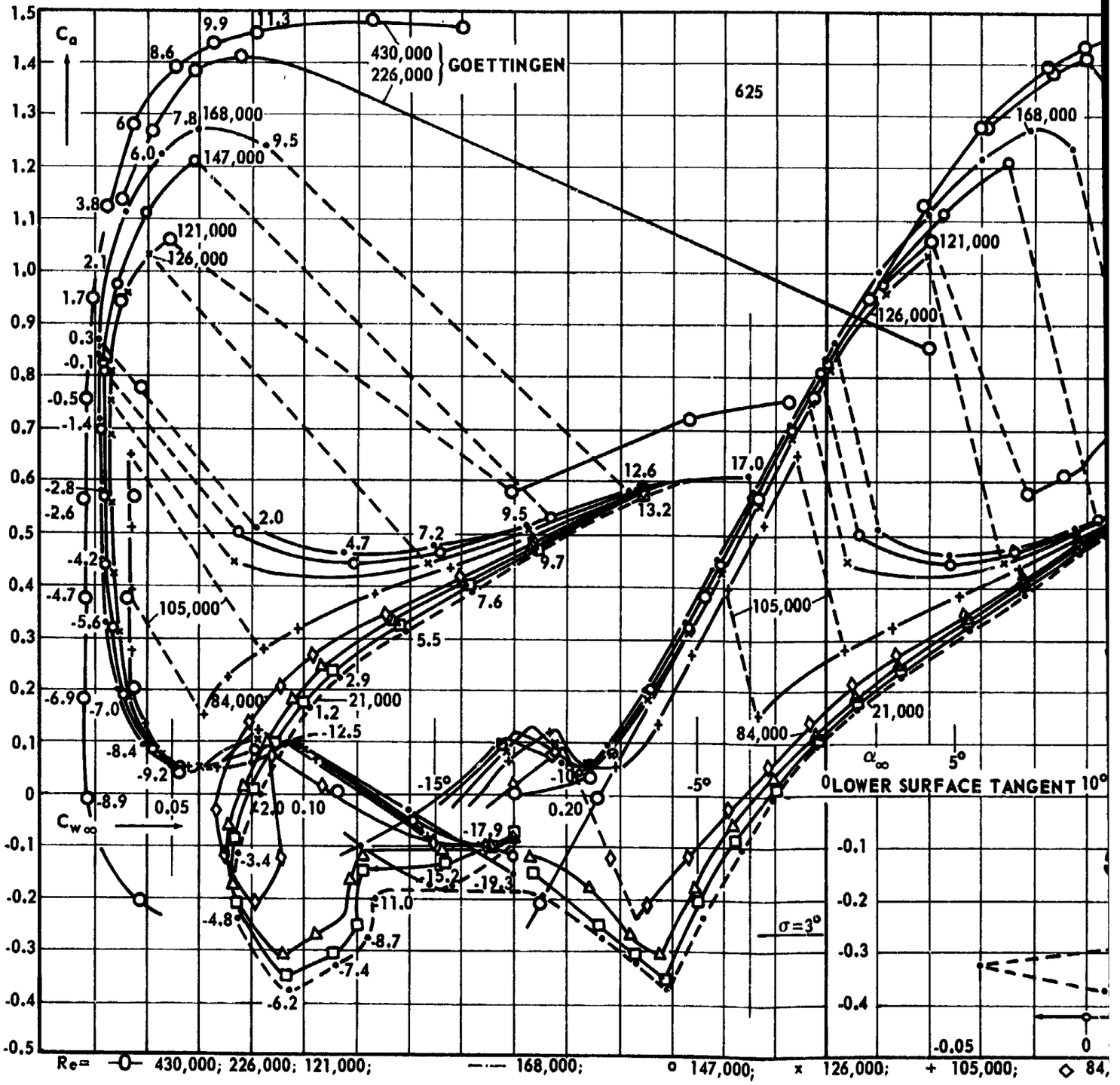

FOLDOUT FRAME

181

E 1: Polar Chart of Wing Section G 625

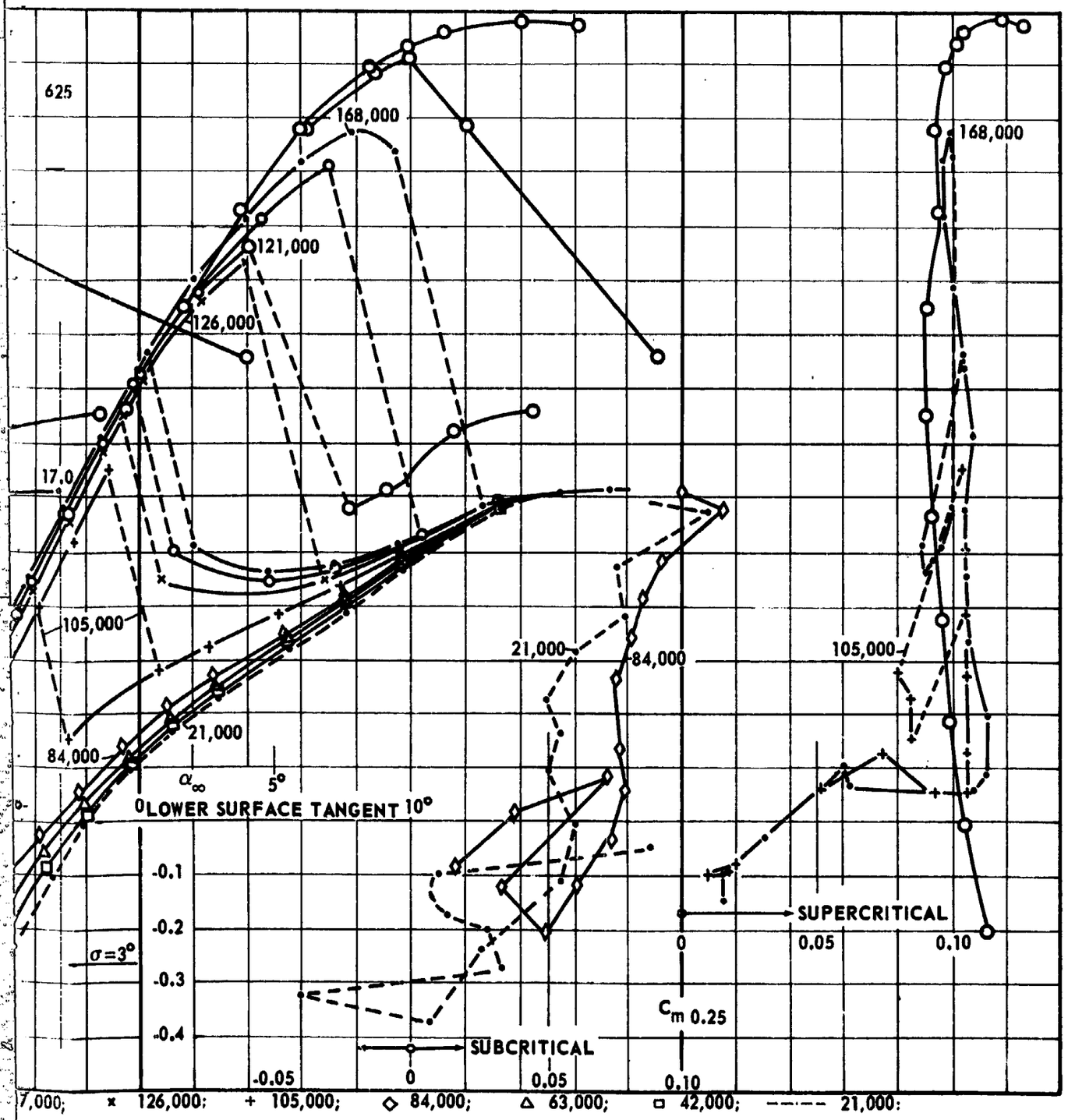

FOLDOUT FRAME 182

TABLE 2: Polar Chart of the Flat Plate

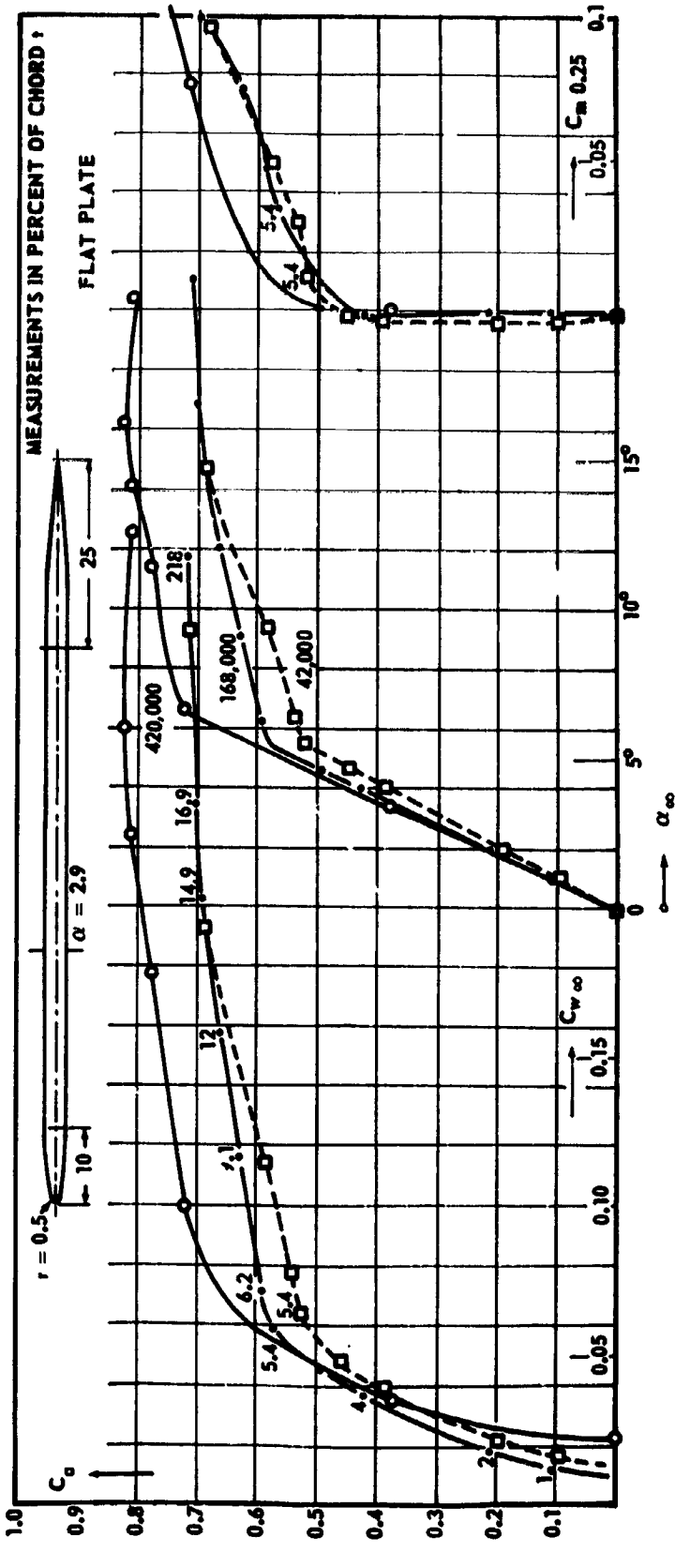

TABLE 3: Polar Chart of the Cambered Plate

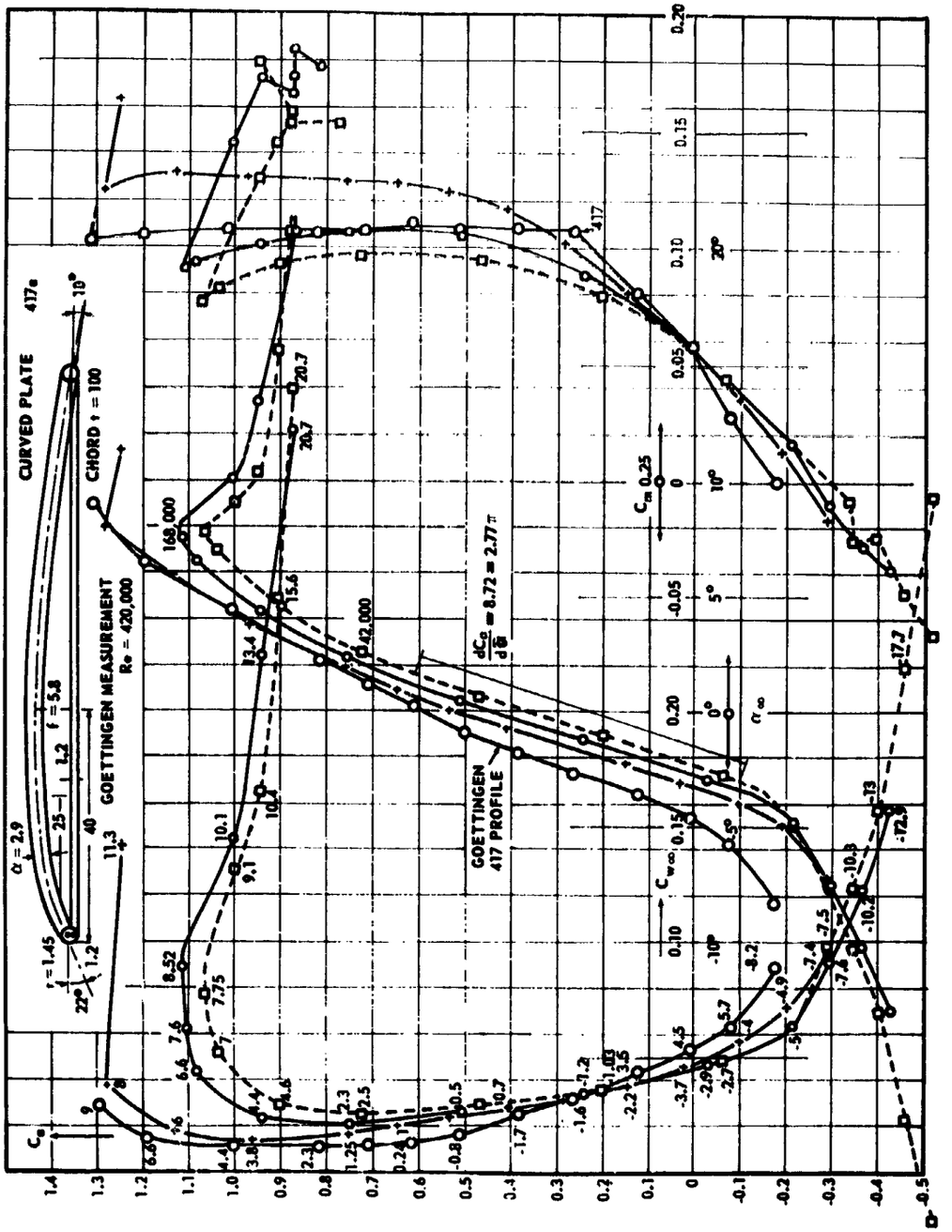

TABLE 4: Polar Chart of Wing Section N 60

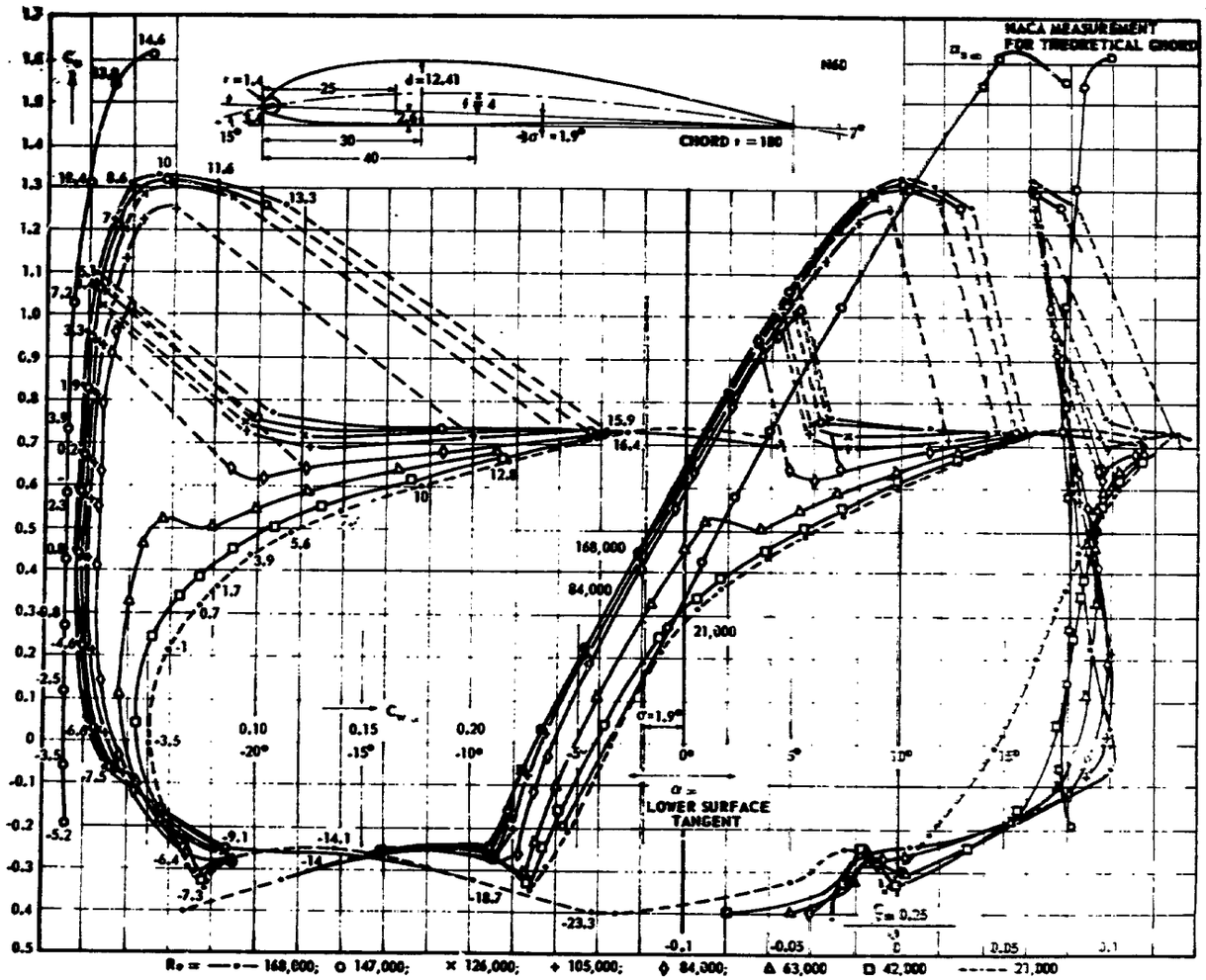

TABLE 5: Polar Chart of Wing Section N 60R

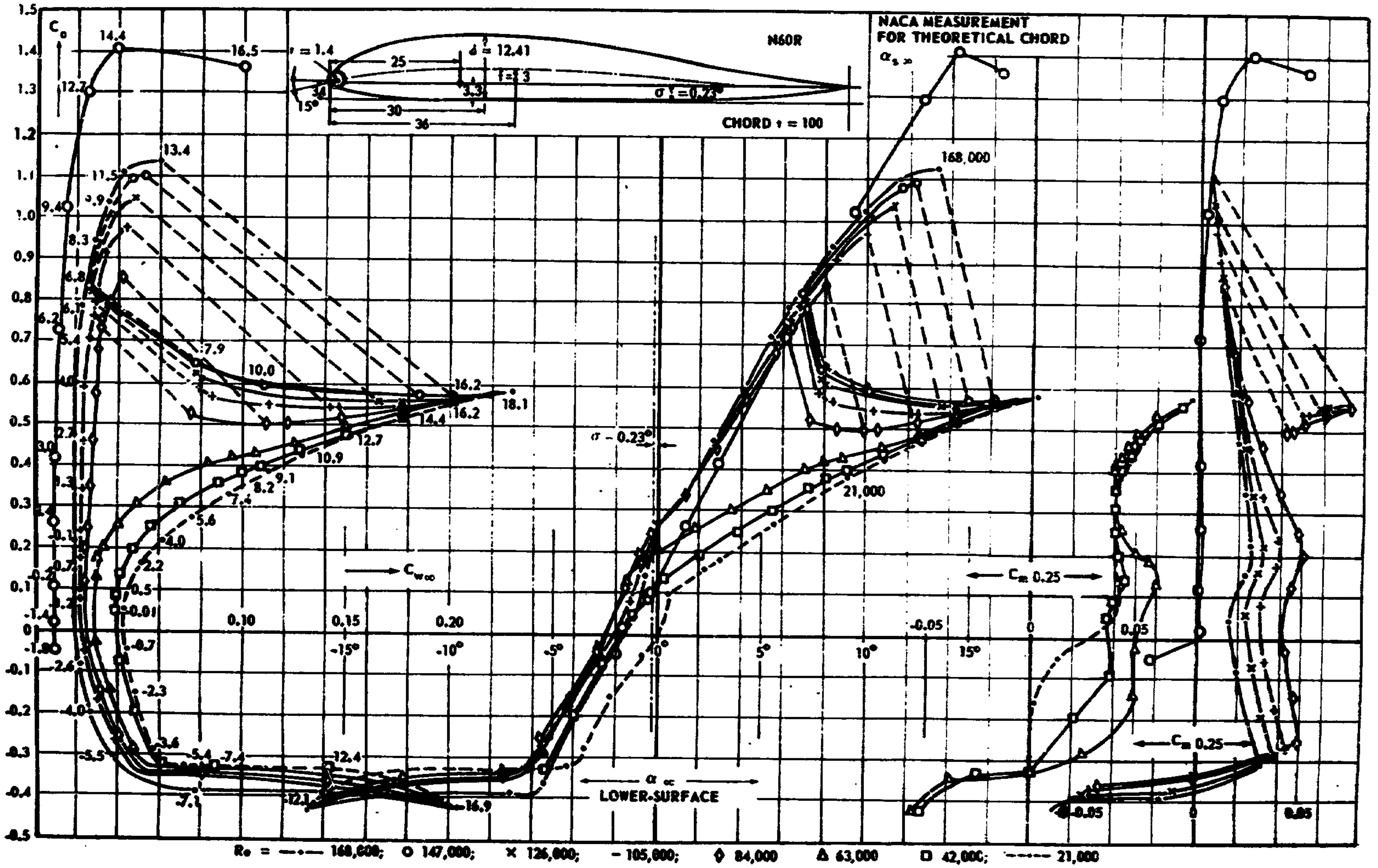

UNCLASSIFIED
Security Classification

DOCUMENT CONTROL DATA - R & D

(Security classification of title, body of abstract and indexing annotation must be entered when the overall report is classified)

ORIGINATING ACTIVITY *(Corporate author)*
Redstone Scientific Information Center
Research and Development Directorate
U. S. Army Missile Command
Redstone Arsenal, Alabama 35809

2a. REPORT SECURITY CLASSIFICATION
Unclassified

2b. GROUP
N/A

REPORT TITLE

AERODYNAMICS OF THE MODEL AIRPLANE
PART I. AIRFOIL MEASUREMENTS

PUBLISHER: C. J. E. Volckmann, Nachf. E. Wette, Berlin-Charlottenburg 2, Germany, 1942.

DESCRIPTIVE NOTES *(Type of report and inclusive dates)*
Translated from the German

AUTHOR(S) *(First name, middle initial, last name)*
F. W. Schmitz

REPORT DATE	7a. TOTAL NO. OF PAGES	7b. NO. OF REFS
16 November 1967	206	19

CONTRACT OR GRANT NO.	9a. ORIGINATOR'S REPORT NUMBER(S)
N/A PROJECT NO. N/A	RSIC-721
	9b. OTHER REPORT NO(S) *(Any other numbers that may be assigned this report)* AD_____

DISTRIBUTION STATEMENT
Each transmittal of this document outside the agencies of the U. S. Government must have prior approval of this Command, ATTN: AMSMI-RBT.

SUPPLEMENTARY NOTES	12. SPONSORING MILITARY ACTIVITY
None	Same as No. 1

ABSTRACT

Discussed are measurements that show the behavior of wing sections in the low-turbulence stream (turbulence factor = 1.06) in a measuring range from Re = 20,000 to 170,000 in which the profiles pass through a critical region. This measuring region corresponds approximately to the Reynolds number range of model airplane wings.

5
PRECEDING PAGE BLANK-NOT FILMED.

D FORM 1 NOV 65 1473 REPLACES DD FORM 1473, 1 JAN 64, WHICH IS OBSOLETE FOR ARMY USE.

UNCLASSIFIED
Security Classification

14. KEY WORDS	LINK A		LINK B		LINK C	
	ROLE	WT	ROLE	WT	ROLE	WT
Sailplane						
Similarity law						
Wing loading						
Drag - lift ratio						
Laminar boundary layer						
Convergent and divergent flow						
Upper surface flow						
Hysteresis loop						